

GL-TR-90-0003

# AD-A220 334

3

Advanced Computational Techniques in  
Regional Wave Studies

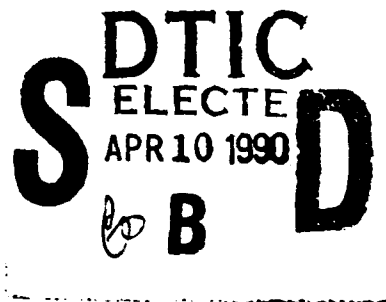
copy

R.B. Herrmann  
M.J. Jost  
D.R. Russell  
C.F. Shieh

St Louis University  
Department of Earth &  
Atmospheric Sciences  
St Louis, MO 63103

3 January 1990

Final Report  
1 July 1987 - 30 November 1989



APPROVED FOR PUBLIC RELEASE; DISTRIBUTION UNLIMITED

GEOPHYSICS LABORATORY  
AIR FORCE SYSTEMS COMMAND  
UNITED STATES AIR FORCE  
HANSCOM AIR FORCE BASE, MASSACHUSETTS 01731-5000

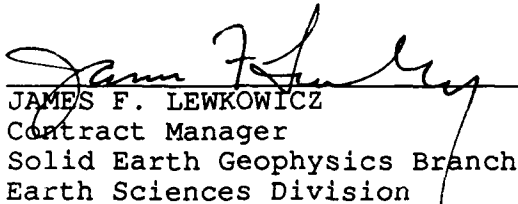
94 100

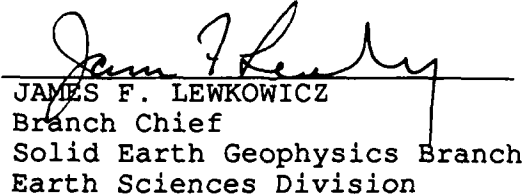
SPONSORED BY  
Defense Advanced Research Projects Agency  
Nuclear Monitoring Research Office  
ARPA ORDER NO.5299

MONITORED BY  
Geophysics Laboratory  
F19628-87-K-0047

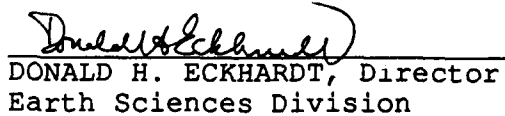
The views and conclusions contained in this document are those of the authors and should not be interpreted as representing the official policies, either expressed or implied, of the Defense Advanced Research Projects Agency or the U.S. Government.

This technical report has been reviewed and is approved for publication.

  
JAMES F. LEWKOWICZ  
Contract Manager  
Solid Earth Geophysics Branch  
Earth Sciences Division

  
JAMES F. LEWKOWICZ  
Branch Chief  
Solid Earth Geophysics Branch  
Earth Sciences Division

FOR THE COMMANDER

  
DONALD H. ECKHARDT, Director  
Earth Sciences Division

This report has been reviewed by the ESD Public Affairs Office (PA) and is releasable to the National Technical Information Service (NTIS).

Qualified requestors may obtain additional copies from the Defense Technical Information Center. All others should apply to the National Technical Information Service.

If your address has changed, or if you wish to be removed from the mailing list, or if the addressee is no longer employed by your organization, please notify GL/IMA, Hanscom AFB, MA 01731-5000. This will assist us in maintaining a current mailing list.

Do not return copies of this report unless contractual obligations or notices on a specific document requires that it be returned.

UNCLASSIFIED

SECURITY CLASSIFICATION OF THIS PAGE

## REPORT DOCUMENTATION PAGE

1a. REPORT SECURITY CLASSIFICATION <b>UNCLASSIFIED</b>		1b. RESTRICTIVE MARKINGS	
2a. SECURITY CLASSIFICATION AUTHORITY		3. DISTRIBUTION/AVAILABILITY OF REPORT approved for public release; distribution unlimited	
2b. DECLASSIFICATION/DOWNGRADING SCHEDULE		4. PERFORMING ORGANIZATION REPORT NUMBER(S)	
4. PERFORMING ORGANIZATION REPORT NUMBER(S)		5. MONITORING ORGANIZATION REPORT NUMBER(S) GL-TR-90-0003	
6a. NAME OF PERFORMING ORGANIZATION Saint Louis University	6b. OFFICE SYMBOL (If applicable)	7a. NAME OF MONITORING ORGANIZATION Geophysics Laboratory	
6c. ADDRESS (City, State and ZIP Code) Dept. of Earth and Atmospheric Sciences St. Louis, MO 63103		7b. ADDRESS (City, State and ZIP Code) Hanscom Air Force Base, MA 01731-5000	
8a. NAME OF FUNDING SPONSORING ORGANIZATION DARPA	8b. OFFICE SYMBOL (If applicable)	9. PROCUREMENT INSTRUMENT IDENTIFICATION NUMBER F19628-87-K-0047	
8c. ADDRESS (City, State and ZIP Code) 1400 Wilson Boulevard Arlington, VA 22209		10. SOURCE OF FUNDING NOS.	
11. TITLE (Include Security Classification) Advanced Computational Techniques in Regional Wave Studies		PROGRAM ELEMENT NO. 61101E	PROJECT NO. 7A10
12. PERSONAL AUTHOR(S) R.B. Herrmann, M.J. Jost, D.R. Russell, C.-F. Shieh		TASK NO. DA	WORK UNIT NO. CO
13a. TYPE OF REPORT Final	13b. TIME COVERED FROM 1 JUL 87 TO 30 NOV 89	14. DATE OF REPORT (Yr., Mo., Day) 1990 January 03	15. PAGE COUNT 136
16. SUPPLEMENTARY NOTATION			
17. COSATI CODES		18. SUBJECT TERMS (Continue on reverse if necessary and identify by block number)	
FIELD	GROUP	SUB. GR.	
		Moment tensor, phase match filtering, polarization filtering, spectral scaling	
19. ABSTRACT (Continue on reverse if necessary and identify by block number)			
<p>Work over the contract period is summarized in an overview of the project and also in four related papers. The common theme is the development of computational tools that can support DARPA sponsored research in nuclear monitoring using seismic techniques.</p> <p>The first paper, "A students guide to and review of moment tensors", provides a general review of moment tensor notation. Special emphasis is taken to relate the excitation due to an arbitrary seismic dipole/couple source to the Green's functions as defined in "Computer Programs in Seismology." Sufficient examples are given to test computer programs connecting <math>M_{ij}</math> to other representations.</p> <p>The next two papers, "Ground roll: rejection using adaptive phase matched filters" and "Ground roll: rejection using polarization filters" demonstrate the use of the tools developed to extract a low amplitude signal hidden within a large amplitude dispersed signal. The first paper utilizes techniques developed for the enhancement of surface waves by phase matched filters. The ground roll (surface wave) is iteratively isolated</p>			
20. DISTRIBUTION/AVAILABILITY OF ABSTRACT UNCLASSIFIED/UNLIMITED <input type="checkbox"/> SAME AS RPT. <input type="checkbox"/> DTIC USERS <input type="checkbox"/>		21. ABSTRACT SECURITY CLASSIFICATION UNCLASSIFIED	
22a. NAME OF RESPONSIBLE INDIVIDUAL James Lewkowicz		22b. TELEPHONE NUMBER (Include Area Code) 617/377-3028	22c. OFFICE SYMBOL GL/LWH

DD FORM 1473 83 APR

EDITION OF 1 JAN 73 IS OBSOLETE.

UNCLASSIFIED

SECURITY CLASSIFICATION OF THIS PAGE

using the data to define the proper dispersion. Once the ground roll is isolated, it is subtracted from the signal in the frequency domain.

The second paper uses the polarization properties of different seismic wave types to isolate the ground roll. This technique requires multi-component detectors to determine the type of polarization of the particle motion. Once the surface wave is isolated, it can be filtered from the data.

The final paper, "On scaling of intra-continental earthquakes," improves previous work by Nuttli on the spectral scaling of earthquakes in continental interiors. The observed magnitude for North American events agree, within scattering limits, with predictions based on the improved scaling predictions.

## SUMMARY

Work over the contract period is summarized in an overview of the project and also in four related papers. The common theme is the development of computational tools that can support DARPA sponsored research in nuclear monitoring using seismic techniques.

The first paper, "A students guide to and review of moment tensors", provides a general review of moment tensor notation. Special emphasis is taken to relate the excitation due to an arbitrary seismic dipole/couple source to the Green's functions as defined in "Computer Programs in Seismology." Sufficient examples are given to test computer programs connecting  $M_{ij}$  to other source representations.

The next two papers, "Ground roll: rejection using adaptive phase matched filters" and "Ground roll: rejection using polarization filters" demonstrate the use of the tools developed to extract a low amplitude signal hidden within a large amplitude dispersed signal. The first paper utilizes techniques developed for the enhancement of surface waves by phase matched filters. The ground roll (surface wave) is iteratively isolated using the data to define the proper dispersion. Once the ground roll is isolated, it is subtracted from the signal in the frequency domain.

The second paper uses the polarization properties of different seismic wave types to isolate the ground roll. This technique requires multi-component detectors to determine the type of polarization of the particle motion. Once the surface wave is isolated, it can be filtered from the data.

The final paper, "On scaling of intra-continental earthquakes," improves previous work by Nuttli on the spectral scaling of earthquakes in continental interiors. The observed magnitude for North American events agree, within scattering limits, with predictions based on the improved scaling predictions.

Accession For	
NTIS GRA&I	<input checked="" type="checkbox"/>
DTIC TAB	<input type="checkbox"/>
Unannounced	<input type="checkbox"/>
Justification	
By _____	
Distribution/	
Availability Codes	
Dist	Avail and/o. Special
A-1	

QUALITY  
INSPECTED  
9

# ADVANCED COMPUTATIONAL TECHNIQUES IN REGIONAL WAVE STUDIES

## DISCUSSION

The purpose of this contract was to perform computational studies that would increase our understanding of the Lg arrival and its coda, especially the use of the coda to define a path specific attenuation operator for the Lg arrival. This is a very difficult problem which requires the incorporation of realistic scattering mechanisms for forward modeling of the phenomena.

### *Work done*

It was realized that stable, well understood, synthetic seismograms for simpler homogeneous plane layers is required first. Toward this end, programs developed for other projects were documented and distributed through the Center for Seismic Studies for use by other researchers. These programs consisted of over 80,000 lines of code and 800 pages of documentation. Much effort was spent refining this package, especially those portions written by students, to ensure legibility and numerically stable results.

The set of six volumes of "Computer Programs in Seismology" were distributed by the Center for Seismic Studies to the following organizations:

<u>Organization</u>	<u>Contact</u>
ENSCO (FLA)	H. Ghalib
ENSCO (VA)	Z. Der
SMU	B. Stump
U. Ruhr	H.-P. Harjes
USGS	S. Sipkin
S. Radiomana	B. Massinon
AFTAC	N. Yacoub

In addition, other DARPA/AFGL contractors have obtained copies directly from Saint Louis University.

Toward the latter part of the project, the computer programs were stable enough to attempt to look at real data. As reported in Quarterly Management Report No. 8, the Lg and surface-wave signals from a strip mining blast 250 km away in western Kentucky were used to infer a source yield of about 0.1 kT. The implication of this result is that more than one wavetype at regional distances can be used to obtain a robust seismic estimate yield of small explosions.

One of the unknowns is the value of  $Q_\beta$  in the upper 3 km of the earth. We have been looking at data from refraction profiles in Maine, from shallow seismic investigations in flood plains, and from regionally recorded mining blasts to define both the robust analysis procedures required and the shallow shear-wave velocity and  $Q_\beta$ .

Three dissertations were completed:

Russell, D. R., (1987). Multi-channel processing of dispersed surface waves.

Shieh, C.-F., (1988). Polarization analysis of complex seismic wave field.

M. L. Jost (1989). Long period strong ground motions and response spectra of large historical earthquakes in the central and eastern United States from kinematic source models, *Ph. D. Dissertation*, Saint Louis University.

David Russell is currently with AFTAC, performing work related to that supported by DARPA/AFGL. Michael Jost has taken a position at the University of the Ruhr, working with the new GERESS data.

The dissertation work emphasized the development and use of advanced computational techniques for studying regional seismic phases. Russell (1987) implemented surface-wave inversion, single and multi-channel phase matched filtering for the analysis of dispersed surface waves. Shieh (1988) focused on polarization filtering, with emphasis on exploration data, but he also considered representative teleseismic signals. Jost (1989) made use of the programs to estimate low frequency ground motion at short distances from large earthquakes. He found it necessary to modify a scaling relationship for continental/plate interiors proposed by Nuttli (Jost's paper is attached). His work provides a better definition of how intra-continental earthquakes should behave.

#### *Recommendations*

The discrimination and quantification problems become difficult for small events. On the other hand, the possibility of new data sources at regional distances permits using previously ignored signals. Unfortunately, these regional signals will travel large distances through a heterogeneous crust. Attempts must be made to use the data to define path dependent attenuation operators and to understand the effects of both source and path heterogeneity on the observed signal. Even though moment tensor inversion may not be used too much for large explosions, such inversion of regional phase data, especially surface-wave, may provide added constraints on whether the small explosive source is point or distributed.

## TABLE OF CONTENTS

Summary .....	iii
Discussion .....	v
Table of Contents .....	vii
A student's guide to and review of moment tensors .....	1
Ground roll: rejection using adaptive phase matched filters .....	22
On scaling of intra-continental earthquakes .....	40
Ground roll: rejection using polarization filter.....	98



A Student's Guide to and Review of Moment Tensors

M. L. Jost and R. B. Herrmann

Department of Earth and Atmospheric Sciences  
Saint Louis University  
P. O. Box 8099  
St. Louis, MO 63156

ABSTRACT

A review of a moment tensor for describing a general seismic point source is presented to show a second order moment tensor can be related to simpler seismic source descriptions such as centers of expansion and double couples. A review of literature is followed by detailed algebraic expansions of the moment tensor into isotropic and deviatoric components. Specific numerical examples are provided in the appendices for use in testing algorithms for moment tensor decomposition.

INTRODUCTION

A major research interest in seismology is the description of the physics of seismic sources. A common approach is the approximation of seismic sources by a model of equivalent forces that correspond to the linear wave equations neglecting non-linear effects in the near source region (Geller, 1976; Aki and Richards, 1980; Kennett, 1983; Bullen and Bolt, 1985). Equivalent forces are defined as producing displacements at the earth's surface that are identical to those from the actual forces of the physical process at the source. The equivalent forces are determined from observed seismograms that contain information about the source and path and distortions due to the recording. Hence, the principle problem of source studies is the isolation of the source effect by correcting for instrument and path.

The classical method of describing seismic sources, having small dimensions compared to the wavelengths of interest (point source approximation) is by their strength (magnitudes, seismic moment) and their fault plane solution (Honda, 1962; Hirasawa and Stauder, 1965; Herrmann, 1975). Recently, seismic moment tensors have been used routinely for describing seismic point sources (e.g. Kanamori and Given, 1982; Dziewonski and Woodhouse, 1983b; Dziewonski *et al.*, 1983a-c, 1984a-c; Giardini, 1984; Ekström and Dziewonski, 1985; Dziewonski *et al.*, 1985a-d, 1986a-c, 1987a-f; Ekström *et al.*, 1987; Sipkin, 1987; PDE monthly listings published by NEIS). Gilbert (1970) introduced moment tensors for calculating the displacement at the free surface which can be expressed as a sum of moment tensor elements times the corresponding Green's function. An elastodynamic Green's function is a displacement field due to an unidirectional unit impulse, i.e. the Green's function is the impulse response of the medium between source and receiver. The response of the medium to any other time function is the convolution (Arfken, 1985) of that time function with the impulse response. The Green's function depends on source and receiver coordinates, the earth model, and is a tensor (Aki and Richards, 1980). The linearity between the moment tensor and Green's function elements was first used by Gilbert (1973) for calculating moment tensor elements from observations (moment tensor inversion). The concept of seismic moment tensors

was further extended by Backus and Mulcahy (1976), and Backus (1977a, b). Moment tensors can be determined from free oscillations of the earth (e.g. Gilbert and Dziewonski, 1975), long-period surface waves (e.g. McCowan, 1976; Mendiguren, 1977; Patton and Aki, 1979; Patton, 1980; Kanamori and Given, 1981, 1982; Romanowicz, 1981; Lay *et al.*, 1982; Nakanishi and Kanamori, 1982, 1984) or long-period body waves (e.g. Stump and Johnson, 1977; Strelitz, 1978, 1980; Ward, 1980a, b; Fitch *et al.*, 1980; Fitch, 1981; Langston, 1981; Dziewonski *et al.*, 1981; Dziewonski and Woodhouse, 1983a, b). Throughout this Student's Guide, we will focus on second-rank, time independent moment tensors (Appendix I). We refer to Dziewonski and Gilbert (1974), Gilbert and Dziewonski (1975), Backus and Mulcahy (1976), Backus (1977a), Stump and Johnson (1977), Strelitz (1980), Sipkin (1982), and Vasco and Johnson (1988) for a description of time dependent moment tensors. Higher order moment tensors are discussed by Backus and Mulcahy (1976), Backus (1977a, b), and Dziewonski and Woodhouse (1983a).

The reason that moment tensors are important is that they completely describe in a first order approximation the equivalent forces of general seismic point sources. The equivalent forces can be correlated to physical source models such as sudden relative displacement at a fault surface (elastic rebound model by H. F. Reid, 1910), rapidly propagating metastable phase transitions (Evison, 1963), sudden volume collapse due to phase transitions, or sudden volume increase due to explosions (Kennett, 1983; Vasco and Johnson, 1988). The equivalent forces representing a sudden displacement on a fault plane form the familiar double couple. The equivalent forces of a sudden change in shear modulus in presence of axial strain are represented by a linear vector dipole (Knopoff and Randall, 1970). In conclusion, a seismic moment tensor is a general concept, describing a variety of seismic source models, the shear dislocation (double couple source) being just one of them.

The equivalent forces can be determined from an analysis of the eigenvalues and eigenvectors of the moment tensor (Appendix I). The sum of the eigenvalues of the moment tensor describes the volume change in the source (isotropic component of the moment tensor). If the

sum is positive, the isotropic component is due to an explosion. The source has an implosive component if the sum is negative. If the sum of the eigenvalues vanishes, then the moment tensor has only deviatoric components. The deviatoric moment tensor represents a pure double couple source if one eigenvalue equals zero. If none of the eigenvalues vanishes and their sum still equals zero, the moment tensor can be decomposed into a major and minor double couple (Kanamori and Given, 1981), or a double couple and a compensated linear vector dipole (CLVD) (Knopoff and Randall, 1970). A CLVD is a dipole that is corrected for the effect of volume change, describing seismic sources which have no volume change, net force, or net moment. In general, a complete moment tensor can be the superposition of an isotropic component and three vector dipoles (or three CLVD's, or three double couples, Ben-Menahem and Singh, 1981).

This Student's Guide is an extension of "A student's guide to the use of P- and S- wave data for focal mechanism determination" (Herrmann, 1975). Hence, emphasis is given illustrating the relations between classical fault plane solutions and seismic moment tensors. Addressing general seismic point sources, we provide examples of moment tensor decompositions into basic equivalent source representations, as contributions of dipoles or double couple sources. Clarification of terms such as major and minor double couple or compensated linear vector dipole is provided. Moment tensor inversion schemes are briefly summarized. In the appendices, examples of the use of notation by different authors are given along with some numerical results which are useful for testing computer programs. Furthermore, the formulation of the basic Green's functions by Herrmann and Wang (1985) is connected to a simple moment tensor inversion scheme.

### GENERAL ELASTODYNAMIC SOURCE

By using the representation theorem for seismic sources (Aki and Richards, 1980), the observed displacement  $d_n$  at an arbitrary position  $\mathbf{x}$  at the time  $t$  due to a distribution of equivalent body force densities,  $f_k$ , in a source region is

$$d_n(\mathbf{x}, t) = \int_{-\infty}^{\infty} \int_V G_{nk}(\mathbf{x}, t; \mathbf{r}, \bar{t}) f_k(\mathbf{r}, \bar{t}) dV(\mathbf{r}) d\bar{t}, \quad (1)$$

where  $G_{nk}$  are the components of the Green's function containing the propagation effects, and  $V$  is the source volume where  $f_k$  are non-zero. We assume the summation convention for repeated indices (Arfken, 1985). The subscript  $n$  indicates the component of the displacement. Throughout, we will use the following coordinate system (Figure 1): The  $x$ -axis points towards north, the  $y$ -axis towards east, and the  $z$ -axis down (this system is right handed). Then,  $\mathbf{e}_x$ ,  $\mathbf{e}_y$ , and  $\mathbf{e}_z$  are the unit vectors towards north, east, and vertically down, respectively.

By assuming that the Green's functions vary smoothly within the source volume in the range of moderate frequencies, the Green's functions can be expanded into a Taylor series around a reference point to facilitate the spatial integration in (1) (Kennett, 1983; Arfken, 1985). The expansion is usually done around the centroid  $\mathbf{r} = \xi$ . The physical source region is characterized by the existence of the equivalent forces. These forces

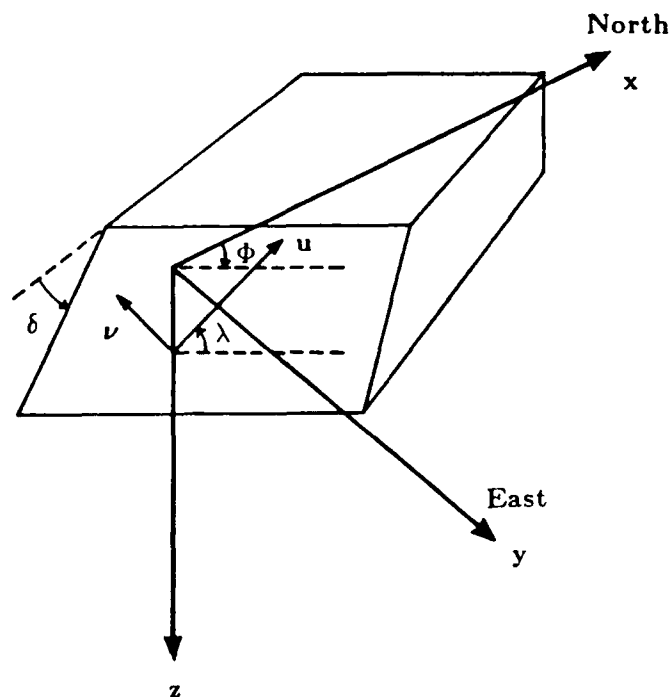


Fig. 1. Definition of the Cartesian coordinates  $(x, y, z)$ . The origin is at the epicenter. Strike is measured clockwise from north, dip from horizontal down, and slip counterclockwise from horizontal.  $\mathbf{u}$  and  $\mathbf{\nu}$  are the slip vector and fault normal, respectively (modified after Aki and Richards, 1980).

arise due to differences between the model stress and the actual physical stress (stress glut, Backus and Mulcahy, 1976). Outside the source region, the stress glut vanishes as do the equivalent forces. The centroid of the stress glut is then a weighted mean position of the physical source region (Backus, 1977a; Aki and Richards, 1980; Dziewonski and Woodhouse, 1983a). It seems that the centroid of the stress glut gives a better position for the equivalent point source of an earthquake than the hypocenter which describes just the position of rupture initialization. The Taylor series expansion of the components of the Green's function around this new reference point is

$$G_{nk}(\mathbf{x}, t; \mathbf{r}, \bar{t}) = \sum_{m=0}^{\infty} \frac{1}{m!} (r_{j_1} - \xi_{j_1}) \cdots (r_{j_m} - \xi_{j_m}) G_{nk, j_1 \cdots j_m}(\mathbf{x}, t; \xi, \bar{t}). \quad (2)$$

The comma between indices in (2) describes partial derivatives with respect to the coordinates after the comma. We define the components of the time dependent force moment tensor as :

$$M_{kj_1 \cdots j_m}(\xi, \bar{t}) = \int_V (r_{j_1} - \xi_{j_1}) \cdots (r_{j_m} - \xi_{j_m}) f_k(\mathbf{r}, \bar{t}) dV. \quad (3)$$

If conservation of linear momentum applies, such as for a source in the interior of a body, then a term in  $M_k$  does not exist in (3). With the Taylor expansion (2) and the definition of the time dependent moment tensor (3), the displacement (1) can be written as a sum of terms which resolve additional details of the source (multipole expansion).

## A Student's Guide to and Review of Moment Tensors

sion, Backus and Mulcahy, 1976; Stump and Johnson, 1977; Aki and Richards, 1980; Kennett, 1983; Dziewonski and Woodhouse, 1983a; Vasco and Johnson, 1988):

$$d_n(\mathbf{x}, t) = \quad (4)$$

$$\sum_{m=1}^{\infty} \frac{1}{m!} G_{nk,j_1, \dots, j_m}(\mathbf{x}, t, \xi, \bar{t}) * M_{kj_1, \dots, j_m}(\xi, \bar{t}),$$

where \* denotes the temporal convolution. By using a seismic signal that has much longer wavelengths than the dimensions of the source (point source approximation), we need to consider only the first term in (4) (Backus and Mulcahy, 1976; Stump and Johnson, 1977). Note, that single forces will not be present in (4) if there are no externally applied forces (indigenous source). The total force, linear and angular momentum must vanish for the equivalent forces of an indigenous source (Backus and Mulcahy, 1976). The conservation of angular momentum for the equivalent forces leads to the symmetry of the seismic moment tensor (Gilbert, 1970).

We assume that all components of the time dependent seismic moment tensor in (4) have the same time dependence  $s(t)$  (synchronous source, Silver and Jordan,

1982). Neglecting higher order terms, we get (Stump and Johnson, 1977)

$$d_n(\mathbf{x}, t) = M_{kj} [ G_{nk,j} * s(\bar{t}) ] \quad (5)$$

$M_{kj}$  are constants representing the components of the second order seismic moment tensor  $\mathbf{M}$ , usually termed *the* moment tensor. Note that the displacement  $d_n$  is a linear function of the moment tensor elements and the terms in the square brackets. If the source time function  $s(t)$  is a delta function, the only term left in the square brackets is  $G_{nk,j}$  describing nine generalized couples. The derivative of a Green's function component with respect to the source coordinate  $\xi_j$  is equivalent to a single couple with arm in the  $\xi_j$  direction. For  $k = j$ , i.e. force in the same direction as the arm, the generalized couples are vector dipoles (Figure 2; Maruyama, 1964). Thus, the moment tensor component  $M_{kj}$  gives the excitation of the generalized (k,j) couple.

### DOUBLE COUPLE SOURCES

The moment tensor components in (5) in an isotropic medium for a double couple of equivalent forces are given by

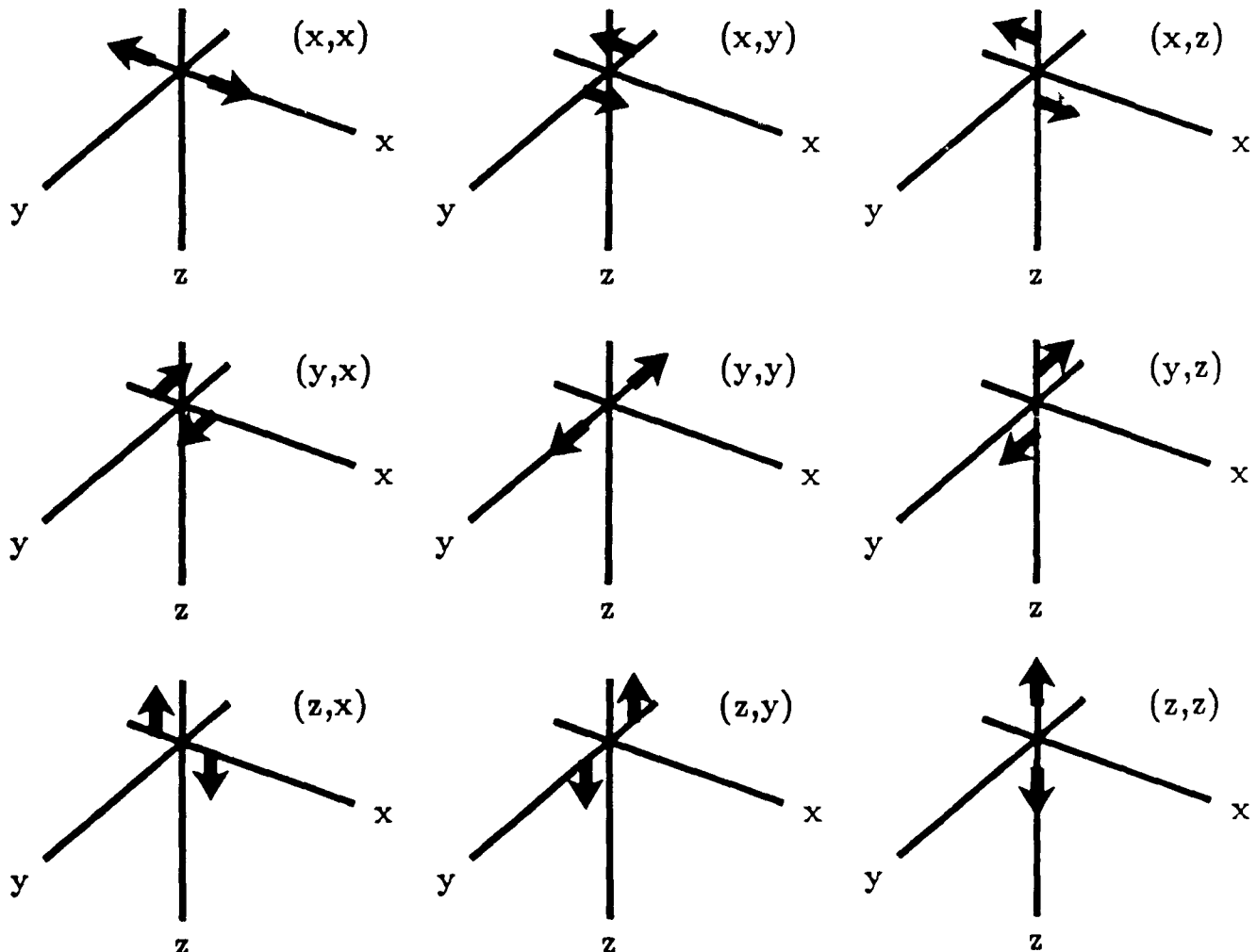


Fig. 2. The nine generalized couples representing  $G_{nk,j}$  in (5) (modified after Aki and Richards, 1980).

$$M_{kj} = \mu A (u_k \nu_j + u_j \nu_k) \quad (6)$$

where  $\mu$  is the shear modulus,  $A$  is the area of the fault plane,  $\mathbf{u}$  denotes the slip vector on the fault surface, and  $\nu$  is the vector normal to the fault plane (Aki and Richards, 1980; Ben-Menahem and Singh, 1981). Note that the contributions of the vector of the fault normal  $\nu$  and the slip vector  $\mathbf{u}$  are symmetric in (6). From the symmetry of  $\mathbf{M}$ , we note that the roles of the vectors  $\mathbf{u}$  and  $\nu$  could be interchanged without affecting the displacement field; i.e. the fault normal could equivalently be the slip vector and vice versa. This well known fault plane - auxiliary plane ambiguity cannot be resolved from the seismic radiation of a point source. Hence studies of locations of aftershocks, surface faulting, rupture directivity, or static final displacements (Backus, 1977a) need to be done in order to resolve this ambiguity.

The term  $u_k \nu_j + u_j \nu_k$  in (6) forms a tensor,  $\mathbf{D}$ , describing a double couple. This tensor is real and symmetric, giving real eigenvalues and orthogonal eigenvectors (Appendix I). The eigenvalues are proportional to (1, 0, -1). Hence, the characteristic properties of a moment tensor representing a double couple are i) one eigenvalue of the moment tensor vanishes, and ii) the sum of the eigenvalues vanishes, i.e. the trace of the moment tensor is zero (the other two eigenvalues are constrained to equal magnitude but opposite sign).

Let  $\mathbf{t}$ ,  $\mathbf{b}$ , and  $\mathbf{p}$  designate the orthogonal eigenvectors to the above eigenvalues (Herrmann, 1975; Backus, 1977a; Dziewonski and Woodhouse, 1983a).

$$\mathbf{t} = \frac{1}{\sqrt{2}} (\nu + \mathbf{u}) \quad (7)$$

$$\mathbf{b} = \nu \times \mathbf{u} \quad (8)$$

$$\mathbf{p} = \frac{1}{\sqrt{2}} (\nu - \mathbf{u}) \quad (9)$$

The tensor  $\mathbf{D}$  corresponding to the terms in the brackets in (6) can be diagonalized (principal axis transformation, see Appendix I), where the eigenvectors give the directions of the principal axes. The eigenvector  $\mathbf{b}$  corresponding to the eigenvalue zero gives the null-axis, the eigenvector  $\mathbf{t}$  corresponding to the positive eigenvalue gives the tension axis,  $T$ , and the eigenvector  $\mathbf{p}$  corresponding to the negative eigenvalue gives the pressure axis,  $P$ , of the tensor. These axes can be related to the corresponding axes of the fault plane solution, since we are focusing on pure double couple sources. The  $P$ -axis is in the direction of maximum compressive motion on the fault surface; the  $T$ -axis is the direction of maximum tensional motion. Note that the  $P$ - and  $T$ -axes inferred from the motion on the fault surface are not necessarily identical to the axes of maximum tectonic stress, since the motion can be on a preexisting plane of weakness rather than on a newly formed fault plane that would correspond to the maximum tectonic stress (McKenzie, 1969). However, this ambiguity cannot be resolved from the seismic radiation. In order to determine the direction of maximum tectonic stress, additional geological data such as *in situ* stress measurements and frictional forces is necessary. Lacking this kind of information, it is generally assumed that the  $P$ - and  $T$ -axes found from the seismic wave radiation are somewhat indicative of the direction of tectonic stress.

The double couple  $u_k \nu_j + u_j \nu_k$  can equivalently be described by its eigenvectors (Gilbert, 1973).

$$u_k \nu_j + u_j \nu_k = t_k t_j - p_j p_k \quad (10)$$

$$= 0.5 [(t_k + p_k)(t_j - p_j) + (t_k - p_k)(t_j + p_j)]$$

Comparing the terms in (10), we find the relation between tension and pressure axes and slip vector and fault normal (Appendix I):

$$\mathbf{u} = \frac{1}{\sqrt{2}} (\mathbf{t} + \mathbf{p}) \quad (11)$$

$$\nu = \frac{1}{\sqrt{2}} (\mathbf{t} - \mathbf{p}) \quad (12)$$

The other nodal plane is defined by

$$\mathbf{u} = \frac{1}{\sqrt{2}} (\mathbf{t} - \mathbf{p}) \quad (13)$$

$$\nu = \frac{1}{\sqrt{2}} (\mathbf{t} + \mathbf{p}) \quad (14)$$

If strike,  $\Phi$ , dip,  $\delta$ , and slip,  $\lambda$ , of the faulting are known, the slip vector  $\mathbf{u}$  and the fault normal  $\nu$  are given by (Aki and Richards, 1980)

$$\begin{aligned} \mathbf{u} = & \bar{u} (\cos \lambda \cos \Phi + \cos \delta \sin \lambda \sin \Phi) \mathbf{e}_x \\ & + \bar{u} (\cos \lambda \sin \Phi - \cos \delta \sin \lambda \cos \Phi) \mathbf{e}_y \\ & - \bar{u} \sin \delta \sin \lambda \mathbf{e}_z \end{aligned} \quad (15)$$

where  $\bar{u}$  is the mean displacement on the fault plane. The fault normal  $\nu$  is

$$\nu = -\sin \delta \sin \Phi \mathbf{e}_x + \sin \delta \cos \Phi \mathbf{e}_y - \cos \delta \mathbf{e}_z \quad (16)$$

The scalar product of  $\mathbf{u}$  and  $\nu$  is zero. The strike of the fault plane,  $\Phi$ , is measured clockwise from north, with the fault plane dipping to the right when looking along the strike direction. Equivalently, the hanging wall is then to the right (Figure 1). The dip,  $\delta$ , is measured down from the horizontal. The slip,  $\lambda$ , is the angle between the strike direction and the direction the hanging wall moved relative to the foot wall (the slip is positive when measured counterclockwise as viewed from the hanging wall side). The range of the fault orientation parameters are  $0 \leq \Phi \leq 2\pi$ ,  $0 \leq \delta \leq \frac{\pi}{2}$ , and  $-\pi \leq \lambda \leq \pi$  (Herrmann, 1975; Aki and Richards, 1980). The scalar seismic moment is

$$M_0 = \mu A \bar{u} \quad (17)$$

Equation (6) together with (15), (16), and (17) lead to the Cartesian components of the symmetric moment tensor in terms of strike, dip, and slip angles.

$$\begin{aligned} M_{xx} &= -M_0 (\sin \delta \cos \lambda \sin 2\Phi + \sin 2\delta \sin \lambda \sin^2 \Phi) \\ M_{yy} &= M_0 (\sin \delta \cos \lambda \sin 2\Phi - \sin 2\delta \sin \lambda \cos^2 \Phi) \\ M_{zz} &= M_0 (\sin 2\delta \sin \lambda) \\ M_{xy} &= M_0 (\sin \delta \cos \lambda \cos 2\Phi + 0.5 \sin 2\delta \sin \lambda \sin 2\Phi) \\ M_{xz} &= -M_0 (\cos \delta \cos \lambda \cos \Phi + \cos 2\delta \sin \lambda \sin \Phi) \\ M_{yz} &= -M_0 (\cos \delta \cos \lambda \sin \Phi - \cos 2\delta \sin \lambda \cos \Phi) \end{aligned} \quad (18)$$

Different notation of the moment tensor elements are discussed in Appendix II. In Appendix III, several simple

## A Student's Guide to and Review of Moment Tensors

moment tensors are related to fault plane solutions. Body-wave and surface wave radiation patterns from a source represented by a moment tensor are discussed by Kennett (1988).

Since the seismic moment tensor is real and symmetric, a principal axis transformation can be found, diagonalizing  $M$  (Appendix I). The diagonal elements are the eigenvalues  $m_i$  of  $M$ . Then, the scalar seismic moment can be determined from a given moment tensor by

$$M_0 = \frac{1}{2} ( |m_1| + |m_2| ) , \quad (19)$$

where  $m_1$  and  $m_2$  are the largest eigenvalues (in the absolute sense). The seismic moment can equivalently be estimated by the relations (Silver and Jordan, 1982):

$$M_0 = \left( \frac{\sum M_{kj}^2}{2} \right)^{\frac{1}{2}} = \left( \frac{\sum m_i^2}{2} \right)^{\frac{1}{2}} . \quad (20)$$

### GENERAL SEISMIC POINT SOURCES

In this section, it is assumed that the seismic source *cannot* be described by a pure double couple mechanism. The moment tensor is represented as sum of an isotropic part, which is a scalar times the identity matrix, and a deviatoric part.

In order to derive a general formulation of the moment tensor decomposition, let's consider the eigenvalues and orthonormal eigenvectors of the moment tensor. Let  $m_i$  be the eigenvalue corresponding to the orthonormal eigenvector  $\mathbf{a}_i = (a_{ix}, a_{iy}, a_{iz})^T$ . Using the orthonormality of the eigenvectors (Appendix I, (A1.5)), we can write the principal axis transformation of  $M$  in reverse order as:

$$\begin{aligned} \mathbf{M} &= \begin{bmatrix} \mathbf{a}_1 & \mathbf{a}_2 & \mathbf{a}_3 \end{bmatrix} \mathbf{m} \begin{bmatrix} \mathbf{a}_1^T \\ \mathbf{a}_2^T \\ \mathbf{a}_3^T \end{bmatrix} \\ &= \begin{bmatrix} a_{1x} & a_{2x} & a_{3x} \\ a_{1y} & a_{2y} & a_{3y} \\ a_{1z} & a_{2z} & a_{3z} \end{bmatrix} \begin{bmatrix} m_1 & 0 & 0 \\ 0 & m_2 & 0 \\ 0 & 0 & m_3 \end{bmatrix} \begin{bmatrix} a_{1x} & a_{1y} & a_{1z} \\ a_{2x} & a_{2y} & a_{2z} \\ a_{3x} & a_{3y} & a_{3z} \end{bmatrix} . \end{aligned} \quad (21)$$

From (21), we find relations between components of the eigenvectors and moment tensor elements:

$$\begin{aligned} M_{xx} &= m_1 a_{1x}^2 + m_2 a_{2x}^2 + m_3 a_{3x}^2 \\ M_{yy} &= m_1 a_{1y}^2 + m_2 a_{2y}^2 + m_3 a_{3y}^2 \\ M_{zz} &= m_1 a_{1z}^2 + m_2 a_{2z}^2 + m_3 a_{3z}^2 \\ M_{xy} &= m_1 a_{1x} a_{1y} + m_2 a_{2x} a_{2y} + m_3 a_{3x} a_{3y} \\ M_{xz} &= m_1 a_{1x} a_{1z} + m_2 a_{2x} a_{2z} + m_3 a_{3x} a_{3z} \\ M_{yz} &= m_1 a_{1y} a_{1z} + m_2 a_{2y} a_{2z} + m_3 a_{3y} a_{3z} . \end{aligned} \quad (22)$$

The effect of the eigenvalue decomposition (21) is that a new orthogonal coordinate system, given by the eigenvectors, has been defined. In this new coordinate system, the source excitation is completely described by a linear combination of these orthogonal dipole sources.

$\mathbf{m}$  in (21) is the diagonalized moment tensor. The elements of  $\mathbf{m}$  are the eigenvalues of  $M$ . We now define the

general moment tensor decomposition by rewriting  $\mathbf{m}$  as

$$\mathbf{m} = \frac{1}{3} \begin{bmatrix} \text{tr}(M) & 0 & 0 \\ 0 & \text{tr}(M) & 0 \\ 0 & 0 & \text{tr}(M) \end{bmatrix} \quad (23)$$

$$\begin{aligned} &+ \begin{bmatrix} m_1' & 0 & 0 \\ 0 & m_2' & 0 \\ 0 & 0 & m_3' \end{bmatrix} \\ &= \frac{1}{3} \begin{bmatrix} \text{tr}(M) & 0 & 0 \\ 0 & \text{tr}(M) & 0 \\ 0 & 0 & \text{tr}(M) \end{bmatrix} + \sum_{i=1}^N \bar{\mathbf{m}}_i , \end{aligned}$$

where  $\text{tr}(M) = m_1 + m_2 + m_3$  is the trace of the moment tensor and  $\bar{\mathbf{m}}_i$  is a set of diagonal matrices whose sum yields the second term in (23). The purely deviatoric eigenvalues  $m_i'$  of the moment tensor are

$$m_i' = m_i - \frac{m_1 + m_2 + m_3}{3} = m_i - \frac{1}{3} \text{tr}(M) . \quad (24)$$

The first term on the right hand side (RHS) of (23) describes the isotropic part of the moment tensor. The eigenvalues of the isotropic part of the moment tensor are important for quantifying a volume change in the source. The second term describes the deviatoric part of the moment tensor consisting of purely deviatoric eigenvalues, which are calculated by subtracting  $1/3 \text{tr}(M)$  from each eigenvalue of  $M$ . This deviatoric part of the moment tensor can be further decomposed, where the number of terms or the specific form of the decomposition will be discussed in the next sections. Obviously, a multitude of different decompositions are possible. In Appendix IV, we give some numerical examples illustrating several methods of moment tensor decomposition.

### Vector Dipoles

A moment tensor can be decomposed into an isotropic part and three vector dipoles. In equation (23) let  $N = 3$  and

$$\bar{\mathbf{m}}_1 = \begin{bmatrix} m_1' & 0 & 0 \\ 0 & 0 & 0 \\ 0 & 0 & 0 \end{bmatrix}, \quad \bar{\mathbf{m}}_2 = \begin{bmatrix} 0 & 0 & 0 \\ 0 & m_2' & 0 \\ 0 & 0 & 0 \end{bmatrix}, \quad \bar{\mathbf{m}}_3 = \begin{bmatrix} 0 & 0 & 0 \\ 0 & 0 & 0 \\ 0 & 0 & m_3' \end{bmatrix} . \quad (25)$$

Applying (21) to  $\bar{\mathbf{m}}_1$ , we get for the first deviatoric term ( $i=1$ ) in the decomposition

$$m_1' \begin{bmatrix} a_{1x}^2 & a_{1x} a_{1y} & a_{1x} a_{1z} \\ a_{1x} a_{1y} & a_{1y}^2 & a_{1y} a_{1z} \\ a_{1x} a_{1z} & a_{1y} a_{1z} & a_{1z}^2 \end{bmatrix} = m_1' \mathbf{a}_1 \mathbf{a}_1 , \quad (26)$$

where we identified the matrix as the dyadic  $\mathbf{a}_1 \mathbf{a}_1$  (Appendix I). The dyadic  $\mathbf{a}_1 \mathbf{a}_1$  describes a dipole in the direction of the eigenvector  $\mathbf{a}_1$ . By applying (21) to  $\bar{\mathbf{m}}_2$  and  $\bar{\mathbf{m}}_3$  in (25), we get similar expressions involving  $\mathbf{a}_2 \mathbf{a}_2$  and  $\mathbf{a}_3 \mathbf{a}_3$ , describing the second and third deviatoric terms in the decomposition. Finally, equation (21) can be written for the decomposition into three linear vector dipoles along the directions of the eigenvectors of  $M$  as

$$\mathbf{M} = \frac{1}{3}(m_1 + m_2 + m_3) \mathbf{I} \quad (27)$$

$$+ m_1' \mathbf{a}_1 \mathbf{a}_1 + m_2' \mathbf{a}_2 \mathbf{a}_2 + m_3' \mathbf{a}_3 \mathbf{a}_3,$$

which is identical to (22) and equation (4.55) in Ben-Menahem and Singh (1981).

### Double Couples

Next, we decompose a moment tensor into an isotropic part and three double couples. For the deviatoric part in (23) let  $N = 6$  and

$$\bar{\mathbf{m}}_1 = \frac{1}{3} \begin{bmatrix} m_1' & 0 & 0 \\ 0 & -m_1' & 0 \\ 0 & 0 & 0 \end{bmatrix}, \quad \bar{\mathbf{m}}_2 = \frac{1}{3} \begin{bmatrix} m_1' & 0 & 0 \\ 0 & 0 & 0 \\ 0 & 0 & -m_1' \end{bmatrix}$$

$$\bar{\mathbf{m}}_3 = \frac{1}{3} \begin{bmatrix} 0 & 0 & 0 \\ 0 & m_2' & 0 \\ 0 & 0 & -m_2' \end{bmatrix}, \quad \bar{\mathbf{m}}_4 = \frac{1}{3} \begin{bmatrix} -m_2' & 0 & 0 \\ 0 & m_2' & 0 \\ 0 & 0 & 0 \end{bmatrix} \quad (28)$$

$$\bar{\mathbf{m}}_5 = \frac{1}{3} \begin{bmatrix} 0 & 0 & 0 \\ 0 & -m_3' & 0 \\ 0 & 0 & m_3' \end{bmatrix}, \quad \bar{\mathbf{m}}_6 = \frac{1}{3} \begin{bmatrix} -m_3' & 0 & 0 \\ 0 & 0 & 0 \\ 0 & 0 & m_3' \end{bmatrix},$$

where each  $\bar{\mathbf{m}}_i$  is equivalent to a pure double couple source (Appendix III). Notice that each double couple consists of two linear vector dipoles (c.f. (25), (26) and (28)), e.g.  $(m_1'/3)(\mathbf{a}_1 \mathbf{a}_1 - \mathbf{a}_2 \mathbf{a}_2)$  for  $\bar{\mathbf{m}}_1$ . Each dipole consists of two forces of equal strength but opposite direction (c.f. Figure 2). Then, the double couple can be seen this way: The first couple is formed by one force of each dipole, one force pointing in the positive  $\mathbf{a}_1$ , the other in the negative  $\mathbf{a}_2$  direction. The corresponding other couple is constructed by the complementary force of each dipole, pointing toward the negative  $\mathbf{a}_1$  and positive  $\mathbf{a}_2$  direction. Using (21) with (23) and (28), we get the result that a moment tensor can be decomposed into an isotropic part and three double couples.

$$\mathbf{M} = \frac{1}{3}(m_1 + m_2 + m_3) \mathbf{I} + \frac{1}{3}(m_1 - m_2)(\mathbf{a}_1 \mathbf{a}_1 - \mathbf{a}_2 \mathbf{a}_2) \quad (29)$$

$$+ \frac{1}{3}(m_2 - m_3)(\mathbf{a}_2 \mathbf{a}_2 - \mathbf{a}_3 \mathbf{a}_3) + \frac{1}{3}(m_3 - m_1)(\mathbf{a}_3 \mathbf{a}_3 - \mathbf{a}_1 \mathbf{a}_1),$$

which is identical to equation (4.57) in Ben-Menahem and Singh (1981).

### CLVD

Alternatively, a moment tensor can be decomposed into an isotropic part and three compensated linear vector dipoles. Adding terms like  $\bar{\mathbf{m}}_1$  and  $\bar{\mathbf{m}}_2$  in (28) gives a CLVD,  $2\mathbf{a}_1 \mathbf{a}_1 - \mathbf{a}_2 \mathbf{a}_2 - \mathbf{a}_3 \mathbf{a}_3$ . This CLVD represents a dipole of strength 2 in the direction of the eigenvector  $\mathbf{a}_1$ , and two dipoles of unit strength in the directions of the eigenvectors  $\mathbf{a}_2$  and  $\mathbf{a}_3$ , respectively. The decomposition can then be expressed as:

$$\mathbf{M} = \frac{1}{3}(m_1 + m_2 + m_3) \mathbf{I} + \frac{1}{3} m_1 (2\mathbf{a}_1 \mathbf{a}_1 - \mathbf{a}_2 \mathbf{a}_2 - \mathbf{a}_3 \mathbf{a}_3) \quad (30)$$

$$+ \frac{1}{3} m_2 (2\mathbf{a}_2 \mathbf{a}_2 - \mathbf{a}_1 \mathbf{a}_1 - \mathbf{a}_3 \mathbf{a}_3) + \frac{1}{3} m_3 (2\mathbf{a}_3 \mathbf{a}_3 - \mathbf{a}_1 \mathbf{a}_1 - \mathbf{a}_2 \mathbf{a}_2),$$

which is identical to equation (4.56) in Ben-Menahem and Singh (1981).

### Major and Minor Couple

Next, we will decompose a moment tensor into an isotropic component, a major and minor double couple. The major couple seems to be the best approximation of a general seismic source by a double couple (Appendix IV), since the directions of the principal axes of the moment tensor remain unchanged. The major double couple is constructed in the following way (Kanamori and Given, 1981; Wallace, 1985): The eigenvector of the smallest eigenvalue (in the absolute sense) is taken as the null-axis. Let's assume that  $|m_3'| \geq |m_2'| \geq |m_1'|$  in (23). In (23), let  $N=2$  and use the deviatoric condition  $m_1' + m_2' + m_3' = 0$  to obtain

$$\bar{\mathbf{m}}_1 = \begin{bmatrix} 0 & 0 & 0 \\ 0 & -m_3' & 0 \\ 0 & 0 & m_3' \end{bmatrix}, \quad \bar{\mathbf{m}}_2 = \begin{bmatrix} m_1' & 0 & 0 \\ 0 & -m_1' & 0 \\ 0 & 0 & 0 \end{bmatrix} \quad (31)$$

Applying (21) to  $\bar{\mathbf{m}}_1$ , we get the first deviatoric term in the decomposition which corresponds to a pure double couple termed *major couple*.

$$\mathbf{M}^{MAJ} = \begin{bmatrix} \mathbf{a}_1 & \mathbf{a}_2 & \mathbf{a}_3 \end{bmatrix} \begin{bmatrix} 0 & 0 & 0 \\ 0 & -m_3' & 0 \\ 0 & 0 & m_3' \end{bmatrix} \begin{bmatrix} \mathbf{a}_1^T \\ \mathbf{a}_2^T \\ \mathbf{a}_3^T \end{bmatrix} \quad (32)$$

Instead of the *major* double couple, a *best* double couple can be constructed similarly by replacing  $m_3'$  in (32) by the average of the largest two eigenvalues (in the absolute sense, Giardini, 1984). Applying (21) to  $\bar{\mathbf{m}}_2$  gives the second deviatoric term in the decomposition which also corresponds to a pure double couple termed *minor couple*.

$$\mathbf{M}^{MIN} = \begin{bmatrix} \mathbf{a}_1 & \mathbf{a}_2 & \mathbf{a}_3 \end{bmatrix} \bar{\mathbf{m}}_2 \begin{bmatrix} \mathbf{a}_1^T \\ \mathbf{a}_2^T \\ \mathbf{a}_3^T \end{bmatrix} \quad (33)$$

The complete decomposition is then:

$$\mathbf{M} = \frac{1}{3}(m_1 + m_2 + m_3) \mathbf{I} \quad (34)$$

$$+ m_3' (\mathbf{a}_3 \mathbf{a}_3 - \mathbf{a}_2 \mathbf{a}_2) + m_1' (\mathbf{a}_1 \mathbf{a}_1 - \mathbf{a}_2 \mathbf{a}_2).$$

### Double Couple - CLVD

Following Knopoff and Randall (1970) and Fitch *et al.* (1980), we can decompose a moment tensor into an isotropic part, a double couple and a compensated linear vector dipole. Let's assume again that  $|m_3'| \geq |m_2'| \geq |m_1'|$  in (23). We can write the deviatoric part in (23) as ( $N = 1$ )

$$\bar{\mathbf{m}}_1 = m_3' \begin{bmatrix} -F & 0 & 0 \\ 0 & (F-1) & 0 \\ 0 & 0 & 1 \end{bmatrix}, \quad (35)$$

where  $F = -m_1' / m_3'$  and  $(F-1) = m_2' / m_3'$ . Note that  $0 \leq F \leq 0.5$ . This constraint on  $F$  arises from the deviatoric condition  $m_1' + m_2' + m_3' = 0$ . We can decompose (35)

into two parts representing a double couple and a CLVD

$$\bar{m}_1 = m_3^* (1 - 2F) \begin{bmatrix} 0 & 0 & 0 \\ 0 & -1 & 0 \\ 0 & 0 & 1 \end{bmatrix} + m_3^* F \begin{bmatrix} -1 & 0 & 0 \\ 0 & -1 & 0 \\ 0 & 0 & 2 \end{bmatrix}, \quad (36)$$

where we assumed that the same principal stresses produce the double couple as well as the CLVD radiation. The complete decomposition (21) is then:

$$M = \frac{1}{3}(m_1 + m_2 + m_3)I + m_3^*(1 - 2F)(a_3 a_3 - a_2 a_2) \quad (37)$$

$$+ m_3^* F (2a_3 a_3 - a_2 a_2 - a_1 a_1).$$

To estimate the deviation of the seismic source from the model of a pure double couple, Dziewonski *et al.* (1981) used the parameter

$$\epsilon = \left| \frac{m_{\min}^*}{m_{\max}^*} \right| \quad (38)$$

where  $m_{\min}^*$  is the smallest eigenvalue (in the absolute sense) and  $m_{\max}^*$  is the largest (in the absolute sense), given by (24). From (35), we see that  $\epsilon = F$ . For a pure double couple source,  $m_{\min}^* = 0$  and  $\epsilon = 0$ ; for a pure CLVD,  $\epsilon = 0.5$ . Alternatively,  $\epsilon$  can be expressed in percentages of CLVD (multiply  $\epsilon$  by 200). The percentage of double couple is  $(1 - 2\epsilon) * 100$ . Dziewonski and Woodhouse (1983b, see also Giardini, 1984) investigated the variation of  $\epsilon$  versus seismic moment and earthquake spatial distribution on the surface of the earth.

### MOMENT TENSOR INVERSION

There are various methods of inversion for moment tensor elements. The inversion can be done in the time or frequency domain. Different data (e.g. free oscillations, surface- and body waves; different seismogram components) can be used separately or combined. In addition, certain *a priori* constraints such as  $tr(M) = 0$ , or  $M_{xx} = M_{yy} = 0$  can be imposed to stabilize the inversion, resulting in a decrease in number of resolved moment tensor elements. In this Student's Guide, we briefly outline certain approaches and refer to the original papers for further reference.

Gilbert (1970) introduced the seismic moment tensor for calculating the excitation of normal modes (Saito, 1967) of free oscillations of the earth. Gilbert (1973) suggested an inversion scheme for moment tensor elements in the frequency domain. Gilbert and Dziewonski (1975) used free oscillation data for their moment tensor inversion. Gilbert and Buland (1976) investigated on the smallest number of stations necessary for a successful inversion (see also Stump and Johnson, 1977). McCowan (1976), Mendiguren (1977), Patton and Aki (1979), Patton (1980), Romanowicz (1981), Kanamori and Given (1981, 1982), Lay *et al.* (1982), Nakanishi and Kanamori (1982, 1984), and Scott and Kanamori (1985) used long-period surface waves (typically low pass filtered at 135 sec). Stump and Johnson (1977), Strelitz (1978, 1980), Ward (1980a, b), Fitch *et al.* (1980), Langston (1981), Dziewonski *et al.* (1981), and Dziewonski and Woodhouse (1983a, b), used moment tensor inversion for body wave data (typically low pass filtered at 45 sec). A comparison between

moment tensors from surface waves and body waves was done by Fitch *et al.* (1981). Dziewonski *et al.* (1981) suggested an iterative inversion method, solving for the moment tensor elements and the centroid location (Backus and Mulcahy, 1976; Backus, 1977a; see Dziewonski and Woodhouse, 1983a for a review). The reason for that approach is that moment tensor elements trade off with the location of the earthquake. The lateral heterogeneity of the earth was considered in inversion methods by Patton (1980), Romanowicz (1981), Nakanishi and Kanamori (1982), and Dziewonski *et al.* (1984c).

The moment tensor inversion in the time domain can use the formulation in (5) (e.g. Gilbert, 1970; McCowan, 1976; Stump and Johnson, 1977; Strelitz, 1978; Fitch *et al.*, 1980; Ward, 1980b; Langston, 1981). If the source time function is not known or the assumption of a synchronous source is dropped (Sipkin, 1986), the frequency domain approach is chosen (e.g. Gilbert, 1973; Dziewonski and Gilbert, 1974; Gilbert and Dziewonski, 1975; Gilbert and Buland, 1976; Mendiguren, 1977; Stump and Johnson, 1977; Patton and Aki, 1979; Patton, 1980; Ward, 1980a, Kanamori and Given, 1981; Romanowicz, 1981):

$$d_n(x, f) = M_{kj}(f) G_{nk,j}(f) \quad (39)$$

Both approaches, (5) and (39) lead to linear inversions in the time or frequency domain, respectively. The advantage of linear inversions is that a large number of fast computational algorithms are available (e.g. Lawson and Hanson, 1974; Press *et al.*, 1987). We can write either (5) or (39) in matrix form:

$$d = G \bar{m} \quad (40)$$

In the time domain, the vector  $d$  consists of  $n$  sampled values of the observed ground displacement at various arrival times, stations, and azimuths.  $G$  is a  $n \times 6$  matrix containing the Green's functions calculated using an appropriate algorithm and earth model, and  $\bar{m}$  is a vector containing the 6 moment tensor elements to be determined (Stump and Johnson, 1977). In the frequency domain, (40) can be written separately for each frequency.  $d$  consists of real and imaginary parts of the displacement spectra. Weighting can be introduced which actually smoothes the observed spectra subjectively (Mendiguren, 1977; see also Ward, 1980b for weighting of body-wave data in the time domain). In the same way,  $G$  and  $\bar{m}$  contain real and imaginary parts.  $\bar{m}$  contains also the transform of the source time function of each moment tensor element. If constraints are applied to the inversion, then  $\bar{m}$  can contain a smaller number of moment tensor elements. In such a case,  $G$  has to be changed accordingly. We refer to Aki and Richards (1980) for the details of solving (40) for  $\bar{m}$  (Note that (40) is identical to their (12.83)).

The following presents an outline of the processing steps in a moment tensor inversion. The first step is the data acquisition and the preprocessing. We need data with good signal to noise ratio that are unclipped and that have a good coverage of the focal sphere (Satake, 1985). Glitches (non-seismic high amplitude spikes due to non-linearity of instruments e.g. Dziewonski *et al.*, 1981) have to be identified and possibly removed. Analog data have to be digitized. The effect of non-orthogonality of the analog recorder must be corrected. The digitized

record has to be interpolated and resampled with a constant sampling rate. At this point, a comparison of the sampled waveform with the original one can help to identify digitization errors. The horizontal components will be rotated into radial and transverse components. Linear trends have to be identified and removed. The instrument effect is considered next (for WWSSN data see Hagiwara, 1958; for SRO data see McCowan and Lacoss, 1978; for IDA data see Agnew *et al.*, 1976). We can use either one of the two approaches: i) we can remove the instrument effect from the observed data and compare with theory or ii) we can apply the instrument response to the synthetic Green's functions and compare with observed data. The nominal instrument response can be used or the calibration of the instrument can be checked by using f.e. the calibration pulse on the record. In addition, the polarity of the instruments should be verified, e.g. from records of known nuclear explosions. High frequency noise in the data is removed by low-pass filtering. Amplitudes are corrected for geometrical spreading and reflections at the free surface of the earth (Bullen and Bolt, 1985). For surface waves, the moving window analysis (Landisman *et al.*, 1969) is applied in order to determine the group velocity dispersion. From this analysis, we can identify the fundamental mode Rayleigh and Love waves which can then be isolated.

Second, synthetic Green's functions are calculated. Notice that the Green's functions are dependent on the earth-model, the location of the point source (centroid of the stress glut, or epicenter and focal depth), and the receiver position.

The third step is the proper inversion, i.e. the solution of (40) (Aki and Richards, 1980). Usually, the inversion is formulated as least squares problem (Gilbert, 1973; Gilbert and Buland, 1976; Mendiguren, 1977; Stump and Johnson, 1977). However, using other norms can have advantages in situations where less sensitivity to gross errors like polarity reversions is required (Claerbout and Muir, 1973; Fitch *et al.*, 1980; Patton, 1980).

The source time function in (5) is often assumed to be a step function (Gilbert, 1970, 1973; McCowan, 1976; Stump and Johnson, 1977; Patton and Aki, 1979; Patton, 1980; Ward, 1980b; Dziewonski *et al.*, 1981; Kanamori and Given, 1981). Aiming at the recovery of source time functions, Burdick and Mellman (1976) used a powerful iterative waveform inversion method based on optimizing the cross-correlation between observed, long-period body-wave trains and synthetics. The same approach was used by Wallace *et al.*, (1981) in order to invert for fault plane solutions. Other methods were employed by Strelitz (1980) and Kikuchi and Kanamori (1982) for large earthquakes (see also Lundgren *et al.*, 1988). Christensen and Ruff (1985) reported on a trade-off between source time function and source depth for shallow events.

If the focal depth is not known, then a linear inversion can be done for each depth out of a number of trial depths. The most probable depth will minimize the quadratic error between observed and theoretical waveforms (Mendiguren, 1977; Patton and Aki, 1979; Patton, 1980; Romanowicz, 1981). The influence of source depth on the results of the moment tensor inversion was investigated by Sipkin (1982; Dziewonski *et al.*, 1987b). Differences in source depth influence the relative excitation of normal

modes, causing systematic errors in the inversion.

Systematic errors in the inversion are also due to deviations of the earth-model from the actual properties of the earth, affecting the synthetic Green's functions. This is a fundamental problem in the sense that we are able to separate the source effect from the observed seismogram only to a limited accuracy (Mendiguren, 1977; Langston, 1981; Silver and Jordan, 1982; O'Connell and Johnson, 1988). A major problem is the effect of lateral heterogeneity of the earth (Engdahl and Kanamori, 1980; Romanowicz, 1981; Gomberg and Masters, 1988; Snieder and Romanowicz, 1988). For example, a relative change of 0.5 % due to lateral heterogeneity can cause a mislocation in the order of of 50 km at epicentral distances of about 90 degrees (Dziewonski and Woodhouse, 1983b). Giardini (1984) and Ekström and Dziewonski (1985) reported on regional shifts in centroid positions due to lateral heterogeneity. In the inversion, lateral heterogeneity is often neglected, i.e. the calculation of the Green's functions is usually based on parallel layers of lateral homogeneity (Harkrider, 1964, 1970; Langston and Helmberger, 1975; Harkrider, 1976). Nakanishi and Kanamori (1982) included the effect of lateral heterogeneity into the moment tensor inversion. Another approach was developed for earthquakes within a small source area: a calibration event is declared (mechanism known); the spectral ratio of any earthquake in that region and the calibration event will result in isolating the difference in source effects - the influence of the path is eliminated (Patton, 1980). It seems that the errors due to lateral heterogeneity are usually large enough to make a statistical significant detection of an isotropic component of the moment tensor difficult (Okal and Geller, 1979; Silver and Jordan, 1982; Vasco and Johnson, 1988).

Patton and Aki (1979) investigated the influence of noise on the inversion of long-period surface wave data. They found that additive noise such as background recording noise does not severely affect the results of a linear inversion. However, multiplicative noise (signal generated noise) caused by focusing, defocusing, multipathing, higher mode or body wave interference, and scattering distorts the inversion results significantly (overestimation or underestimation of moment tensor elements, deviation from the source mechanism; Patton, 1980; Ward, 1980b). Finally, body waves of events with moments larger than  $10^{27}$  dyne-cm are severely affected by finiteness of the source and directivity. If not corrected for, an inversion can lead to severe errors in the moment tensor elements (Dziewonski *et al.*, 1981; Kanamori and Given, 1981; Patton and Aki, 1979; Lay *et al.*, 1982; Giardini, 1984).

The inversion has only a limited resolution of moment tensor elements for certain data. If we have spectra of fundamental mode Rayleigh waves only, the constraint that the trace of the moment tensor vanishes (no volume change) must be applied (Mendiguren, 1977; Patton and Aki, 1979). This constraint is linear. Another constraint which is often applied in addition is that one eigenvalue vanishes (approximating the source by a double couple). This constraint is not linear (Strelitz, 1978; Ward, 1980b). In such a case, the inversion is iterative, using a linearized version of the constraints (Ward, 1980b). For earthquakes at shallow depths (less than



## A Student's Guide to and Review of Moment Tensors

about 30 km), the moment tensor elements  $M_{xx}$  and  $M_{yy}$  corresponding to vertical dip slip faulting are not well constrained from long-period surface wave data since the related excitation functions assume very small values near the surface of the earth (Fitch *et al.*, 1981; Dziewonski *et al.*, 1981; Kanamori and Given, 1981, 1982; Dziewonski and Woodhouse, 1983a). In order to overcome this problem, additional independent data, such as fault strike (observed surface breakage) can be introduced into the inversion. Another approach is to constrain these moment tensor elements to be zero. Thus, possible fault mechanisms are restricted to vertical strike slip or 45 degree dip slip (Kanamori and Given, 1981, 1982).

In Appendix V, we relate the Green's functions in the formulation of Herrmann and Wang (1985) to a simple moment tensor inversion scheme. This inversion example is aimed at testing computer programs.

### CONCLUSION

A seismic moment tensor describes the equivalent forces of a seismic point source. The eigenvectors are the principal axes of the seismic moment tensor. For pure double couple sources, the principal axis corresponding to the negative eigenvalue is the pressure axis, the principal axis corresponding to the positive eigenvalue is the tension axis, and the principal axis corresponding to the eigenvalue zero gives the null axis. The pressure, tension, and null axes can be displayed in the familiar focal mechanism plot (fault plane solution). For general seismic sources, we can decompose the seismic moment tensor. First, we can separate out the isotropic component which describes the volume change in the source. The leftover part of the moment tensor has, in general, three nonvanishing eigenvalues. This deviatoric part of the moment tensor can be decomposed into a number of simple combinations of equivalent forces. Obviously, there is no unique moment tensor decomposition, i.e. unique model of equivalent forces. We outlined methods of determining moment tensor elements from observations, indicating that recording noise as well as systematic errors due to an insufficient knowledge of the Green's functions can introduce errors into the moment tensor elements. This suggests caution when apparent non-double couple sources result from the inversion.

Randall and Knopoff (1970), Gilbert and Dziewonski (1975), Dziewonski *et al.* (1981), Kanamori and Given (1981, 1982), Dziewonski and Woodhouse (1983b), Giardini (1984), and Scott and Kanamori (1985) reported that some seismic sources cannot be described by a pure double couple. One explanation is that some fault planes show a complex geometry (Dziewonski and Woodhouse, 1983b). Another explanation can be that some sources deviate from the model of a sudden shear dislocation; they can be due to a rapidly propagating phase transition (Knopoff and Randall, 1970; Dziewonski and Woodhouse, 1983b). However, the simple inversion experiment in Appendix V pointed out that the deviation from a pure double couple can also be due to the presence of noise in the data (Stump and Johnson, 1977; Patton and Aki, 1979; Patton, 1980; Ward, 1980b; Wallace, 1985; O'Connell and Johnson, 1988).

### ACKNOWLEDGMENTS

We thank two anonymous reviewers for their helpful criticism of the manuscript. Critical remarks by Oznur Mindevalli are appreciated. Funds for this research were provided by the Defense Advanced Research Projects Agency under contract F49628-87-K-0047 monitored by the Air Force Geophysics Laboratory.

### APPENDIX I

In the following, we give some mathematical definitions of tensors, the eigenvalue problem and dyadics following Arfken (1985).

Let  $\mathbf{M}$  be a moment tensor of second rank (order). Then,  $\mathbf{M}$  is represented as a  $3 \times 3$  matrix in a given reference frame. Let  $a_{pk}$  be the cosine of the angle between the  $p$  axis of another coordinate system and the  $k$  axis. Then the components of  $\mathbf{M}$ ,  $M_{kj}$ , transform into the new reference frame by the relation

$$M_{pq} = a_{kp} a_{jq} M_{kj} \quad (A1.1)$$

where we need to sum over repeated indices (summation convention).

Given a moment tensor  $\mathbf{M}$ , let's assume that there is a vector  $\mathbf{a}$  and a scalar  $m$  such that

$$\mathbf{M} \mathbf{a} = m \mathbf{a} \quad (A1.2)$$

$\mathbf{a}$  is called eigenvector of  $\mathbf{M}$  and  $m$  is the corresponding eigenvalue. For calculating the eigenvalues and eigenvectors of a given moment tensor (solving the eigenvalue problem), we transform (A1.2)

$$(\mathbf{M} - m \mathbf{I}) \mathbf{a} = 0 \quad (A1.3)$$

where  $\mathbf{I}$  is the identity matrix. (A1.3) is a system of 3 simultaneous homogeneous linear equations in  $a_k$ . Non-trivial solutions are found by solving the secular equation (characteristic polynomial)

$$\det(\mathbf{M} - m \mathbf{I}) = 0 \quad (A1.4)$$

where "det" means the determinant. (A1.4) is a polynomial of third degree. It has three real roots, i.e. eigenvalues, since the moment tensor is real and symmetric (Faddeeva, 1950). Substituting each eigenvalue  $m_i$  into (A1.3) gives the corresponding eigenvector  $\mathbf{a}_i$ . The eigenvectors are orthogonal. Multiplying each eigenvector by its inverse norm, we get the orthonormal eigenvectors, renaming them as  $\mathbf{a}_i$ :

$$\mathbf{a}_i \cdot \mathbf{a}_j = \delta_{ij} \quad (A1.5)$$

Knowing the eigenvectors, we can diagonalize  $\mathbf{M}$  (principal axis transformation). Let  $\mathbf{A}$  be the matrix whose columns are the orthonormal eigenvectors of  $\mathbf{M}$ . From (A1.5), we see that  $\mathbf{A}$  is orthogonal:  $\mathbf{A}^T = \mathbf{A}^{-1}$ . Then  $\mathbf{A}^T \mathbf{M} \mathbf{A} = \mathbf{m}$ , where  $\mathbf{m}$  is diagonal, consisting of the eigenvalues of  $\mathbf{M}$ .

We represent a dyadic by writing two vectors  $\mathbf{a}$  and  $\mathbf{b}$  together as  $\mathbf{ab}$  (see Appendix A in Ben-Menahem and Singh, 1981). These two vectors forming the dyadic are not operating on each other, but define a  $3 \times 3$  matrix. Let  $\mathbf{i}$ ,  $\mathbf{j}$ , and  $\mathbf{k}$  be unit vectors along a right handed Cartesian coordinate system. The dyadic  $\mathbf{ab}$  is defined as

$$\begin{aligned}
 \mathbf{ab} &= (a_x \mathbf{i} + a_y \mathbf{j} + a_z \mathbf{k}) (b_x \mathbf{i} + b_y \mathbf{j} + b_z \mathbf{k}) \\
 &= i a_x b_x + j a_y b_y + k a_z b_z \\
 &+ j i a_y b_x + j j a_y b_y + j k a_y b_z \\
 &+ k i a_z b_x + k j a_z b_y + k k a_z b_z \quad (\text{A1.6}) \\
 &= \begin{bmatrix} a_x b_x & a_x b_y & a_x b_z \\ a_y b_x & a_y b_y & a_y b_z \\ a_z b_x & a_z b_y & a_z b_z \end{bmatrix}
 \end{aligned}$$

For  $\mathbf{a} = \mathbf{b}$ , we get (26). The multiplication of a vector  $\mathbf{c}$  from the left is

$$\mathbf{c} \cdot \mathbf{ij} = (i c_x + j c_y + k c_z) \mathbf{ij} = c_x \mathbf{j} \quad (\text{A1.7})$$

If the dyadic is symmetric, the multiplication of any vector with the dyadic is commutative, i.e.  $\mathbf{ab} = \mathbf{ba}$ . In general, we can understand a dyadic as a tensor of second rank. By a proper choice of the coordinate system, a symmetric dyadic can always be transformed into diagonal form (principal axis transformation). As an example, we can rewrite (10) using dyadics (Gilbert, 1973):

$$\begin{aligned}
 \mathbf{uv} + \mathbf{vu} &= \mathbf{tt} - \mathbf{pp} \quad (\text{A1.8}) \\
 &= 0.5 [(t+p)(t-p) + (t-p)(t+p)].
 \end{aligned}$$

### APPENDIX II

The PDE monthly listings (NEIS) routinely publish centroid moment tensor solutions in the notation of the normal mode theory following Dziewonski *et al.* (1981). For reference, the spherical moment tensor elements,  $f_i$ , in the notation of Gilbert and Dziewonski (1975), Dziewonski *et al.* (1981), and Dziewonski and Woodhouse (1983a) are compared to the moment tensor elements as given in (18) following Aki and Richards (1980).

$$\begin{aligned}
 f_1 &= M_{rr} = M_{zz} \\
 f_2 &= M_{\theta\theta} = M_{xx} \\
 f_3 &= M_{\phi\phi} = M_{yy} \\
 f_4 &= M_{r\theta} = M_{zx} \quad (\text{A2.1}) \\
 f_5 &= M_{r\phi} = -M_{yz} \\
 f_6 &= M_{\theta\phi} = -M_{xy}
 \end{aligned}$$

where  $(r, \theta, \phi)$  are the geographical coordinates at the source.  $\theta$  is the colatitude ( $\theta = 0$  at the north pole) and  $\phi$  is the longitude of the point source. The sign of the off-diagonal moment tensor elements depend on the orientation of the coordinate system (Fitch *et al.*, 1981). But the eigenvalues and the eigenvectors of the moment tensor in the formulation of (18) or (A2.1) are identical, which can be shown by comparing the solutions to the secular equation (Appendix I). This result is expected since physical laws should not depend on the choice of the reference frame. The slip vector  $\mathbf{u}$  and fault normal  $\mathbf{v}$  are (Dziewonski and Woodhouse, 1983a)

$$\begin{aligned}
 \mathbf{u} &= \bar{u} (-\cos \lambda \cos \Phi - \cos \delta \sin \lambda \sin \Phi) \mathbf{e}_\theta \\
 &+ \bar{u} (\cos \lambda \sin \Phi - \cos \delta \sin \lambda \cos \Phi) \mathbf{e}_\phi \quad (\text{A2.2}) \\
 &+ \bar{u} \sin \lambda \sin \delta \mathbf{e}_r,
 \end{aligned}$$

and

$$\mathbf{v} = \sin \delta \sin \Phi \mathbf{e}_\theta + \sin \delta \cos \Phi \mathbf{e}_\phi + \cos \delta \mathbf{e}_r \quad (\text{A2.3})$$

These two equations are identical to (4.122) in Ben-Menahem and Singh (1981). The differences in sign compared to (15) and (16) can be fully explained by noting that  $\mathbf{e}_r = -\mathbf{e}_z$ ,  $\mathbf{e}_\phi = \mathbf{e}_y$ , and  $\mathbf{e}_\theta = -\mathbf{e}_x$ ; in other words,  $\mathbf{e}_\theta$ ,  $\mathbf{e}_\phi$ , and  $\mathbf{e}_r$  are unit vectors towards south, east, and up, respectively (defining a right handed system).

### APPENDIX III

In order to gain some experience in the relationships between a moment tensor and a fault plane solution, three simple focal mechanisms are discussed in detail. These will be vertical strike slip, 45 degree dip slip, and vertical dip slip faults. These three fault plane solutions form a complete set: The seismic radiation from a dislocation on a plane dipping an arbitrary angle (but striking north-south) can be expressed as a linear combination of these three solutions (Burridge *et al.*, 1964; Ben-Menahem and Singh, 1968).

#### Vertical strike slip fault

The following focal mechanism is assumed: (strike)  $\Phi = 0^\circ$ , (dip)  $\delta = 90^\circ$ , and (slip)  $\lambda = 0^\circ$ . From (15) and (16), the slip vector on the fault plane is  $\mathbf{u} = (1, 0, 0)$  and the vector normal to the fault plane is  $\mathbf{v} = (0, 1, 0)$ . The moment tensor can be determined from (18).

$$\mathbf{M} = \begin{bmatrix} 0 & M_0 & 0 \\ M_0 & 0 & 0 \\ 0 & 0 & 0 \end{bmatrix} \quad (\text{A3.1})$$

The eigenvalues and eigenvectors of this tensor (Example 4.6.1 in Arfken, 1985, see also Appendix I) are shown in Table A.1 (The components of the eigenvectors are north, east, and down).

TABLE A.1

EIGENVALUE	EIGENVECTOR
0	(0.0000, 0.0000, -1.0000)
$M_0$	(0.7071, 0.7071, 0.0000)
$-M_0$	(-0.7071, 0.7071, 0.0000)

The eigenvector  $\mathbf{b}$  corresponding to the eigenvalue zero is the null-axis, the eigenvector  $\mathbf{t}$  corresponding to the positive eigenvalue gives the tension axis, T, and the eigenvector  $\mathbf{p}$  corresponding to the negative eigenvalue gives the pressure axis, P, of a focal mechanism.

The focal mechanism is obtained by using (7)-(14) (Herrmann, 1975). For the trend and plunge (in degrees) of the X-, Y-, null-, T-, and P-axes, we get (90, 0), (180, 0), (270, 90), (45, 0), and (135, 0), respectively. The trend of both the P and T axes can be shifted by  $180^\circ$  (Figure A.1a); i.e. the P-axis can also be described by (315, 0) and the T-axis by (225, 0). This ambiguity can be followed through to the moment tensor: The sign of an eigenvector is not constrained by the solution of the eigenvalue problem (Arfken, 1985). However, any choice of sign leads to the same focal mechanism.

A Student's Guide to and Review of Moment Tensors

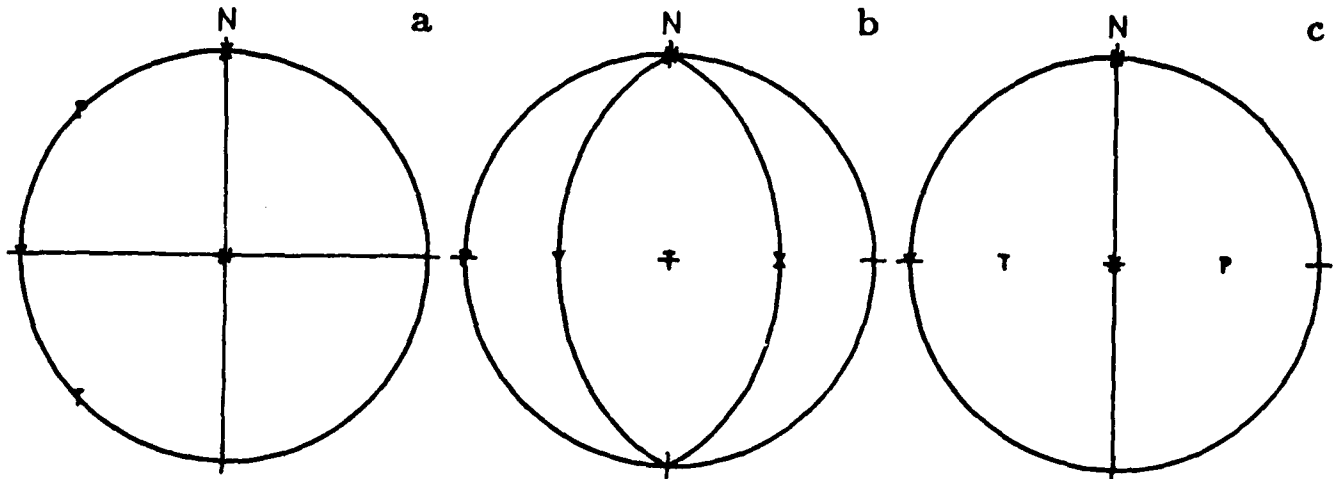


Fig. A.1. Focal mechanisms of a vertical strike slip fault (strike = 0°, dip = 90°, slip = 0°), (a), a 45 degree dip slip fault (strike = 0°, dip = 45°, slip = 90°), (b), and a vertical dip slip fault (strike = 0°, dip = 90°, slip = 90°), (c) (Appendix III).

45 degree dip slip fault

The following focal mechanism is assumed: (strike)  $\Phi = 0^\circ$ , (dip)  $\delta = 45^\circ$ , and (slip)  $\lambda = 90^\circ$ . From (15) and (16),  $\mathbf{u} = (0, -0.7071, -0.7071)$  and  $\mathbf{v} = (0, 0.7071, -0.7071)$ . The moment tensor is calculated from (18).

$$\mathbf{M} = \begin{bmatrix} 0 & 0 & 0 \\ 0 & -M_0 & 0 \\ 0 & 0 & M_0 \end{bmatrix} \quad (\text{A3.2})$$

The corresponding eigenvalues and eigenvectors are shown in Table A.2.

TABLE A.2

EIGENVALUE	EIGENVECTOR
0	(-1, 0, 0)
$M_0$	(0, 0, -1)
$-M_0$	(0, 1, 0)

The fault plane solution is obtained from (7)-(14) (Herrmann, 1975). For the trend and plunge (in degrees) of the X-, Y-, null-, T-, and P-axes, we get (90, 45), (270, 45), (360, 0), (180, 90), and (270, 0), respectively. The trend of the P and null axes can be shifted by 180° (Figure A.1b) to (90°, 0°) and (180°, 0°), respectively.

Vertical dip slip fault

The following focal mechanism is assumed: (strike)  $\Phi = 0^\circ$ , (dip)  $\delta = 90^\circ$ , and (slip)  $\lambda = 90^\circ$ . From (15) and (16),  $\mathbf{u} = (0, 0, -1)$  and  $\mathbf{v} = (0, 1, 0)$ . The moment tensor is calculated from (18).

$$\mathbf{M} = \begin{bmatrix} 0 & 0 & 0 \\ 0 & 0 & -M_0 \\ 0 & -M_0 & 0 \end{bmatrix} \quad (\text{A3.3})$$

The corresponding eigenvalues and eigenvectors are shown in Table A.3.

TABLE A.3

EIGENVALUE	EIGENVECTOR
0	(-1.0000, 0.0000, 0.0000)
$M_0$	(0.0000, 0.7071, -0.7071)
$-M_0$	(0.0000, 0.7071, 0.7071)

The fault plane solution is obtained from (7)-(14) (Herrmann, 1975). For the trend and plunge (in degrees) of the X-, Y-, null-, T-, and P-axes, we get (0, 90), (90, 0), (180, 0), (270, 45), and (90, 45), respectively. The trend of the null axis can be shifted by 180° (Figure A.1c) to (360°, 0°).

APPENDIX IV

In the following, examples of the five methods of moment tensor decomposition are presented.

In order to construct a moment tensor that *does not* lead to a simple double couple mechanism, let

$$\mathbf{M}_1 = 1 \begin{bmatrix} 1 & 0 & 0 \\ 0 & 1 & 0 \\ 0 & 0 & 1 \end{bmatrix} \quad (\text{A4.1})$$

$$\mathbf{M}_2 = 6 \begin{bmatrix} 0 & 1 & 0 \\ 1 & 0 & 0 \\ 0 & 0 & 0 \end{bmatrix} \quad (\text{A4.2})$$

$$\mathbf{M}_3 = 3 \begin{bmatrix} 0 & 0 & 0 \\ 0 & -1 & 0 \\ 0 & 0 & 1 \end{bmatrix} \quad (\text{A4.3})$$

$$\mathbf{M}_4 = 1 \begin{bmatrix} 0 & 0 & 0 \\ 0 & 0 & -1 \\ 0 & -1 & 0 \end{bmatrix} \quad (\text{A4.4})$$

The first moment tensor represents an explosion, the others are the familiar ones from Appendix III, representing a vertical strike-slip, a 45 degree dip-slip, and a vertical dip-slip fault, respectively. All four moment tensors are superimposed in order to describe a complex source that is dominated by a vertical strike slip mechanism.

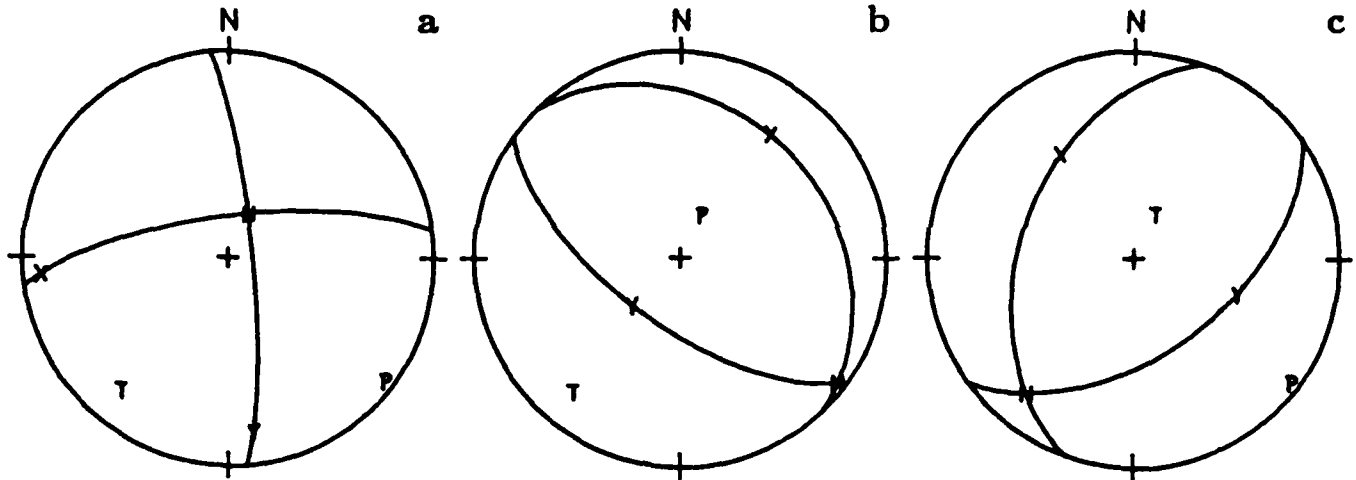


Fig. A.2. Focal mechanisms of the double couples from the moment tensor decomposition (Appendix IV). (a) major couple of the moment tensor in (A4.5), elementary moment tensor EMT3 in (A4.6), and second term on the RHS of (A4.9) (strike = 355°, dip = 80°, slip = 16°), (b) elementary moment tensor EMT2 in (A4.6) (strike = 125°, dip = 63°, slip = -95°), (c) elementary moment tensor EMT4 in (A4.6) (strike = 199°, dip = 44°, slip = 63°).

The result is

$$M = \begin{bmatrix} 1 & 6 & 0 \\ 6 & -2 & -1 \\ 0 & -1 & 4 \end{bmatrix} \quad (A4.5)$$

Table A.4 shows the eigenvalues of (A4.5) and the corresponding eigenvectors, which are the principal axes of M.

TABLE A.4

EIGENVALUE	EIGENVECTOR
3.8523	(-0.2938, -0.1397, -0.9456)
5.8904	(0.7352, 0.5992, -0.3170)
-6.7427	(0.6109, -0.7883, -0.0734)

The sum of the eigenvalues is equal to 3, which is the expected value for the sum of the eigenvalues of (A4.1), describing an explosion.

In order to calculate the deviatoric part of the given moment tensor, the isotropic part is removed by subtracting one third of the trace of (A4.5) from each diagonal element. The solution to the corresponding eigenvalue problem leads to the same eigenvectors as above. This indicates that the principal axes of the complete moment tensor are the same as the principal axes of the corresponding deviatoric tensor. The deviatoric eigenvalues are 2.8523, 4.8904, and -7.7427 in the order of Table A.4 (see (24)). From (38),  $\epsilon = 0.37$ , i.e. the given moment tensor has a double couple component of 26 % and a CLVD component of 74 %.

For the determination of the *major couple* from (32), we identify the eigenvector (0.6109, -0.7883, -0.0734) corresponding to the deviatoric eigenvalue of -7.7 as the P-axis, the eigenvector (0.7352, 0.5992, -0.3170) corresponding to the eigenvalue of 4.9 as the T-axis, and

the eigenvector (-0.2938, -0.1397, -0.9456) with eigenvalue 2.9 as the null-axis. The fault plane solution of the major double couple gives for the X-, Y-, null-, T-, and P-axes (in degrees): (172, 16), (265, 10), (25, 71), (219, 18), and (128, 4), respectively (Figure A.2a). The major double couple gives a good estimate of the major contribution to the faulting which is predominantly strike slip (compare Figures A.1a and A.2a).

Next, the moment tensor in (A4.5) is decomposed into an isotropic part and three double couples following (29) which is evaluated by using (26) together with the data in Table A.4. The numbering of the eigenvalues and eigenvectors in (29) follows the columns of Table A.4, but that is not relevant to the solution. The calculation gives

$$M = 1 \begin{bmatrix} 1 & 0 & 0 \\ 0 & 1 & 0 \\ 0 & 0 & 1 \end{bmatrix} + 0.6794 \begin{bmatrix} 0.4542 & 0.3995 & -0.5109 \\ 0.3995 & 0.3396 & -0.3220 \\ -0.5109 & -0.3220 & -0.7936 \end{bmatrix} + 4.2110 \begin{bmatrix} 0.1673 & 0.9221 & -0.1882 \\ 0.9221 & -0.2623 & -0.2477 \\ -0.1882 & -0.2477 & 0.0951 \end{bmatrix} + 3.5316 \begin{bmatrix} -0.2869 & 0.5226 & 0.3227 \\ 0.5226 & -0.6019 & 0.0743 \\ 0.3227 & 0.0743 & 0.8887 \end{bmatrix} \quad (A4.6)$$

This equation is identical to (A4.5). The first elementary moment tensor (EMT1) on the RHS of (A4.6) describes the explosion (isotropic component of (A4.5)) and is identical to (A4.1). The last three elementary moment tensors on the RHS (EMT2, EMT3, EMT4, respectively) represent pure double couple sources since the eigenvalues of each tensor is 0 and  $\pm 1$ . The three elementary moment tensors have identical eigenvectors which are the same vectors as shown in Table A.4. However, the correlation between eigenvector and eigenvalue (i.e. null-, P-, and T-axes) varies. Note that replac-

### A Student's Guide to and Review of Moment Tensors

ing  $M_{ij}$  by  $-M_{ij}$  switches the sign of the eigenvalues (leaving the eigenvectors untouched), which is identical to interchanging the P- and T-axes.

From the eigenvalues and the eigenvectors, the fault plane solution for each elementary moment tensor is determined and shown in Table A.5.

TABLE A.5

AXIS	EMT2	EMT2	EMT3	EMT3	EMT4	EMT4
	TRD	PLG	TRD	PLG	TRD	PLG
	(deg.)	(deg.)	(deg.)	(deg.)	(deg.)	(deg.)
X	36	26	172	16	324	38
Y	226	63	265	10	109	46
NULL	128	4	25	71	219	18
T	219	18	219	18	25	71
P	25	71	128	4	128	4

The focal mechanisms corresponding to EMT2 - EMT4 are shown in Figures A.2b, A.2a, and A.2c, respectively. Note that the positions of the axes remain fixed in these figures, where only the correlation to the eigenvalues changes. The fault plane solution representing the third elementary moment tensor EMT3 in (A4.6) is identical to the fault plane solution of the major couple (Figure A.2a). Notice that this solution has also the largest coefficient in (A4.6). This solution is an approximation to the major contributor of the moment tensor (Figure A.1a and (A4.2)). However, the other fault plane solutions (Figure A.2b and A.2c) do not show similarities to the input fault mechanisms (Figure A.1b and A.1c).

The seismic moments of the elementary moment tensors are given by the coefficients in (A4.6). The sum of the seismic moments of the elementary moment tensors is 1.4 times larger than the seismic moment of the composite moment tensor in (A4.5).

Next, the moment tensor in equation (A4.5) is decomposed into an isotropic part and three vector dipoles following (27) which is evaluated by using (26) together with Table A.4.

$$\begin{aligned}
 \mathbf{M} = & \mathbf{1} \begin{bmatrix} 1 & 0 & 0 \\ 0 & 1 & 0 \\ 0 & 0 & 1 \end{bmatrix} + 2.8523 \begin{bmatrix} 0.0863 & 0.0410 & 0.2779 \\ 0.0410 & 0.0195 & 0.1321 \\ 0.2779 & 0.1321 & 0.8941 \end{bmatrix} \\
 & + 4.8904 \begin{bmatrix} 0.5405 & 0.4405 & -0.2330 \\ 0.4405 & 0.3591 & -0.1899 \\ -0.2330 & -0.1899 & 0.1005 \end{bmatrix} \\
 & - 7.7427 \begin{bmatrix} 0.3732 & -0.4816 & -0.0448 \\ -0.4816 & 0.6214 & 0.0578 \\ -0.0448 & 0.0578 & 0.0054 \end{bmatrix}
 \end{aligned} \tag{A4.7}$$

This equation is identical to (A4.5). In the notation used above, each of the elementary moment tensors EMT2, EMT3, and EMT4 have two eigenvalues equal to zero, the third one equals one. EMT2 is represented by the eigenvector (0.2938, 0.1397, 0.9456), EMT3 by (-0.7352, -0.5992, 0.3170), and EMT4 by (0.6109, -0.7883, -0.0734). These vector dipoles are mutually orthonormal. Notice that these vector dipoles are identical to the eigenvectors of equation (A4.5), which are the principal axes of the tensor (Table A.4). EMT2 represents the null-, EMT3 the tension-, and EMT4 the pressure axis. The seismic

moments of the elementary moment tensors are given by the coefficients in (A4.7) which are identical to the deviatoric eigenvalues of (A4.5). This exercise demonstrated that vector dipoles are related to the eigenvectors scaled by the corresponding eigenvalue of a given moment tensor, which makes an evaluation of (A4.7) obsolete.

Alternatively, the moment tensor in equation (A4.5) can be decomposed into an isotropic part and three compensated linear vector dipoles using (30).

$$\begin{aligned}
 \mathbf{M} = & \mathbf{1} \begin{bmatrix} 1 & 0 & 0 \\ 0 & 1 & 0 \\ 0 & 0 & 1 \end{bmatrix} + 1.2841 \begin{bmatrix} -0.7411 & 0.1231 & 0.8336 \\ 0.1231 & -0.9415 & 0.3963 \\ 0.8336 & 0.3963 & 1.6823 \end{bmatrix} \\
 & + 1.9635 \begin{bmatrix} 0.6215 & 1.3216 & -0.6991 \\ 1.3216 & 0.0773 & -0.5697 \\ -0.6991 & -0.5697 & -0.6985 \end{bmatrix} \\
 & - 2.2476 \begin{bmatrix} 0.1196 & -1.4447 & -0.1345 \\ -1.4447 & 0.8642 & 0.1734 \\ -0.1345 & 0.1734 & -0.9838 \end{bmatrix}
 \end{aligned} \tag{A4.8}$$

This equation is identical to (A4.5). The seismic moments of the elementary moment tensors are given by the product of the respective coefficient and  $\sqrt{3}$ . The eigenvalues and eigenvectors for (A4.8) are shown in Table A.6, using the same notation as above. Note that the eigenvectors are identical to those in Table A.4.

TABLE A.6

EMT	EIGENVALUE	EIGENVECTOR
2	-1	(0.6109, -0.7883, -0.0734)
	-1	(0.7352, 0.5992, -0.3170)
	2	(-0.2938, -0.1397, -0.9456)
3	-1	(-0.2938, -0.1397, -0.9456)
	-1	(0.6109, -0.7883, -0.0734)
	2	(0.7352, 0.5992, -0.3170)
4	-1	(0.7352, 0.5992, -0.3170)
	-1	(-0.2938, -0.1397, -0.9456)
	2	(0.6109, -0.7883, -0.0734)

Next, the moment tensor in (A4.5) is decomposed into an isotropic part, a double couple and CLVD following (37), where  $\epsilon = F = 0.3684$ .

$$\begin{aligned}
 \mathbf{M} = & \mathbf{1} \begin{bmatrix} 1 & 0 & 0 \\ 0 & 1 & 0 \\ 0 & 0 & 1 \end{bmatrix} + 2.0379 \begin{bmatrix} 0.1673 & 0.9221 & -0.1882 \\ 0.9221 & -0.2623 & -0.2477 \\ -0.1882 & -0.2477 & 0.0951 \end{bmatrix} \\
 & - 2.8523 \begin{bmatrix} 0.1196 & -1.4447 & -0.1345 \\ -1.4447 & 0.8642 & 0.1734 \\ -0.1345 & 0.1734 & -0.9838 \end{bmatrix}
 \end{aligned} \tag{A4.9}$$

This equation is identical to (A4.5). Notice that the second term on the RHS corresponds to EMT3 in (A4.6) and to the major double couple. These three tensors all have the same fault plane solution (Figure A.2a). The third term in (A4.9) corresponds to EMT4 in (A4.8), representing a CLVD (see Table A.6).

As final remark, let's consider the decomposition equations (27), (29), and (30) for a simple double couple source ( $\epsilon = 0$ ), e.g. let  $m_1 = -m_2 = 1$ , and  $m_3 = 0$ . Then,  $\mathbf{M} = \mathbf{a}_1\mathbf{a}_1 - \mathbf{a}_2\mathbf{a}_2$  for all three equations. That is, we get one pure double couple out of the decomposition. For a CLVD ( $\epsilon = 0.5$ ), let's assume that  $m_1 = m_2 = -1$ ,

and  $m_3 = 2$ . Then all three formulas give  $M = 2 a_3 a_3 - a_1 a_1 - a_2 a_2$ , representing one C.I.V.D.

### APPENDIX V

In this section, we relate the Green's functions in the formulation of Herrmann and Wang (1985) to a moment tensor inversion scheme. Following the theory given by Herrmann and Wang (1985), the Fourier transformed displacements at the free surface at the distance  $r$  from the origin due to an arbitrarily oriented double couple without moment is

$$\begin{aligned} d_z(r, z=0, \omega) &= ZSS A_1 + ZDS A_2 + ZDD A_3 \\ d_r(r, z=0, \omega) &= RSS A_1 + RDS A_2 + RDD A_3 \\ d_\phi(r, z=0, \omega) &= TSS A_4 + TDS A_5 \end{aligned} \quad (A5.1)$$

where  $d_z$  is the vertical displacement (positive upward),  $d_r$  is the radial displacement, and  $d_\phi$  is the tangential displacement (positive in a direction clockwise from north). The functions ZSS, ZDS, ZDD, RSS, RDS, RDD, TSS, and TDS together with ZEP and REP are the ten Green's functions required to calculate a wave field due to an arbitrary point dislocation source or point explosion buried in a plane layered medium (Wang and Herrmann, 1980; Herrmann and Wang, 1985). As before, let  $\mathbf{u}=(u_x, u_y, u_z)$  and  $\boldsymbol{\nu}=(\nu_x, \nu_y, \nu_z)$  be the dislocation vector and vector normal to the fault plane, respectively. Note that (15) and (16) are identical to the formulation used by Herrmann and Wang (1985), where our  $\mathbf{u}$  equals their  $\mathbf{f}$  and our  $\boldsymbol{\nu}$  equals their  $\mathbf{n}$  (1 = x-axis, 2 = y-axis, 3 = z-axis). Then

$$\begin{aligned} A_1 &= (u_x \nu_x - u_y \nu_y) \cos(2az) + (u_x \nu_y + u_y \nu_x) \sin(2az) \\ A_2 &= (u_x \nu_z + u_z \nu_x) \cos(az) + (u_y \nu_z + u_z \nu_y) \sin(az) \\ A_3 &= u_x \nu_x \\ A_4 &= (u_x \nu_x - u_y \nu_y) \sin(2az) - (u_x \nu_y + u_y \nu_x) \cos(2az) \\ A_5 &= (u_x \nu_z + u_z \nu_x) \sin(az) - (u_y \nu_z + u_z \nu_y) \cos(az) \end{aligned} \quad (A5.2)$$

where  $az$  is the azimuth of observation. Equivalently,

$$\begin{aligned} A_1 &= \frac{1}{2}(M_{xx} - M_{yy}) \cos(2az) + M_{xy} \sin(2az) \\ A_2 &= M_{xz} \cos(az) + M_{yz} \sin(az) \\ A_3 &= -\frac{1}{2}(M_{xx} + M_{yy}) \\ A_4 &= \frac{1}{2}(M_{xx} - M_{yy}) \sin(2az) - M_{xy} \cos(2az) \\ A_5 &= -M_{yz} \cos(az) + M_{xz} \sin(az) \end{aligned} \quad (A5.3)$$

These equations are identical to (A5.2) which can be proven by using (18) together with (15) and (16). Note that the coefficients given in (A5.3) agree with the moment tensor elements as defined by Aki and Richards (1980; (A5.3) differs in sign with the coefficients of Langston (1981) due to conventions on displacements and Green's functions).

Note that either definition of the coefficients of the Green's functions can be used for the calculation of the displacement at the free surface, depending on whether the focal mechanism or the moment tensor is given. Here, equations (A5.3) and (A5.1) are used in order to develop an inversion scheme for the moment tensor elements. We

regroup and assume the presence of an isotropic component ( $ZEP \neq 0$ ,  $REP \neq 0$ ):

$$\begin{aligned} d_z(r, z=0, \omega) &= M_{zz} \left[ \frac{ZSS}{2} \cos(2az) - \frac{ZDD}{2} + \frac{ZEP}{3} \right] \\ &+ M_{yy} \left[ \frac{-ZSS}{2} \cos(2az) - \frac{ZDD}{2} + \frac{ZEP}{3} \right] \\ &+ M_{zz} \left[ \frac{ZEP}{3} \right] \\ &+ M_{zy} [ZSS \sin(2az)] \\ &+ M_{zz} [ZDS \cos(az)] \\ &+ M_{yz} [ZDS \sin(az)] \end{aligned} \quad (A5.4)$$

$$\begin{aligned} d_r(r, z=0, \omega) &= M_{zz} \left[ \frac{RSS}{2} \cos(2az) - \frac{RDD}{2} + \frac{REP}{3} \right] \\ &+ M_{yy} \left[ \frac{-RSS}{2} \cos(2az) - \frac{RDD}{2} + \frac{REP}{3} \right] \\ &+ M_{zz} \left[ \frac{REP}{3} \right] \\ &+ M_{zy} [RSS \sin(2az)] \\ &+ M_{zz} [RDS \cos(az)] \\ &+ M_{yz} [RDS \sin(az)] \end{aligned} \quad (A5.5)$$

$$\begin{aligned} d_\phi(r, z=0, \omega) &= M_{zz} \left[ \frac{TSS}{2} \sin(2az) \right] \\ &+ M_{yy} \left[ \frac{-TSS}{2} \sin(2az) \right] \\ &+ M_{zy} [-TSS \cos(2az)] \\ &+ M_{zz} [TDS \sin(az)] \\ &+ M_{yz} [-TDS \cos(az)] \end{aligned} \quad (A5.6)$$

Equations (A5.4), (A5.5), and (A5.6) each set up a moment tensor inversion scheme. Equations (A5.4) and (A5.5) are formulated for the general case where the inversion expects a moment tensor that is a composition of an isotropic part and a deviatoric part. An inversion based on transverse data, (A5.6), cannot resolve  $M_{zz}$ . In such a case, we assume that the moment tensor is purely deviatoric and constrain  $M_{zz} = -(M_{xx} + M_{yy})$ . The same constraint can be applied to (A5.4) and (A5.5) in the case of

### A Student's Guide to and Review of Moment Tensors

an inversion that looks for a pure deviatoric moment tensor (set formally  $ZEP = REP = 0$  in (A5.4) and (A5.5), Dziewonski *et al.*, 1981).

From the last three equations we see that the observed displacement at the free surface is a linear combination of the station specific Green's functions, within the square brackets, with the moment tensor elements as scalar multipliers. We also note that if the source time function is known and a point source approximation is acceptable, the moment tensor elements are independent of frequency (linear inversion) and similar equations arise relating observed time histories to temporal Green's functions within the square brackets.

Next, we performed a simple moment tensor inversion using the vertical component of synthetic teleseismic P-wave first motion peak amplitudes as suggested by Stump and Johnson (1977). We assumed a pure deviatoric source ( $ZEP = 0$  in (A5.4)).

Let  $az_1, \dots, az_n$  be azimuths of  $n$  different stations. Then the expressions in the square brackets of (A5.4) define components of a matrix as  $a_{i1}(az_i), \dots, a_{i5}(az_i)$  for the  $i$ -th azimuth. A system of linear equations arises:

$$\begin{bmatrix} d_z(az_1) \\ \vdots \\ d_z(az_n) \end{bmatrix} = \begin{bmatrix} a_{11}(az_1) & \dots & a_{15}(az_1) \\ \vdots & \ddots & \vdots \\ a_{n1}(az_n) & \dots & a_{n5}(az_n) \end{bmatrix} \begin{bmatrix} M_{xx} \\ M_{yy} \\ M_{xy} \\ M_{zz} \\ M_{yz} \end{bmatrix} \quad (\text{A5.7})$$

For observations at more than 5 distinct azimuths, the system (A5.7) is overdetermined. The solution can be reached by the classical least squares approach. The five moment tensor elements can be determined by using the numerical stable singular value decomposition. We imposed the deviatoric constraint  $M_{zz} = -(M_{xx} + M_{yy})$ . Hence the inversion gives a purely deviatoric source. However, we were *not* constraining one eigenvalue as zero (double couple), letting the inversion tell us about double couple and CLVD components. The eigenvalues and eigenvectors can be calculated using the Householder transformation with further QL decomposition. The implementation of these numerical concepts was done using code by Press *et al.* (1987).

In the following, some results of inverting synthetic data are presented. First, Green's functions were calculated using a Haskell formalism for a simple half-space model ( $V_p = 8$  km/sec,  $V_s = 4.6$  km/sec and  $\rho = 3.3$  g/cm<sup>3</sup>,  $h = 30$  km). Figure A.3 shows the three basic Green's functions ZSS, ZDD, and ZDS. The assumed focal mechanism (Figure A.4: strike = 180°, dip = 40°, slip = 110°) is the same as used by Herrmann (1975, Figure 2). Teleseismic P-wave first motions were synthesized at 12 equidistant azimuths (epicentral distance = 50°). Note that an instrument response was not included in the synthetics. Due to the simple model and the fact that all stations are equidistant from the source, a correction for anelastic attenuation ( $t^* = 0.7$ ) or geometrical spreading is not required. A correction for an extended source is not necessary since the moment used is  $10^{20}$  dyne-cm and the duration of the source time function is 0.2 sec. We used (A5.4) for time domain measurements.

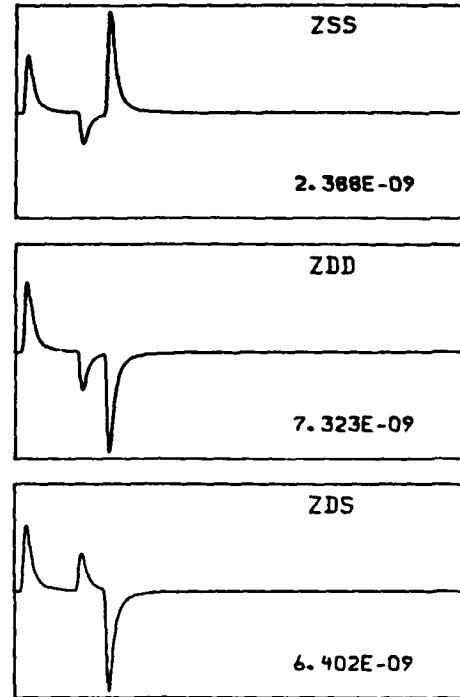


Fig. A.3. Synthetic Green's functions ZSS, ZDD, and ZDS (Herrmann and Wang, 1985) for a half-space model ( $V_p = 8$  km/sec,  $V_s = 4.6$  km/sec,  $\rho = 3.3$  g/cm<sup>3</sup>,  $h = 30$  km,  $t^* = 0.7$ ) calculated by using the Haskell formalism. The time window ranges from 4.0 to 55.1 sec ( $dt = 0.05$  sec). Maximum amplitudes are in cm (Appendix V).

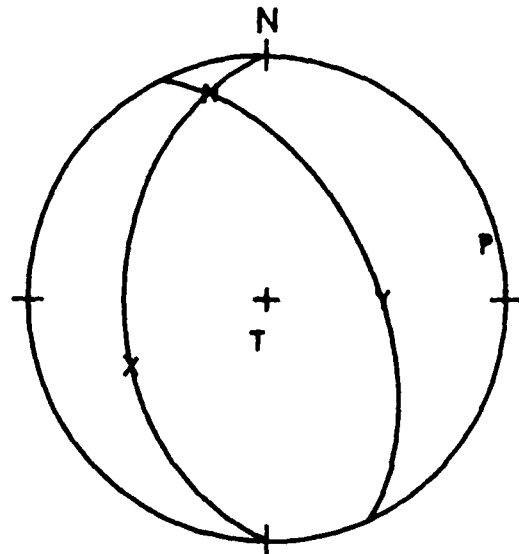


Fig. A.4. Assumed focal mechanism for the synthetic seismograms: strike = 180°, dip = 40°, slip = 110° (Appendix V).

TABLE A.7: RESULTS OF THE MOMENT TENSOR INVERSION (MAJOR COUPLE)

	Case 0	Case I	Case II	Case III	Case IV	Case V
$M_{xx}$	0	-0.037	-0.050	-0.109	-0.202	0.301
$M_{yy}$	-0.925	-0.902	-0.951	-0.966	-1.023	-1.091
$M_{zz}$	0.925	0.939	1.002	1.075	1.225	0.791
$M_{xy}$	-0.220	-0.199	-0.200	-0.194	-0.176	0.257
$M_{xz}$	-0.262	-0.262	-0.260	-0.264	-0.257	-0.172
$M_{yz}$	-0.163	-0.168	-0.162	-0.168	-0.156	-0.324
EV(NULL)	0.00	-0.04	-0.05	-0.11	-0.20	0.26
EV(T)	1.00	1.01	1.07	1.14	1.28	0.92
EV(P)	-1.00	-0.97	-1.02	-1.03	-1.08	-1.18
% of DC	100	92	90	81	69	56
% of CLVD	0	8	10	19	31	44
$M_0$	1.00	0.99	1.04	1.09	1.19	1.07
STRIKE	180.0	179.5	179.2	177.8	176.4	211.8
DIP	40.0	39.7	40.1	39.9	40.5	40.8
SLIP	110.0	109.0	107.8	106.1	103.2	123.1
STRIKE	334.6	335.4	336.5	337.2	339.3	351.1
DIP	52.8	52.9	52.2	51.9	50.8	56.8
SLIP	74.0	74.9	75.6	77.0	79.0	64.8
T (TRD)	192.7	194.9	194.7	196.8	198.2	209.7
T (PLG)	75.6	76.2	77.1	78.1	80.0	67.3
P (TRD)	75.9	76.1	76.7	76.4	77.1	98.8
P (PLG)	6.6	6.7	6.2	6.1	5.2	8.5

For Case 0, moment tensor elements are calculated from (18) assuming a double couple source (strike = 180°, dip = 40°, slip = 110°). The eigenvalues of the moment tensor corresponding to the null-, T-, and P-axes are shown as EV(NULL), EV(T), and EV(P), respectively. Equation (38) is used to determine the percentage of double couple or CLVD from the eigenvalues of the moment tensor. The seismic moment is calculated using (20). The orientation of the fault plane and auxiliary plane is given together with the trend and plunge of the T- and P-axes (Herrmann, 1975). Cases I - IV are for additive pseudo-random noise (0 %, 14 %, 28 %, and 56 %, respectively) in the synthetic seismograms at 12 different azimuths. Case V assumes that one of the 12 seismograms has a reversed polarity (0 % pseudo random noise).

Table A.7 displays the inversion results for the major couple. The moment tensor elements, the percentage of double couple and CLVD, the seismic moment, and the focal mechanism parameters are shown. For Case 0, the moment tensor elements were calculated from the given fault plane solution and (18). Next, three experiments were performed: 1.) synthetic seismograms were calculated using the Haskell method (Case I). Figure A.5a shows the vertical component of a synthetic seismogram at an azimuth of 0 degrees. 2.) Different amounts of pseudo-random noise were added to the synthetic seismograms calculated in Case I with amplitudes of  $\pm 0.25 \times 10^{-9}$  cm (Case II, Figure A.5b),  $\pm 0.5 \times 10^{-9}$  cm (Case III, Figure A.5c), and  $\pm 1.0 \times 10^{-9}$  cm (Case IV, Figure A.5d). Averaged over the 12 azimuths, these noise levels correspond to 14 %, 28 %, and 56 % pseudo-random additive noise, respectively. 3.) The final experiment (Case V) relates to possible polarity errors of seismo-

graphs. Hence it was assumed that one of the 12 seismograms of Case I had a wrong polarity.

The theoretical focal parameters (Case 0) agree within the measurement errors with the observed ones (Case I). This justifies the technique. The effect of noise is to severely distort the moment tensor elements. The isotropic moment tensor components seem to be more sensitive to noise than the deviatoric ones. Notice that the moment tensor gains a contribution of a CLVD due to the noise. The percentage of CLVD versus double couple increases with increasing noise. The effect of random noise on the fault plane solution that is derived from the moment tensor elements is minor; i.e. the fault plane solution for the major double couple is very close to the original focal mechanism. However, with increasing noise, the fault plane solution deteriorates. 8 % polarization errors in otherwise perfect data lead to worse results than 56 % additive random noise (Case IV). A doubling of the



REFERENCES

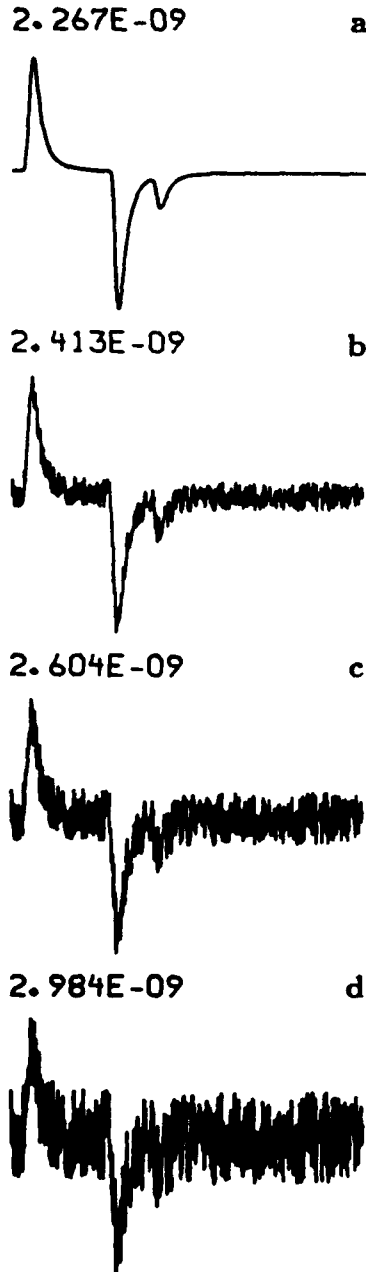


Fig. A.5. Vertical components of synthetic teleseismic seismograms at 50 degrees and azimuth of  $0^\circ$ . The time window ranges from 4.0 to 29.6 sec ( $dt = 0.05$  sec). Maximum amplitudes are in cm. (a) No pseudo-random noise added; (b) - (d) pseudo-random noise is added with amplitudes of  $\pm 0.25 \times 10^{-9}$  cm,  $\pm 0.50 \times 10^{-9}$  cm,  $\pm 1.0 \times 10^{-9}$  cm, respectively (Appendix V).

polarization errors gives meaningless results. Due to the setup of the experiment, a minor couple would be a pure artifact of the noise.

Agnew, D., J. Berger, R. Buland, W. Farrell, and F. Gilbert (1976). International deployment of accelerometers: a network for very long-period seismology, *EOS, Trans. Am. Geophys. Union* **57**, 180-188.

Aki, K. and P. G. Richards (1980). *Quantitative Seismology: Theory and Methods*, W. H. Freeman and Co., New York, San Francisco, 932 pp.

Arfken, G. (1985). *Mathematical Methods for Physicists*, 3rd ed., Academic Press Inc., Orlando, Florida, 985 pp.

Backus, G. E. (1977a). Interpreting the seismic glut moments of total degree two or less, *Geophys. J. R. Astr. Soc.* **51**, 1-25.

Backus, G. E. (1977b). Seismic sources with observable glut moments of spatial degree two, *Geophys. J. R. Astr. Soc.* **51**, 27-45.

Backus, G. and M. Mulcahy (1976). Moment tensors and other phenomenological descriptions of seismic sources - I. continuous displacements, *Geophys. J. R. Astr. Soc.* **46**, 341-381.

Ben-Menahem, A. and S. J. Singh (1968). Eigenvector expansions of Green's dyads with applications to geophysical theory, *Geophys. J. R. Astr. Soc.* **16**, 417-452.

Ben-Menahem, A. and S. J. Singh (1981). *Seismic Waves and Sources*, Springer Verlag, New York, 1108 pp.

Bullen, K. E. and B. A. Bolt (1985). *An Introduction to the Theory of Seismology*, 4th ed., Cambridge University Press, Cambridge, 409 pp.

Burdick, L. J. and G. R. Mellman (1976). Inversion of the body waves from the Borrego Mountain earthquake to the source mechanism, *Bull. Seism. Soc. Am.* **66**, 1485-1490.

Burridge, R., E. R. Lapwood, and L. Knopoff (1964). First motions from seismic sources near a free surface, *Bull. Seism. Soc. Am.* **54**, 1889-1913.

Christensen, D. H. and L. J. Ruff (1985). Analysis of the trade-off between hypocentral depth and source time function, *Bull. Seism. Soc. Am.* **75**, 1637-1656.

Claerbout, J. F. and F. Muir (1973). Robust modeling with erratic data, *Geophysics* **38**, 826-844.

Dziewonski, A. M. and F. Gilbert (1974). Temporal variation of the seismic moment tensor and the evidence of precursive compression for two deep earthquakes, *Nature* **247**, 185-188.

- Dziewonski, A. M. and J. H. Woodhouse (1983a). Studies of the seismic source using normal-mode theory, in *Earthquakes: Observation, Theory and Interpretation*, H. Kanamori and E. Boschi, Editors, North-Holland, Amsterdam, New York, Oxford, 608 pp.
- Dziewonski, A. M. and J. H. Woodhouse (1983b). An experiment in systematic study of global seismicity: centroid-moment tensor solutions for 201 moderate and large earthquakes of 1981, *J. Geophys. Res.* **88**, 3247-3271.
- Dziewonski, A. M., T.-A. Chou, and J. H. Woodhouse (1981). Determination of earthquake source parameters from waveform data for studies of global and regional seismicity, *J. Geophys. Res.* **86**, 2825-2852.
- Dziewonski, A. M., A. Friedman, D. Giardini, and J. H. Woodhouse (1983a). Global seismicity of 1982: centroid-moment tensor solutions for 308 earthquakes, *Phys. Earth Planet. Interiors* **33**, 76-90.
- Dziewonski, A. M., A. Friedman, and J. H. Woodhouse (1983b). Centroid-moment tensor solutions for January-March 1983, *Phys. Earth Planet. Interiors* **33**, 71-75.
- Dziewonski, A. M., J. E. Franzen, and J. H. Woodhouse (1983c). Centroid-moment tensor solutions for April-June 1983, *Phys. Earth Planet. Interiors* **33**, 243-249.
- Dziewonski, A. M., J. E. Franzen, and J. H. Woodhouse (1984a). Centroid-moment tensor solutions for July-September 1983, *Phys. Earth Planet. Interiors* **34**, 1-8.
- Dziewonski, A. M., J. E. Franzen, and J. H. Woodhouse (1984b). Centroid-moment tensor solutions for October-December 1983, *Phys. Earth Planet. Interiors* **34**, 129-136.
- Dziewonski, A. M., J. E. Franzen, and J. H. Woodhouse (1984c). Centroid-moment tensor solutions for January-March 1984, *Phys. Earth Planet. Interiors* **34**, 209-210.
- Dziewonski, A. M., J. E. Franzen, and J. H. Woodhouse (1985a). Centroid-moment tensor solutions for April-June 1984, *Phys. Earth Planet. Interiors* **37**, 87-96.
- Dziewonski, A. M., J. E. Franzen, and J. H. Woodhouse (1985b). Centroid-moment tensor solutions for July-September 1984, *Phys. Earth Planet. Interiors* **38**, 203-213.
- Dziewonski, A. M., J. E. Franzen, and J. H. Woodhouse (1985c). Centroid-moment tensor solutions for October-December 1984, *Phys. Earth Planet. Interiors* **39**, 147-156.
- Dziewonski, A. M., J. E. Franzen, and J. H. Woodhouse (1985d). Centroid-moment tensor solutions for January-March 1985, *Phys. Earth Planet. Interiors* **40**, 249-258.
- Dziewonski, A. M., J. E. Franzen, and J. H. Woodhouse (1986a). Centroid-moment tensor solutions for April-June 1985, *Phys. Earth Planet. Interiors* **41**, 215-224.
- Dziewonski, A. M., J. E. Franzen, and J. H. Woodhouse (1986b). Centroid-moment tensor solutions for July-September 1985, *Phys. Earth Planet. Interiors* **42**, 205-214.
- Dziewonski, A. M., J. E. Franzen, and J. H. Woodhouse (1986c). Centroid-moment tensor solutions for October-December 1985, *Phys. Earth Planet. Interiors* **43**, 185-195.
- Dziewonski, A. M., G. Ekström, J. E. Franzen, and J. H. Woodhouse (1987a). Centroid-moment tensor solutions for January-March 1986, *Phys. Earth Planet. Interiors* **45**, 1-10.
- Dziewonski, A. M., G. Ekström, J. E. Franzen, and J. H. Woodhouse (1987b). Global seismicity of 1977: centroid-moment tensor solutions for 471 earthquakes, *Phys. Earth Planet. Interiors* **45**, 11-36.
- Dziewonski, A. M., G. Ekström, J. E. Franzen, and J. H. Woodhouse (1987c). Centroid-moment tensor solutions for July-September 1986, *Phys. Earth Planet. Interiors* **46**, 305-315.
- Dziewonski, A. M., G. Ekström, J. E. Franzen, and J. H. Woodhouse (1987d). Global seismicity of 1978: centroid-moment tensor solutions for 512 earthquakes, *Phys. Earth Planet. Interiors* **46**, 316-342.
- Dziewonski, A. M., G. Ekström, J. H. Woodhouse and G. Zwart (1987e). Centroid-moment tensor solutions for October-December 1986, *Phys. Earth Planet. Interiors* **48**, 5-17.
- Dziewonski, A. M., G. Ekström, J. E. Franzen, and J. H. Woodhouse (1987f). Global seismicity of 1979: centroid-moment tensor solutions for 524 earthquakes, *Phys. Earth Planet. Interiors* **48**, 18-46.
- Ekström, G. and A. M. Dziewonski (1985). Centroid-moment tensor solutions for 35 earthquakes in Western North America (1977-1983), *Bull. Seism. Soc. Am.* **75**, 23-30.
- Ekström, G., A. M. Dziewonski, and J. H. Woodhouse (1987). Centroid-moment tensor solutions for the 51 IASPEI selected earthquakes, 1980-1984, *Phys. Earth Planet. Interiors* **47**, 62-66.
- Engdahl, E. R. and H. Kanamori (1980). Determination of earthquake parameters, *EOS, Trans. Am. Geophys. Union* **61**, 60-65.

### A Student's Guide to and Review of Moment Tensors

- Evison, F. F. (1963). Earthquakes and faults, *Bull. Seism. Soc. Am.* **53**, 873-891.
- Faddeeva (1959). *Computational Methods of Linear Algebra*, Dover, New York, 252 pp.
- Fitch, T. J. (1981). Correction and addition to 'Estimation of the seismic moment tensor from teleseismic body wave data with applications to intraplate and mantle earthquakes' by T. J. Fitch, D. W. McCowan, and M. W. Shields, *J. Geophys. Res.* **86**, 9375-9376.
- Fitch, T. J., D. W. McCowan, and M. W. Shields (1980). Estimation of the seismic moment tensor from teleseismic body wave data with applications to intraplate and mantle earthquakes, *J. Geophys. Res.* **85**, 3817-3828.
- Fitch, T. J., R. G. North, and M. W. Shields (1981). Focal depths and moment tensor representations of shallow earthquakes associated with the great Sumba earthquake, *J. Geophys. Res.* **86**, 9357-9374.
- Geller, R. J. (1976). Body force equivalents for stress-drop seismic sources, *Bull. Seism. Soc. Am.* **66**, 1801-1804.
- Giardini, D. (1984). Systematic analysis of deep seismicity: 200 centroid-moment tensor solutions for earthquakes between 1977 and 1980, *Geophys. J. R. Astr. Soc.* **77**, 883-914.
- Gilbert, F. (1970). Excitation of the normal modes of the earth by earthquake sources, *Geophys. J. R. Astr. Soc.* **22**, 223-226.
- Gilbert, F. (1973). Derivation of source parameters from low-frequency spectra, *Phil. Trans. R. Soc. A* **274**, 369-371.
- Gilbert, F. and R. Buland (1976). An enhanced deconvolution procedure for retrieving the seismic moment tensor from a sparse network, *Geophys. J. R. Astr. Soc.* **47**, 251-255.
- Gilbert, F. and A. M. Dziewonski (1975). An application of normal mode theory to the retrieval of structural parameters and source mechanisms from seismic spectra, *Phil. Trans. R. Soc. A* **278**, 187-260.
- Gomberg, J. S. and T. G. Masters (1988). Waveform modeling using locked-mode synthetic and differential seismograms: application to determination of the structure of Mexico, *Geophys. J.* **94**, 193-218.
- Hagiwara, T. (1958). A note on the theory of the electromagnetic seismograph, *Bull. Earthquake Res. Inst. Tokyo Univ.* **36**, 139-164.
- Harkrider, D. G. (1961). Surface waves in multilayered elastic media, 1. Rayleigh and Love waves from buried sources in a multilayered elastic half-space, *Bull. Seism. Soc. Am.* **54**, 627-679.
- Harkrider, D. G. (1970). Surface waves in multilayered elastic media, 2. Higher mode spectra and spectral ratios from point sources in plane layered earth models, *Bull. Seism. Soc. Am.* **60**, 1937-1987.
- Harkrider, D. G. (1976). Potentials and displacements for two theoretical seismic sources, *Geophys. J. R. Astr. Soc.* **47**, 97-133.
- Herrmann, R. B. (1975). A student's guide to the use of P and S wave data for focal mechanism determination, *Earthquake Notes* **46**, 29-39.
- Herrmann, R. B. and C. Y. Wang (1985). A comparison of synthetic seismograms, *Bull. Seism. Soc. Am.* **75**, 41-56.
- Hirasawa, T. and W. Stauder, S.J. (1965). On the seismic body waves from a finite moving source, *Bull. Seism. Soc. Am.* **55**, 237-262.
- Honda, H. (1962). Earthquake mechanism and seismic waves, *Geophysical Notes, Geophys. Inst. Fac. of Science, Tokyo Univ.* **15**, 1-97.
- Kanamori, H. and J. W. Given (1981). Use of long-period surface waves for rapid determination of earthquake-source parameters, *Phys. Earth Planet. Interiors* **27**, 8-31.
- Kanamori, H. and J. W. Given (1982). Use of long-period surface waves for rapid determination of earthquake source parameters: 2. Preliminary determination of source mechanisms of large earthquakes ( $M_s \geq 6.5$ ) in 1980, *Phys. Earth Planet. Interiors* **30**, 260-268.
- Kennett, B. L. N. (1983). *Seismic Wave Propagation in Stratified Media*, Cambridge University Press, Cambridge, 342 pp.
- Kennett, B. L. N. (1988). Radiation from a moment-tensor source, in *Seismological Algorithms - Computational Methods and Computer Programs*, D. J. Doornbos, Editor, Academic Press, San Diego, California, 427-441.
- Kikuchi, M. and H. Kanamori (1982). Inversion of complex body waves, *Bull. Seism. Soc. Am.* **72**, 491-506.
- Knopoff, L. and M. J. Randall (1970). The compensated linear-vector dipole: a possible mechanism for deep earthquakes, *J. Geophys. Res.* **75**, 4057-4063.
- Landisman, M., A. Dziewonski, and Y. Sato (1969). Recent improvements in the analysis of surface wave observations, *Geophys. J. R. Astr. Soc.* **17**, 369-403.

- Langston, C. A. (1981). Source inversion of seismic waveforms: The Koyna, India, earthquakes of 13 September 1967, *Bull. Seism. Soc. Am.* **71**, 1-24.
- Langston, C. A. and D. V. Helmberger (1975). A procedure for modeling shallow dislocation sources, *Geophys. J. R. Astr. Soc.* **42**, 117-130.
- Lawson, C. H. and R. J. Hanson (1974). *Solving Least Squares Problems*, Prentice-Hall, Englewood Cliffs, New Jersey.
- Lay, T., J. W. Given, and H. Kanamori (1982). Long-period mechanism of the 8 November 1980 Eureka, California, earthquake, *Bull. Seism. Soc. Am.* **72**, 439-456.
- Lundgren, P. R., E. A. Okal, and S. Stein (1988). Body-wave deconvolution for variable source parameters; application to the 1978 December 6 Kuriles earthquake, *Geophys. J.* **94**, 171-180.
- Maruyama, T. (1964). Statical elastic dislocations in an infinite and semi-infinite medium, *Bull. Earthquake Res. Inst.* **42**, 289-368.
- McCowan, D. W. (1976). Moment tensor representation of surface wave sources, *Geophys. J. R. Astr. Soc.* **44**, 595-599.
- McCowan, D. W. and R. T. Lacos (1978). Transfer functions for the seismic research observatory seismograph system, *Bull. Seism. Soc. Am.* **68**, 501-512.
- McKenzie, D. P. (1969). The relation between fault plane solutions for earthquakes and the directions of the principal stresses, *Bull. Seism. Soc. Am.* **59**, 591-601.
- Mendiguren, J. A. (1977). Inversion of surface wave data in source mechanism studies, *J. Geophys. Res.* **82**, 889-894.
- Nakanishi, I. and H. Kanamori (1982). Effects of lateral heterogeneity and source process time on the linear moment tensor inversion of long-period Rayleigh waves, *Bull. Seism. Soc. Am.* **72**, 2063-2080.
- Nakanishi, I. and H. Kanamori (1984). Source mechanisms of twenty-six large, shallow earthquakes ( $M_S \geq 6.5$ ) during 1980 from P-wave first motion and long-period Rayleigh wave data, *Bull. Seism. Soc. Am.* **74**, 805-818.
- O'Connell, D. R. H. and L. R. Johnson (1988). Second order moment tensors of microearthquakes at The Geysers geothermal field, California, *Bull. Seism. Soc. Am.* **78**, 1674-1692.
- Okal, E. A. and R. J. Geller (1979). On the observability of isotropic seismic sources: the July 31, 1970 Colombian earthquake, *Phys. Earth Planet. Interiors* **18**, 176-196.
- Patton, H. (1980). Reference point equalization method for determining the source and path effects of surface waves, *J. Geophys. Res.* **85**, 821-848.
- Patton, H. and K. Aki (1979). Bias in the estimate of seismic moment tensor by the linear inversion method, *Geophys. J. R. Astr. Soc.* **59**, 479-495.
- Press, W. H., B. P. Flannery, S. A. Teukolsky, and W. T. Vetterling (1987). *Numerical Recipes: The Art of Scientific Computing*, Cambridge University Press, Cambridge, 818 pp.
- Randall, M. J. and L. Knopoff (1970). The mechanism at the focus of deep earthquakes, *J. Geophys. Res.* **75**, 4965-4976.
- Reid, H. F. (1910). Elastic rebound theory, *Univ. Calif. Publ., Bull. Dept. Geol. Sci.* **6**, 413-433.
- Romanowicz, B. (1981). Depth resolution of earthquakes in central Asia by moment tensor inversion of long-period Rayleigh waves: Effects of phase velocity variations across Eurasia and their calibration, *J. Geophys. Res.* **86**, 5063-5084.
- Saito, M. (1967). Excitation of free oscillations and surface waves by a point source in a vertically heterogeneous earth, *J. Geophys. Res.* **72**, 3689-3699.
- Satake, K. (1985). Effects of station coverage on moment tensor inversion, *Bull. Seism. Soc. Am.* **75**, 1657-1667.
- Scott, D. R. and H. Kanamori (1985). On the consistency of moment tensor source mechanisms with first-motion data, *Phys. Earth Planet. Interiors* **37**, 97-107.
- Silver, P. G. and T. H. Jordan (1982). Optimal estimation of scalar seismic moment, *Geophys. J. R. Astr. Soc.* **70**, 755-787.
- Sipkin, S. A. (1982). Estimation of earthquake source parameters by the inversion of waveform data: synthetic waveforms, *Phys. Earth Planet. Interiors* **30**, 242-255.
- Sipkin, S. A. (1986). Interpretation of non-double-couple earthquake mechanisms derived from moment tensor inversion, *J. Geophys. Res.* **91**, 531-547.
- Sipkin, S. A. (1987). Moment tensor solutions estimated using optimal filter theory for 51 selected earthquakes, 1980-1984, *Phys. Earth Planet. Interiors* **47**, 67-79.
- Snieder, R. and B. Romanowicz (1988). A new formalism for the effect of lateral heterogeneity on normal modes and surface waves - I: isotropic perturbations, perturbations of interfaces and gravitational perturbations, *Geophys. J.* **92**, 207-222.

A Student's Guide to and Review of Moment Tensors

- Strelitz, R. A. (1978). Moment tensor inversions and source models, *Geophys. J. R. Astr. Soc.* **52**, 359-364.
- Strelitz, R. A. (1980). The fate of the downgoing slab: A study of the moment tensors from body waves of complex deep-focus earthquakes, *Phys. Earth Planet. Interiors* **21**, 83-96.
- Stump, B. W. and L. R. Johnson (1977). The determination of source properties by the linear inversion of seismograms, *Bull. Seism. Soc. Am.* **67**, 1489-1502.
- Vasco, D. W. and L. R. Johnson (1988). Inversion of waveforms for extreme source models with an application to the isotropic moment tensor component, in *Regional Studies with Broadband Data*, T. V. McEvelly and L. R. Johnson, Editors, Report No. 1, Air Force Geophysics Laboratory AFGL-TR-88-0131.
- Wallace, T. C. (1985). A reexamination of the moment tensor solutions of the 1980 Mammoth Lakes earthquakes, *J. Geophys. Res.* **90**, 11,171-11,176.
- Wallace, T. C., D. V. Helmberger, and G. R. Mellman (1981). A technique for the inversion of regional data in source parameter studies, *J. Geophys. Res.* **86**, 1679-1685.
- Wang C. Y. and R. B. Herrmann (1980). A numerical study of P-, SV-, and SH-wave generation in a plane layered medium, *Bull. Seism. Soc. Am.* **70**, 1015-1036.
- Ward, S. N. (1980a). Body wave calculations using moment tensor sources in spherically symmetric, inhomogeneous media, *Geophys. J. R. Astr. Soc.* **60**, 53-66.
- Ward, S. N. (1980b). A technique for the recovery of the seismic moment tensor applied to the Oaxaca, Mexico earthquake of November 1978, *Bull. Seism. Soc. Am.* **70**, 717-734.

Received June 23, 1988  
Revised October 4, 1988  
Accepted November 1, 1988

## **Ground roll: rejection using adaptive phase matched filters**

Robert B. Herrmann\* and David R. Russell\*\*

### **ABSTRACT**

The technique of phase match filtering dispersive surface waves is extended to permit an adaptive, iterative process by which the signal itself in a seismic trace designs a filter to remove the surface wave. The technique is robust and well behaved, and requires the specification of only simple parameters for its operation.

The technique is applied to data sets from three regions, representing a wide range in the ratio of surface-wave noise to exploration signal. The technique works very well with poor data sets and also improves good data sets. Since the technique is applied to individual traces, it works in situations for which f-k filtering might not be feasible due to poor spatial sampling. The technique is computationally more intensive than recursive digital bandpass filtering of individual traces, but is less intensive than filtering in the f-k domain.

---

\*Department of Earth and Atmospheric Sciences, Saint Louis University, 3507 Laclede Avenue, St. Louis, MO 63103.

\*\*Formerly Department of Earth and Atmospheric Sciences, Saint Louis University; presently AFTAC, Patrick AFB, FL.

## INTRODUCTION

Surface-wave noise, the ground roll, on reflection seismograms is always a part of land based data acquisition. As such it has always been something to be eliminated in order to focus on the underlying reflection data. Dobrin (1951) studied the ground roll, showing that it possessed the properties of dispersive surface waves. Al-Husseini et al (1981) inverted the surface-wave data obtained in special tests to characterize the ground roll in a region of eastern Saudi Arabia and thus to provide the necessary information for proper group array design for its elimination. Under optimal conditions, proper group array design succeeds in attenuating the low phase velocity surface-wave arrivals, enhancing the high phase velocity reflections.

Earthquake seismology has historically taken the opposite approach, that the surface wave is a very useful signal for defining earth structure as well as the seismic source. Because of this emphasis many techniques for surface-wave analysis have been developed in this field. Our technique makes use of phase matched filtering of surface waves (Herrin and Goforth, 1977; Goforth and Herrin, 1979; and Beresford-Smith and Mason, 1980). In earthquake seismology, the objective of phase matched filtering is to isolate a dispersed surface wave mode from a noise background consisting of body-wave arrivals or secondary surface-wave arrivals due to multipathing. The isolated surface wave has a smoother amplitude spectrum and also a better defined dispersion for use in source and earth structure studies, respectively. From this point of view, the typical exploration reflection signal is viewed as noise. The essence of the technique described in this paper is the recognition that the surface-wave signal in earthquake seismology is the exploration noise, and vice versa.

### Phase matched filtering

Consider a frequency domain representation,  $S(f)$ , of a time domain signal,  $s(t)$  at a distance  $x$ , consisting of  $N$  arrivals:

$$S(f) = \sum_{i=1}^N A_i(f) e^{-jk_i(f)x} \quad (1)$$

Here, a propagating wave notation is used to represent each arrival.  $A_i(f)$  and  $k_i(f)$  are the complex amplitude and wavenumber spectra of the  $i$ 'th arrival. If the wavenumber  $k_i(f)$  is purely linear in frequency, then its corresponding time domain signal is just time shifted as a function of distance; otherwise it is dispersed. In addition, as long as we focus on a single distance, equation (1) is general enough to also include a non-propagating noise components.

Suppose further that the  $m$ 'th arrival is not desired, and that the wavenumber function  $\kappa_m(f)$  is a reasonable approximation to the unknown  $k_m(f)$ . Now multiply  $S(f)$  by an inverse propagating wave function to yield

$$\begin{aligned} S(f) e^{j\kappa_m(f)x} &= \sum_{i=1, i \neq m}^N A_i(f) e^{-j[k_i(f) - \kappa_m(f)]x} \\ &+ A_m(f) e^{-j[k_m(f) - \kappa_m(f)]x} \end{aligned} \quad (2)$$

If the terms  $[k_i(f) - \kappa_m(f)]x$  for  $i \neq m$  are sufficiently different from zero, and if the term  $[k_m(f) - \kappa_m(f)]x$  is sufficiently close to zero, then the inverse transform of

equation (2) will yield a pulse at zero lag, which will be the compressed, or undispersed,  $m$ 'th arrival. The other arrivals will be either spread out, or if compressed, not compressed as much, and certainly not located at zero lag.

In earthquake seismology, the signal so compressed and shifted to zero lag is the one of interest. It is windowed about zero lag, transformed into the frequency domain, uncompressed using the dispersion operator

$$e^{-j\kappa_m(f)x}, \quad (3)$$

and then inverse transformed into the time domain. This operation yields a clean surface-wave signal (Herrin and Goforth, 1977; Goforth and Herrin, 1979). To obtain the exploration signal one can either subtract the isolated  $m$ 'th arrival from the original time series, the technique used here, or mute the inverse transform of equation (2) about zero lag, and then take a Fourier transform of the resultant trace, apply the operator of equation (3), and then inverse transform the result to the time domain (Beresford-Smith and Rango, 1988; Saatçilar and Canitez, 1988). The result in either case will now be a multi-arrival signal lacking the  $m$ 'th arrival.

While conceptually very simple, the success of this technique lies in the correct specification of the function  $\kappa_m(f)$ . If multitrace data are available, and if a coherent  $k-f$  or  $p-\omega$  (McMechan and Yedlin, 1981) display can be made, then this may be possible. The resulting  $\kappa_m(f)$  would represent a spatial average over the data set, which may not be appropriate if there are lateral variations in the surface-wave dispersion. On the other hand, if the objective is only to remove the undesired surface-wave signal and not to define the correct phase velocity dispersion function, then this same technique can be applied using single trace data, e.g., treating each trace as an independent data set. The trick is to make the processing iterative, allowing the data itself to define its own dispersion operator by improving an initial estimate. This is in fact the heart of the Herrin and Goforth (1977) and Goforth and Herrin (1979) technique.

In order to reject a signal, it must be isolated. Compressing it perfectly should yield a zero phase wavelet centered at zero lag. The degree to which this is not true, indicates the subtle differences between the unknown  $k_m(f)$  and the trial function  $\kappa_m(f)$ . By windowing the compressed signal about zero lag, Fourier transforming it, and unwrapping the phase delay, the difference can be defined. This phase difference is then used to adjust the  $\kappa_m(f)$ .

To control this procedure, we force the function  $\kappa_m(f)$  to be initially a simple dispersion function by approximating it by B-splines with a small number of nodes. At each iteration, a least-squares B-spline is fit to the phase differences, to yield a simple, smooth perturbation on the current estimate of  $\kappa_m(f)$ . This smoothing technique maintains the assumption that a smooth dispersion operator is required to model surface waves.

To start the process, an initial estimate of  $\kappa_m(f)$  is required. For simplicity of use, we use the following approach. By visual examination of all traces or by application of multiple filter techniques (Dziewonski et al., 1969; Herrmann, 1973), an estimate is made of the group velocity window and bandwidth associated with each signal that is to be removed. Let the group velocity window be defined by the group



velocities  $U_0$  and  $U_1$ , and let the corresponding frequencies associated with these velocities be  $f_0$  and  $f_1$ , respectively. Following Saatçilar and Canitez (1988), we approximate the group velocity dispersion function by requiring that the group slowness be a linear function of frequency. Since the relation of wavenumber  $k(f)$  to group slowness  $U^{-1}(f)$  is given by the definition  $k(f) = k_0 + 2\pi \int_{f_0}^f U^{-1}(x) dx$ , the initial  $\kappa_m(f)$  estimate is defined once we specify a  $k_0$ . We choose the value  $k_0 = 2\pi \left[ \frac{f_0 + f_1}{2} \right] \left[ \frac{U_0^{-1} + U_1^{-1}}{2} \right]$  to guarantee that the desired signal at the effective center of the group velocity window is shifted to zero lag on the first application of equation (2).

In applying this technique, the input trace is windowed within the specified group velocity window by using a window with a width twice the longest period in order to focus the processing on the desired signal, and three iterations are performed. The number of Fast Fourier Transforms required are  $2(1 + N_I)$ , where  $N_I$  is the number of iterations.

This processing technique is adaptive since the surface wave signal itself improves the dispersion function. The technique is robust since an initial poor guess of the dispersion curve may yield nothing of consequence near zero lag when the signal is reduced to zero distance, in which case the phase match filtered signal is almost non-existent, and the result of the signal subtraction is essentially the same as the initial signal.

## DATA PROCESSING

### Oklahoma

As part of a sensor evaluation test, four data sets were collected at a field test site at Oklahoma. Both dynamite and vertical vibrator sources were used with receiver group arrays spaced 15.2 m apart between 152.4 and 441.9 m from the source. Each group array consisted of six geophones. The vibrator acted at the surface while the dynamite was buried at a depth of 15.2 m. The four vertical component data sets acquired are as follow:

**DynGrp** - dynamite source with a 30.5 m geophone group array

**DynNoGrp** - dynamite source with a 1 m geophone group array

**VibGrp** - vibrator source with a 30.5 m geophone group array

**VibNoGrp** - vibrator source with a 1 m geophone group array

The receiver group arrays were not designed to maximally reduce the surface waves ; at most they reduce the surface-wave signal by 6-10 db over the usable signal range (5-85 Hz).

Figure 1 presents the input time histories, showing 1000 ms of data sampled at 4 ms intervals. Within each panel, the trace on the left is at a distance of 152.4 m and the one at the right is at a distance of 441.9 m. An automatic gain correction with a 500 ms window has been applied to each plotted trace. In this figure, a set of reflections is seen at a two way traveltime of about 500 ms. This is from the well known Woodford shale formation at about 610 m. In addition well developed surface

waves are observed. The data sets are arranged such that the ratio of reflection signal to surface wave noise is greatest on the far left panel and decreases to the right. This is well understood theoretically in that buried sources excite the surface wave less than surface sources, and receiver group arrays of reasonable lateral dimensions also reduce the low phase velocity arrivals. We note that the 500 ms reflection is not apparent in the VibNoGrp, Figure 1d, data set at all.

One technique for reducing the surface wave in a record uses the fact that the surface wave usually has a lower frequency content than the reflections. In this area the peak surface-wave amplitude is at 18 Hz. Application of a high pass filter to the record section will attenuate the surface wave. Figure 2 shows the result of applying a 2 pole, zero-phase high-pass Butterworth filter with a low-cut corner frequency at 32 Hz to the field data. It is obvious that the low frequency surface wave is virtually eliminated in the case of the data set with the best S/N ratio, DynGrp, Figure 2a. However, low velocity surface-wave and shear-wave arrivals can be seen in the other time histories. The corner frequency of the filter could be increased to further reduce the surface-wave arrivals, but this would in turn reduce the bandwidth of the reflections.

To test the effectiveness of the phase matched rejection filter technique, we processed each trace through three different filters, with control parameters given in Table 1. For each filter so defined, three iterations were used to adaptively refine the filter, phase delays were smoothed using a 5 point least square B-spline. An AGC was applied to the data prior to phase match filtering each trace to amplify the signal at the end of the trace. The AGC gain as a function of time was saved so that, after the phase match filtering, the effects of the AGC could be removed to preserve the true amplitudes of the underlying reflections.

Figures 3 and 4 show the initial data sets and the output of each phase of processing for the best, DynGrp, and worst, VibNoGrp, data sets in terms of S/N, respectively. The parameters of the first pass were determined following the application of standard techniques for determining group velocities from single traces (Dziewonski et al, 1969) The first pass clearly removes the fundamental mode surface wave. For the DynGrp data set, further processing does not change the character of the record section in Figure 3.

The processing parameters used in the second pass were an attempt to remove the direct shear-wave arrivals observed between the first P break and the 500 ms reflection that is prominent in the DynNoGrp, VibGrp and VibNoGrp data sets. This has a higher frequency content than the fundamental mode surface wave and travels at a higher phase velocity. The result of this pass is quite significant in the case of VibNoGrp for which the 500 ms reflection now emerges. The last pass is an attempt to remove the very low group velocity arrivals that may be generated by the air wave.

Figure 5 compares the results of applying the three pass phase matched filtering operation to the original data sets. Comparing this figure to initial data sets shown in Figure 1, it is obvious that there has been a significant improvement in the reflection signal to surface-wave noise ratio.

To see how these results compare to that of simple high-pass filtering, Figure 6 shows the result of high-pass filtering the phase matched processing output using the

same filter used in Figure 2. Comparing this to Figure 2 shows the value of reducing the shear wave arrivals through phase match filtering. In addition the faster surface wave seen in the DynNoGrp, VibGrp and VibNoGrp data sets, Figures 2b, 2c, and 2d, respectively, has been eliminated.

This data set demonstrates how phase matched filtering can be applied to high resolution data collection strategies using either small or zero length group arrays. A more positive view is that good results may be obtained using fewer instruments in the group arrays as long as there is numerically resolvable signal beneath the surface wave.

### West Texas

The second data set comes from a high density mini-refraction profile in west Texas which was notable for its lack of reflections, but which was useful for other studies because of the sharp P-wave first breaks. The displays of the data set and phase matched outputs are AGC'd with a 500 ms window. Figure 7a presents the original data set. Traces are at 15.2 m intervals from 15.2 to 731.5 m. Each trace consists of 1000 samples at a 2 ms sampling interval. The initial P waves and their reverberations near the surface are apparent, as is a high frequency air wave arrival, e.g., at 2.00 s at a distance of 701.0 m. In addition there are a number of overlapping dispersed low frequency arrivals.

The phase matched filter was run as for the Oklahoma data set except the dispersion parameters of Table 2 were used. The parameters for the first pass were chosen on the basis of a  $p-f$  stack and group velocity analysis. The next passes were designed to remove the surface wave following the air wave and the direct shear wave. The final pass was an attempt to remove the dispersed reverberation following the direct P arrival. The reduction in surface-wave signal is evidenced by the relative enhancement of the air wave arrival in the AGC display. The interesting aspect of this data set was the dispersed surface wave following the air wave. These arrivals were set up by a moving surface source, the air wave propagating across the array at 300 m/s (Press and Ewing, 1951; Mooney and Kaasa, 1962; René et al, 1986). The third pass chose a group velocity window from the air wave to a point later in the trace. The final result, Figure 7b demonstrates a significant reduction in the surface wave, whether set up directly by the source or indirectly by the propagation air wave disturbance.

### Permafrost

Data sets in the arctic regions are notorious for poor signal to noise, and often are excellent candidates for phase match filters. Barton et al (1986), McConnell et al (1986), and Beresford-Smith and Rango (1988) discuss the problems with data acquisition on floating ice sheets. Our data set, Figure 8a, was acquired on land, and is not overwhelmed by the dispersive flexural waves. The traces range in distance from 1542 m on the left to 100 m on the right. There are some very strong undispersed arrivals with group velocities of 1400 m/s and 300 m/s. The large amplitude of these arrivals is indicated by the apparent muting introduced immediately prior because of the AGC process. These signals are also very narrow band with center frequency near 15 Hz. The result of processing this data set with the parameters of Table 3 is shown in Figure 8b. The air wave is still present as a very high frequency arrival, but the

1400 m/s arrival is virtually eliminated. The reduction of peak amplitude is indicated by the lack of a muting by the AGC.

This data set demonstrates the inherent control of our technique, in that it can be applied to a very narrow group velocity window and that if no dispersion is present, it defaults to bandlimited mute.

## CONCLUSIONS

A technique well known in earthquake seismology has been applied to an exploration problem with the underlying idea that the earthquake noise is the exploration signal and that the earthquake signal is the exploration noise. The adaptive phase matched filter technique differs from  $k-f$  filter techniques in that each trace is independently analyzed. This means that our method will work for data sets which would be severely aliased in  $k-f$  analysis. To some extent it is similar to time variant spectral whitening technique described by Yilmaz (1987) in that undesired signal is removed from a single trace in a time variant manner. However, our technique essentially subtracts a coherent noise from the trace, leaving the underlying signal undistorted in frequency and time, thus preserving true amplitude.

A similar technique has been applied to the problem of seismic data acquisition on ice to remove the dispersive flexural wave (Barton et al, 1986; McConnell et al, 1986; Beresford-Smith and Rango, 1988). These approaches used a phase matched filter and used an  $f-k$  analysis to define the dispersion operator, though Barton et al (1986) recognized the problems with lateral changes in dispersion. They then applied a phase matched rejection filter to the data sets. The adaptive phase matched filter technique presented here does not require such a well defined dispersion operator. Only a reasonable estimate is required. We used simple group velocity windows, which are easily chosen by an analyst. This simple approach works since the dispersed seismic signal itself defines its own rejection filter.

The processing shown was done on a number of different UNIX (TM AT&T Technologies) machines. Using the present unoptimized code, we found that 38% of the execution time was spent doing Fast Fourier Transforms, implemented in FORTRAN. This indicates that the code can be run faster using array hardware. In addition, this also indicates that the technique may be faster than transformation to the  $k-f$  domain for excising the surface wave and inverse transformation to the  $x-t$  domain.

Since Saatçilar and Canitez (1988) have shows that phase match filtering to remove ground roll significantly improves stacked sections, our focus was on making the technique easier to use and understand. Our implementation of adaptive phase matched filter technique is very robust since only simple control parameters are required and since it is well behaved, even for data with no noticeable dispersion. With future 24-bit field data acquisition, the subtractive nature of the coherent noise removal may significantly improve marginally collected data, without distorting the underlying exploration signal.

**ACKNOWLEDGEMENTS**

The development of the phase match filter program was sponsored in part by the Defense Advanced Research Projects Agency under Contract F19628-87-K-0049.

**REFERENCES**

- Al-Husseini, M. I., Glover, J. B., and Barley, B. J., 1981, Dispersion patterns of the ground roll in eastern Saudi Arabia: *Geophysics*, **46**, 121-137.
- Barton, C., Beresford-Smith, G., and Rango, R., 1986, Flexural waves on Arctic data: application of new techniques for S/N enhancement: 56th Ann. Internat. Mtg., Soc. Explor. Geophys., Expanded Abstracts, 458-461.
- Beresford-Smith, G., and Mason, I. M., 1980, A parametric approach to the compression of seismic signals by frequency transformation: *Geophys. Prosp.*, **28**, 551-571.
- Beresford-Smith, G., and Rango, R. N., 1988, Dispersive noise removal in t-x: Application to Arctic data: *Geophysics*, **53**, 346-358.
- Dobrin, M. B., 1951, Dispersion in seismic surface waves: *Geophysics*, **16**, 63-80.
- Dziewonski, A., Bloch, S., and Landisman, M., 1969. A technique for analysis of transient seismic signals: *Bull., Seis. Soc. Am.*, **59**, 427-444.
- Goforth, T., and Herrin, E., 1979, Phase-matched filters: application to the study of Love waves: *Bull., Seis. Soc. Am.*, **69**, 27-44.
- Herrin, E., and Goforth, T., 1977, Phase-matched filters: application to the study of Rayleigh waves: *Bull., Seis. Soc. Am.*, **67**, 1259-1275.
- Herrmann, R. B., 1973, Some aspects of band-pass filtering of surface waves, *Bull., Seis. Soc. Am.*, **63**, 703-711.
- McConnell, J. R., Potts, M. J., Schleicher, K. L., and Wason, C. B., 1986, Dispersive Noise Attenuation: 56th Ann. Internat. Mtg., Soc. Explor. Geophys., Expanded Abstracts, 455-458.
- McMechan, G. A., and Yedlin, M. J., 1981, Analysis of dispersive waves by wave field transformation: *Geophysics*, **46**, 869-874.
- Mooney, H. M., and Kaasa, R. A., 1962, Air waves in engineering seismology: *Geophys. Prosp.*, **10**, 84-92.
- Press, F., and Ewing, M., 1951, Ground roll coupling to atmospheric compressional waves: *Geophysics*, **16**, 416-430.

René, R. M., Fitter, J. L., Forsyth, P. M., Kim, K. Y., Murray, D. J., Walters, J. K., and Westerman, J. D., 1986, Multicomponent seismic studies using complex trace analysis: *Geophysics*, **51**, 1235-1251.

Saatçılar, R., and Canitez, N., 1988, A method of ground-roll elimination: *Geophysics*, **53**, 894-902.

Yilmaz, O., 1987, *Seismic Data Processing*, Society of Exploration Geophysicists, Tulsa.

**Table 1. Matched filter control parameters**

PASS	$f_0$ (Hz)	$U_0$ (m/sec)	$f_1$ (Hz)	$U_1$ (m/sec)
1	6	914	20	305
2	8	1219	40	610
3	8	610	40	305

**Table 2. Matched filter control parameters**

PASS	$f_0$ (Hz)	$U_0$ (m/sec)	$f_1$ (Hz)	$U_1$ (m/sec)
1	2	366	30	183
2	5	914	30	305
3	5	366	20	61
4	10	2743	40	914

**Table 3. Matched filter control parameters**

PASS	$f_0$ (Hz)	$U_0$ (m/sec)	$f_1$ (Hz)	$U_1$ (m/sec)
1	7	320	40	290
2	7	1829	40	1219

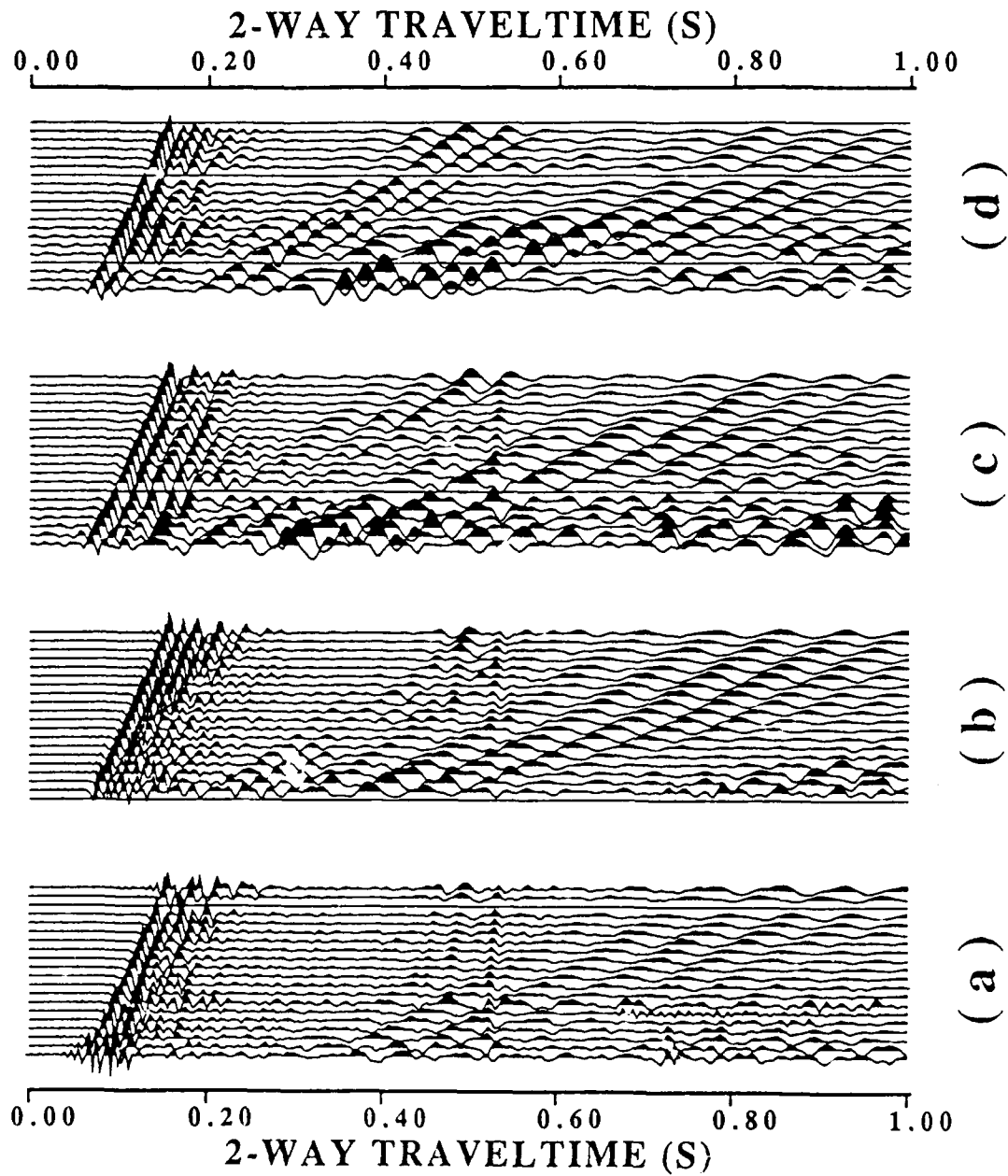


Fig. 1. Input data sets from the Oklahoma test site. a) dynamite source, group array DynGrp; b) dynamite source 1 m group array DynNoGrp; c) vibrator source, group array VibGrp; d) vibrator source, 1 m group array VibNoGrp. All traces are AGC'd with a 500 ms window.



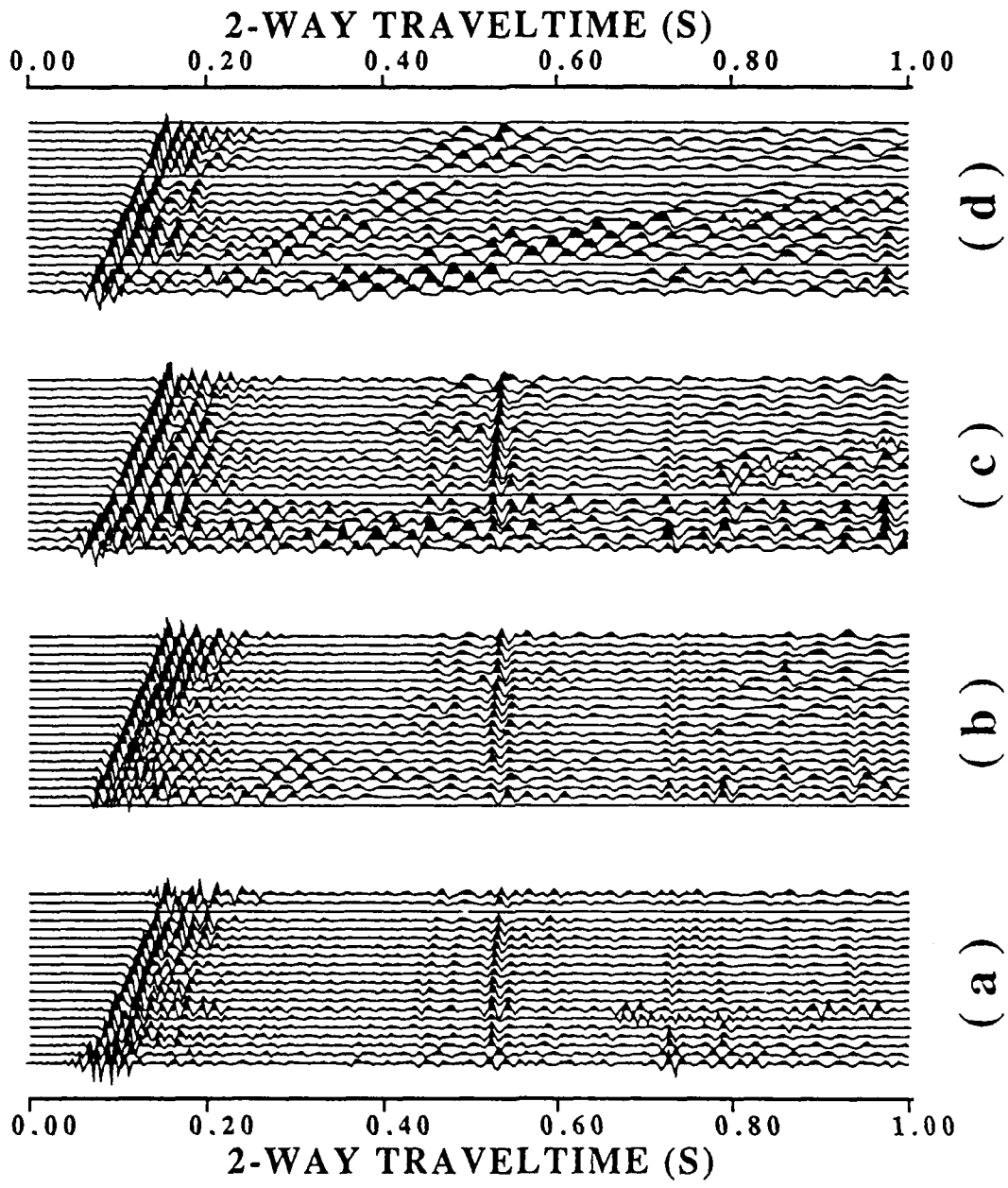


Fig. 2. Data from Oklahoma test site high pass filtered with a corner at 32 Hz. a) DynGrp, b) DynNoGrp, c) VibGrp, and d) VibNoGrp data sets. All traces are AGC'd with a 500 ms window.

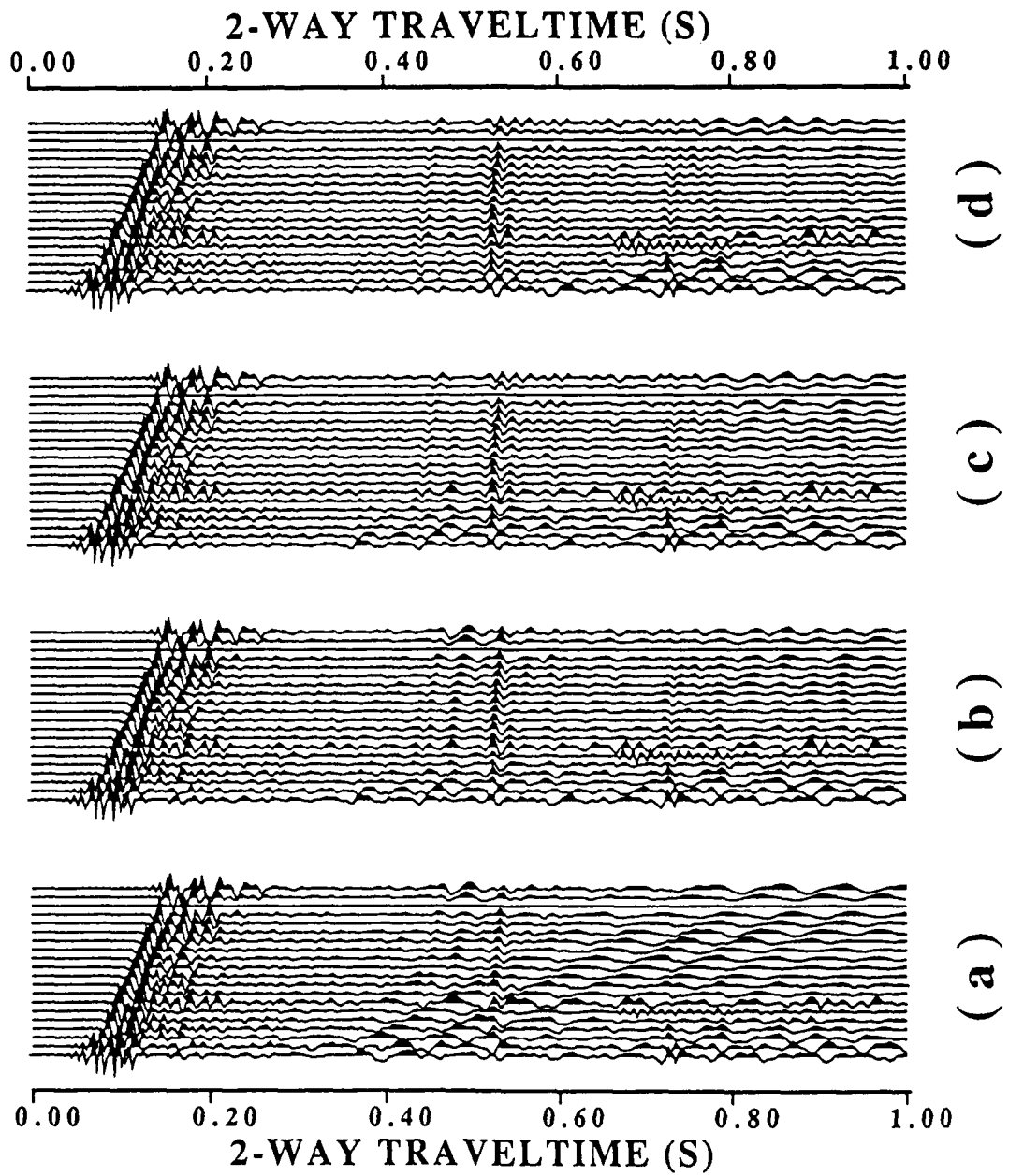


Fig. 3. Phase matched filter processing results for data set DynGrp. a) Original data set, b) output of pass 1, c) output of pass 2, d) output of pass 3. All traces are AGC'd with a 500 ms window.

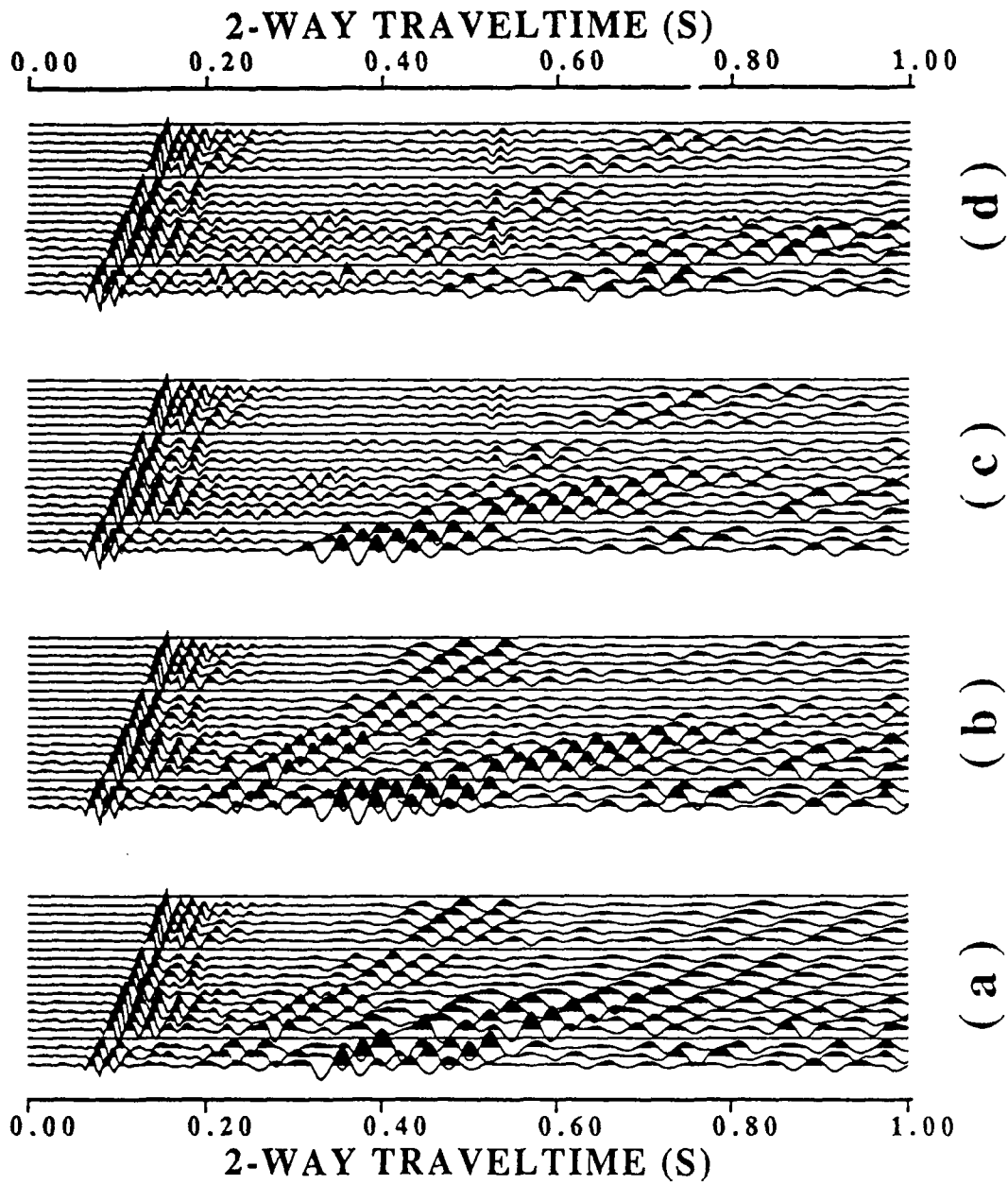


Fig. 4. Phase matched filter processing results for data set **VibNoGrp**. a) Original data set, b) output of pass 1, c) output of pass 2, d) output of pass 3. All traces are AGC'd with a 500 ms window.

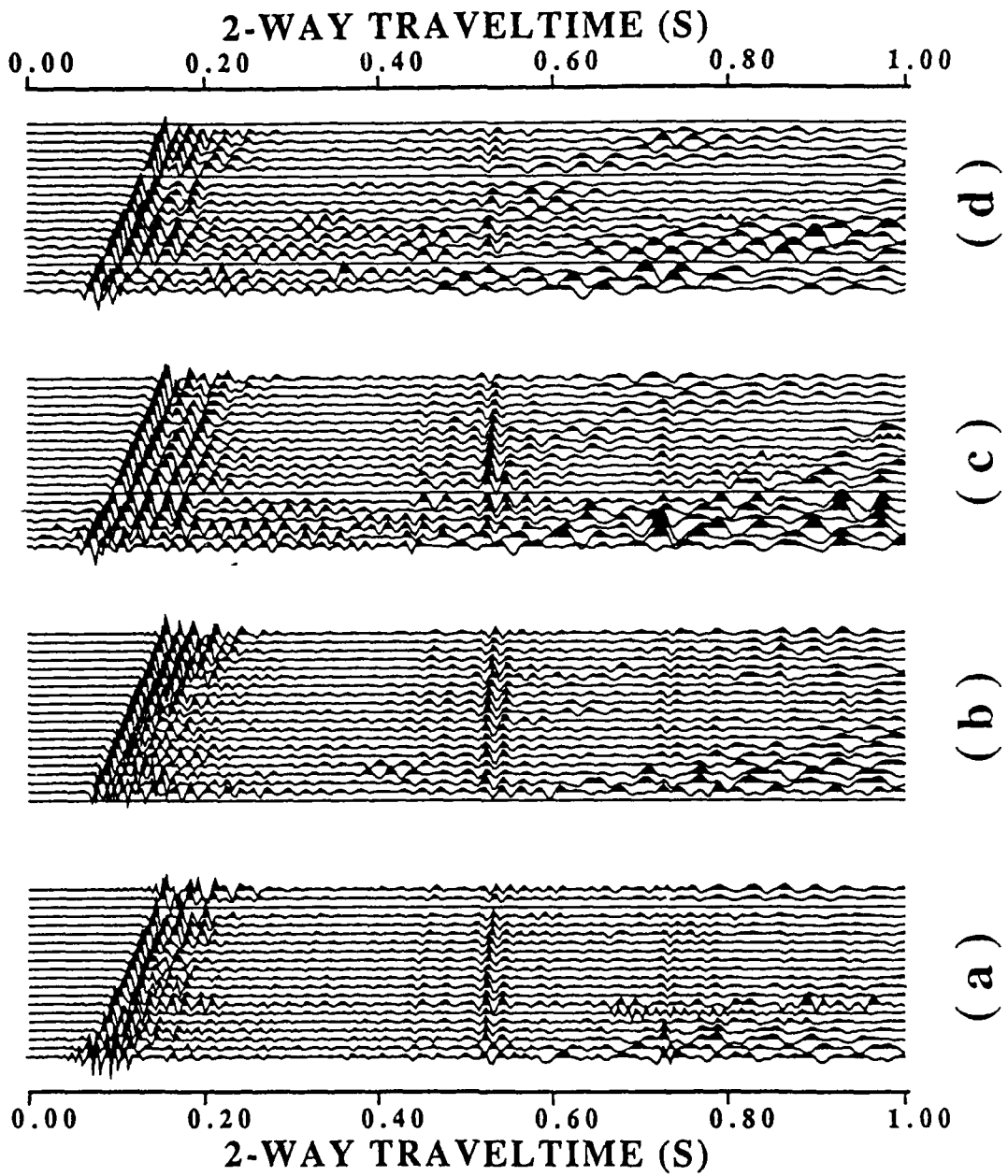


Fig. 5. Final phase matched filter record sections for the Oklahoma test site. a) DynGrp, b) DynNoGrp, c) VibGrp, and d) VibNoGrp data sets. All traces are AGC'd with a 500 ms window.

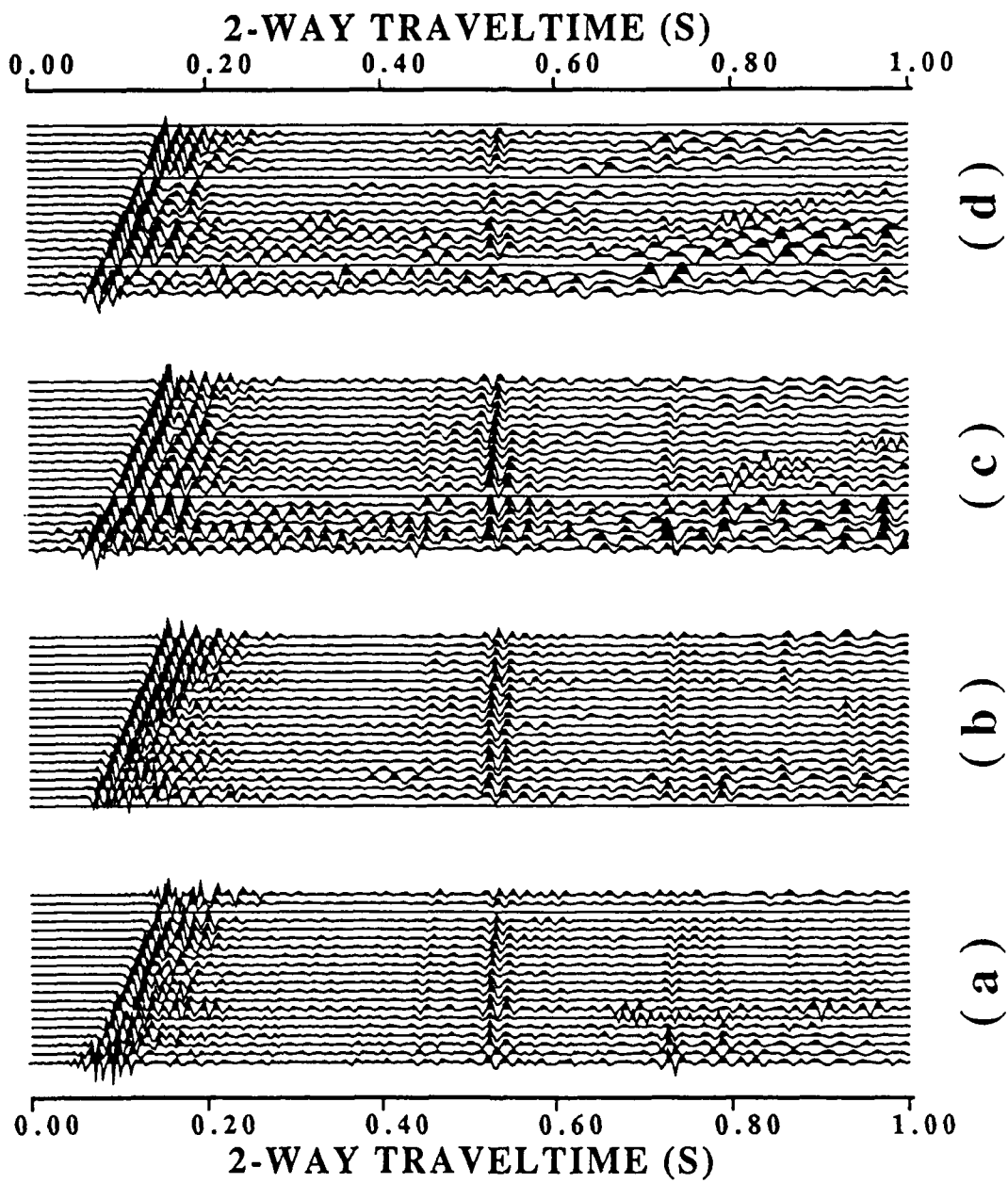


Fig. 6. Results of passing a high pass filter with a corner at 32 Hz to the phase matched filter output of Figure 5. a) DynGrp, b) DynNoGrp, c) VibGrp, and d) VibNoGrp data sets. All traces are AGC'd with a 500 ms window.

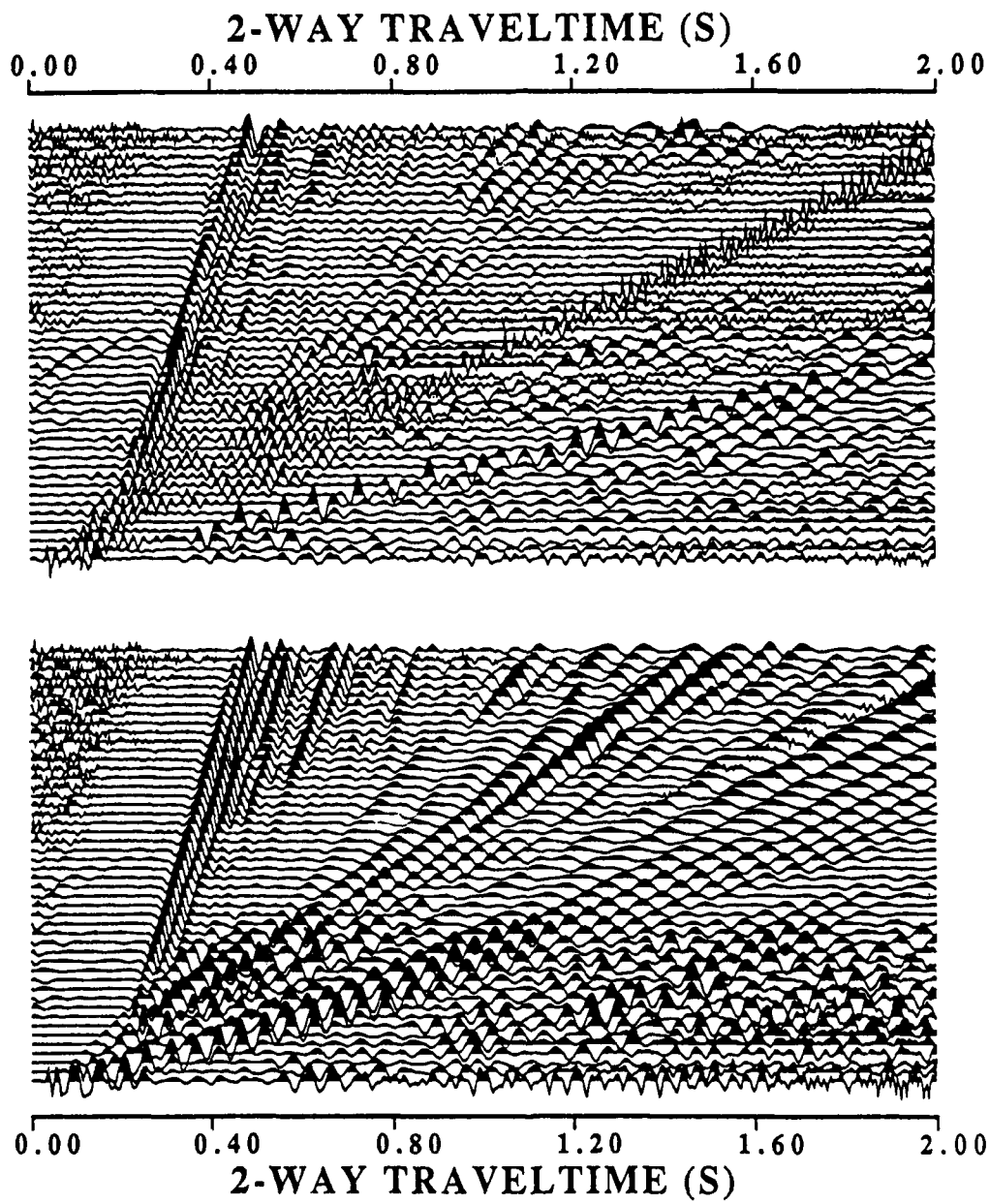


Fig. 7. a) Initial west Texas record section. b) result of a 4 passes of phase match filters. All traces are AGC'd with a 500 ms window.

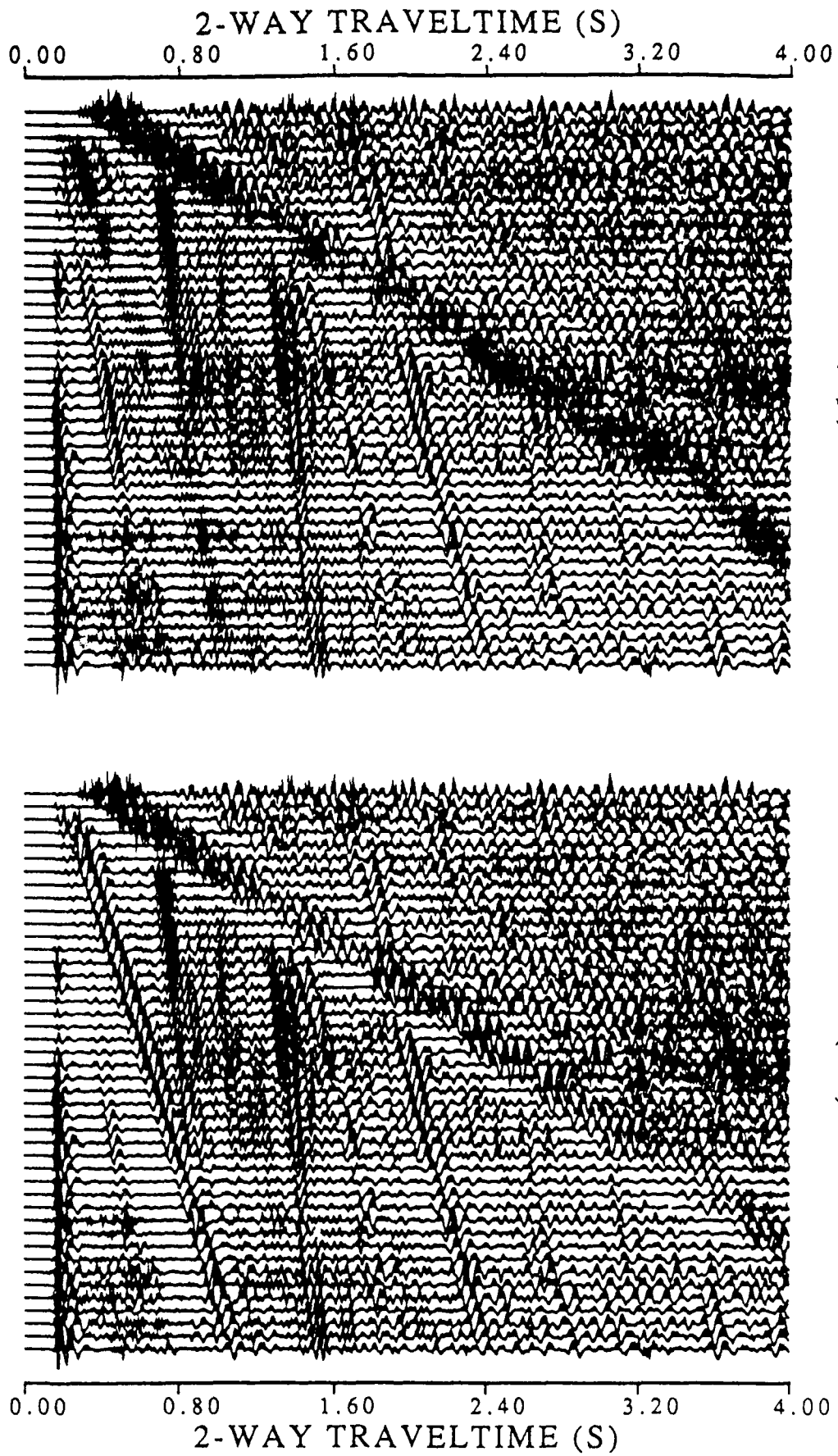


Fig. 8. a) Initial permafrost record section. b) result of 2 passes of phase match filters. All traces are AGC'd with a 500 ms window.

**On Scaling of Intra-Continental Earthquakes**

by

**M. L. Jost and R. B. Herrmann**

November 28, 1989

Revised December xx, 1989

Department of Earth and Atmospheric Sciences

Saint Louis University

3507 Laclede

St. Louis, MO 63103



## ABSTRACT

Source parameters of 59 large intra-continental earthquakes as given in recent literature are used to derive seismic scaling relations using constrained least-squares for the purpose of comparison with previously proposed scaling relations for eastern North America. The world-wide data of intra-continental earthquakes are consistent with a power 3.0 spectral scaling (constant stress drop) as previously suggested by Somerville et al. (1987) from a much smaller data set. On the other hand, the data do not preclude a power 3.3 spectral scaling. Consequently, this interpretation permits stress drop to increase with seismic moment, but with a smaller slope and at a lower level than suggested by the revised mid-plate scaling relation of Nuttli et al. (1989). Both interpretations of the data predict very similar corner periods. Using the proposed scaling relations, magnitudes determined from random process theory and finite source modeling compare reasonably well with observations in eastern North America. In addition, the estimated source parameters of selected large historical earthquakes are only slightly different from those previously suggested.

## INTRODUCTION

Eastern North America has experienced significant historical earthquakes such as that of 1663 in the St. Lawrence Valley, that of 1755 near Cape Ann, Mass., those of 1811-1812 near New Madrid, Mo., and that of 1886 near Charleston, S.C. (Coffman and von Hake, 1973). No major damaging earthquake, however, has occurred there since the installation of regional networks. Large intra-continental earthquakes, which are several hundred *kilometers* distant from any plate boundary (Scholz *et al.*, 1986), occur infrequently, but have a high potential for destruction. In order to estimate ground motions due to such large events, seismic scaling relations must be employed. These relations enable an estimate of magnitude or seismic moment from observed fault dimensions (geologic observations and microseismicity studies, e.g., Wyss, 1979) and a determination of peak ground motion parameters (e.g., Boore, 1983; Atkinson, 1984; Joyner, 1984; Boore and Atkinson, 1987; EPRI, 1988; Herrmann and Jost, 1988; Heaton and Hartzell, 1989). The basic

assumption of seismic scaling laws is that the physics of material failure is independent of the size of an event, i.e., lacking a scale length (Mandelbrot, 1983). This seems to be valid, however, only for certain subsets of earthquakes, i.e., shallow plate margin, mid-plate, or deep earthquakes.

For mid-plate earthquakes, several seismic scaling relations have been proposed that were based on data from eastern North America (Nuttli, 1983; Hasegawa, 1983; Nuttli *et al.*, 1989). However, it is currently a matter of debate whether or not scaling for mid-plate earthquakes differ from that for plate margin earthquakes (Haar *et al.*, 1986; Somerville *et al.*, 1987; Nuttli *et al.*, 1989). Due to the lack of large instrumentally recorded events, a decision on this issue for North America is hard to reach, thus making it difficult to evaluate seismic hazard (Boore and Atkinson, 1987; Somerville *et al.*, 1987; Coppersmith and Youngs, 1989).

In general, four essential differences are noted between large earthquakes in eastern North America and those of western North America (e.g., San Francisco, 1906). First, the felt areas in eastern North America are fundamentally larger than those in the west. Heinrich (1941) pointed out that the Charleston, Missouri earthquake of 1895 caused only moderate damage in the epicentral region, but was felt as far away as the Atlantic coast, the Gulf coast, New Mexico, and Canada. Gutenberg and Richter (1949) attributed the wider area of perceptibility for given magnitude to greater focal depth. This conclusion was contradicted by recent data that show the maximum focal depth for earthquakes in the central United States is about 25 km (Nuttli and Herrmann, 1987). Nuttli (1973b) proposed another explanation: he inferred that the coefficient of anelastic attenuation for 1-Hz Lg-waves is about  $0.0006 \text{ km}^{-1}$  for eastern North America, as compared to  $0.005 \text{ km}^{-1}$  for coastal California. Further studies (e.g., Johns *et al.*, 1977; Bollinger, 1979; Singh and Herrmann, 1983) on the coefficient of anelastic attenuation, or apparent Q, in the central and eastern United States confirmed Nuttli's results which completely explain the differences in areas of perceptibility. By using this attenuation relation, Nuttli (1973b) was able to present a reliable method of Lg-wave magnitude determination (Baker, 1967).

Second, none of the historical earthquakes in eastern North America has produced

observable surface rupture (Nuttli and Herrmann, 1987). Large events like those near Charleston in 1886 or near New Madrid in 1811 - 1812 produced numerous sand-blows, and the latter even rapids in the Mississippi river due to subsidence (Street and Nuttli, 1984); however, surface traces of faulting comparable to those observed in the western United States have not been found.

Third, assuming that magnitude estimates of historical events are not grossly in error, earthquakes in eastern North America seem to have significantly smaller fault dimensions than in western North America for a given magnitude. For example, standard scaling relations require fault lengths between 300 to 1000 km for earthquakes with  $M_S = 8.0$  to 8.8 (e.g., Kanamori and Anderson, 1975; Nuttli, 1985).

Finally, recurrence rates are low in eastern North America compared to the west (Bakun *et al.*, 1986; Johnston and Nava, 1984, 1985). In general, repeat times are related to tectonic loading and the strength of preexisting zones of weakness (Talwani, 1989). Since the historical record is significantly smaller than one complete recurrence cycle of large earthquakes, future large events may occur at somewhat unexpected locations, e.g., Meers fault, Oklahoma (Hinze, 1988; Coppersmith and Youngs, 1989; Mitchell *et al.*, 1989).

The last two features of large earthquakes in eastern North America imply that long repeat times correspond to short fault rupture lengths. Kanamori and Allen (1986), extrapolating laboratory experiments, proposed that frictional strength on the fault plane increases as the contact-time increases, which explains the observed higher stress drops for intraplate events (Kanamori and Anderson, 1975). Put differently, events with long repeat times seem to have a larger number of asperities than events with short repeat times (Kanamori and Allen, 1986). The same conclusion was reached by Scholz *et al.* (1986) who inferred that large intraplate earthquakes have about 6 times larger slip than interplate events of the same size, indicating a 6 times larger stress drop. Previously, Madariaga (1979) indicated that larger stress drops for a given seismic moment indicate a rougher fault in agreement with the above arguments.

Nuttli (1983) concluded that mid-plate earthquakes in eastern North America are

characterized by source spectra for which the corner period,  $T_{02}$ , is proportional to the one-fourth power of the seismic moment,  $M_0$ , for earthquakes with seismic moments between  $10^{20}$  and  $10^{28}$  *dyne-cm* (see also Street and Turcotte, 1977; Iio, 1986). This scaling requires an increasing stress drop for increasing seismic moment. Haar *et al.* (1986) questioned Nuttli's (1983) conclusion. They inferred that the corner period is proportional to the one-third power of the seismic moment for both western and eastern North American earthquakes of seismic moments between  $10^{17}$  and  $10^{26}$  *dyne-cm*. This scaling renders the stress drop constant, independent of seismic moment (Kanamori and Anderson, 1975). Constant stress drop scaling is a result of assuming a similarity condition between large and small events (Aki, 1967), i.e., fault area proportional to (fault length)<sup>2</sup>,  $\bar{u}$  proportional to fault length (constant strain drop; Kanamori and Anderson, 1975; Scholz, 1982), and rupture velocity independent of seismic moment.

Somerville *et al.* (1987) related source duration to seismic moment for earthquakes in eastern and western North America and for earthquakes in continental interiors. They inferred a logarithmic slope of three for all three classes of earthquakes. In addition, they found that the spectral scaling relations of Nuttli (1983) predicted source durations substantially larger than they obtained from waveforms of short-period P waves. Part of this incompatibility may be related to differences of duration of P-waves versus S-waves or higher mode surface waves (Hanks and Wyss, 1972; Savage, 1972; Cohn *et al.*, 1982; Hasegawa, 1983; Nuttli, 1983; Silver, 1983). Scholz *et al.* (1986) compared large interplate and intraplate earthquakes and concluded that though stress drops are different, both populations follow the same scaling relation. In addition, recent data suggest that relating a corner frequency of 1.0 Hz to a seismic moment of  $10^{22}$  *dyne-cm* is inappropriate (e.g., Shin and Herrmann, 1987; Chun *et al.*, 1989).

The primary purpose of this study is to develop scaling relations for medium to large intra-continental earthquakes based on a world-wide data set and to compare these relations to the proposed scaling laws for eastern North America (c.f., forthcoming EPRI study on maximum earthquakes, Coppersmith and Youngs, 1989). In the following, we first analyze the revised mid-plate scaling law (Nuttli *et al.*, 1989). Second, recent literature is searched for source parameters of large intra-continental earthquakes world-wide.

These source parameters are used to derive seismic scaling relations which are constrained to be consistent with fundamental seismic laws. Finally, these relations are compared to the revised mid-plate scaling relation (Nuttli *et al.*, 1989), the scaling relation for eastern Canada (Hasegawa, 1983), and the scaling law of Somerville *et al.* (1987). Applying the intra-continental scaling relations for eastern North America, estimates of source parameters of selected large historical events are discussed.

### REVISED MID-PLATE SCALING RELATION

In the following, we give an analysis of the recently revised mid-plate scaling relation (Nuttli *et al.*, 1989). The reduced far-field displacement spectra were constructed by trial and error to fit the relation between corner frequency and seismic moment, observational data of body-wave magnitude versus surface-wave magnitude, and of body-wave magnitude and surface-wave magnitude versus seismic moment. In addition, the scaling relations were constrained to give reasonable values of the fault length and width, of average fault displacement, and of static stress drop versus seismic moment. In general, the determination of source spectra trades off with frequency dependent anelastic attenuation, site amplifications, instrument influence (band-limitation), and radiation pattern effects (Chun *et al.*, 1989).

Figure 1 displays the revised, reduced far-field displacement spectra by Nuttli *et al.* (1989) which show the following characteristics: At long periods, each spectrum parallels the period axis (slope = 0); the level is proportional to the seismic moment (Keilis-Borok, 1959). At intermediate periods, spectra of small earthquakes have one corner period  $T_{02}$ , where the slope of the spectrum changes from 0 to 2 (assuming the  $\omega^2$  model, Aki, 1967). This corner period is proportional to the linear dimension of the fault (Savage, 1972). Larger earthquakes can have two corner periods  $T_{12}$  and  $T_{01}$ , the shorter proportional to the width, the longer to the length of the fault plane, respectively. The slope of the spectrum between the two corner periods is unity, indicating a non-uniform stress release on the fault plane or a partial stress drop (Brune 1970, 1971; Savage, 1972; Brune *et al.*, 1986). The short-period trend of the spectra follows an  $\omega$ -power law (Aki, 1967; Brune, 1970, 1971). Data from eastern North America seem to follow the  $\omega$ -square model (Aki,

1967; Chun *et al.*, 1989), and not the  $\omega$ -cube model (Aki, 1967; Savage, 1972).

The core of a scaling relation is a function describing the increase of corner period (for larger earthquakes a corner period  $T_{02}$  can be simply constructed) with seismic moment (similarity condition). By accepting this relation, which is determined from small to medium size events in eastern North America, for all earthquakes, it is possible to predict reduced far-field displacement spectra for earthquakes of any given size. The revised mid-plate scaling law is described by the following relations between corner period and seismic moment (Figure 2). For  $\log M_0 \leq 23$  :

$$\log T_{02} = -5.872 + 0.251 \log M_0 \quad , \quad (1a)$$

or for the corner frequency  $f_c = 1/T_{02}$

$$f_c = 7.45 \times 10^5 M_0^{-1/4} \quad , \quad (1b)$$

where corner periods are in *sec*, corner frequencies in *Hz*, and seismic moments in *dyn-cm*. Note that  $T_{01} = T_{02} = T_{12}$  for  $\log M_0 \leq 23$  rendering the aspect ratio (fault width/fault length) constant for small events. For larger seismic moments, the revised mid-plate scaling relation causes the aspect ratio to differ from unity (Kanamori and Anderson, 1975; Heaton and Hartzell, 1988). For  $23 \leq \log M_0 \leq 24$  :

$$\log T_{01} = -7.214 + 0.309 \log M_0 \quad (2)$$

$$\log T_{02} = -6.373 + 0.273 \log M_0 \quad , \quad (3a)$$

or for the corner frequency  $f_c$

$$f_c = 2.36 \times 10^6 M_0^{-1/3.67} \quad (3b)$$

$$\log T_{12} = -5.455 + 0.233 \log M_0 \quad . \quad (4)$$

For  $\log M_0 \geq 24$  :

$$\log T_{01} = -8.033 + 0.343 \log M_0 \quad (5)$$

$$\log T_{02} = -6.589 + 0.282 \log M_0 \quad , \quad (6a)$$

or for the corner frequency  $f_c$

$$f_c = 3.88 \times 10^6 M_0^{-1/3.55} \quad (6b)$$

$$\log T_{12} = -5.155 + 0.220 \log M_0 \quad . \quad (7)$$

The relation between corner frequency and seismic moment can be compared to Nuttli's (1983) formula ( $20 \leq \log M_0 \leq 28$ ):

$$f_c = 3.55 \times 10^5 M_0^{-1/4} \quad , \quad (8)$$

and that for plate margin events assuming a constant stress drop of 100 *bar* (Boore and Atkinson, 1987)

$$f_c = 7.96 \times 10^7 M_0^{-1/3} \quad (9)$$

Furthermore, it can be compared to the relation by Atkinson (1984, equation (11)) which is based on large eastern Canadian events ( $23.9 \leq \log M_0 \leq 25.8$ ):

$$f_c = 2.00 \times 10^6 M_0^{-1/3.57} \quad (10)$$

Note the close agreement with the revised mid-plate scaling law (6b).

The revised mid-plate scaling relation can also be described by (Figure 1):

$$\log M_0 = 1.0 m_b + 17.5 \quad \text{for } m_b \leq 4.2 \quad (11)$$

$$\log M_0 = 2.0 m_b + 13.1 \quad \text{for } m_b \geq 4.2 \quad (12)$$

$$\log M_0 = 1.0 M_S + 18.85 \quad \text{for } M_S \leq 8.15 \quad (13)$$

$$\log M_0 = 4.0 \log T_{02} + 23.4 \quad \text{for } T_{02} \leq 1 \text{ s} \quad (14)$$

$$\log M_0 = 3.55 \log T_{02} + 23.4 \quad \text{for } T_{02} \geq 1 \text{ s} \quad (15)$$

Table 1 gives values of body-wave magnitude, surface-wave magnitude, moment magnitude, and the corner periods  $T_{01}$ ,  $T_{12}$  and  $T_{02}$  for seismic moments between  $10^{20}$  and  $10^{28}$  *dyne-cm*. It also contains estimated values of the fault rupture length (measured along strike) and width (measured along dip), the static stress drop, and the average fault displacement that are calculated from equations given in Brune (1970, 1971), Savage (1972), and Geller (1976):

$$L = 3.57 \beta T_{01}/2\pi \quad (16)$$

$$W = 2.30 v_R T_{12}/\pi \quad (17)$$

$$\Delta\sigma = 7 M_0/16 (LW/\pi)^{3/2} \quad (18)$$

$$M_0 = \mu L W \bar{u} \quad (19)$$

In the following, fault length and width,  $L$  and  $W$ , are in *cm*; the corner periods in seconds; the shear-wave velocity,  $\beta$ , and the rupture velocity,  $v_R$ , in *cm/s*; the stress drop  $\Delta\sigma$  in *bar*; the average displacement,  $\bar{u}$ , in *cm*; and the shear modulus,  $\mu$ , in *dyne/cm<sup>2</sup>*. The rupture velocity is assumed to be constant and equal to  $0.9 \times \beta$ . The value of  $\mu$  is assumed to be  $3.3 \times 10^{11}$  *dynes/cm<sup>2</sup>*. Bonilla *et al.* (1984) estimated that  $\mu$  can vary between  $1.7 \times 10^{11}$  *dyne/cm<sup>2</sup>* and  $3.4 \times 10^{11}$  *dyne/cm<sup>2</sup>*.

Following Kanamori (1978) and Hanks and Kanamori (1979), the moment magni-

tude  $M_W$  is given by

$$M_W = \frac{2}{3} \log M_0 - 10.73 \quad , \quad (20)$$

which was introduced to extrapolate the surface-wave magnitude scale beyond its saturation point at about  $M_S = 8.0$  (e.g., Figure 7 in Geller, 1976; Nuttli, 1985). On the other hand, Singh and Havskov (1980) pointed out that the equivalence between values of  $M_W$  and  $M_S$  for  $M_S < 8.0$  is valid only for interplate events. For intraplate earthquakes, Singh and Havskov (1980) proposed a correction term of 0.27 to the moment magnitude as given in (20) rendering

$$M_W = \frac{2}{3} \log M_0 - 10.46 \quad . \quad (21)$$

In Table 1, the definition (21) is used. However, the correspondence between  $M_S$  and  $M_W$  is poor for the revised mid-plate scaling relation (Table 1). This fit is not improved if (20) instead of (21) is used.

Table 2 shows similarity conditions (Kanamori and Anderson, 1975) and rise times (Geller, 1976) for the revised mid-plate scaling relation. For small events, the aspect ratio is one and decreases for larger events as the fault length increases with respect to fault width. The strain drop ( $\bar{u}/L$ ) increases with increasing moment indicating that large mid-plate events release more strain than small events. Finally, the dynamic similarity decreases slightly, implying somewhat different effective stress for small and large events.

Nuttli *et al.* (1989) pointed out that the revised scaling relation (Table 1) gives a slightly better fit to observational data of  $m_b$  versus  $M_S$ ,  $m_b$  versus  $M_0$ , and  $M_S$  versus  $M_0$  than the earlier spectral scaling model of Nuttli (1983). The improvement is significant for earthquakes of moment less than  $10^{22}$  dyne-cm. For larger earthquakes, the predicted curves given by Figure 1 and Table 1 are almost identical to the original (Nuttli, 1983) curves. The fit of the corner period ( $T_{02}$ ) data (e.g., Fletcher, 1982; Shin and Herrmann, 1987; Somerville *et al.*, 1987) to those predicted by the revised spectral scaling relation (Figure 3) seems to be superior to the fit of the relations by Nuttli (1983) and Somerville *et al.* (1987). Hasegawa's (1983) relation is essentially identical to that of Nuttli *et al.* (1989). Furthermore, stress drops can be compared to source duration (Figure 4). Again,



the revised mid-plate scaling relation seems to produce a superior fit to the data of Somerville *et al.* (1987) and of Shin and Herrmann (1987) after neglecting stress drops larger than 200 *bar*. However, the predicted stress drop values are somewhat larger than the values given in Street and Turcotte (1977, Figure 4) which may be due to differences in corner period estimates (e.g., Haar *et al.*, 1986; Anderson, 1986; Andrews, 1986). From (18), a small error in measuring corner periods from data will significantly alter the stress drop value (Kanamori and Anderson, 1975; Brune *et al.*, 1979; Atkinson, 1984). Note, that the presence of asperities on the fault plane can also alter the corner period (e.g., Figure 6.16 in Kostrov and Das, 1988).

Recently, Chun *et al.* (1989) investigated source spectra of Miramichi earthquakes with  $m_{Lg} = 2.6 - 5.4$ . They found strong support for an increase of stress drop with seismic moment (Nuttli, 1983) after correlating a seismic moment of  $5.6 \times 10^{23}$  *dyne-cm* to a corner frequency of 1 *Hz* following Shin and Herrmann (1987).

On the other hand, Hanks (1982) and Boore (1986b) pointed out that the observed increase of stress drop with seismic moment (breakdown in similarity) for earthquakes with magnitudes less than about 5 could be due to a process that limits high frequencies ( $f_{max}$ ), where it is irrelevant whether the process is due to instrument, source, or site. This band-limiting effect can lead to significant differences in scaling for large and small earthquakes (Boore, 1986b). If such an effect is present in eastern North America where there are no data for large events, the extrapolation of properties of small to large events can be in error. It is interesting to note that the revised mid-plate scaling relation (Nuttli *et al.*, 1989) indeed shows different scaling for small and large earthquakes (Figure 2).

#### SCALING RELATIONS FOR INTRA-CONTINENTAL EARTHQUAKES

To test the revised mid-plate scaling relation derived from earthquakes in eastern North America, a search of the recent literature for observed source properties of worldwide intra-continental earthquakes was performed. In this study, we restrict *intraplate earthquakes* as recently reviewed by Talwani (1989) to continental areas. However, *intra-continental* events are understood to be less restrictive than events in *stable continental interiors* as defined by Johnston (1989). In this way, we could include high quality data

for events in central Asia (Figure 5) which is considered an active plate interior by Johnston (1989, his Figure 1). On the other hand, none of the events chosen were located on the Himalayan Frontal Thrust, the plate boundary between India and Asia. For example, we omitted the events Bihar-Nepal in 1934 and Assam in 1950 (Chen and Molnar, 1977). We also omitted events in the Garm region (e.g., Markansu, 1974; Jackson *et al.*, 1979; Hamburger *et al.*, 1988). Table 3 gives the hypocenters and fault plane solutions of the events used and Table 4 the source parameters. In both tables, the source of the data is indicated. All events chosen were located in the crust.

In Table 4, fault lengths determined from observed fault scarps or fault lengths determined by waveform matching (e.g., Cipar, 1979) were preferred over values determined from aftershock studies. Darragh and Bolt (1987) pointed out that there can be a discrepancy between the extent of the aftershock zone and the surface scarp of faulting. Zhou *et al.* (1983b) concluded that there are earthquakes (e.g., 1967 Ganzi, 1975 Haicheng) where the aftershock zone significantly overestimates the fault length. Cipar (1979) and Shedlock *et al.* (1985) found the aftershock zone for the Haicheng earthquake significantly larger than the surface trace of faulting. Furthermore, aftershock zones vary with time (Upadhyay and Duda, 1980) and their location might not be well constrained. On the other hand, surface rupture might not be observable (e.g., events in eastern North America) or if observable (e.g., in Australia) might not extend over the whole length that actually ruptured below surface even for shallow events (Wyss, 1979; Bonilla *et al.*, 1984). Bonilla *et al.* (1984) argued that the surface rupture length can be taken as fault length for steeply dipping faults and aspect ratios smaller than 0.5.

Most of the average displacement values of Table 4 are from field observations. Average slips measured at the earth's surface show a large degree of variability especially for the very largest events (e.g., Deng *et al.*, 1986; Zhang *et al.*, 1987). This makes the determination of an average value of displacement along the surface fault trace difficult. In addition, it is then assumed that the observed displacements at the earth's surface are representative for the whole fault plane.

Rupture widths as given in Table 4 are determined from the distribution of aft-

ershocks or microseismicity studies indicating the extent of the seismogenic zone. Fredrich *et al.* (1988) argued for taking the lower bound of Australian earthquakes at 2 times the centroid depth.

Most duration values given in Table 4 were determined from waveform matching and seem to follow the definition by Cohn *et al.* (1982).

### *Linear Regression Analysis*

Following Mark (1977), a linear regression of source parameter Y (e.g., logarithm of fault length) on  $\log M_0$  is written as  $Y = A + B \log M_0$ . This equation passes through the most probable value of Y for any given  $\log M_0$  and this equation is to be used for estimating Y from a given seismic moment.

To obtain the most probable seismic moment from a given source parameter Y, we need to do the regression  $\log M_0 = A' + B' Y$ . The use of this equation for estimating Y from a given seismic moment can lead to noticeable errors (Mark, 1977; Bonilla *et al.*, 1984).

In this study, we accept the seismic moment as the fundamental parameter of earthquake size, consequently using the former regression analysis. The data are least squares fit to a straight line (Singh *et al.*, 1980; Bonilla *et al.*, 1984) using a routine by Press *et al.* (1986). In that routine, the independent variable ( $\log M_0$ ) is assumed error free (Bolt, 1978) and a standard deviation is associated with Y acting as a weight. We feel we are not able to assign objective weights to the observations in Table 4 since the number of independent observations of source parameters for each earthquake is not significantly larger than 1 (Coppersmith and Youngs, 1989). Therefore, we assume a constant standard deviation of 0.3 in the logarithmic domain for all points, which is a conservative estimate for most source parameters (Wyss, 1979; Bonilla *et al.*, 1984).

### *Magnitude Relations*

Body-wave magnitudes from Table 4 are shown in Figure 6. The observed scatter leads to question the usefulness of the  $m_b$  magnitude scale for the classification of earthquakes according to *size*. One explanation of the observed scatter in Figure 6 might be

that observed  $m_b$  values are not strongly related to the size (i.e., seismic moment) of an earthquake (Dziewonski and Woodhouse, 1983). Since both estimates of the size of an earthquake are from different parts of the radiated spectrum, these differences might indicate spectral variations of source radiation as suggested by Duda and Nortmann (1983). On the other hand, Hanks (1979) showed that differences in radiated spectral amplitudes need not translate into differences of the 1 Hz time domain amplitudes used for determining  $m_b$ , due to the characteristics of energy release during the duration of faulting. Another cause of the scatter seen in Figure 6 might be related to the rather inhomogeneous sources of  $m_b$  values (differences in observatory practice; e.g., Willmore, 1979; Aki and Richards, 1980 (Appendix 2); Houston and Kanamori, 1986; Boore, 1986a; McLaughlin and Jih, 1988). In addition,  $m_b$  values of dip-slip earthquakes are approximately 0.3 magnitude units larger than for strike-slip earthquakes (Houston and Kanamori, 1986). In conclusion, the above arguments seem to suggest that the  $m_b$  magnitude scale is not very useful for classifying large earthquakes.

Accepting seismic moment as fundamental parameter of earthquake size, we performed a regression of observed  $m_b$  magnitudes on  $\log M_0$ , assuming a standard deviation of 0.3 for each magnitude value.

$$m_b = 0.23(\pm 1.26) + 0.22(\pm 0.05) \log M_0 \quad (22a)$$

The correlation coefficient is 0.63 indicating a poor fit of the data to a straight line. This poor correlation leads to a significantly different relation if we take  $m_b$  as the fundamental parameter of earthquake size, performing a regression of  $\log M_0$  on  $m_b$  (written in reverse order)

$$m_b = -8.52 + 0.56 \log M_0 \quad (22b)$$

(22a) is significantly different from the relation (12) by Nuttli *et al.* (1989) for  $m_b \geq 4.2$  (short dashes in Figure 6):

$$m_b = -6.55 + 0.50 \log M_0 \quad (23)$$

or Hasegawa's (1983) relation for  $4.2 < M < 6.6$

$$M = -7.30 + 0.54 \log M_0 \quad (24)$$

where  $M = m_N$  (i.e.,  $m_{Lg}$ ) or derived from  $M_L$ . Note the similarity of (22b), (23), and

(24).

In this study, we estimate the most likely magnitude for a given seismic moment, whereas Nuttli *et al.* (1989) and Hasegawa (1983) estimated the most likely seismic moment from a given magnitude. From Figure 6, we see that Nuttli *et al.* (1989) did not consider the saturation of the  $m_b$  scale (e.g., Figure 1 in Boore, 1986a). On the other hand, (22a) seems also biased due to including the saturation, hence predicting too large  $m_b$  values at smaller seismic moments. A change of slope in the body-wave magnitude relation at about  $\log M_0 = 24.5$  seems necessary to account for the saturation of the  $m_b$  scale.

The surface-wave magnitudes of Table 4 are shown in Figure 7. For the linear regression of  $M_S$  on  $\log M_0$ , magnitude values larger than 8.0 and moments larger than  $10^{28}$  *dyne-cm* were rejected, and a standard deviation of 0.3 magnitude unit was assigned to each magnitude.

$$M_S = -13.87(\pm 1.14) + 0.79(\pm 0.04) \log M_0 \quad , \quad (25)$$

which can be compared to (21) (Singh and Havskov, 1980), assuming  $M_W = M_S$  for  $L < 100$  *km*. Comparing magnitude values predicted by (25) (solid line in Figure 7) and (21) (long dashes in Figure 7) in the moment range of  $10^{25}$  and  $10^{28}$  *dyne-cm* shows that magnitude differences are smaller than the usual standard deviation of magnitude observations of 0.3 magnitude units. On the other hand, (13) of the revised mid-plate scaling relation (Nuttli *et al.*, 1989) predicts larger  $M_S$  values for the same moment range (short dashes in Figure 7). If we reverse the order of the linear regression, we get a relation very similar to (25), predicting magnitude values identical to those from (25) in the moment range studied. Equally, the correlation coefficient is 0.96 indicating a good fit of the data to a straight line.

#### *Fault Areas and Average Displacements*

Fault areas,  $A = L W$ , and average displacements on the fault,  $\bar{u}$ , taken from Table 4 are displayed in Figure 8 and 9, respectively. In the linear regression routine, each logarithmic value of fault area or average displacement was assigned a standard deviation of 0.3. For fault areas, a factor of 2 uncertainty is a conservative estimate (Geller, 1976); for

average displacements, it may actually be on the low side. To be consistent, we use *cm* as unit of length.

$$\log A = -2.872(\pm 1.544) + 0.593(\pm 0.058) \log M_0 \quad (26)$$

$$\log \bar{u} = -6.730(\pm 1.396) + 0.337(\pm 0.052) \log M_0 \quad (27)$$

If we neglect the standard deviations, these separate regressions are not consistent with (19). Combined and constrained regressions can be used to force agreement with (19). We fit the data of fault areas and average displacements simultaneously to two different straight lines, imposing the following constraints: the sum of the slopes had to be unity, and the sum of the intercepts had to equal  $-\log \mu$  with  $\mu = 3.0 \times 10^{11}$  dynes/cm<sup>2</sup>. The corresponding coefficients had somewhat large standard deviations indicating that the data can be fit by a multitude of relations. Therefore, we decided to employ further constraints to yield two sets of regression relations. For the first, we note that (26) seems compatible with  $\log A$  proportional to  $0.667 \log M_0$  of Kanamori and Anderson (1975). Hence, we also constrain the slope of the straight line for the area relation to  $0.667$ . This first approach leads to constant stress drop scaling. The combined, constrained regression gives:

$$\log A = -4.843 + 0.667 \log M_0 \quad (28)$$

$$\log \bar{u} = -6.631 + 0.333 \log M_0 \quad (29)$$

For the second approach, we note that fault area is better constrained than average fault displacements, e.g., the correlation coefficients are 0.90 and 0.78 in (26) and (27), respectively. Hence our second approach assumes a slope of  $0.600$  in (26). This second approach leads to variable stress drop scaling. The combined, constrained regression gives

$$\log A = -3.059 + 0.600 \log M_0 \quad (30)$$

$$\log \bar{u} = -8.415 + 0.400 \log M_0 \quad (31)$$

Note that the results of the combined, constrained regressions, i.e., (28) - (31), are modifications of (26) and (27) that are within the range of their standard deviations.

### *Stress Drops*

From (28), an equivalent fault radius can be determined assuming Brune's model (1970, 1971). Using (18) yields:

$$\Delta\sigma = 45 \text{ bar} \quad (32)$$

Hence, the data in Table 4 can be described by constant stress drop scaling. The value of the stress drop is somewhat lower than suggested by Somerville *et al.* (1987) (Figure 10).

Equivalently, (30) gives with (18)

$$\Delta\sigma = 9.45 \times 10^{-2} M_0^{0.1} \quad (33)$$

indicating increasing stress drop (Figure 10) as proposed by Nuttli *et al.* (1989). However, (33) gives a stress drop that increases slower and at a lower level than suggested by Nuttli *et al.* (1989) (Figure 10), i.e., from 20 bar at  $10^{23}$  dyne-cm to 60 bar at  $10^{28}$  dyne-cm.

The observed values of stress drop show a rather large scatter of an approximately circular shape (the correlation coefficient is less than 0.3) and are somewhat lower than those of the intra-plate events studied by Kanamori and Anderson (1975). However, Hasegawa (1983) noted the stress drop to range between 10 - 50 bar for  $4.2 < M < 6.6$  for eastern Canadian events. Both relations, (32) and (33), seem to pass closer to the center of that circular distribution of observed stress drop values than the relations by Somerville *et al.* (1987) or Nuttli *et al.* (1989).

#### *Durations*

Most of the durations given in Table 4 are the lengths of the source time functions (triangular or trapezoidal pulses) as defined by Cohn *et al.* (1982). We excluded very large events with durations longer than 20 seconds from the least squares fit which gives (Figure 11)

$$\log \tau = -7.673(\pm 1.547) + 0.326(\pm 0.061) \log M_0 \quad (34)$$

with a correlation coefficient of 0.85. From Brune (1970, 1971)

$$\log M_0 = 3 \log T_c + \log \Delta\sigma + 21.70 \quad (35)$$

For constant stress drop scaling, we substitute (32) and (34) into (35) assuming  $\tau = T_c$  (Somerville *et al.*, 1987). This consistency check gives a residual of 0.33 in the predicted  $\log M_0$  and a slight difference in  $M_0$  dependence. To match the  $M_0$  dependence, we fix the slope to 0.333 in (34) and solve in the regression for the intercept, obtaining

$$\log \tau = -7.859 + 0.333 \log M_0 \quad , \quad (36)$$

which gives a residual of -0.23, that can be completely explained by a shear wave velocity of 4.2 km/s in the derivation of (35).

Next, we investigate increasing stress drop scaling. Substituting (33) and (34) into (35) gives a residual of -2.34 and a slight difference in  $M_0$  dependence. To match the  $M_0$  dependence in (35), we suggest

$$\log \tau = -7.010 + 0.300 \log M_0 \quad , \quad (37)$$

resulting in a residual of -0.35.

Iio (1986) and Somerville *et al.* (1987) implied that duration essentially equals corner period. But Herrmann and Goertz (1981) showed that a symmetric triangular pulse of duration  $\tau$  has a spectral corner period of  $\pi \tau/2$ . Assuming that all durations in Table 4 are from symmetric triangular pulses, we need to add 0.2 to all values of  $\log \tau$  changing the intercept in (37) to -6.814. The consistency check on Brune's model gives then a residual of +0.23, which could be completely explained by a shear wave velocity of 3.0 km/s, which is rather low.

Another way of testing (36) and (37) is to compare it to predictions of the duration as given by Cohn *et al.* (1982):

$$\tau = \frac{R}{0.8\beta} + \frac{R \sin \delta}{\beta} + \frac{16 R}{7\pi\beta} \quad , \quad (38)$$

where  $\delta$  is the angle between the normal to the fault plane and the ray path to the station. The first two terms describe the rupture propagation time; the third term denotes the rise time (Geller, 1976). Assuming  $\beta = 3.5$  km/s and  $\langle \sin \delta \rangle = 0.64$  (Cohn *et al.*, 1982), and using (28) and (30) to determine the equivalent fault radius gives relations for  $\tau$  that completely agree with (36) and (37), respectively. This is expected since Cohn *et al.* (1982) also followed Brune (1970, 1971).

In conclusion, the revised duration relation (36) suggests a power 3.0 spectral scaling relation as previously inferred by Somerville *et al.* (1987) from a much smaller data set. On the other hand, the data seem also compatible with a power 3.3 spectral scaling as indicated by (37). Hasegawa (1983) inferred for large eastern Canadian earthquakes

$$\log T_c = -6.50 + 0.28 \log M_0 \quad , \quad (39)$$



which is essentially identical to (10) (Atkinson, 1984) and (6a) (Nuttli *et al.*, 1989). Hence, both (36) and (37) are different from the power 3.6 spectral scaling relation proposed for eastern North America.

#### *Fault Lengths and Rupture Velocities*

Fault lengths from Table 4 are plotted in Figure 12. Conservatively assuming a standard deviation in the logarithmic domain of 0.3 for each data point, we get from the linear regression (Figure 12)

$$\log L = -4.681(\pm 1.080) + 0.425(\pm 0.041) \log M_0 \quad (40)$$

The correlation coefficient is 0.93. Note that (40) supports proportionality of fault length and average displacement if (31) for variable stress drop scaling is used.

For estimating rupture velocities, we make the assumption that the duration can be interpreted as  $\tau = R/v_R$  or  $\tau = 2R/v_R$  for bilateral and unilateral rupture propagation, respectively (Sato and Hirasawa, 1973; Boatwright, 1980; Iio, 1986). Using (28) and (36), we get  $v_R = 1.5 \text{ km/s}$  and  $3.1 \text{ km/s}$  for bilateral and unilateral rupture propagation, respectively (assuming constant stress drop scaling). Using (30) and (37), we get  $1.7 \text{ km/s}$  and  $3.4 \text{ km/s}$  for bilateral and unilateral rupture propagation, respectively. Note that those values are consistent with observed rupture velocities that vary between  $1.0 \text{ km/s} - 4.8 \text{ km/s}$  (Purcaru and Berckhemer, 1982).

Using a rupture length as determined from slightly modifying (40) ( $L \propto M_0^{0.4}$ ) would lead to  $v_R \propto M_0^{0.1}$ . For a bilateral rupture propagation,  $v_R \propto L^{0.25}$  which would be similar to Iio's (1986) suggestion of  $v_R \propto L^{0.20} - L^{0.38}$  (see also Purcaru and Berckhemer, 1982).

#### *Spectral scaling*

The scaling relations derived above are used in an effort to construct a spectral scaling model. We follow the approach of Nuttli (1983) and Nuttli *et al.* (1989) and take  $v_R = 0.9 \beta$ . Assuming the  $\omega$ -squared model, it is sufficient to specify the corner periods to completely describe the spectral scaling.

For constant stress drop scaling, we follow Savage (1972), i.e., (16), and using (40)

$$\log T_{01} = -9.980 + 0.425 \log M_0 \quad (41)$$

From (17), (28), and (40), we find

$$\log T_{12} = -5.525 + 0.242 \log M_0 \quad (42)$$

Furthermore, we take (36) for  $T_{02}$ . A quick test shows that the relation for  $T_{12}$  seems incompatible with (36) and (41). We choose to adapt  $T_{12}$  and take  $T_{12} = 0.62$  s for  $\log M_0 = 23$ . Using the geometry of the reduced far-field displacement spectra, we get  $T_{12} = 19.3$  s for  $\log M_0 = 28.0$ . Then

$$\log T_{12} = -7.058 + 0.298 \log M_0 \quad (43)$$

Figure 13a shows that the spectral scaling relations (solid lines) predict longer corner periods than those from Nuttli *et al.* (1989, dashed lines). At smaller moments, however, both spectral scaling relations predict similar corner periods. Included in Figure 13a are corner periods estimated from one station for events # 40 and # 41 (Upadhyay and Duda, 1980). The scaling relations for intra-continental earthquakes using constant stress drop scaling are summarized in Table 5, where its last four columns will be discussed below.

Figure 13b shows a comparison of scaling relations derived for the case of constant and variable stress drop ( $\log T_{12} = -5.416 + 0.233 \log M_0$ ). Note that both relations predict corner periods that are very similar (Table 6).

Table 7a shows the similarity conditions (Kanamori and Anderson, 1975) and rise times (Geller, 1976) for constant stress drop scaling. For small events, the aspect ratio is one and decreases for larger events as the fault length increases with respect to fault width. Values of the aspect ratio were derived from fault length and fault width values in Table 5. Following Savage (1972), note that  $T_{01}$  is proportional to  $L$ , and  $T_{12}$  proportional to  $W$ . Using (41) and (43) gives

$$\frac{W}{L} = \frac{T_{12}}{T_{01}} = 8.4 \times 10^2 M_0^{-0.127} \quad (44)$$

which gives similar values for the aspect ratio.

The strain drop decreases with increasing moment (Table 7a). The dynamic similarity decreases slightly, similar to the relation by Nuttli *et al.* (1989), implying somewhat

different effective stress for small and large events. Table 7b shows similarity conditions for the case of variable stress drop. Note that the strain drop remains constant.

## DISCUSSION AND APPLICATION TO EASTERN NORTH AMERICAN EARTHQUAKES

### *Comparison With Other Scaling Relations*

The data used in this study suggest several differences to the revised mid-plate scaling relation of Nuttli *et al.* (1989). Fault lengths predicted by Nuttli *et al.* (1989) tend to be shorter (Figure 12), fault areas smaller (Figure 8), and average displacements larger (Figure 9) than suggested from world-wide data of intra-continental earthquakes. On the other hand, four spectral scaling relations (Hasegawa, 1983; Atkinson, 1984; Nuttli *et al.*, 1989; and this study) predict very similar durations in the moment range under study (Figure 11), and the data of Table 4 seem to be fit by any of these relations (c.f., Joyner, 1984).

The data can be interpreted using a constant stress drop model as well as a variable stress drop scaling. However, the spectral scaling relations of both models are very similar. A spectral scaling with slopes between 3.0 - 3.3 can explain the data. A spectral slope of 3.0 was inferred by Somerville *et al.* (1987) from an analysis of a much smaller data set. A spectral slope of 3.6 as inferred for earthquakes in eastern North America (Hasegawa, 1983; Atkinson, 1984; Nuttli *et al.*, 1989) is not supported by the data.

We notice however that events in Table 4 scatter about the mean of a scaling relation. For example, events # 9, 14, and 39 have smaller fault dimensions, larger average displacements, and larger stress drops; and hence are better described by the relation of Nuttli *et al.* (1989). Events like these caution the application of scaling relations in earthquake hazard studies since anomalous events with small fault dimensions could produce destructive earthquakes.

The linear regression of observed body-wave magnitudes versus seismic moment has a smaller slope than that of Nuttli *et al.* (1989), who did not take the saturation of the magnitude scale into account. The relation of this study will overpredict magnitudes for

small seismic moments, and a straight line is not suitable for fitting the data for all seismic moments.

### *Consistency Check on Scaling Laws*

Next, we will predict earthquake magnitudes for events in eastern North America using the proposed scaling relations and compare these synthetic magnitudes to the model input (to check for internal consistency) and to observations in eastern North America.

First, we modified random process theory (e.g., (19) in Herrmann, 1987) to include our proposed scaling models. Following Herrmann (1987), we chose  $f_{\max} = 50 \text{ Hz}$  and  $Q(f) = 900 * f^{0.20}$ . The ground motions generated by random process theory were used to determine  $m_{Lg}$  following Herrmann and Kijko (1983). We calculated synthetic time histories at only one epicentral distance (300 km) since  $m_{Lg}$  values are essentially independent of distance (Boore and Atkinson, 1987). Lg-wave magnitudes from random process theory using our constant stress drop scaling are displayed as  $m_{Lg}^{(1)}$  in Table 5 and 6 for constant and increasing stress drop, respectively. The latter are essentially identical to values given by Toro and McGuire (1987) for a constant stress drop of 100 bar. This equivalence also holds with respect to our constant stress drop scaling, except for large seismic moments where our magnitudes are somewhat lower. Comparing the synthetic Lg-wave magnitudes to the observed teleseismic body-wave magnitudes,  $m_b$ , shows that the postulated equivalence of both magnitude scales does not hold for large events. The obvious reason is the saturation of the  $m_b$  scale.

As a second approach, we employed a deterministic modeling technique for a finite source (Herrmann and Jost, 1988; Jost and Herrmann, 1988; Jost, 1989). This technique was developed to study low-frequency ground motions at regional distances due to large mid-plate earthquakes. We assumed that any earthquake is a superposition of subevents, and that the rupture initiates from a point that is equidistant from both fault ends. The rupture initiation depth was held constant at 10 km as the fault dimensions change. The rupture initiated at the bottom of the fault plane for small events. For larger events, the point of rupture initiation moved more to the middle of the fault plane (the upper fault boundary was fixed at 3 km below earth-surface). Two focal mechanisms were considered: a

steeply dipping ( $80^\circ$ ) strike-slip and a  $45^\circ$  dip-slip faults. The sub-events on the fault plane were generated using normal mode theory (Herrmann and Wang, 1985) and the Central United States earth-model (Herrmann, 1986). Assuming  $Q_\alpha = 2 Q_\beta$ , we used  $Q_\alpha$  values of 100 for the first 0.5 km, 500 for the second 0.5 km, 1000 for the next 19 km, and 4000 thereafter. Greens-functions, serving as subevents, were calculated at source depths of 4, 6, 8, 10, 20, 30, and 40 km. These source-depth values were associated with the depths of the subevents on the finite fault. Rupture velocities (90 % the shear wave velocity) and the seismic moments of the subevents were somewhat randomized to prevent artificial periodicities due to the uniform grid. Synthetic time histories were generated at 16 azimuths, equally distributed about the source. Lg-wave magnitudes (Herrmann and Kijko, 1983) were calculated for each trace and averaged with respect to azimuth and focal mechanism. Furthermore, teleseismic magnitudes were determined using the same technique employing Green's functions at  $50^\circ$  (Hudson, 1969). In addition, a maximum  $m_b$ , i.e.,  $\hat{m}_b$ , was determined following Houston and Kanamori (1986). The results of this magnitude estimation are displayed in Tables 5 and 6, labeled  $m_{Lg}^{(2)}$ ,  $m_b^{(3)}$ , and  $\hat{m}_b$ .

Lg-wave magnitudes from random process theory and those from the finite source modeling essentially agree. Observed and predicted teleseismic body-wave magnitudes also show reasonable agreement thus supporting the internal consistency of the scaling. Values of  $m_b$  and  $m_{Lg}$  are not similar. However values of  $\hat{m}_b$  and  $m_{Lg}$  are comparable in the full moment range under study.

The results of our kinematic source modeling showed that the Lg-wave magnitudes of a strike-slip fault are 0.3 magnitude units smaller than those of a  $45^\circ$  dip-slip fault. At teleseismic distances, the difference in magnitudes between strike-slip and dip-slip faulting was found to be somewhat larger, the strike-slip  $m_b$  being smaller by 0.5 magnitude units. The standard deviations in magnitude values in Tables 5 and 6 reflect the focal mechanism and azimuthal differences in the observations. They are somewhat large since our numerical technique does not consider scattering which may smooth the radiation pattern. Hence we observed very pronounced nodes, which are not present in observations, at certain azimuths for the strike slip case.

### *Comparison to Eastern North American Earthquakes*

Next, we will compare the magnitude relation in Table 5 to well observed events in eastern North America. The Oct. 21, 1965 Missouri event had  $m_b = 4.85 \pm 0.23$ ,  $m_{Lg} = 5.04 \pm 0.12$ ,  $M_S = 4.13 \pm 0.32$ , and  $M_0 = 9.0 * 10^{22}$  *dyne-cm* (Nuttli, 1973b, 1983). Accepting the seismic moment as error free, we note that our relations predict somewhat larger magnitudes than observed for this event, where predictions in Table 6 fit the data slightly better than those in Table 5. The Nov. 9, 1968 Illinois event had  $m_b = 5.50 \pm 0.40$ ,  $m_{Lg} = 5.38 \pm 0.23$ ,  $M_S = 5.26 \pm 0.28$ , and  $M_0 = 9.7 * 10^{23}$  *dyne-cm* (Nuttli, 1973b, 1983). These observed source parameters are in agreement with those in Tables 5 and 6, except the Lg-wave magnitude, which is overpredicted by 0.5 magnitude units in both tables. The Jan. 9, 1982 New Brunswick event had  $m_b = 5.8$ ,  $m_{Lg} = 5.7$ ,  $M_S = 5.1$ , and  $M_0 = 2.2 * 10^{24}$  *dyne-cm* (North *et al.*, written communication, 1989). For this event, all source parameters essentially agree with the predictions of Tables 5 and 6. Finally, the Nov. 25, 1988 Saguenay event had  $m_b = 5.9$ ,  $m_{Lg} = 6.5$ ,  $M_S = 5.7$ , and  $M_0 = 8.0 * 10^{24}$  *dyne-cm* (North *et al.*, written communication, 1989). We note a reasonable agreement with Tables 5 and 6; however, the observed Lg-wave magnitude of this event is larger than predicted by the scaling relations (North *et al.*, written communication, 1989). In conclusion, the scaling relations proposed seem to predict magnitudes for eastern North America reasonably well, with a tendency though to overestimate  $m_{Lg}$  by 0.3 magnitude units for the central United States and to underestimate it for Saguenay.

Using the proposed scaling relations for intr-continental earthquakes (Table 5), we can estimate source parameters for some of the largest historical events in the eastern United States. However, published seismic moments for these events cannot be used since they have been estimated from magnitudes using empirical relations. The observations available for these historical events are intensity values which have been used to determine magnitudes such as  $m_b$ ,  $m_{Lg}$ , or  $M_S$  (e.g., Nuttli, 1973a; Nuttli *et al.*, 1979).

For the 1886 earthquake near Charleston, S. C., Nuttli (1983) estimated a Lg-wave magnitude of 6.7 (Campbell, 1986). This magnitude is a slight revision of his earlier estimate of 6.6 based on a relation of intensity versus magnitude (Nuttli *et al.*, 1979). Using

Table 5, we would expect a body-wave magnitude of 6.0, an  $M_S$  of 6.8, a seismic moment of  $1.0 * 10^{26}$  dyne-cm, a fault length of 23 km, a fault width of 11 km, and an average displacement on the fault plane of 1.1 m. Assuming that present day micro-earthquake activity occurs on the fault plane that ruptured in 1886, we can compare our prediction of fault dimensions with observations by Shedlock (1987). She inferred a length extent of 22 km and depth extent of 12 km for the hypocenter distribution of recent micro-earthquakes in the hypocenter region of the 1886 event (c.f., Talwani, 1982). Earlier estimates by Nuttli *et al.* (1979) and Nuttli (1983) indicated a fault length of 30 km (Nuttli *et al.*, 1989). We conclude that fault dimensions from recent micro-earthquakes are in good agreement to predictions from our proposed scaling model.

Next, we address the earthquakes near New Madrid in 1811-1812. Based on a relation between intensity and Lg-wave magnitude, Nuttli *et al.* (1979) estimated a Lg-wave magnitude of 7.3 for the earthquake on December 16, 1811, 7.2 for the event on January 23, 1812, and 7.5 for the earthquake on February 7, 1812. These estimates were based on a curve of intensity falloff versus distance calibrated by using intra- and interplate earthquakes (Nuttli *et al.*, 1979). Assuming that including events from California for the calibration procedure in Nuttli *et al.* (1979) did not bias the magnitude estimates for New Madrid, we estimate the following source parameters for the historical events (Table 5). For the Dec. 16 earthquake, we obtain an  $m_b$  of 6.2, an  $M_S$  of 7.6, a seismic moment  $1.0 * 10^{27}$  dyne-cm, a fault length of 62 km, a fault width of 22 km, and a mean displacement on the fault plane of 2.3 m. A similar estimate would also hold if we assume increasing stress drop scaling (Table 6). Noting the slight differences between Lg-wave magnitudes estimated from finite source modeling and random process theory, we get somewhat larger source parameters by assuming the magnitude from random process theory. The January 23, 1812 earthquake (Nuttli *et al.*, 1979) was only slightly smaller than the shock in 1811, and had probably very similar source parameters. However, the event on Feb. 7, 1812 was larger. From Table 5, we get  $m_b = 6.3$ ,  $M_S = 8.0$ ,  $M_0 = 3.0 * 10^{27}$  dyne-cm, fault length = 100 km, fault width = 32 km, and mean displacement on the fault = 3.4 m. These estimates could also be somewhat larger if Lg-wave magnitudes from random process theory rather than from finite source modeling would be used.

Studies of microseismicity in the New Madrid Seismic Zone (Stauder *et al.*, 1976) indicate a length of about 125 km for the southern segment which is associated with the event on December 16, 1811 and its two major aftershocks. This segment of the fault could easily contain a rupture length of 60 -100 km corresponding to an event with seismic moment between  $1.0 \times 10^{27}$  dyne-cm and  $3.0 \times 10^{27}$  dyne-cm. The whole length of 125 km could have ruptured in several events rather than in one. The above estimate of fault width is more problematic since present day seismicity in the New Madrid Seismic Zone extends only to a depth of about 14 km (Himes *et al.*, 1988). On the other hand, the November 9, 1968 Illinois earthquake had a confirmed depth of 25 km, suggesting that deeper parts in the mid-continental crust can be seismogenic. The earthquake near New Madrid on January 23, 1812 is associated with the central section of the New Madrid Seismic Zone. Its length is about 60 km which agrees well with our above estimate. For the third event on February 7, 1812, the length of microseismicity of about 85 km on the northern part of the New Madrid Seismic Zone (Nuttli, 1983) is only slightly smaller than our estimate from above. Considering the variability in our source parameters, even a seismic moment of  $8 \times 10^{27}$  dyne-cm as proposed by Johnston (1989) and Nuttli *et al.* (1989) could be reasonable for this event.

These estimates of source parameters apply only if the corresponding events were average intra-continental earthquakes. As discussed before, actual events show a scatter of source parameter values such that each estimate of source dimension, average displacement, and stress drop could vary by a factor of 2 (Bonilla *et al.*, 1984). Another problem is related to the thickness of the seismogenic zone which can reach up to 45 km according to the intra-continental scaling relations assuming constant stress drop (Table 5). In regions like the central United States, this value for the thickness of the seismogenic zone seems too large (Joyner, 1984). It is interesting to note that the increasing stress drop scaling for intra-continental earthquakes (Table 6) would suggest fault widths of 10, 17, and 23 km for the events in 1886, 1811, and 1812 (February 7), respectively.

Purcaru and Berckhemer (1982) expressed doubts that a classification of earthquakes according to plate tectonics (e.g., mid-plates, plate margins) leads to meaningful results. This contrasts with other studies suggesting a grouping according to type of plate



boundary (e.g., Kanamori and Anderson, 1975; Singh *et al.*, 1980; Nuttli, 1983, 1985). As more and better quality data become available, scaling relations will need further updating to investigate possible regional differences in scaling (Acharya, 1979; Hasegawa, 1983; Bonilla *et al.*, 1984). Further refinement could also come from including focal mechanisms or other parameters into scaling relations (Purcaru and Berckhemer, 1982; Bonilla *et al.*, 1984).

## CONCLUSION

A data set of 59 intra-continental earthquakes has been used to derive seismic scaling relations. The data can be explained by a constant stress drop scaling (slope of 3.0) as suggested by Somerville *et al.* (1987). On the other hand, an increasing stress drop scaling (slope of 3.3) cannot be ruled out. This range of variability in spectral scaling has also been observed for the Nahanni earthquake sequence (Boore and Atkinson, 1989) assuming these events to be intra-continental. Corner periods are very similar in this range of spectral scaling exponents. However, the world-wide data do not support a spectral slope of 3.6 as suggested for eastern North America by Nuttli *et al.* (1989). Comparing Table 5 to Table 1 in Nuttli (1985) for plate margin events indicates smaller fault lengths for intra-continental versus plate-margin events. On the other hand, stress drops and average displacements do not seem to be fundamentally different.

The proposed scaling relations have been used to determine synthetic Lg-wave and teleseismic body-wave magnitudes to check for internal consistency. Observed magnitudes of events from North America show agreement with predictions of the scaling relations considered the scatter in source data. Source parameters also have been derived for the largest historical earthquakes in the central and eastern United States using the proposed scaling relations. Fault rupture lengths show a reasonable agreement with observed distributions of microseismicity. The relations based on increasing stress drop predict fault rupture widths that are in closer agreement with observed distributions of microseismicity in the central and eastern United States than those of the constant stress drop model.

## ACKNOWLEDGMENTS

Helpful criticism of an earlier version of the manuscript by Dr. Mitchell and Dr. Stauder, S. J. is greatly acknowledged. Funds for this research were provided by the Defense Advanced Research Projects Agency under contract F49628-87-K-0047 monitored by the Air Force Geophysics Laboratory.

## REFERENCES

- Acharya, H. K. (1979). Regional variations in the rupture-length magnitude relationships and their dynamical significance, *Bull. Seism. Soc. Am.* **69**, 2063-2084.
- Aki, K. (1967). Scaling law of seismic spectrum, *J. Geophys. Res.* **72**, 1217-1231.
- Aki, K. and P. G. Richards (1980). *Quantitative Seismology: Theory and Methods*, W. H. Freeman and Co., San Francisco, California, 932 pp.
- Anderson, J. G. (1986). Implication of attenuation for studies of the earthquake source, in *Earthquake Source Mechanics*, S. Das, J. Boatwright, and C. H. Scholz, Editors, Geophysical Monograph 37, American Geophysical Union, Washington, D.C., 311-318.
- Andrews, D. J. (1986). Objective determination of source parameters and similarity of earthquakes of different size, in *Earthquake Source Mechanics*, S. Das, J. Boatwright, and C. H. Scholz, Editors, Geophysical Monograph 37, American Geophysical Union, Washington, D.C., 259-267.
- Assumpcao, M. and G. Suarez (1988). Source mechanisms of moderate size earthquakes and stress orientation in mid-plate South America, *Geophys. J.* **92**, 253-267.
- Atkinson, G. M. (1984). Attenuation of strong ground motion in Canada from a random vibrations approach, *Bull. Seism. Soc. Am.* **74**, 2629-2653.
- Baker, R. G. (1967). Preliminary study for determining magnitude from Lg, *Earthquake Notes* **38**, 23-28.
- Bakun, W. H., G. C. P. King, and R. S. Cockerham (1986). Seismic slip, aseismic slip, and the mechanics of repeating earthquakes on the Calaveras fault, California, in *Earthquake Source Mechanics*, S. Das, J. Boatwright, and C. H. Scholz, Editors, Geophysical Monograph 37, American Geophysical Union, Washington, D.C., 195-207.
- Boatwright, J. (1980). A spectral theory for circular seismic sources; simple estimates of source dimension, dynamic stress drop, and radiated seismic energy, *Bull. Seism. Soc. Am.* **70**, 1-27.
- Bollinger, G. A. (1979). Attenuation of the Lg phase and the determination of  $m_b$  in the southeastern United States, *Bull. Seism. Soc. Am.* **69**, 45-63.
- Bolt, B. A. (1978). Incomplete formulations of the regression of earthquake magnitude with surface rupture length, *Geology* **6**, 233-235.
- Bonilla, M. G., R. K. Mark, and J. J. Lienkaemper (1984). Statistical relations among earthquake magnitude, surface rupture length, and surface fault displacement, *Bull. Seism. Soc. Am.* **74**, 2379-2411.
- Boore, D. M. (1983). Stochastic simulation of high-frequency ground motions based on seismological models of the radiated spectra, *Bull. Seism. Soc. Am.* **73**, 1865-1984.
- Boore, D. M. (1986a). Short-period P- and S- wave radiation from large earthquakes: implications for spectral scaling relations, *Bull. Seism. Soc. Am.* **76**, 43-64.
- Boore, D. M. (1986b). The effect of finite bandwidth on seismic scaling relationships, in *Earthquake Source Mechanics*, S. Das, J. Boatwright, and C. H. Scholz, Editors, Geophysical Monograph 37, American Geophysical Union, Washington, D.C., 275-283.

- Boore, D. M. and G. M. Atkinson (1987). Stochastic prediction of ground motion and spectral response parameters at hard-rock sites in eastern North America, *Bull. Seism. Soc. Am.* **77**, 440-467.
- Boore, D. M. and G. M. Atkinson (1989). Spectral scaling of the 1985-1988 Nahanni, Northwest Territories, earthquakes, *Bull. Seism. Soc. Am.* **79**, (in press).
- Brune, J. N. (1970). Tectonic stress and the spectra of seismic shear waves from earthquakes, *J. Geophys. Res.* **75**, 4997-5009.
- Brune, J. N. (1971). Tectonic stress and the spectra of seismic shear waves from earthquakes (correction), *J. Geophys. Res.* **76**, 5002.
- Brune, J. N., R. J. Archuleta, and S. Hartzell (1979). Far-field S-wave spectra, corner frequencies, and pulse shapes, *J. Geophys. Res.* **84**, 2262-2272.
- Brune, J. N., J. Fletcher, F. Vernon, L. Haar, T. Hanks, and J. Berger (1986). Low stress-drop earthquakes in the light of new data from the Anza, California telemetered digital array, in *Earthquake Source Mechanics*, S. Das, J. Boatwright, and C. H. Scholz, Editors, Geophysical Monograph 37, American Geophysical Union, Washington, D.C., 237-245.
- Butler, R., G. S. Stewart, and H. Kanamori (1979). The July 27, 1976 Tangshan, China earthquake - a complex sequence of intraplate events, *Bull. Seism. Soc. Am.* **69**, 207-220.
- Campbell, K. W. (1986). An empirical estimate of near-source ground motion for a major,  $m_b = 6.8$ , earthquake in the Eastern United States, *Bull. Seism. Soc. Am.* **76**, 1-17.
- Chen, W.-P. and P. Molnar (1977). Seismic moments of major earthquakes and the average rate of slip in central Asia, *J. Geophys. Res.* **82**, 2945-2969.
- Chun, K.-Y., R. J. Kokoski, and G. F. West (1989). Source spectral characteristics of Miramichi earthquakes: results from 115 P-wave observations, *Bull. Seism. Soc. Am.* **79**, 15-30.
- Chung, W.-Y. and J. J. Cipar (1983). Source modeling of the Hsingtai, China earthquakes of March 1966, *Phys. Earth Planet. Interiors* **33**, 111-125.
- Chung, W.-Y., B. J. Brantley, and A. C. Johnston (1988). Source mechanisms, surface rupture, and relative locations of the 22 January 1988 Tennant Creek earthquakes, Central Australia, *EOS, Trans. Am. Geophys. Union* **69**, 1301.
- Cipar, J. (1979). Source processes of the Haicheng, China earthquake from observations of P and S waves, *Bull. Seism. Soc. Am.* **69**, 1903-1916.
- Cisternas, A., J. Dorel, and R. Gaulon (1982). Models of the complex source of the El Asnam earthquake, *Bull. Seism. Soc. Am.* **72**, 2245-2266.
- Coffman, J. L. and C. A. von Hake (1973). *Earthquake History of the United States*, U.S. Department of Commerce Publ. 41-1, 208 pp.
- Cohn, S. N., T.-L. Hong, and D. V. Helmberger (1982). The Oroville earthquakes: a study of source characteristics and site effects, *J. Geophys. Res.* **87**, 4584-4594.
- Coppersmith, K. J. and R. R. Youngs (1989). Issues regarding earthquake source characterization and seismic hazard analysis within passive margins and stable continental interiors, in *Earthquakes at North-Atlantic Passive Margins: Neotectonics and Postglacial Rebound*, S. Gregersen and P. W. Basham, Editors, Kluwer Acad.

Publ., 601-631.

- Darragh, R. B. and B. A. Bolt (1987). A comment on the statistical regression relation between earthquake magnitude and fault rupture length, *Bull. Seism. Soc. Am.* **77**, 1479-1484.
- Deng, Q., F. Song, S. Zhu, M. Li, T. Wang, W. Zhang, B. C. Burchfiel, P. Molnar, and P. Zhang (1984). Active faulting and tectonics of the Ningxia-Hui Autonomous Region, China, *J. Geophys. Res.* **89**, 4427-4445.
- Deng, Q., S. Chen, F. Song, S. Zhu, Y. Wang, W. Zhang, D. Jiao, B. C. Burchfiel, P. Molnar, L. Royden, and P. Zhang (1986). Variations in the geometry and amount of slip on the Haiyuan (Nanxishaushan) fault zone, China and the surface rupture of the 1920 Haiyuan earthquake, in *Earthquake Source Mechanics*, S. Das, J. Boatwright, and C. H. Scholz, Editors, Geophysical Monograph 37, American Geophysical Union, Washington, D.C., 169-182.
- Deschamps, A., Y. Gaudemer, and A. Cisternas (1982). The El Asnam, Algeria earthquake of 10 October 1980: Multiple-source mechanism determined from long-period records, *Bull. Seism. Soc. Am.* **72**, 1111-1128.
- Duda, S. J. and R. Nortmann (1983). Normal, blue, and red earthquakes - a new way of earthquake classification on the basis of body-wave magnitudes, *Tectonophysics* **93**, 295-306.
- Dziewonski, A. M. and J. H. Woodhouse (1983). An experiment in systematic study of global seismicity: centroid-moment tensor solutions for 201 moderate and large earthquakes of 1981, *J. Geophys. Res.* **88**, 3247-3271.
- Electric Power Research Institute (1988). Engineering Model of Earthquake Ground Motion for Eastern North America, EPRI NP-6074.
- Eyidogan, H., J. Nabelek, and M. N. Toksoz (1985). The Gazli, USSR, 19 March 1984 earthquake: The mechanism and tectonic implications, *Bull. Seism. Soc. Am.* **75**, 661-675.
- Fletcher, M. (1982). A comparison between the tectonic stress measured *in situ* and stress parameters for induced seismicity at Monticello Reservoir, South Carolina, *J. Geophys. Res.* **87**, 6931-6944.
- Fredrich, J., R. McCaffrey, and D. Denham (1988). Source parameters of seven large Australian earthquakes determined by body waveform inversion, *Geophys. J.*, **95**, 1-13.
- Geller, R. J. (1976). Scaling relations for earthquake source parameters and magnitudes, *Bull. Seism. Soc. Am.* **66**, 1501-1523.
- Gutenberg, B. and C. F. Richter (1949). *Seismicity of the Earth and associated phenomena*, Princeton University Press.
- Haar, L. C., C. S. Mueller, J. B. Fletcher, and D. M. Boore (1986). Comments on "Some recent Lg phase displacement spectral densities and their implications with respect to prediction of ground motions in eastern North America" by R. Street, *Bull. Seism. Soc. Am.* **76**, 291-295.
- Hamburger, M. W., G. L. Pavlis, M. Eneva, and W. Swanson (1988). Spatial and temporal patterns of seismicity in the Garm region, USSR: Applications to earthquake prediction and collisional tectonics, in M. L. Jacobson, Editor, National Earthquake Hazards Reduction Program, Summaries of Technical Reports, Vol. XXVII, U.S.

*Geological Survey, Open-File Rept. 88-673, 61-65.*

- Hanks, T. C. (1979).  $b$  values and  $\omega^{-\gamma}$  seismic source models: implications for tectonic stress variations along active crustal fault zones and the estimation of high-frequency strong ground motion, *J. Geophys. Res.* **84**, 2235-2242.
- Hanks, T. C. (1982).  $f_{\max}$ , *Bull. Seism. Soc. Am.* **72**, 1867-1879.
- Hanks, T. C. and H. Kanamori (1979). A moment magnitude scale, *J. Geophys. Res.* **84**, 2348-2350.
- Hanks, T. C. and M. Wyss (1972). The use of body-wave spectra in the determination of seismic source parameters, *Bull. Seism. Soc. Am.* **62**, 561-589.
- Hartzell, S. (1980). Faulting process of the May 17, 1976 Gazli, USSR earthquake, *Bull. Seism. Soc. Am.* **70**, 1715-1736.
- Hasegawa, H. S. (1983). Lg spectra of local earthquakes recorded by the eastern Canada telemetered network and spectral scaling, *Bull. Seism. Soc. Am.* **73**, 1041-1061.
- Heaton, T. H. and S. H. Hartzell (1988). Earthquake ground motions, *Ann. Rev. Earth Planet. Sci.* **16**, 121-145.
- Heaton, T. H. and S. H. Hartzell (1989). Estimation of strong ground motions from hypothetical earthquakes on the Cascadia Subduction zone, Pacific Northwest, *Pure Appl. Geoph.* **129**, (in press).
- Heinrich, R. R. (1941). A contribution to the seismic history of Missouri, *Bull. Seism. Soc. Am.* **31**, 187-224.
- Herrmann, R. B. (1986). Surface-wave studies of some South Carolina earthquakes, *Bull. Seism. Soc. Am.* **76**, 111-121.
- Herrmann, R. B. (1987). Broadband Lg magnitude, *Seism. Res. Letters* **58**, 125-133.
- Herrmann, R. B. and M. J. Goertz (1981). A numerical study of peak ground motion scaling, *Bull. Seism. Soc. Am.* **71**, 1963-1979.
- Herrmann, R. B. and M. L. Jost (1988). Simulation of long period ground motions for a large New Madrid earthquake, in M. A. Cassaro and J. D. Cooper, Editors, *Seismic Design and Construction of Complex Civil Engineering Systems*, American Society of Civil Engineers, New York, 1-15.
- Herrmann, R. B. and A. Kijko (1983). Short-period Lg magnitudes: instrument, attenuation, and source effects, *Bull. Seism. Soc. Am.* **73**, 1835-1850.
- Herrmann, R. B. and C. Y. Wang (1985). A comparison of synthetic seismograms, *Bull. Seism. Soc. Am.* **75**, 41-56.
- Himes, L., W. Stauder, and R. B. Herrmann (1988). Indication of active faults in the New Madrid Seismic Zone from precise location of hypocenters, *Seism. Res. Letters* **59**, 123-131.
- Hinze, W. J., L. W. Braile, G. R. Keller, and E. G. Lidiak (1988). Models for midcontinent tectonism : an update, *Rev. Geophys.* **26**, 699-717.
- Houston, H. and H. Kanamori (1986). Source spectra of great earthquakes: teleseismic constraints on rupture process and strong motion, *Bull. Seism. Soc. Am.* **76**, 19-42.

- Hudson, J. A. (1969). A quantitative evaluation of seismic signals at teleseismic distances - II. Body waves and surface waves from an extended source, *Geophys. J. R. Astr. Soc.* **18**, 353-370.
- Iio, Y. (1986). Scaling relation between earthquake size and duration of faulting for shallow earthquakes in seismic moment between  $10^{10}$  and  $10^{25}$  dyne-cm, *J. Phys. Earth* **34**, 127-169.
- Jackson, J., P. Molnar, H. Patton, and T. Fitch (1979). Seismotectonic aspects of the Markansu Valley, Tadjikstan, earthquake of August 11, 1974, *J. Geophys. Res.* **84**, 6157-6167.
- Johns, F. B., T. L. Long, and J. H. McKee (1977). Study of the attenuation and azimuthal dependence of seismic wave propagation in the southeastern United States, *Bull. Seism. Soc. Am.* **67**, 1503-1513.
- Johnston, A. (1989). The seismicity of 'Stable Continental Interiors', in *Earthquakes at North-Atlantic Passive Margins: Neotectonics and Postglacial Rebound*, S. Gregeresen and P. W. Basham, Editors, Kluwer Acad. Publ., 299-327.
- Johnston, A., and S. J. Nava (1984). Recurrence rates and probability estimates for the New Madrid seismic zone, in Proc. Symposium on The New Madrid Seismic Zone, U.S. Geological Survey, Open-File Rept. 84-770, 279-329.
- Johnston, A., and S. J. Nava (1985). Recurrence rates and probability estimates for the New Madrid seismic zone, *J. Geophys. Res.* **90**, 6737-6753.
- Jost, M. L. and R. B. Herrmann (1988). Numerical simulation of ground motions at Chicago and Atlanta for a large New Madrid earthquake, *EOS, Trans. Am. Geophys. Union* **69**, 1335.
- Jost, M. L. (1989). Long-period strong ground motions and response spectra of large historical earthquakes in the central and eastern United States from kinematic source models, *Ph. D. Thesis*, Saint Louis University.
- Joyner, W. B. (1984). A scaling law for the spectra of large earthquakes, *Bull. Seism. Soc. Am.* **74**, 1167-1188.
- Kanamori, H. (1978). Quantification of earthquakes, *Nature* **271**, 411-414.
- Kanamori, H. and C. R. Allen (1986). Earthquake repeat time and average stress drop, in *Earthquake Source Mechanics*, S. Das, J. Boatwright, and C. H. Scholz, Editors, Geophysical Monograph 37, American Geophysical Union, Washington, D.C., 227-235.
- Kanamori, H. and D. L. Anderson (1975). Theoretical basis of some empirical relations in seismology, *Bull. Seism. Soc. Am.* **65**, 1073-1095.
- Keilis-Borok, V. I. (1959). An estimation of the displacement in an earthquake source and of the source dimensions, *Ann. Geofis. (Rome)* **12**, 205-214.
- Kostrov, B. V. and S. Das (1988). *Principles of Earthquake Source Mechanics*, Cambridge University Press, Cambridge, 286 pp.
- Kristy, M. J., L. J. Burdick, and D. W. Simpson (1980). The focal mechanisms of the Gazli, USSR, earthquakes, *Bull. Seism. Soc. Am.* **70**, 1737-1750.
- Langer, C. J., M. G. Bonilla, and G. A. Bollinger (1987). Aftershocks and surface faulting associated with the intraplate Guinea, West Africa, earthquake of 22 December

- 1983, *Bull. Seism. Soc. Am.* **77**, 1579-1601.
- Langston, C. A. (1976). A body wave inversion of the Koyna, India, earthquake of December 10, 1967, and some implications for body wave focal mechanisms, *J. Geophys. Res.* **81**, 2517-2530.
- Liu, H. L. and H. Kanamori (1980). Determination of source parameters of mid-plate earthquakes from the waveforms of body waves, *Bull. Seism. Soc. Am.* **70**, 1989-2004.
- Madariaga, R. (1979). On the relation between seismic moment and stress drop in the presence of stress and strength heterogeneity, *J. Geophys. Res.* **84**, 2243-2250.
- Mandelbrot, B. B. (1983). *The Fractal Geometry of Nature*, rev. ed., Freeman, New York, 468 pp.
- Marion, G. E. and L. T. Long (1980). Microearthquake spectra in the southeastern United States, *Bull. Seism. Soc. Am.* **70**, 1037-1054.
- Mark, R. K. (1977). Application of linear statistical models of earthquake magnitude versus fault length in estimating maximum expectable earthquakes, *Geology* **5**, 464-466.
- McLaughlin, K. L. and R.-S. Jih (1988). Scattering from near-source topography: teleseismic observations and numerical simulations, *Bull. Seism. Soc. Am.* **78**, 1399-1414.
- Mitchell, B. J., O. W. Nuttli, R. B. Herrmann, and W. Stauder (1989). Seismotectonics of the central United States, in *Neotectonics of the Central United States*, Geological Society of America, (in press).
- Nabelek, J., W.-P. Chen, and H. Ye (1987). The Tangshan earthquake sequence and its implications for the evolution of the North China Basin, *J. Geophys. Res.* **92**, 12,615-12,628.
- Nelson, M. R., R. McCaffrey, and P. Molnar (1987). Source parameters for 11 earthquakes in the Tien Shan, Central Asia, determined by P and SH waveform inversion, *J. Geophys. Res.* **92**, 12,629-12,648.
- Nuttli, O. W. (1973a). The Mississippi Valley earthquakes of 1811 and 1812: Intensities, ground motion and magnitudes, *Bull. Seism. Soc. Am.* **63**, 227-248.
- Nuttli, O. W. (1973b). Seismic wave attenuation and magnitude relations for eastern North America, *J. Geophys. Res.* **78**, 876-885.
- Nuttli, O. W. (1983). Average seismic source-parameter relations for mid-plate earthquakes, *Bull. Seism. Soc. Am.* **73**, 519-535.
- Nuttli, O. W. (1985). Average seismic source-parameter relations for plate-margin earthquakes, *Tectonophysics* **118**, 161-174.
- Nuttli, O. W. and R. B. Herrmann (1987). Ground motion relations for eastern North American earthquakes, in *Ground Motion and Engineering Seismology*, A. S. Cakmak, Editor, Elsevier, Amsterdam, 231-241.
- Nuttli, O. W., G. A. Bollinger, and D. W. Griffiths (1979). On the relation between Modified Mercalli intensity and body-wave magnitude, *Bull. Seism. Soc. Am.* **69**, 893-909.



- Nuttl, O. W., G. A. Bollinger, and R. B. Herrmann (1986). The 1886 Charleston, South Carolina, earthquake - A 1986 perspective, *U.S. Geological Survey Circular 985*, 52 pp.
- Nuttl, O. W., M. L. Jost, R. B. Herrmann, and G. A. Bollinger (1989). Numerical models of the rupture mechanics and far-field ground motion of the 1886 South Carolina earthquake, *U.S. Geological Survey Bulletin 1586*, (in press).
- Okal, E. A. (1976). A surface-wave investigation of the rupture mechanism of the Gobi-Altai (4 December, 1957) earthquake, *Phys. Earth Planet. Interiors* **12**, 319-328.
- Okal, E. A. (1977). The July 9 and 23, 1905, Mongolian earthquakes: a surface wave investigation, *Earth Planet. Sc. Letters*, **34**, 326-331.
- Okal, E. A. and L. M. Stewart (1981). A negative search for an ultra slow component to the source of the Yunnan earthquakes of May 29, 1976, *Phys. Earth Planet. Interiors* **26**, 208-216.
- Ouyed, M., M. Meghraoui, A. Cisternas, A. Deschamps, J. Dorel, J. Frechet, R. Gaulon, D. Hatzfeld, and H. Philip (1981). Seismotectonics of the El Asnam earthquake, *Nature* **292**, 26-30.
- Press, W. H., B. P. Flannery, S. A. Teukolsky, and W. T. Vetterling (1987). *Numerical Recipes: The Art of Scientific Computing*, Cambridge University Press, Cambridge, 818 pp.
- Purcaru, G. and H. Berckhemer (1982). Quantitative relations of seismic source parameters and a classification of earthquakes, *Tectonophysics* **84**, 57-128.
- Sato, T. and T. Hirasawa (1973). Body wave spectra from propagating shear cracks, *J. Phys. Earth* **21**, 415-431.
- Savage, J. C. (1972). Relation of corner frequency to fault dimensions, *J. Geophys. Res.* **77**, 3788-3795.
- Scholz, C. H. (1982). Scaling laws for large earthquakes: Consequences for physical models, *Bull. Seism. Soc. Am.* **72**, 1-14.
- Scholz, C. H., C. A. Aviles, and S. G. Wesnousky (1986). Scaling differences between large interplate and intraplate earthquakes, *Bull. Seism. Soc. Am.* **76**, 65-70.
- Shedlock, K. M. (1987). Earthquakes recorded by the South Carolina seismic network (1974-1986), *U.S. Geological Survey Open-File Report 87-437*, 92 pp.
- Shedlock, K. M., L. M. Jones, and M. Xiufang (1985). Determination of elastic wave velocity and relative hypocenter locations using refracted waves. II. Application to the Haicheng, China, aftershock sequence, *Bull. Seism. Soc. Am.* **75**, 427-439.
- Shin T.-C. and R. B. Herrmann (1987). Lg attenuation and source studies using 1982 Miramichi data, *Bull. Seism. Soc. Am.* **77**, 384-397.
- Silver, P. G. (1983). Retrieval of source-extent parameters and the interpretation of corner frequency, *Bull. Seism. Soc. Am.* **73**, 1499-1511.
- Singh, S. K. and J. Havskov (1980). On moment-magnitude scale, *Bull. Seism. Soc. Am.* **70**, 379-383.
- Singh, S. and R. B. Herrmann (1983). Regionalization of crustal Q in the continental United States, *J. Geophys. Res.* **88**, 527-538.

- Singh, S. K., E. Bazan, and L. Esteva (1980). Expected earthquake magnitude from a fault, *Bull. Seism. Soc. Am.* **70**, 903-914.
- Somerville, P. G., J. P. McLaren, L. V. LeFevre, R. W. Burger, and D. V. Helmberger (1987). Comparison of source scaling relations of eastern and western North American earthquakes, *Bull. Seism. Soc. Am.* **77**, 322-346.
- Stauder, W., M. Kramer, G. Fischer, S. Schaefer, and S. T. Morrissey (1976). Seismic characteristics of southeast Missouri as indicated by a regional telemetered microearthquake array, *Bull. Seism. Soc. Am.* **66**, 1953-1964.
- Street, R. L. and O. W. Nuttli (1984). The central Mississippi Valley earthquakes of 1811-1812, in Proc. Symposium on The New Madrid Seismic Zone, *U.S. Geological Survey, Open-File Rept. 84-770*, 33-62.
- Street, R. L. and F. T. Turcotte (1977). A study of northeastern North American spectral moments, magnitudes, and intensities, *Bull. Seism. Soc. Am.* **67**, 599-614.
- Talwani, P. (1982). Internally consistent pattern of seismicity near Charleston, South Carolina, *Geology* **10**, 654-658.
- Talwani, P. (1989). Characteristic features of intraplate earthquakes and the models proposed to explain them, in *Earthquakes at North-Atlantic Passive Margins: Neotectonics and Postglacial Rebound*, S. Gregersen and P. W. Basham, Editors, Kluwer Acad. Publ., 563-579.
- Upadhyay, S. K. and S. J. Duda (1980). Source parameters of earthquakes from the Himalayan region, *J. Geophys.* **48**, 67-79.
- Vogfjörd, K. S. and C. A. Langston (1987). The Meckering earthquake of 14 October 1968: a possible downward propagating rupture, *Bull. Seism. Soc. Am.* **77**, 1558-1578.
- Willmore, P. L., Editor (1979). Manual of seismological observatory practice, *NOAA, U. S. Department of Commerce, Report SE-20*.
- Wyss, M. (1979). Estimating maximum expectable magnitude of earthquakes from fault dimensions, *Geology* **7**, 336-340.
- Zhang, W., D. Jiao, P. Zhang, P. Molnar, B. C. Burchfiel, Q. Deng, Y. Wang, and F. Song (1987). Displacement along the Haiyuan fault associated with the great 1920 Haiyuan, China, earthquake, *Bull. Seism. Soc. Am.* **77**, 117-131.
- Zhou, H. L., C. R. Allen, and H. Kanamori (1983a). Rupture complexity of the 1970 Tonghai and 1973 Luhuo earthquakes, China, from P-wave inversion, and relationship to surface faulting, *Bull. Seism. Soc. Am.* **73**, 1585-1597.
- Zhou, H., H. L. Liu, and H. Kanamori (1983b). Source processes of large earthquakes along the Xianshuihe fault in southwestern China, *Bull. Seism. Soc. Am.* **73**, 537-551.

TABLE 1

AVERAGE SOURCE PARAMETERS FOR MID-PLATE  
EARTHQUAKES (NUTTLI ET AL., 1989)\*

$m_b$	$M_s$	$M_w$	$\log M_0$ [dyne-cm]	$T_{01}^{**}$ [s]	$L^{**}$ [km]	$T_{12}^{**}$ [s]	$W^{**}$ [km]	$T_{02}^{**}$ [s]	$\Delta\sigma^{**}$ [bars]	$\bar{u}^{**}$ [m]
2.5	1.15	2.87	20.0	0.14	0.28	0.14	0.28	0.14	11	0.004
3.5	2.15	3.54	21.0	0.25	0.50	0.25	0.50	0.25	20	0.012
4.4	3.15	4.21	22.0	0.45	0.89	0.45	0.89	0.45	35	0.038
4.9	4.15	4.87	23.0	0.79	1.6	0.79	1.6	0.79	59	0.12
5.4	5.15	5.54	24.0	1.61	3.2	1.35	3.1	1.48	78	0.31
5.95	6.15	6.21	25.0	3.55	7.1	2.25	5.2	2.82	110	0.82
6.45	7.15	6.87	26.0	7.82	16	3.73	8.6	5.40	150	2.2
6.7	7.65	7.21	26.5	11.6	23	4.80	11	7.47	190	3.8
6.95	8.15	7.54	27.0	17.3	34	6.18	14	10.3	230	6.4
7.2	8.55	7.87	27.5	25.6	51	7.96	18	14.3	280	10
7.45	8.90	8.21	28.0	38.0	76	10.3	24	19.8	310	17

\* Assumes a shear-wave velocity of 3.5 km/s and a rupture velocity of 3.15 km/s.

\*\*The meaning of the symbols is:

$M_w$  moment magnitude for intraplate events (Singh and Havskov, 1980)

L fault length

W fault width

$T_{01}$  corner period between slope zero and one in Figure 1

$T_{02}$  corner period between slope zero and two in Figure 1

$T_{12}$  corner period between slope one and two in Figure 1

$\Delta\sigma$  average static stress drop

$\bar{u}$  average fault displacement on the rupture surface.

TABLE 2  
SIMILARITY CONDITIONS FOR MID-PLATE EARTHQUAKES

log $M_0$ [dyne-cm]	$t_r^{**}$ [s]	$W/L^{**}$	$\bar{u}/L^{**}$ $10^{-5}$	$v_R t_r/L^{**}$
20.0	0.03	1.00	1.4	0.34
21.0	0.06	1.00	2.4	0.38
22.0	0.10	1.00	4.3	0.35
23.0	0.19	1.00	7.5	0.37
24.0	0.37	0.97	9.7	0.36
25.0	0.71	0.73	11.5	0.32
26.0	1.38	0.54	13.8	0.27
26.5	1.87	0.48	16.5	0.26
27.0	2.56	0.41	18.8	0.24
27.5	3.55	0.35	19.6	0.22
28.0	5.01	0.32	22.4	0.21

\*\*The meaning of the symbols is:

$t_r$  Rise Time (Circular Fault, Geller, 1976)

$W/L$  Aspect Ratio (Kanamori and Anderson, 1975)

$\bar{u}/L$  Strain Drop (Kanamori and Anderson, 1975)

$v_R t_r/L^*$  Dynamic Similarity (Kanamori and Anderson, 1975)

\* Assumes a rupture velocity of 3.15 km/s.

TABLE 3

HYPOCENTERS AND FOCAL MECHANISMS  
FOR INTRA-CONTINENTAL EARTHQUAKES

No.	Region	Date D/M/Y	Time	Lat.	Long.	h [km]	T - TRD	axis PLG	P - TRD	axis PLG
1	Bolnai	09/07/05	09:40:24.0	49.00N	98.00E	15 <sup>j</sup>	143	14	237	14 <sup>j</sup>
2	Bolnai	23/07/05	02:46:24.0	49.00N	94.50E	15 <sup>j</sup>	143	14	237	14 <sup>j</sup>
3	Kebin	03/01/11	23:25:45.0	42.80N	77.30E	25 <sup>A</sup>	0	90	160	0 <sup>A</sup>
4	Haiyuan	16/12/20	12:05:48.0	36.62N	105.40E	25 <sup>A</sup>	306	59	50	8 <sup>A</sup>
5	Ku-long	22/05/27	22:32:42.0	38.05N	102.37E	25 <sup>A</sup>	316	59	60	8 <sup>A</sup>
6	Fuh-Yun	10/08/31	21:18:40.0	46.89N	90.06E	25 <sup>A</sup>	115	0	25	0 <sup>A</sup>
7	Khait	10/07/49	03:53:36.0	39.27N	70.59E	25 <sup>A</sup>	0	90	360	0 <sup>A</sup>
8	S. Tibet	18/11/51	09:35:47.0	30.98N	91.49E	25 <sup>A</sup>	233	8	129	59 <sup>A</sup>
9	Mato Grosso	31/01/55	05:03:07.0	12.42S	57.30W	33 <sup>H</sup>	342	86	142	4 <sup>H</sup>
10	Muya	27/06/57	00:09:28.0	56.20N	116.59E	25 <sup>A</sup>	173	1	82	43 <sup>A</sup>
11	Gobi-Altai	04/12/57	03:37:45.0	45.31N	99.21E	25 <sup>A</sup>	312	46	50	7 <sup>F</sup>
12	Mato Grosso	13/02/64	11:21:46.0	18.06S	56.69W	5 <sup>H</sup>	345	46	254	1 <sup>H</sup>
13	Hsingtai	07/03/66	21:29:14.0	37.35N	114.92E	10 <sup>G</sup>	343	1	73	2 <sup>G</sup>
14	Hsingtai	22/03/66	08:11:36.0	37.50N	115.08E	9 <sup>G</sup>	163	4	73	7 <sup>G</sup>
15	Hsingtai	22/03/66	08:19:46.0	37.53N	115.05E	9 <sup>G</sup>	340	4	249	20 <sup>G</sup>
16	Hsingtai	26/03/66	15:19:04.0	37.68N	115.27E	15 <sup>G</sup>	161	4	253	27 <sup>G</sup>
17	Mogod	05/01/67	00:14:40.1	48.15N	102.90E	24 <sup>I</sup>	135	0	45	0 <sup>F</sup>
18	Ganzi	30/08/67	04:22:05.1	31.60N	100.30E	8 <sup>Y</sup>	141	2	238	76 <sup>Y</sup>
19	Ganzi	30/08/67	11:08:50.1	31.70N	100.30E	10 <sup>Y</sup>	323	5	143	85 <sup>Y</sup>
20	Koyna	10/12/67	22:51:24.3	17.38N	73.75E	4 <sup>K</sup>	68	2	336	36 <sup>J</sup>
21	Acre	27/08/68	05:17:36.0	8.90S	72.89W	26 <sup>H</sup>	212	43	107	15 <sup>H</sup>
22	Meckering	14/10/68	02:58:51.8	31.54S	117.00E	3 <sup>L</sup>	121	71	273	17 <sup>L</sup>
23	Tien Shan	11/02/69	22:08:51.0	41.42N	79.24E	10 <sup>a</sup>	205	84	339	4 <sup>a</sup>
24	Bohai	18/07/69	05:24:45.0	38.43N	119.47E	10 <sup>c</sup>				
25	Ceres	29/09/69	20:02:32.1	33.16S	19.31E	11 <sup>K</sup>				
26	Tonghai	04/01/70	17:00:39.0	24.10N	102.50E	15 <sup>b</sup>	71	3	341	3 <sup>b</sup>
27	Lake McKay	24/03/70	10:35:16.9	22.08S	126.65E	8 <sup>L</sup>	345	83	78	1 <sup>L</sup>
28	Alma-ata	05/06/70	04:53:07.4	42.48N	78.71E	17 <sup>a</sup>	242	74	354	6 <sup>a</sup>
29	Tien Shan	23/03/71	20:47:16.0	41.42N	79.20E	11 <sup>a</sup>	44	87	160	1 <sup>a</sup>
30	Dzhanbul	10/05/71	14:51:45.0	42.85N	71.29E	15 <sup>a</sup>	237	66	330	2 <sup>a</sup>
31	Tien Shan	09/04/72	04:10:48.9	42.09N	84.58E	13 <sup>a</sup>	12	86	190	4 <sup>a</sup>
32	Simpson Desert	28/08/72	02:18:59.4	25.01S	136.37E	8 <sup>L</sup>	325	75	145	15 <sup>L</sup>
33	Luhuo	06/02/73	10:37:10.1	31.40N	100.60E	10 <sup>Y</sup>	170	3	260	1 <sup>Y</sup>
34	Luhuo	07/02/73	16:06:25.0	31.50N	100.30E	10 <sup>Y</sup>	300	15	120	75 <sup>Y</sup>
35	Tien Shan	02/06/73	23:57:02.4	44.14N	83.60E	26 <sup>a</sup>	162	60	27	22 <sup>a</sup>
36	Yunnan	10/05/74	19:25:17.0	28.19N	103.98E	17 <sup>c</sup>				
37	Markansu	11/08/74	01:13:55.0	39.38N	73.81E	23 <sup>X</sup>	84	0	174	0 <sup>X</sup>
38	Colombia	27/09/74	04:09:02.0	2.72N	71.37W	6 <sup>H</sup>	195	2	285	5 <sup>H</sup>
39	Haicheng	04/02/75	11:36:07.5	40.65N	122.80E	12 <sup>N</sup>	336	4	244	21 <sup>N</sup>
40	Gazli	08/04/76	02:40:25.0	40.36N	63.73E	10 <sup>O</sup>	265	82	14	3 <sup>T</sup>
41	Gazli	17/05/76	02:58:40.0	40.37N	63.44E	13 <sup>V</sup>	257	75	124	10 <sup>T</sup>
42	Lung Ling	29/05/76	12:23:18.4	24.51N	98.95E	3 <sup>I</sup>	66	7	335	13 <sup>d</sup>
43	Lung Ling	29/05/76	14:00:19.4	24.54N	98.60E	4 <sup>I</sup>	215	51	321	13 <sup>d</sup>
44	Tangshan	27/07/76	19:42:54.6	39.60N	118.00E	16 <sup>V</sup>	170	16	260	2 <sup>Z</sup>
45	Luanxian	28/07/76	10:45:37.2	39.71N	118.37E	16 <sup>V</sup>	356	5	120	82 <sup>Z</sup>

46	Isfara	31/01/77	14:26:15.1	40.11N	70.86E	12 <sup>a</sup>	116	82	344	6 <sup>a</sup>
47	Gazli	04/06/78	19:30:20.4	40.41N	63.60E	9 <sup>Q</sup>	103	81	343	5 <sup>Q</sup>
48	Tien Shan	29/03/79	02:01:32.1	41.95N	83.38E	13 <sup>a</sup>	318	82	164	8 <sup>a</sup>
49	Cadoux	02/06/79	09:47:58.7	30.73S	117.21E	3 <sup>L</sup>	233	78	75	11 <sup>L</sup>
50	W. Amazon	06/03/80	09:46:18.0	6.17S	71.16W	18 <sup>H</sup>	182	85	40	4 <sup>H</sup>
51	El Asnam	10/10/80	12:25:25.1	36.17N	1.41E	14 <sup>f</sup>	107	80	320	9 <sup>B</sup>
52	S. Para	12/11/80	21:23:05.0	8.07S	50.24W	33 <sup>H</sup>	197	10	93	55 <sup>H</sup>
53	Ceara	20/11/80	03:29:42.0	4.30S	38.40W	5 <sup>H</sup>	199	0	109	3 <sup>H</sup>
54	Daofu	23/01/81	21:13:51.7	30.93N	101.10E	8 <sup>Y</sup>	6	0	96	0 <sup>Y</sup>
55	Paraguay	08/04/82	05:58:52.0	24.80S	58.10W	12 <sup>H</sup>	351	1	81	3 <sup>H</sup>
56	Sokh	06/05/82	15:42:22.2	40.15N	71.54E	20 <sup>a</sup>	139	80	337	9 <sup>a</sup>
57	Codajas	05/08/83	06:21:42.0	3.59S	62.17W	23 <sup>H</sup>	264	62	14	10 <sup>H</sup>
58	Guinea	22/12/83	04:11:29.2	11.87N	13.53W	11 <sup>e</sup>	34	2	125	35 <sup>i</sup>
59	Gazli	19/03/84	20:28:38.3	40.30N	63.30E	9 <sup>Q</sup>	346	83	125	5 <sup>Q</sup>
60	Marryat Creek	30/03/86	08:53:52.0	26.30S	132.77E	2 <sup>L</sup>	275	78	66	10 <sup>L</sup>
61	Tennant Creek	22/01/88	00:35:58.0	19.85S	133.80E	5 <sup>P</sup>	177	73	20	16 <sup>i</sup>
62	Tennant Creek	22/01/88	03:57:25.2	19.80S	133.91E	5 <sup>P</sup>	199	67	360	22 <sup>i</sup>
63	Tennant Creek	22/01/88	12:04:57.8	19.83S	133.88E	5 <sup>P</sup>	177	73	20	16 <sup>i</sup>

References : A Chen and Molnar (1977); B Singh and Havskov (1980); C Deng *et al.* (1984); D Deng *et al.* (1986); E Zhang *et al.* (1987); F Okal (1976); G Chung and Cipar (1983); H Assumpcao and Suarez (1988); I ISC; J Langston (1976); K Somerville *et al.* (1987); L Fredrich *et al.* (1988); M Vogfjörd and Langston (1987); N Cipar (1979); P PDE; Q Eyidogan *et al.* (1985); R Hartzell (1980); T Kristy *et al.* (1980); U Liu and Kanamori (1980); V Butler *et al.* (1979); W Kanamori and Allen (1986); X Jackson *et al.* (1979); Y Zhou *et al.* (1983b); Z Nabelek *et al.* (1987); a Nelson *et al.* (1987); b Zhou *et al.* (1983a); c Purcaru and Berckhemer (1982); d Okal and Stewart (1981); e Langer *et al.* (1987); f Cirtemas *et al.* (1982); g Deschamps *et al.* (1982); h Ouyed *et al.* (1981); i Chung *et al.* (1988); j Okal (1977).

TABLE 4  
SOURCE PARAMETERS FOR INTRA-CONTINENTAL EARTHQUAKES

No.	Date D/M/Y	$m_b$	$M_s$	$\log M_0$ [dyne-cm]	$\tau$ [sec]	L [km]	W* [km]	$\bar{u}$ [m]	$\Delta\sigma$ [bar]
1	09/07/05		7.90 <sup>j</sup>	28.74 <sup>j</sup>		200 <sup>j</sup>	50 <sup>c</sup>	14.0 <sup>c</sup>	65 <sup>c</sup>
2	23/07/05		8.25 <sup>j</sup>	28.70 <sup>j</sup>		300 <sup>j</sup>	50 <sup>c</sup>	8.2 <sup>c</sup>	37 <sup>c</sup>
3	03/01/11		8.40 <sup>B</sup>	27.69 <sup>A</sup>		180 <sup>A</sup>	40 <sup>A</sup>	2.3 <sup>A</sup>	
4	16/12/20		8.50 <sup>B</sup>	28.08 <sup>C</sup>		220 <sup>D</sup>	20 <sup>C</sup>	8.0 <sup>E</sup>	55 <sup>c</sup>
5	22/05/27		7.90 <sup>B</sup>	27.63 <sup>A</sup>		150 <sup>A</sup>	40 <sup>A</sup>	2.4 <sup>A</sup>	31 <sup>c</sup>
6	10/08/31		7.90 <sup>B</sup>	27.93 <sup>A</sup>		300 <sup>A</sup>	50 <sup>A</sup>	1.9 <sup>A</sup>	30 <sup>c</sup>
7	10/07/49		7.60 <sup>B</sup>	27.38 <sup>A</sup>		70 <sup>A</sup>	30 <sup>A</sup>	3.7 <sup>A</sup>	33 <sup>c</sup>
8	18/11/51			27.66 <sup>A</sup>		200 <sup>A</sup>			
9	31/01/55	6.20 <sup>H</sup>	5.50 <sup>H</sup>						
10	27/06/57		7.90 <sup>B</sup>	27.15 <sup>A</sup>		35 <sup>A</sup>	30 <sup>A</sup>	4.5 <sup>A</sup>	76 <sup>c</sup>
11	04/12/57		8.10 <sup>B</sup>	28.11 <sup>A</sup>		270 <sup>A</sup>	50 <sup>A</sup>	3.2 <sup>A</sup>	26 <sup>F</sup>
12	13/02/64	5.40 <sup>H</sup>	4.50 <sup>H</sup>						
13	07/03/66	5.60 <sup>G</sup>	6.80 <sup>G</sup>	26.00 <sup>G</sup>	5.0 <sup>G</sup>	14 <sup>G</sup>		1.6 <sup>G</sup>	112 <sup>G</sup>
14	22/03/66	5.60 <sup>G</sup>	6.70 <sup>G</sup>	25.48 <sup>G</sup>	4.5 <sup>G</sup>	13 <sup>G</sup>		0.7 <sup>G</sup>	53 <sup>G</sup>
15	22/03/66	5.90 <sup>G</sup>	7.20 <sup>G</sup>	26.25 <sup>G</sup>	5.0 <sup>G</sup>	14 <sup>G</sup>		2.9 <sup>G</sup>	194 <sup>G</sup>
16	26/03/66	5.20 <sup>G</sup>	6.20 <sup>G</sup>	25.15 <sup>G</sup>	3.5 <sup>G</sup>	10 <sup>G</sup>		0.6 <sup>G</sup>	53 <sup>G</sup>
17	05/01/67	6.10 <sup>I</sup>	7.40 <sup>B</sup>	26.58 <sup>A</sup>		40 <sup>A</sup>	30 <sup>A</sup>	1.0 <sup>A</sup>	24 <sup>c</sup>
18	30/08/67	6.10 <sup>I</sup>	6.10 <sup>Y</sup>	25.65 <sup>Y</sup>	2.5 <sup>Y</sup>	9 <sup>Y</sup>		1.5 <sup>Y</sup>	35 <sup>Y</sup>
19	30/08/67	5.20 <sup>I</sup>	5.10 <sup>Y</sup>	24.34 <sup>Y</sup>	2.5 <sup>Y</sup>				
20	10/12/67	5.90 <sup>I</sup>	6.50 <sup>I</sup>	25.51 <sup>J</sup>	6.4 <sup>K</sup>	32 <sup>c</sup>	11 <sup>c</sup>	0.6 <sup>c</sup>	20 <sup>K</sup>
21	27/08/68	4.90 <sup>H</sup>	3.90 <sup>H</sup>						
22	14/10/68	5.90 <sup>I</sup>	6.80 <sup>I</sup>	26.02 <sup>L</sup>	5.4 <sup>L</sup>	37 <sup>L</sup>	10 <sup>M</sup>	2.0 <sup>L</sup>	100 <sup>M</sup>
23	11/02/69	5.80 <sup>I</sup>	6.60 <sup>I</sup>	25.30 <sup>a</sup>	6.9 <sup>a</sup>				
24	18/07/69	6.20 <sup>I</sup>	7.30 <sup>c</sup>	26.90 <sup>c</sup>		45 <sup>c</sup>	25 <sup>c</sup>	2.2 <sup>c</sup>	
25	29/09/69	5.60 <sup>I</sup>	6.30 <sup>I</sup>	25.65 <sup>K</sup>	5.0 <sup>K</sup>				70 <sup>K</sup>
26	04/01/70	5.90 <sup>c</sup>	7.50 <sup>b</sup>	26.94 <sup>b</sup>	50.0 <sup>b</sup>	90 <sup>b</sup>	15 <sup>b</sup>	2.1 <sup>b</sup>	27 <sup>b</sup>
27	24/03/70	6.20 <sup>I</sup>	5.90 <sup>I</sup>	25.07 <sup>L</sup>	2.5 <sup>K</sup>	6 <sup>U</sup>			175 <sup>U</sup>
28	05/06/70	5.90 <sup>I</sup>	6.60 <sup>I</sup>	25.49 <sup>a</sup>	3.8 <sup>a</sup>				
29	23/03/71	5.80 <sup>I</sup>	5.80 <sup>I</sup>	24.77 <sup>a</sup>	7.0 <sup>a</sup>				
30	10/05/71	5.60 <sup>I</sup>	5.40 <sup>I</sup>	24.11 <sup>a</sup>	1.3 <sup>a</sup>				
31	09/04/72	5.80 <sup>I</sup>	5.30 <sup>I</sup>	24.11 <sup>a</sup>	1.0 <sup>a</sup>				
32	28/08/72	5.60 <sup>I</sup>		24.00 <sup>L</sup>	1.8 <sup>L</sup>				
33	06/02/73	6.10 <sup>P</sup>	7.50 <sup>Y</sup>	27.26 <sup>Y</sup>	32.0 <sup>Y</sup>	90 <sup>Y</sup>	15 <sup>Y</sup>	3.8 <sup>Y</sup>	50 <sup>Y</sup>
34	07/02/73	5.80 <sup>P</sup>	5.90 <sup>Y</sup>	24.77 <sup>Y</sup>	2.5 <sup>Y</sup>				
35	02/06/73	5.70 <sup>I</sup>	5.60 <sup>I</sup>	24.32 <sup>a</sup>	0.8 <sup>a</sup>				
36	10/05/74	5.80 <sup>I</sup>	6.80 <sup>I</sup>	25.81 <sup>c</sup>		45 <sup>c</sup>	20 <sup>c</sup>	0.2 <sup>c</sup>	6 <sup>c</sup>
37	11/08/74	6.40 <sup>X</sup>	7.30 <sup>X</sup>	26.70 <sup>X</sup>		30 <sup>X</sup>	20 <sup>X</sup>	2.5 <sup>X</sup>	21 <sup>X</sup>
38	27/09/74	5.50 <sup>H</sup>	5.80 <sup>P</sup>						
39	04/02/75	6.40 <sup>N</sup>	7.40 <sup>N</sup>	26.48 <sup>N</sup>	7.0 <sup>N</sup>	22 <sup>N</sup>	12 <sup>N</sup>	2.8 <sup>N</sup>	53 <sup>N</sup>
40	08/04/76	6.20 <sup>R</sup>	7.00 <sup>R</sup>	26.32 <sup>Q</sup>	5.0 <sup>K</sup>	30 <sup>c</sup>	15 <sup>c</sup>		400 <sup>K</sup>
41	17/05/76	6.20 <sup>R</sup>	7.00 <sup>R</sup>	26.30 <sup>Q</sup>	7.8 <sup>R</sup>	15 <sup>R</sup>	10 <sup>R</sup>	3.3 <sup>R</sup>	200 <sup>R</sup>
42	29/05/76	5.90 <sup>I</sup>	6.90 <sup>I</sup>	25.70 <sup>c</sup>		35 <sup>c</sup>	20 <sup>c</sup>		
43	29/05/76	5.70 <sup>I</sup>	7.00 <sup>I</sup>	25.98 <sup>c</sup>		45 <sup>c</sup>	20 <sup>c</sup>		
44	27/07/76	6.30 <sup>V</sup>	7.70 <sup>V</sup>	27.26 <sup>V</sup>	25.0 <sup>Z</sup>	80 <sup>W</sup>	15 <sup>W</sup>		100 <sup>K</sup>
45	28/07/76	6.10 <sup>I</sup>	7.20 <sup>V</sup>	26.90 <sup>V</sup>	10.0 <sup>Z</sup>	35 <sup>V</sup>	15 <sup>V</sup>		40 <sup>c</sup>
46	31/01/77	6.00 <sup>I</sup>	5.90 <sup>I</sup>	24.72 <sup>a</sup>	1.0 <sup>a</sup>				

47	04/06/78	5.90 <sup>Q</sup>	5.70 <sup>Q</sup>		0.2 <sup>Q</sup>				
48	29/03/79	5.80 <sup>I</sup>	5.80 <sup>I</sup>	24.36 <sup>a</sup>	1.3 <sup>a</sup>				
49	02/06/79	5.90 <sup>I</sup>	6.00 <sup>I</sup>	25.17 <sup>L</sup>	6.4 <sup>L</sup>	15 <sup>L</sup>	6 <sup>L</sup>	1.5 <sup>L</sup>	200 <sup>K</sup>
50	06/03/80	4.80 <sup>H</sup>	3.60 <sup>H</sup>						
51	10/10/80	6.50 <sup>f</sup>	7.30 <sup>f</sup>	26.70 <sup>B</sup>	12.0 <sup>h</sup>	36 <sup>B</sup>	10 <sup>B</sup>	4.0 <sup>B</sup>	110 <sup>B</sup>
52	12/11/80	4.70 <sup>H</sup>	3.30 <sup>H</sup>						
53	20/11/80	5.20 <sup>H</sup>	4.40 <sup>H</sup>	23.85 <sup>H</sup>	1.1 <sup>H</sup>	3 <sup>H</sup>			90 <sup>H</sup>
54	23/01/81	5.70 <sup>J</sup>	6.80 <sup>Y</sup>	26.11 <sup>Y</sup>	12.0 <sup>Y</sup>	44 <sup>Y</sup>	10 <sup>Y</sup>	1.0 <sup>Y</sup>	20 <sup>Y</sup>
55	08/04/82	4.90 <sup>H</sup>	4.00 <sup>H</sup>						
56	06/05/82	5.50 <sup>I</sup>	5.70 <sup>I</sup>	24.30 <sup>a</sup>	3.6 <sup>a</sup>				
57	05/08/83	5.50 <sup>H</sup>	4.50 <sup>H</sup>	24.00 <sup>H</sup>	1.0 <sup>H</sup>	3 <sup>H</sup>			100 <sup>H</sup>
58	22/12/83	6.40 <sup>e</sup>	6.20 <sup>e</sup>	25.32 <sup>K</sup>	5.0 <sup>K</sup>	9 <sup>e</sup>		0.1 <sup>e</sup>	30 <sup>K</sup>
59	19/03/84	6.50 <sup>Q</sup>	7.00 <sup>Q</sup>	26.40 <sup>Q</sup>	12.0 <sup>Q</sup>				30 <sup>K</sup>
60	30/03/86	5.70 <sup>I</sup>	5.80 <sup>I</sup>	24.76 <sup>L</sup>	4.0 <sup>L</sup>	13 <sup>L</sup>	3 <sup>L</sup>	0.3 <sup>L</sup>	
61	22/01/88	6.10 <sup>P</sup>	6.30 <sup>P</sup>	25.21 <sup>i</sup>		12 <sup>i</sup>			
62	22/01/88	6.10 <sup>P</sup>	6.40 <sup>P</sup>	25.43 <sup>i</sup>		9 <sup>i</sup>			
63	22/01/88	6.50 <sup>P</sup>	6.70 <sup>P</sup>	25.90 <sup>i</sup>		14 <sup>i</sup>			

\* estimated. References : A Chen and Molnar (1977); B Singh and Havskov (1980); C Deng *et al.* (1984); D Deng *et al.* (1986); E Zhang *et al.* (1987); F Okal (1976); G Chung and Cipar (1983); H Assumpcao and Suarez (1988); I ISC; J Langston (1976); K Somerville *et al.* (1987); L Fredrich *et al.* (1988); M Vogfjörd and Langston (1987); N Cipar (1979); P PDE; Q Eyidogan *et al.* (1985); R Hartzell (1980); T Kristy *et al.* (1980); U Liu and Kanamori (1980); V Butler *et al.* (1979); W Kanamori and Allen (1986); X Jackson *et al.* (1979); Y Zhou *et al.* (1983b); Z Nabelek *et al.* (1987); a Nelson *et al.* (1987); b Zhou *et al.* (1983a); c Purcaru and Berckhemer (1982); d Okal and Stewart (1981); e Langer *et al.* (1987); f Cisternas *et al.* (1982); g Deschamps *et al.* (1982); h Ouyed *et al.* (1981); i Chung *et al.* (1988); j Okal (1977).



TABLE 5

AVERAGE SOURCE PARAMETERS FOR INTRA-CONTINENTAL  
EARTHQUAKES ASSUMING CONSTANT STRESS DROP SCALING\*

$m_b$	$M_s$	$M_w$	$\log M_0$ [dyne-cm]	$T_{01}$ [s]	L [km]	$T_{12}$ [s]	W [km]	$T_{02}$ [s]	$\bar{u}$ [m]	$m_{Lg}^{(1)}$	$m_{Lg}^{(2)}$	$m_b^{(3)}$	$\bar{m}_b$
5.3	4.40	4.87	23.0	0.62	1.3	0.62	1.3	0.62	0.11	5.32	5.28±0.25	5.1±0.4	5.1±0.4
5.6	5.19	5.54	24.0	1.66	3.3	1.24	2.9	1.36	0.23	5.93	5.87±0.33	5.5±0.4	5.8±0.3
5.8	5.98	6.21	25.0	4.42	8.8	2.47	5.7	2.92	0.49	6.41	6.31±0.32	5.9±0.4	6.4±0.3
6.0	6.78	6.87	26.0	11.7	23	4.90	11	6.30	1.1	6.78	6.71±0.24	6.2±0.4	6.7±0.3
6.1	7.17	7.21	26.5	19.2	38	6.90	16	9.24	1.6	6.93	6.97±0.26	6.3±0.2	6.7±0.3
6.2	7.57	7.54	27.0	31.3	62	9.72	22	13.6	2.3	7.09	7.28±0.23	6.3±0.3	6.9±0.3
6.3	7.97	7.87	27.5	51.0	101	13.7	32	19.9	3.4	7.22	7.53±0.24	6.4±0.3	7.2±0.4
6.5	8.37	8.21	28.0	83.2	166	19.3	45	29.2	4.9	7.35	7.76±0.27	6.6±0.4	7.5±0.3

\* Assumes a shear-wave velocity of 3.5 km/s, a rupture velocity of 3.15 km/s, and a constant stress drop of 45 bar.

The meaning of the symbols is:

$m_b$  body-wave magnitude from (22a)

$M_s$  surface-wave magnitude from (25)

$M_w$  moment magnitude for intraplate events (Singh and Havskov, 1980) from (21)

L fault length from (40)

W fault width from (17) and (43)

$T_{01}$  corner period between slope zero and one in Figure 1 from (41)

$T_{02}$  corner period between slope zero and two in Figure 1 from (36)

$T_{12}$  corner period between slope one and two in Figure 1 from (43)

$\bar{u}$  average fault displacement on the rupture surface from (29).

$m_{Lg}^{(1)}$  Lg-wave magnitude from random process theory (Herrmann, 1987; Herrmann and Kijko, 1983)

$m_{Lg}^{(2)}$  Lg-wave magnitude from numerical modeling using a finite source (average of SS and 45° DS faults; Herrmann and Kijko, 1983)

$m_b^{(3)}$  body-wave magnitude from numerical modeling using a finite source (average of SS and 45° DS faults)

$\bar{m}_b$  maximum  $m_b$  (Houston and Kanamori, 1986) from numerical modeling using a finite source (average of SS and 45° DS faults)

TABLE 6  
 AVERAGE SOURCE PARAMETERS FOR INTRA-CONTINENTAL  
 EARTHQUAKES ASSUMING INCREASING STRESS DROP SCALING\*

$m_b$	$M_S$	$M_W$	$\log M_0$ [dyne-cm]	$T_{01}$ [s]	L [km]	$T_{12}$ [s]	W [km]	$T_{02}$ [s]	$\Delta\sigma$ [bar]	$\bar{u}$ [m]	$m_{Lg}^{(1)}$	$m_{Lg}^{(2)}$	$m_b^{(3)}$	$\hat{m}_b$
5.3	4.40	4.87	23.0	0.78	1.5	0.78	1.5	0.78	19	0.06	5.22	5.21±0.25	5.0±0.4	5.1±0.4
5.6	5.19	5.54	24.0	1.66	3.3	1.50	3.3	1.55	24	0.15	5.85	5.80±0.34	5.5±0.4	5.7±0.3
5.8	5.98	6.21	25.0	4.42	8.8	2.56	5.9	3.09	30	0.38	6.37	6.16±0.33	5.7±0.4	6.3±0.3
6.0	6.78	6.87	26.0	11.7	23	4.39	10	6.17	38	0.97	6.80	6.75±0.29	6.0±0.3	6.6±0.3
6.1	7.17	7.21	26.5	19.2	38	5.73	13	8.71	42	1.5	6.99	6.99±0.26	6.1±0.2	6.7±0.2
6.2	7.57	7.54	27.0	31.3	62	7.50	17	12.3	47	2.4	7.18	7.31±0.28	6.3±0.3	6.9±0.3
6.3	7.97	7.87	27.5	51.0	101	9.81	23	17.4	53	3.8	7.35	7.55±0.27	6.4±0.3	7.2±0.3
6.5	8.37	8.21	28.0	83.2	166	12.8	30	24.5	60	6.1	7.52	7.88±0.25	6.6±0.3	7.5±0.3

\* Assumes a shear-wave velocity of 3.5 km/s, a rupture velocity of 3.15 km/s, and a variable stress drop (33).

The meaning of the symbols is:

- $m_b$  body-wave magnitude from (22a)
- $M_S$  surface-wave magnitude from (25)
- $M_W$  moment magnitude for intraplate events (Singh and Havskov, 1980) from (21)
- L fault length from (40)
- W fault width from (17)
- $T_{01}$  corner period between slope zero and one in Figure 1 from (41)
- $T_{02}$  corner period between slope zero and two in Figure 1 from (37)
- $T_{12}$  corner period between slope one and two in Figure 1
- $\Delta\sigma$  average static stress drop from (33)
- $\bar{u}$  average fault displacement on the rupture surface from (31).
- $m_{Lg}^{(1)}$  Lg-wave magnitude from random process theory (Herrmann, 1987; Herrmann and Kijko, 1983)
- $m_{Lg}^{(2)}$  Lg-wave magnitude from numerical modeling using a finite source (average of SS and 45° DS faults; Herrmann and Kijko, 1983)
- $m_b^{(3)}$  body-wave magnitude from numerical modeling using a finite source (average of SS and 45° DS faults)
- $\hat{m}_b$  maximum  $m_b$  (Houston and Kanamori, 1986) from numerical modeling using a finite source (average of SS and 45° DS faults)

TABLE 7  
SIMILARITY CONDITIONS FOR INTRA-CONTINENTAL EARTHQUAKES

a) Constant Stress Drop

$\log M_0$ [dyne-cm]	$t_r^{**}$ [s]	$W/L^{**}$	$\bar{u}/L^{**}$ $10^{-5}$	$v_R t_r/L^{**}$
23.0	0.21	1.00	8.5	0.51
24.0	0.45	0.88	7.0	0.43
25.0	0.97	0.65	5.6	0.35
26.0	2.08	0.48	4.8	0.28
26.5	3.06	0.42	4.2	0.25
27.0	4.49	0.35	3.7	0.23
27.5	6.59	0.32	3.4	0.21
28.0	9.68	0.27	3.0	0.18

b) Increasing Stress Drop

$\log M_0$ [dyne-cm]	$t_r^{**}$ [s]	$W/L^{**}$	$\bar{u}/L^{**}$ $10^{-5}$	$v_R t_r/L^{**}$
23.0	0.28	1.00	4.0	0.59
24.0	0.55	1.00	4.5	0.53
25.0	1.10	0.67	4.3	0.39
26.0	2.19	0.43	4.2	0.30
26.5	3.09	0.34	3.9	0.26
27.0	4.36	0.27	3.9	0.22
27.5	6.16	0.23	3.8	0.19
28.0	8.70	0.18	3.7	0.17

\*\*The meaning of the symbols is:

- $t_r$             Rise Time (Circular Fault, Geller, 1976)
- $W/L$          Aspect Ratio (Kanamori and Anderson, 1975)
- $\bar{u}/L$          Strain Drop (Kanamori and Anderson, 1975)
- $v_R t_r/L^*$     Dynamic Similarity (Kanamori and Anderson, 1975)

\* Assumes a rupture velocity of 3.15 km/s.

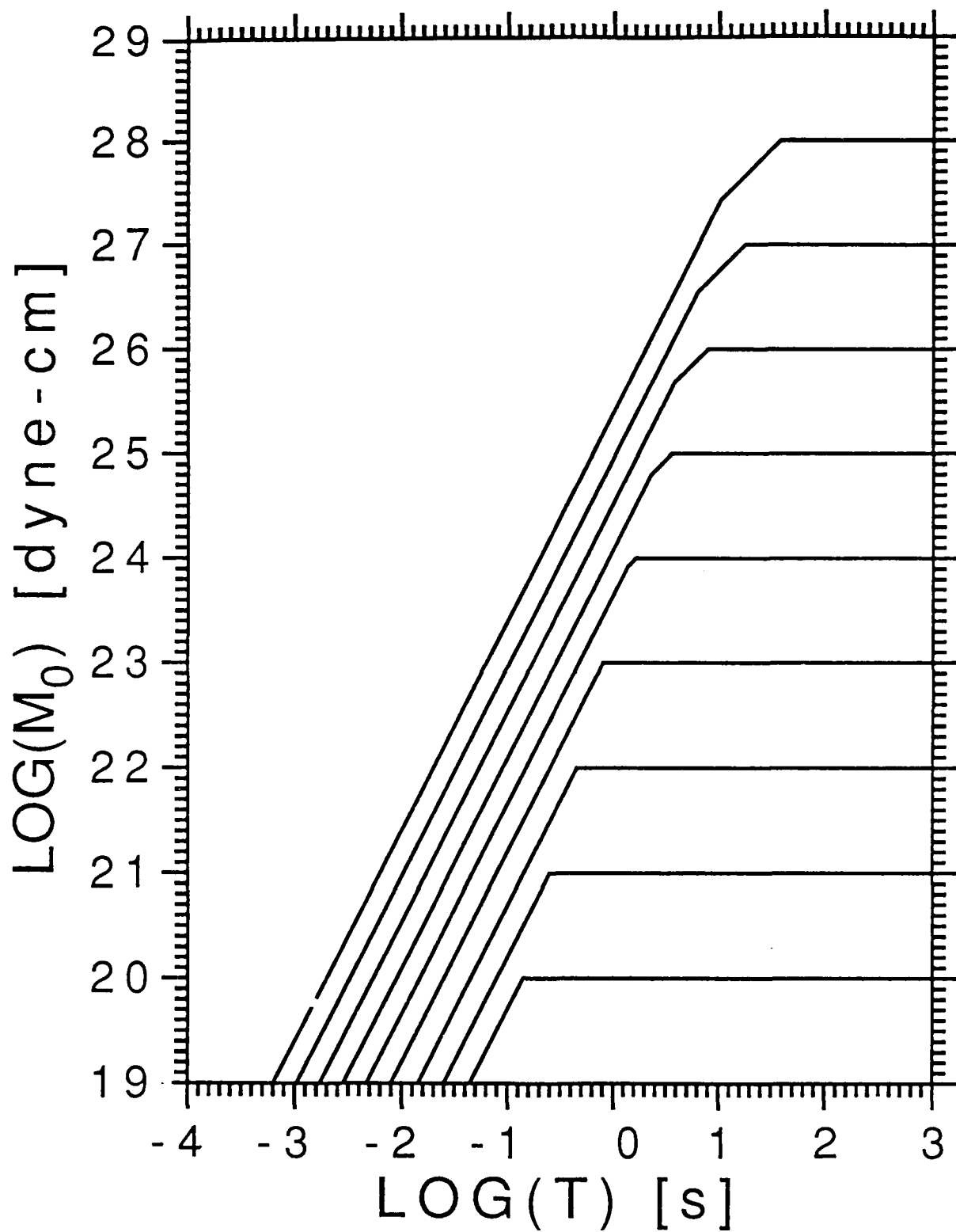


Figure 1. Reduced far-field displacement spectra for central and eastern North American earthquakes defining the revised mid-plate scaling relation by Nuttli *et al.* (1989).

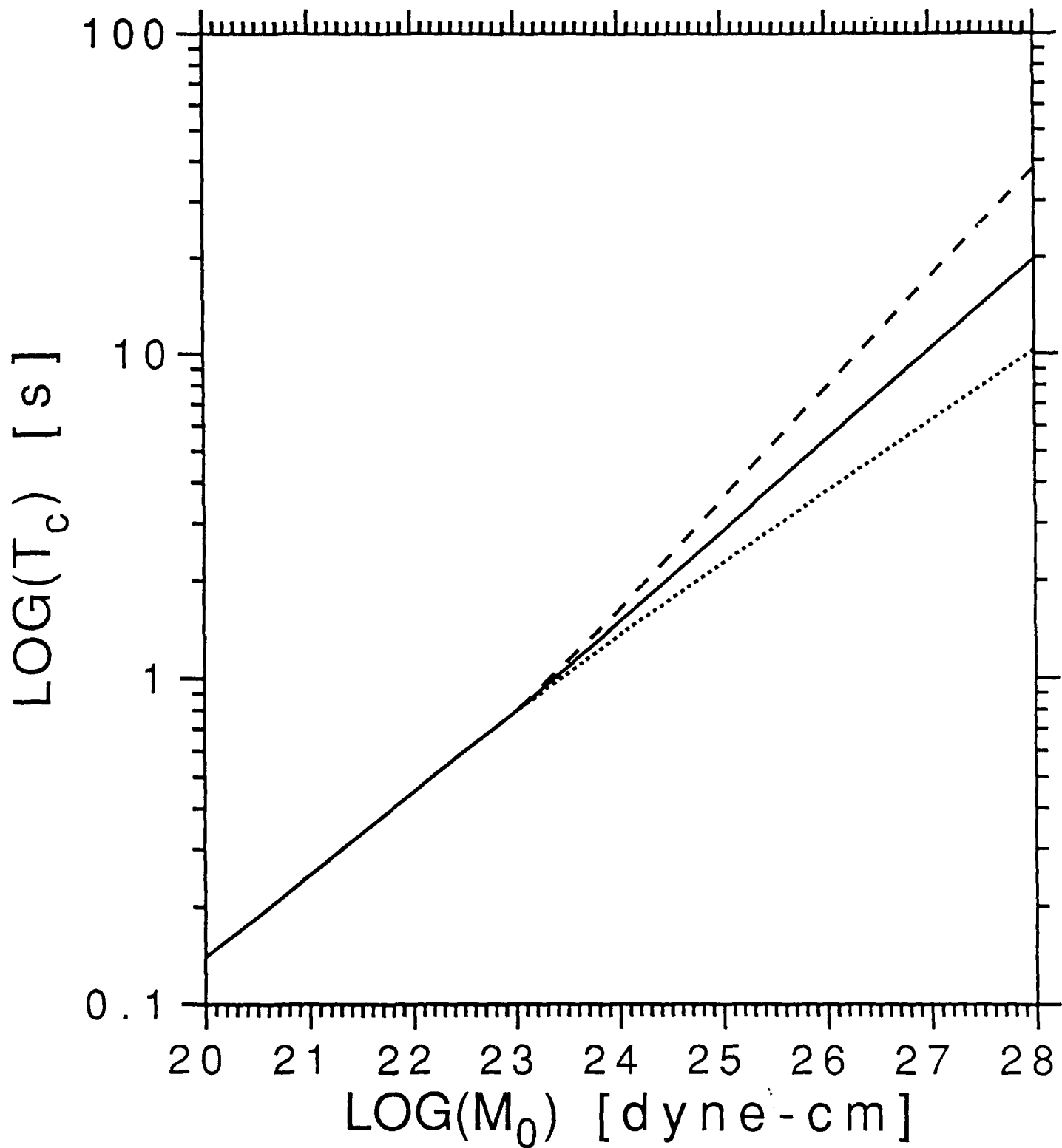


Figure 2. Relation between the logarithm of seismic moment,  $M_0$ , and corner periods,  $T_c$ , of the revised mid-plate scaling relation by Nuttli *et al.* (1989). The solid line is for the corner period  $T_{02}$  (equations 1a, 3a, 6a), long dashes are for  $T_{01}$  (equations 1a, 2, 5), and short dashes are for  $T_{12}$  (equations 1a, 4, 7), where the indices refer to the slopes of the reduced far-field displacement spectra (Figure 1).

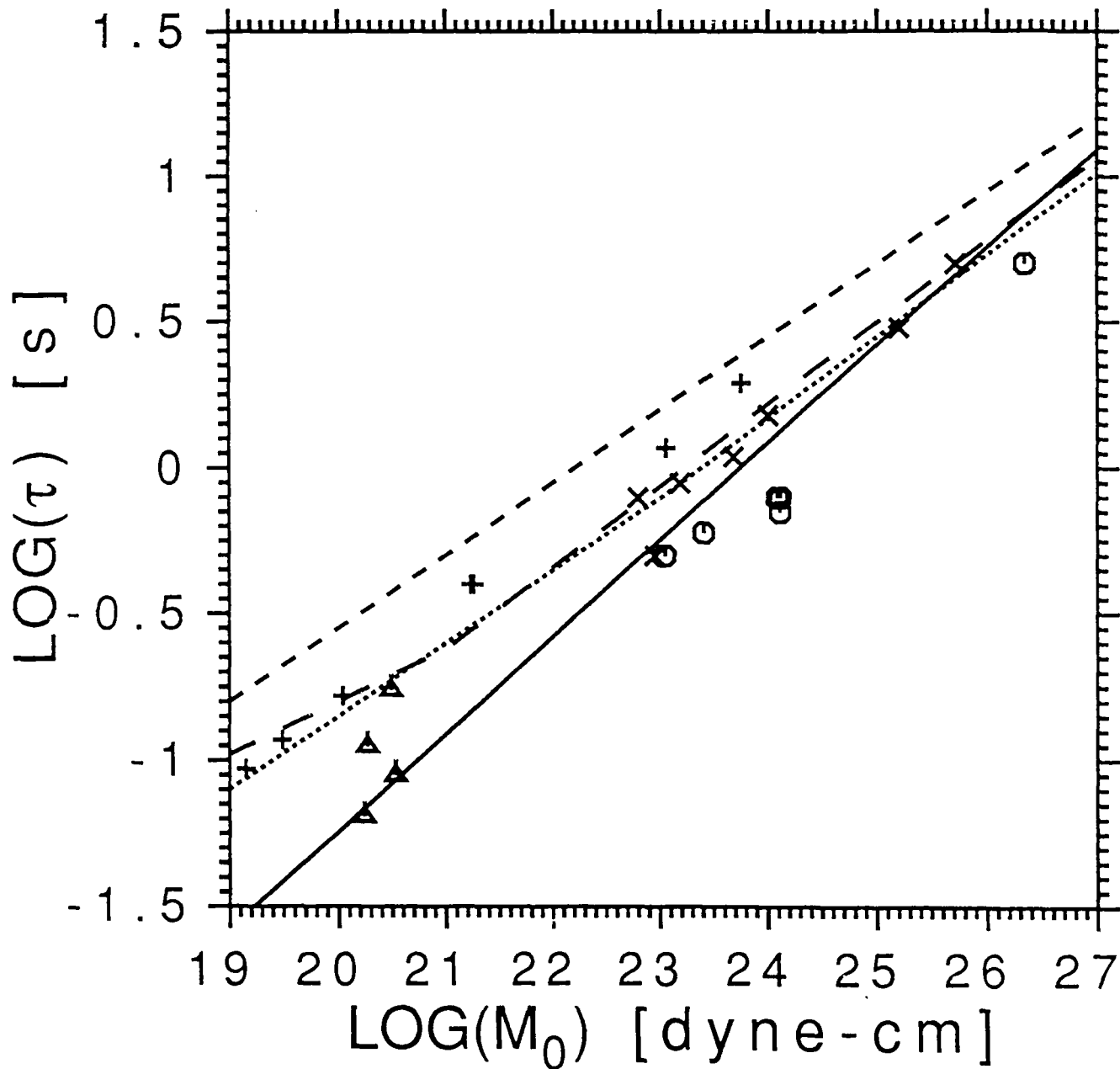


Figure 3. Source duration versus seismic moment for eastern North American earthquakes. Data are from Somerville *et al.* (1987, circles for events with stress drops larger or equal 200 bar, x's for events with stress drops smaller than 200 bar), Fletcher (1982, triangles), and Shin and Herrmann (1987, crosses). Included are the relations by Hasegawa (1983, long dashes), Nuttli (1983, intermediate dashes), Somerville *et al.* (1987, solid line), and Nuttli *et al.* (1989, short dashes).

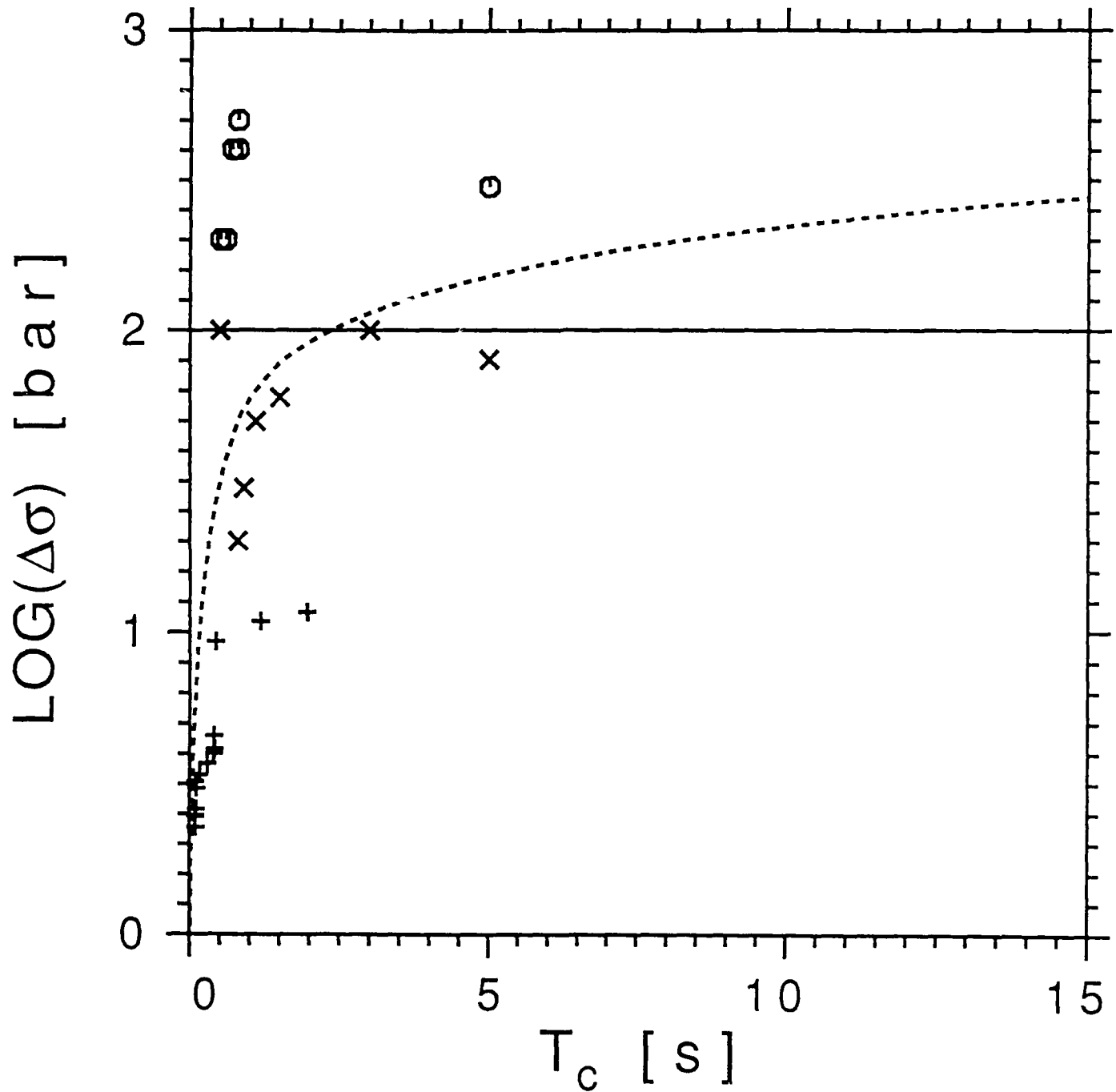


Figure 4. Static stress drop versus source duration (i.e. corner period  $T_{02}$ ) for eastern North American earthquakes. Data are from Somerville *et al.* (1987, circles for events with stress drops larger or equal 200 bar, x's for events with stress drops smaller than 200 bar), and Shin and Herrmann (1987, crosses). Included are the relations by Somerville *et al.* (1987, solid line) and Nuttli *et al.* (1989, dashes).

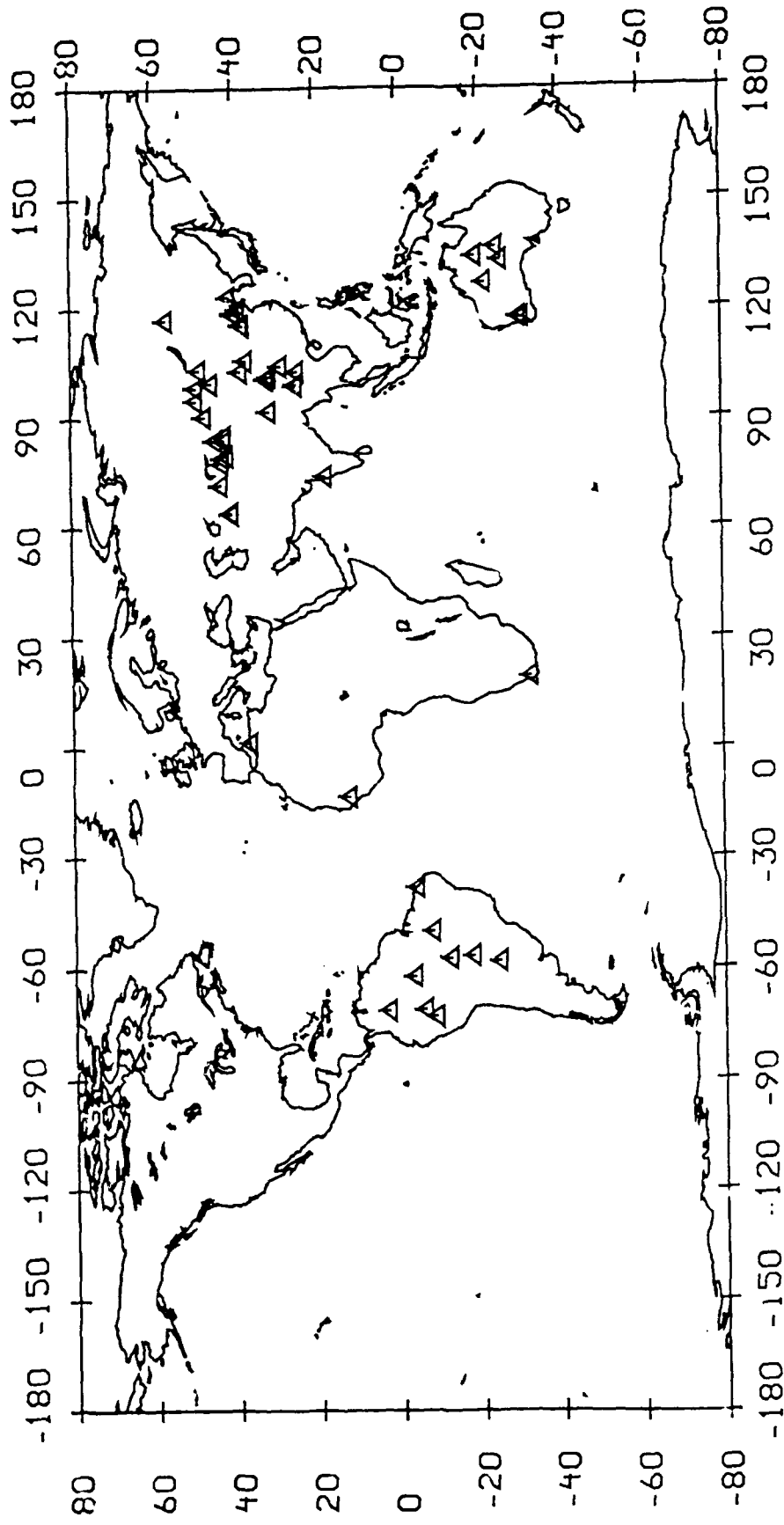


Figure 5. Epicenters of the intra-continental earthquakes used in this study (Tables 3 and 4).



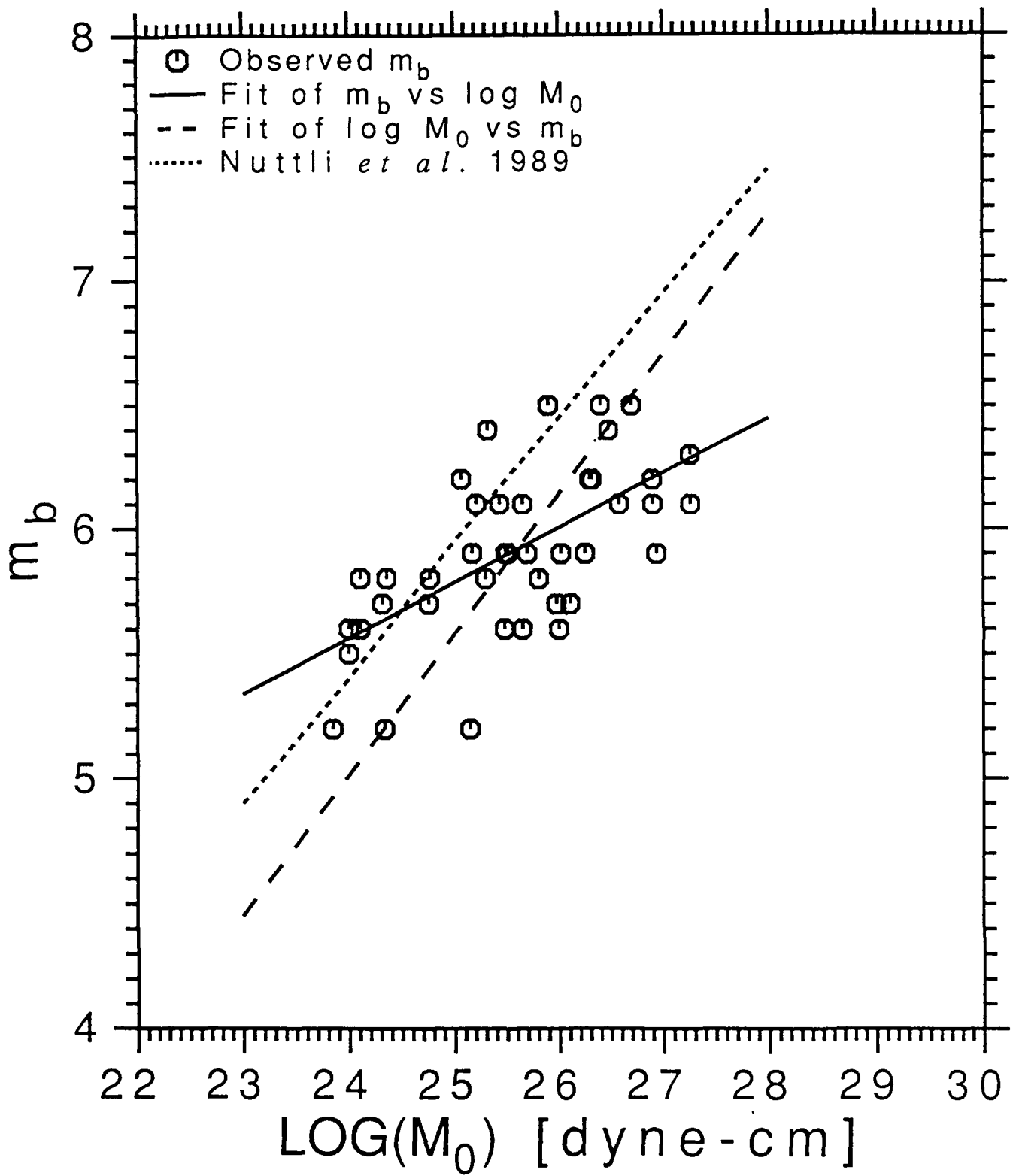


Figure 6. Observed P-wave magnitudes,  $m_b$ , versus seismic moment from Table 4. The solid line is for the regression of  $m_b$  versus  $\log M_0$ , (22a), the long dashes for the regression of  $\log M_0$  versus  $m_b$ , (22b). Short dashes are from the revised mid-plate scaling relation by Nuttli *et al.* (1989), (23).

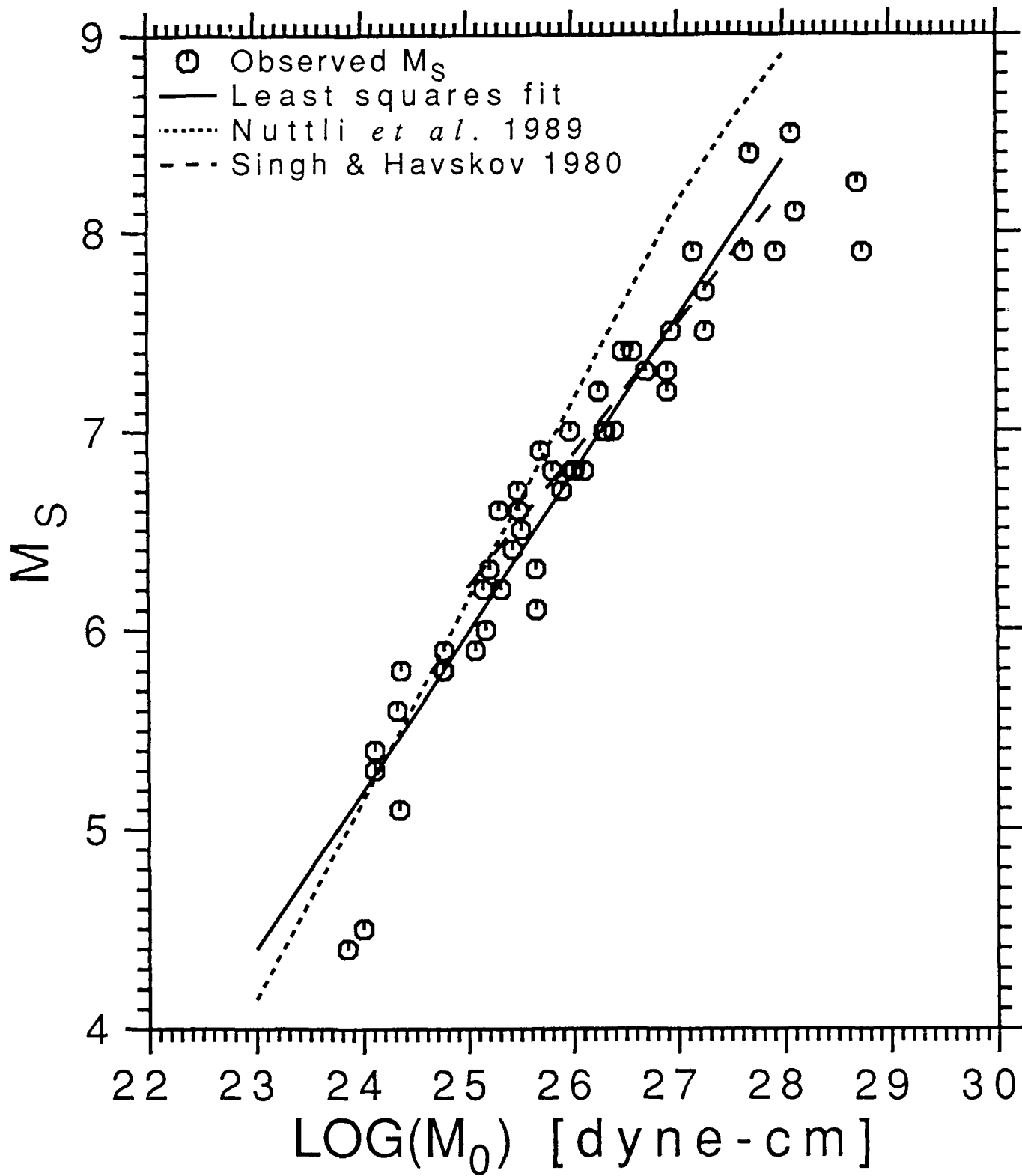


Figure 7. Observed surface-wave magnitudes,  $M_S$ , versus seismic moment from Table 4. The solid line is from the least-squares fit, (25), short dashes are from the revised mid-plate scaling relation by Nuttli *et al.* (1989), (13), and long dashes are for  $M_W$  (Singh and Havskov, 1980), (21).

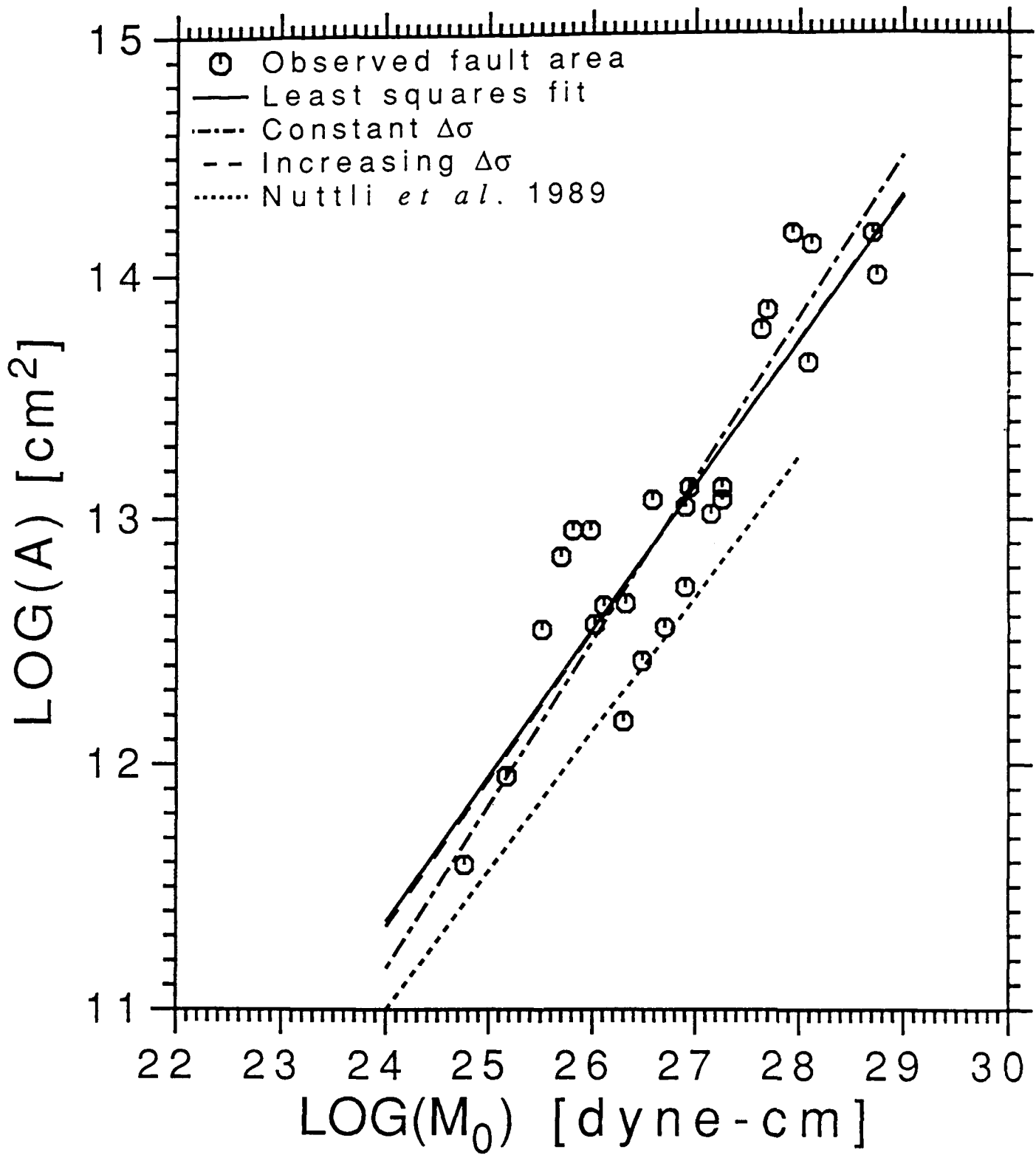


Figure 8. Fault areas,  $A$ , versus seismic moment from Table 4. The solid line is from the least-squares fit, (26), dash-dots are from relations assuming constant stress drop scaling, (28), long dashes from relations assuming increasing stress drop, (30). Short dashes are from the revised mid-plate scaling relation by Nuttli *et al.* (1989).

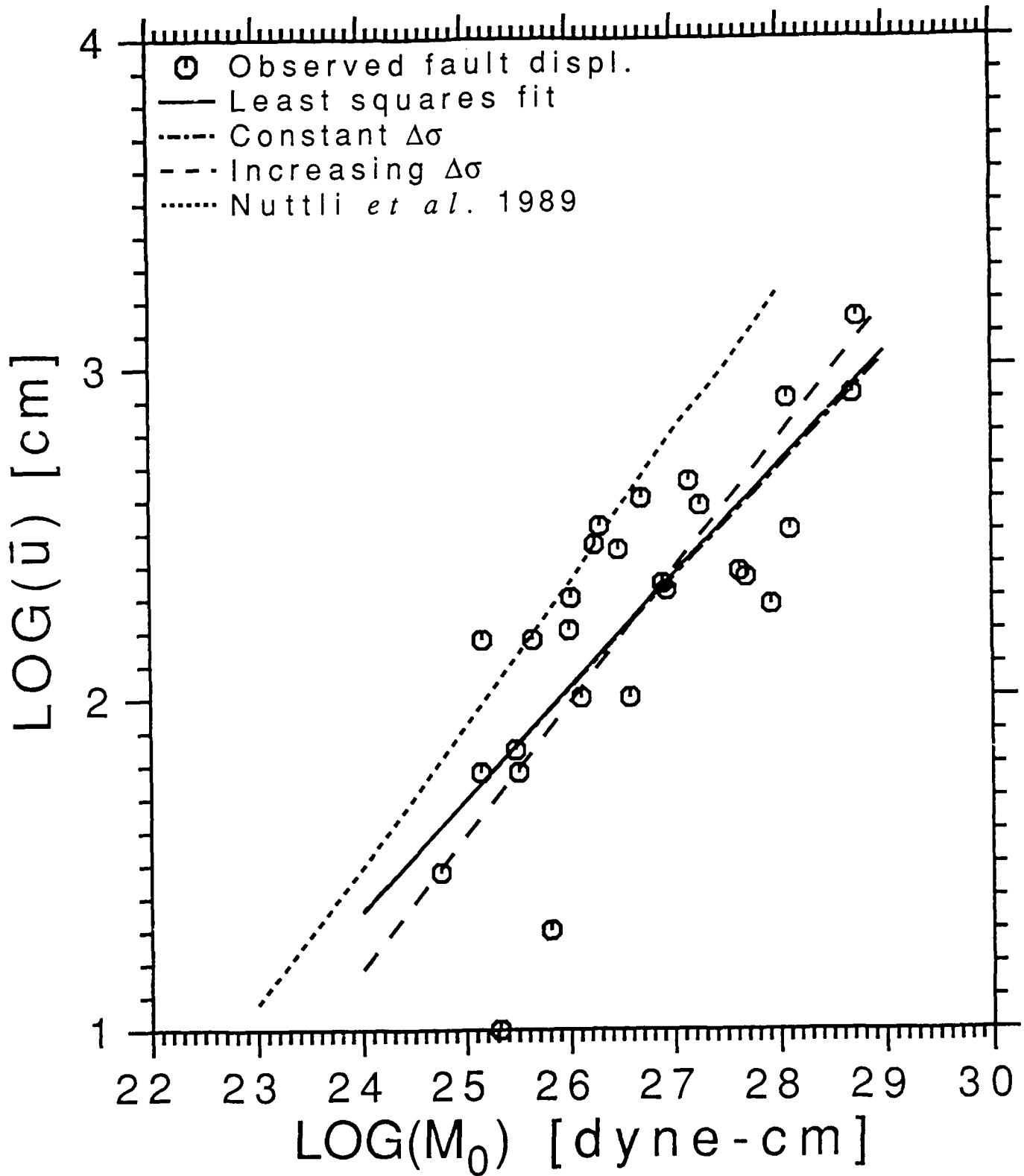


Figure 9. Average displacements,  $\bar{u}$ , versus seismic moment from Table 4. The solid line is from the least-squares fit, (27), dash-dots are from relations assuming constant stress drop scaling, (29), long dashes from relations assuming increasing stress drop, (31). Short dashes are from the revised mid-plate scaling relation by Nuttli *et al.* (1989).

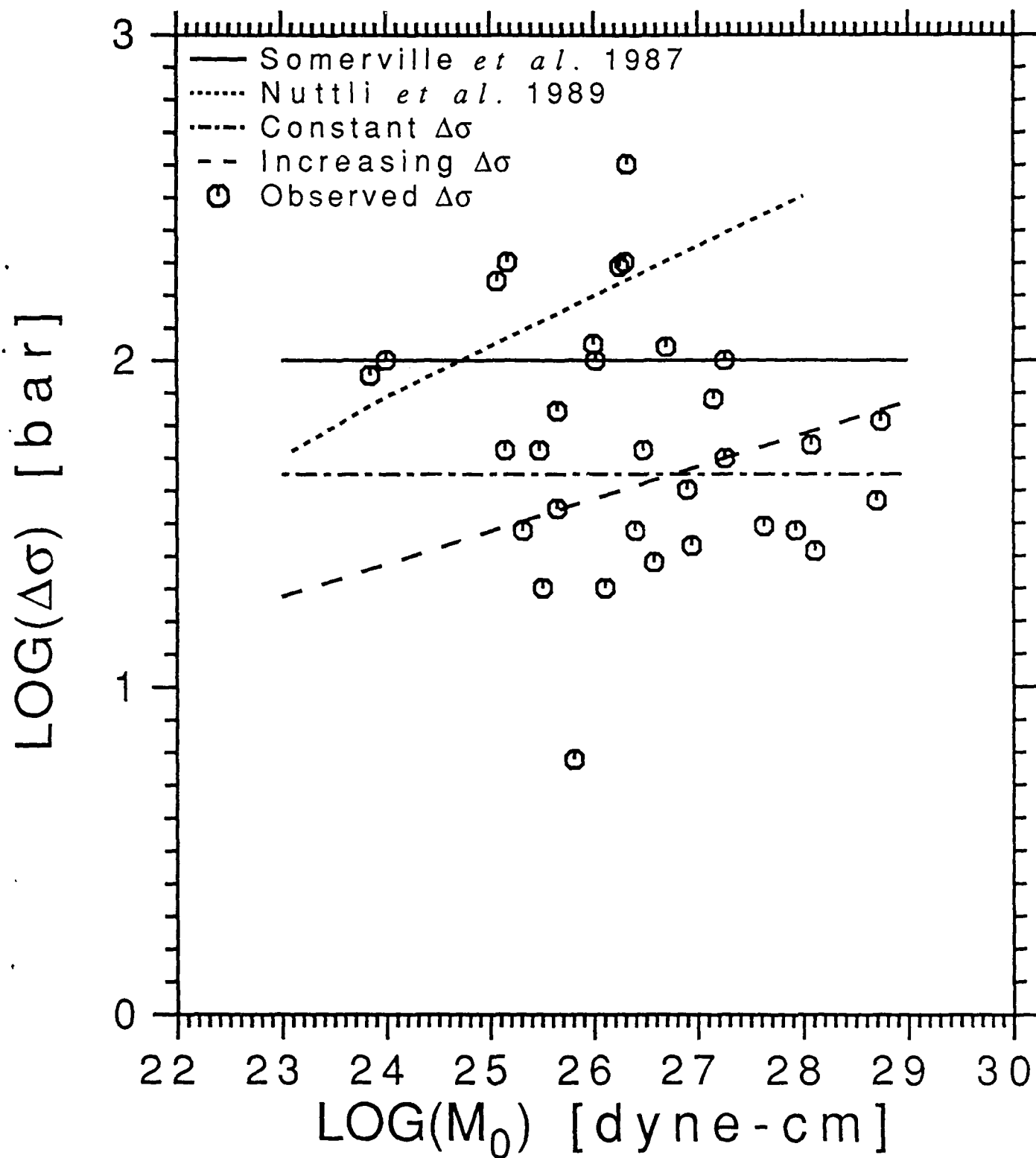


Figure 10. Observed static stress drops,  $\Delta\sigma$ , versus seismic moment from Table 4. For intra-continental earthquakes, dash-dots indicate constant stress drop (45 bar, (32)), long dashes increasing stress drop, (33). Short dashes are from the revised mid-plate scaling relation by Nuttli *et al.* (1989), and the solid line is from Somerville *et al.* (1987).

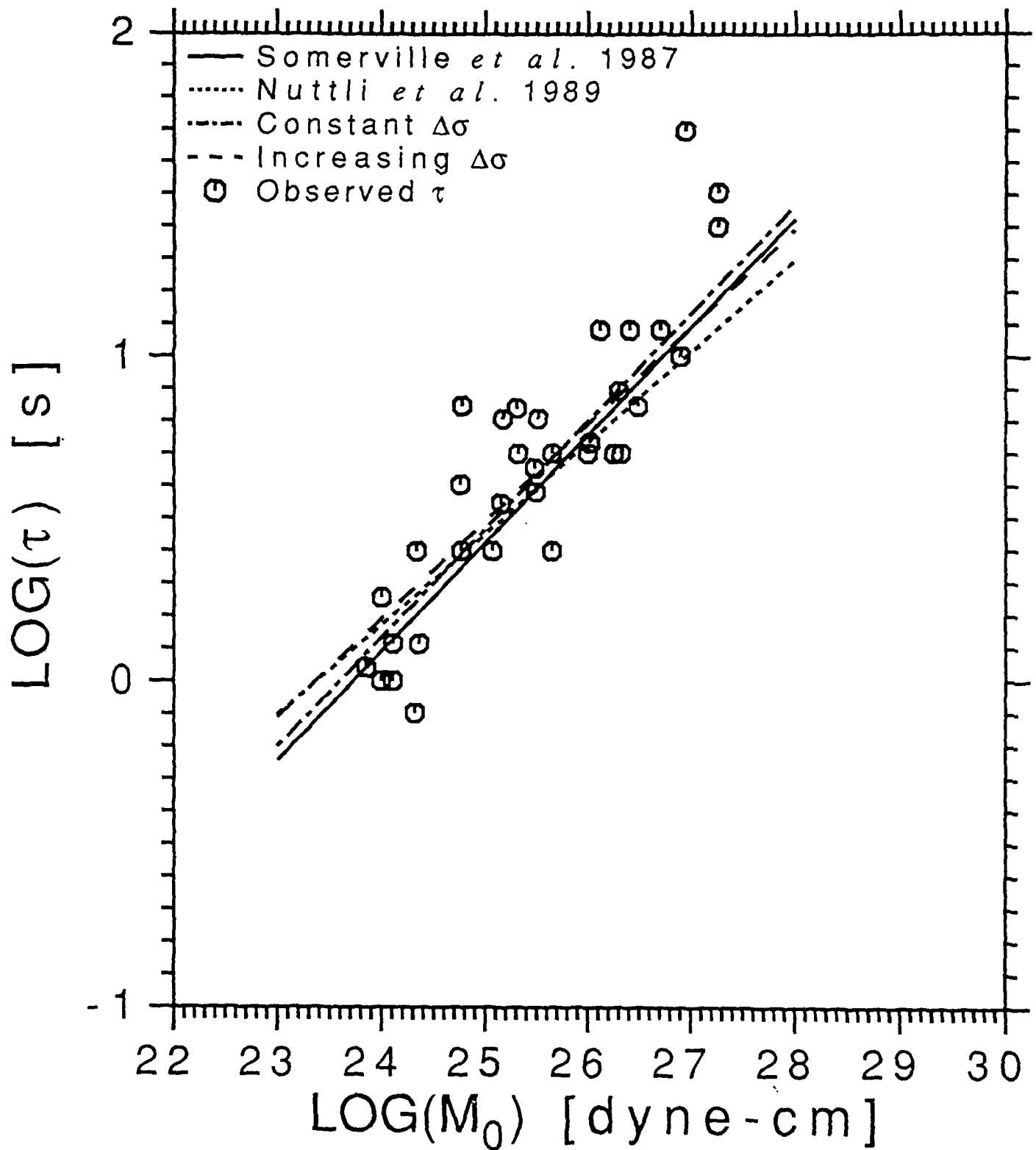


Figure 11. Observed durations,  $\tau$ , versus seismic moment from Table 4. Dash-dots are from relations assuming constant stress drop scaling, (36), long dashes from relations assuming increasing stress drop, (37). Short dashes are from the revised mid-plate scaling relation by Nuttli *et al.* (1989), and the solid line is from Somerville *et al.* (1987).

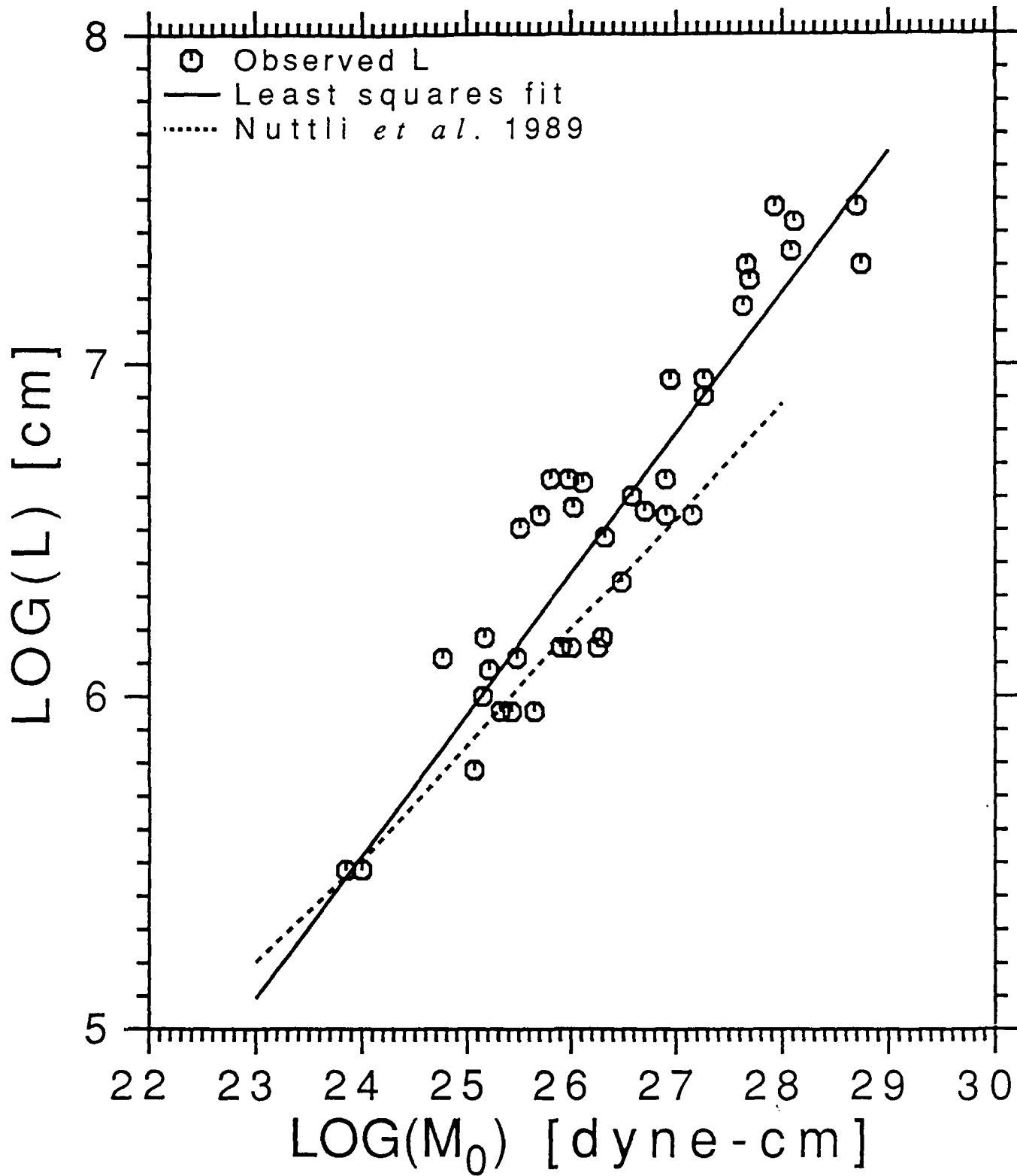


Figure 12. Observed fault lengths,  $L$ , versus seismic moment from Table 4. The solid line is from the least-squares fit, (40), and short dashes are from the revised mid-plate scaling relation by Nuttli *et al.* (1989).

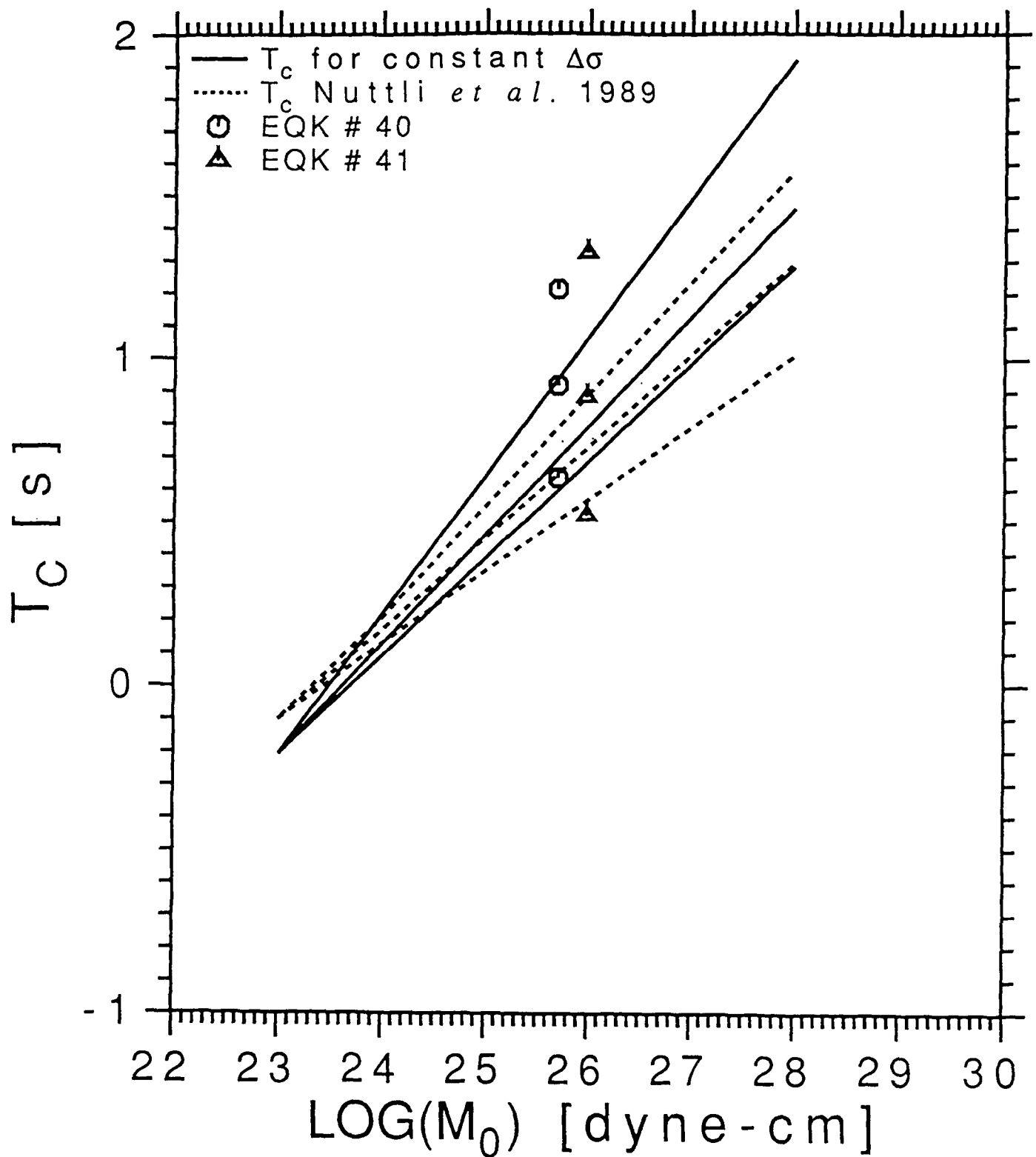


Figure 13. Corner periods versus seismic moments derived from scaling relations for intra-continental earthquakes. (a) Constant stress drop scaling: The solid lines are from top to bottom for  $T_{01}$ , (41),  $T_{02}$ , (36), and  $T_{12}$ , (43), respectively. For comparison, short dashes are from the revised mid-plate scaling relation by Nuttli *et al.* (1989), i.e., Figure 2, for  $T_{01}$ ,  $T_{02}$ , and  $T_{12}$ , respectively. Observed corner periods are displayed for events 40 and 41 (Upadhyay and Duda, 1980).



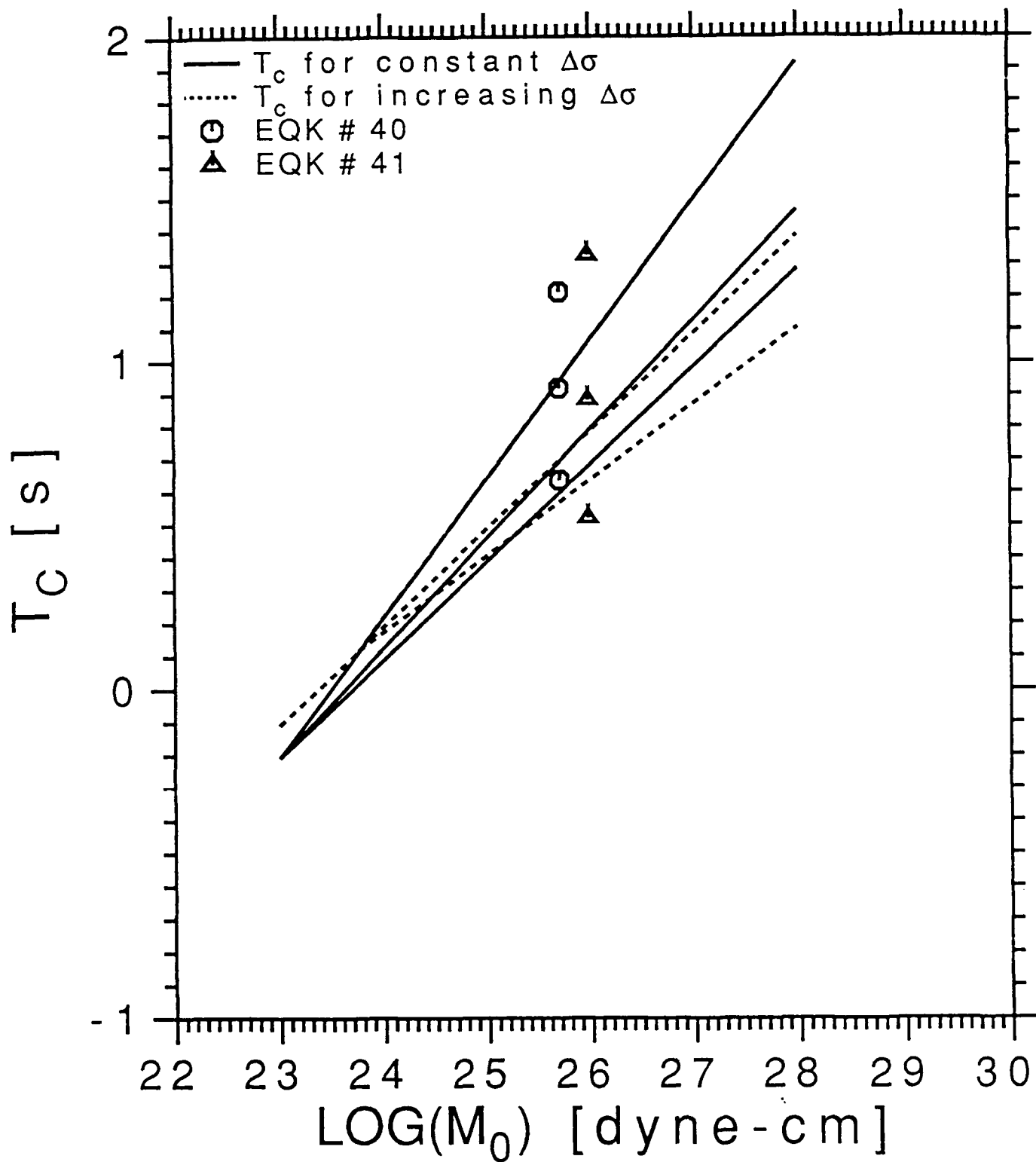


Figure 13. Corner periods versus seismic moments derived from scaling relations for intra-continental earthquakes. (b) Comparison of corner periods derived from constant stress drop (solid lines) and increasing stress drop scaling (short dashed lines).

## Ground roll: rejection using polarization filters

Chiou-Fen Shieh\* and Robert B. Herrmann§

### ABSTRACT

Ground roll noise on land data sets overwhelms the desired reflection seismic signal unless special steps are taken in data acquisition and processing to control it. This is usually done in the field by the design of group arrays for data acquisition. On the other hand, if multicomponent data are acquired, it is possible to remove the ground roll during processing by using polarization analysis. Even though this processing is computationally intensive, the potential exists for obtaining results similar to conventional data acquisition with the deployment of fewer sensors in the field with minimal group array effects as well as deriving new information.

We describe a two-dimensional polarization filter analysis for use with vertical and inline sensors. A time-domain spectral matrix technique is developed to account for the fact that the recorded seismic signal is the superposition of multiple signals in the time domain, each with different frequency content and time-varying polarization. This technique is implemented by decomposing the signal into individual frequency components by using narrow bandpass filters and defining the polarization characteristic using sliding time windows. We show that both incoherent noise and specific linearly polarized constituents can be successfully filtered.

### INTRODUCTION

Ground roll can be eliminated from a seismic trace by exploiting its specific characteristics. For example, one may focus on the dispersion, and design numerical filters to remove the dispersed signal from the trace (Herrmann and Russell, 1990). An alternative approach is to realize that the recorded seismic wave field may be represented to a first approximation by the superposition of surface-wave modes (Harvey, 1981). The surface-wave signal in an isotropic elastic medium has the feature that the vertical and inline components are 90° out of phase and that the ellipticity is frequency and mode dependent (Mooney and Bolt, 1966; Harkrider, 1970). This suggests that an analysis of the instantaneous particle motion, or its polarization if the motion is elliptical, may lead to another method of ground roll removal.

Polarization analysis has been used to introduce extra parameters for the description of complex wave fields. (René et al, 1986). If one can calculate those parameters accurately, identification and isolation of signal components can be achieved. Methods have been presented to perform this analysis in either the frequency or time domains.

---

\*Formerly Department of Earth and Atmospheric Sciences, Saint Louis University; currently Taipei Teachers College, Taipei, Taiwan, ROC.

§Department of Earth and Atmospheric Sciences, Saint Louis University, 3507 Laclede Avenue, St. Louis, MO 63103

A spectral matrix method was first introduced by Samson (1973). A series of papers involving both practical and theoretical studies has been written by Samson (1973, 1977) and Samson and Olson (1980, 1981). The coherency matrix defined in the time domain was first proposed by Vidale (1986).

All the techniques use a moving window in either the frequency or the time domain to define the polarization characteristics. The moving window faces two difficulties: 1) when the polarization is processed in the frequency domain, different arrivals separated in time, but with the same frequency content will be mixed together such that they can not be separated in the frequency domain; 2) when polarization is processed in the time domain, signals with different frequency content arriving in the same time segment can not be separated in the time domain.

Jurkevics (1988) developed a rigorous time and frequency decomposition technique in which a 50% overlap cosine window and bandpass filters were used in combination. His technique may be modified to overcome the two problems mentioned above.

Because of the complexity of analyzing 3-D particle motion, we will focus on the simpler 2-D problem for which the data consist of vertical and inline time histories at each receiver location. In the absence of lateral variations in earth structure, we would expect the ground roll to consist solely of Rayleigh waves on these components. This is not to say that the full 3-D problem is not important or will not provide interesting results, but rather that our purpose is to remove the ground roll from the component that usually has good reflections, the vertical component.

### THEORY

The purpose of polarization analysis is to characterize the phase difference between two signals. If the signals differ in phase by a constant 0 or  $\pi$  radians, then their crosscorrelation at zero lag will be a maximum. If there is a constant phase difference of  $\frac{\pi}{2}$  or  $\frac{3\pi}{2}$  radians, then their crosscorrelation will be zero. In the frequency domain, by virtue of the crosscorrelation theorem, the Fourier transforms of the two crosscorrelations will be pure real or pure imaginary, respectively, for the two cases. On the other hand, if a crosscorrelation is formed between one signal and the Hilbert transform of the other, then a maximum crosscorrelation occurs when the original signals differed in phase by  $\frac{\pi}{2}$  radians. Thus the formation of crosscorrelations can characterize the phase differences between two signals.

We define the spectral matrix from the observed data as

$$J = \begin{bmatrix} \langle zz^* \rangle & \langle zr^* \rangle \\ \langle rz^* \rangle & \langle rr^* \rangle \end{bmatrix} = \begin{bmatrix} J_{zz} & J_{zr} \\ J_{rz} & J_{rr} \end{bmatrix} \quad (1)$$

where  $z$ ,  $r$  are the vertical and inline seismic field components. The symbol  $\langle \rangle$  indicates a frequency or time average with the asterisks denoting the complex conjugate.

The input data are expressed in complex form such that the matrix  $J$  is a non-negative Hermitian, and contains all the information needed to characterize the polarization parameters. Since the  $J$  matrix can be expressed in the frequency domain (Samson, 1973) or in the time domain (Vidale, 1986), it is, for simplicity, called the spectral matrix when it is defined as in (1). To construct the  $J$  matrix in the time domain, the observed real time series is transformed into a complex time series through the use of a Hilbert transform.

For a quasi-monochromatic signal produced by a physical source, the ellipticity and orientation of the polarization are independent of time. In general, such a wave field is partially polarized (Goodman, 1985). In particular, if the wave is a single-frequency wave, it can be expressed as the sum of one wave field which is completely polarized and one which is completely unpolarized. It can be shown that this representation is unique: any matrix can be uniquely decomposed into the form

$$J = S + N \quad (2)$$

where  $S$ ,  $N$  are the spectral matrices of completely polarized and completely unpolarized waves respectively.

Usually the observed spectral matrix contains signal and noise where the signal yields the completely polarized matrix and the noise yields the completely unpolarized matrix. If noise is completely unpolarized and has the same variance on the two components, then the  $N$  matrix can be expressed by a diagonal matrix with two equal elements:

$$N = \begin{bmatrix} n & 0 \\ 0 & n \end{bmatrix} \quad (3)$$

Equal off-diagonal elements requires that the noise be uncorrelated between components, and the two equal diagonal elements requires that the noise energy is the same at each component. In other words, to satisfy the completely unpolarized condition the noise must be random and isotropic. A detailed proof for the general case can be found in Mott (1986), and, for the seismic wave case, in Shieh (1988). The assumption of random and isotropic noise may not be true for some cases or for some frequencies ranges, but we find that this assumption works well for the seismic data we examined. If this assumption is not correct, the  $J$  matrix cannot be algebraically decomposed into the  $S$  and  $N$  components. In such a case, noise prior to the signal arrival may be used together with the technique of Samson (1983) to reduce the effect of this noise on the signal.

We assume that the  $J$  matrix can be written as

$$J = \begin{bmatrix} s_{zz} & s_{zr} \\ s_{rz} & s_{rr} \end{bmatrix} + \begin{bmatrix} n & 0 \\ 0 & n \end{bmatrix} \quad (4)$$

For a completely polarized signal, the matrix  $S$  has a zero determinant. This is easily seen from the frequency domain representation of (1) because in the absence of noise  $zz \ rr^* - zr^* \ z \ r = 0$ . Applying this condition leads to a

characteristic eigenvalue equation

$$(J_{zz} - n)(J_{rr} - n) - J_{rz}J_{zr} = 0.$$

Born and Wolf (1964) and Mott (1986) showed that the elements of the **S** and **N** can be calculated from the following equations:

$$s_{zz} = \frac{1}{2}(J_{zz} - J_{rr}) + \frac{1}{2}((J_{zz} + J_{rr})^2 - 4\text{DET}[J])^{\frac{1}{2}} \quad (5.1)$$

$$s_{rr} = \frac{1}{2}(J_{rr} - J_{zz}) + \frac{1}{2}((J_{zz} + J_{rr})^2 - 4\text{DET}[J])^{\frac{1}{2}} \quad (5.2)$$

$$n = \frac{1}{2}(J_{zz} + J_{rr}) - \frac{1}{2}((J_{zz} + J_{rr})^2 - 4\text{DET}[J])^{\frac{1}{2}} \quad (5.3)$$

$$s_{zr} = J_{zr} \quad (5.4)$$

$$s_{rz} = J_{rz} \quad (5.5)$$

where

$$\text{DET}[J] = J_{zz}J_{rr} - J_{zr}J_{rz}$$

In equations 5.1 and 5.2,  $s_{zz}$  and  $s_{rr}$  are, respectively, the noise-free smoothed spectrum squared at each frequency, or energy at each time, for the vertical and inline components. Equation 5.3 yields the smoothed noise spectrum squared at each frequency, or energy at each time sample. The square root of these quantities represents the smoothed Fourier amplitude spectra in the frequency domain or an RMS amplitude in the time domain.

Once the signal and noise characteristics are isolated, the degree of polarization  $P^2$  is defined by

$$P^2 = \frac{\text{trace } \mathbf{S}}{\text{trace } \mathbf{J}} = \left(1 - \frac{4\text{DET}[\mathbf{J}]}{(J_{zz} + J_{rr})^2}\right)^{1/2} \quad (6)$$

We note that

$$0 \leq P^2 \leq 1$$

Since  $\text{DET } \mathbf{S} = 0$ , one of the eigenvalues of **S** must equal zero, and the other equals the  $\text{trace } \mathbf{S} = s_{zz} + s_{rr}$ . Note that a physical interpretation of  $s_{zz}$  is that it is proportional to the energy of the coherent signal on the z-component, with a similar interpretation for  $s_{rr}$  and  $n$ . Thus  $P^2$  equals the ratio of the signal energy to the total energy. The complex eigenvector corresponding to the non-zero eigenvalue of **S** is

$$\begin{aligned} \mathbf{x} &= \begin{bmatrix} 1, s_{rr}/s_{zr} \end{bmatrix} \\ &= \begin{bmatrix} x_1, x_2 e^{j\psi} \end{bmatrix} \end{aligned} \quad (7)$$

where  $x_1$  and  $x_2$  are real and  $\psi$  is the phase.

In order to define the ellipticity,  $e$ , it is convenient to form another vector

$$\mathbf{v}_1 + j\mathbf{v}_2 = \mathbf{x}e^{j\phi},$$

by multiplying the vector in equation 7 by a constant phase term. Because of the way that the  $\mathbf{J}$  matrix and consequently the  $\mathbf{S}$  matrix are defined, this new vector will also be an eigenvector of the  $\mathbf{S}$  matrix. To define the ellipticity, Samson and Olson (1980) show that using

$$\phi = \frac{1}{2} \tan^{-1} \left( \frac{x_2^2 \sin 2\psi}{x_1^2 + x_2^2 \cos 2\psi} \right)$$

leads to the real vectors  $\mathbf{v}_1$  and  $\mathbf{v}_2$ , with the constraint  $\mathbf{v}_1^T \mathbf{v}_2 = 0$ . The ellipticity  $e$  is defined as the ratio of the Euclidian norms  $|\mathbf{v}|_e$  of the  $\mathbf{v}$  vectors. The ratio is defined to be less than 1. If for example,  $|\mathbf{v}_1|_e > |\mathbf{v}_2|_e$ , then

$$e = |\mathbf{v}_2|_e / |\mathbf{v}_1|_e. \quad (8)$$

We now have a number of parameters that characterize the polarization of the signal,  $s_{rr}$ ,  $s_{zz}$ ,  $s_{zr}$ ,  $e$ ,  $P^2$ ,  $\mathbf{v}_1$ , and  $\mathbf{v}_2$ . Any combination of these can be used to modify the input vertical and in-line signals. For example, the motion could be projected onto the major axis, P-wave linear motion could be rejected, or SV-linear motion could be rejected.

To construct simple polarization filter functions, we combine the two parameters obtained from the spectral matrix, which are the degree of polarization and the ellipticity. A filter function to reject noise and to pass linear motion is of the form

$$G_l = P^m (1-e)^n. \quad (9)$$

A second filter to reject linear motion and noise and to pass elliptical motion would be of the form

$$G_e = P^m e^n \quad (10)$$

where  $m$  and  $n$  are integers. The use of the term filter is appropriate since we will decompose the two-component signal into frequency and time components, apply the filter function to each component, and then combine the results to yield the output traces.

### PROCESSING ALGORITHM

The theory described above is applicable to the analysis of a single coherent signal in the presence of isotropic noise. As mentioned in the introduction, real data will have multiple arrivals, each with different polarization and frequency characteristics. The algorithm presented here takes this into account. Numbers within parentheses refer to specific equations in the text.

- a) Form Complex Z and R traces using Hilbert transform
- b) Loop over bandpass filter center frequencies

- c) Zerophase bandpass filter complex traces
- d) Apply moving  $\cos^2$  window specified by filter frequency
- e) Construct J matrix (1)
- f) Construct signal matrix (5)
- g) Construct degree of polarization (6)
- h) Calculate ellipticity (7)
- i) Calculate rectilinearity  $(1-e)$
- j) Compute filter constant  $G_l$
- k) If *reject* low frequency P and real  $J_{zr} > 0$
- l)  $G_l = 0.02 P^m (1-e)^n$
- m) Else if *reject* low frequency SV and real  $J_{zr} < 0$
- n)  $G_l = 0.02 P^m (1-e)^n$
- o) Else
- p)  $G_l = P^m (1-e)^n$
- q) Multiply windowed segment by  $G_l$
- r) Sum windowed segments
- s) Advance window
- t) Adjust level
- u) Sum filtered, bandpassed traces
- v) Change filter frequency
- w) Output polarization filtered inline and vertical traces

---

To deal with multiarrival signals, the vertical, Z, and inline, R, traces are decomposed into a series of bandpass filtered traces (Steps b and c). Next polarization analysis is performed on segments of the filtered trace obtained by using overlapping  $\cos^2$  windows (Step d). A  $\cos^2$  window is used rather than the  $\cos$  window of Jurkevics (1988) since overlapping windows, shifted by a half window length, will yield a temporally flat overall window except at the first and last segments because of the trigonometric identity  $\sin^2 x + \cos^2 x = 1$ . The length of the  $\cos^2$  window trades off with the ability to remove incoherent noise (equation 5.3) since time averaging over a long window will reduce the noise, so that the extra analysis in equations 5.1-5.3 may not be significant. Steps e through q perform the polarization analysis and define the filter function,  $G_l$ . If this filter function were forced to be  $G_l = 1.0$ , then we would like the original signal to pass through unchanged. Unfortunately, since the bandpass filters are implemented by successive zero phase lowpass and highpass filtering using Butterworth recursive digital filters, the frequency domain representation will have other than unit gain, and in addition, as the various frequency windows are summed, the response function will be other than flat. To account for this, we initialize the process by determining the frequency response of the filtering operation, but having the polarization section pass the input signal completely, and compute a normalizing gain factor. This normalization is applied in Step t. The result of this is that a linearly polarized chirp or single frequency signal is passed without any change in amplitude or phase.

Steps e through i follow the equations in the text. However, one other feature is built into the algorithm, that makes use of the fact that vector particle motion data are acquired. If vertical ground motion upward and inline ground motion away from the source are defined positive, then the sign of the real part of  $J_{zr}$  can be used to specify whether the ground motion is of P or SV character, according to whether the sign is positive or negative, respectively. In Steps k through p we can specify a rejection of P or SV motion at the same time as we reject incoherent noise and non-linear particle motion. This is applied to remove low frequency linearly polarized ground roll components in the signal.

The parameters used for default processing are  $m = 2$ ,  $n = 6$ , signal processing with center frequencies,  $f_c$ , up to 100 Hz, and a bandwidth of  $10\Delta f$ , where  $\Delta f$  is the Fast Fourier transform sampling frequency, obtained as a result of performing the Hilbert transform through frequency domain operations. The choice of  $m$  and  $n$  is not critical; the values used were chosen after some experimentation with real data sets. The time domain moving  $\cos^2$  window has a window width equal to  $2 / f_c$ . If rejection of low frequency P or SV components is requested, it is done for frequencies less than  $f_L = 35\text{Hz}$ .

## DATA PROCESSING

Several different data sets will be presented to test the operation of the technique as well as to consider its applicability under different conditions of reflection signal to ground roll noise level.

### Synthetic Data Set

Figure 1 presents some synthetic data sets together with the results of our polarization analysis. The synthetic vertical component time history consisted of four 30 Hz Ricker wavelets centered at two way travel times of 0.20, 0.35, 0.50, 0.65 and 0.80 seconds. The synthetic inline time history consisted of 30 Hz Ricker wavelets phase shifted by  $0^\circ$ ,  $45^\circ$ ,  $90^\circ$ ,  $135^\circ$  and  $180^\circ$ , at the corresponding times. The vertical component wavelets had a peak amplitude of 1.0. In addition zero mean random noise with a Gaussian distribution and a standard deviation of  $A$ , where  $A$  is an amplitude level, was added to the polarized signals. Since polarization analysis would usually be applied to data prior to the NMO stack, it is also useful to see how it affects the stack.

Figure 1 consists of four groups of six traces. In each group, the sixth and rightmost trace is a simple stacked sum of the preceding five traces. Figure 1a corresponds to the five vertical component time history realizations for  $A=0.2$  and the resulting stack. Figure 1b shows the result of polarization filtering each of the five input traces and the corresponding stacked output. We see that the polarization filter did reject the wavelets with phases other than  $0^\circ$  or  $180^\circ$ . In addition, there is some improvement in the signal to noise ratio within the individual traces, indicating some value in attempting to define the isotropic noise component in the signal. The stack of the polarization filtered traces has slightly less noise than the stack of the input traces. Figures 1c and 1d compare the input and polarization filter output traces and



stacks for the case when the noise is doubled,  $A=0.4$ . The stacked traces again show the benefit of noise reduction by stacking, but again the non-linearly polarized wavelets are rejected by the filter. Another simulation was run with  $A=0.8$ , but the results indicated a reduction in the ability to reduce the noise and also to reduce the non-linearly polarized signal.

#### Oklahoma Field Data

As part of an sensor evaluation test, four data sets were collected at a field test site in Oklahoma. Both dynamite and vertical vibrator sources were used with receiver group arrays spaced 15.2 meters apart between 152.4 and 441.9 meters from the source. Each group array consisted of six geophones. The vibrator acted at the surface while the dynamite was buried at a depth of 15.2 meters. The four data sets acquired are as follows:

**DynGrp** - dynamite source with a 30.5 meter geophone group array

**DynNoGrp** - dynamite source with a 1 meter geophone group array

**VibGrp** - vibrator source with a 30.5 meter geophone group array

**VibNoGrp** - vibrator source with a 1 meter geophone group array

The receiver group arrays were not designed to maximally reduce the surface waves; at most they reduce the surface-wave signal by 6-10 db over the usable signal range (5-85 Hz).

Figure 2 presents the acquired vertical component time histories, which consist of 1000 ms of data sampled at 4 ms intervals. Within each panel, the trace on the left is at a distance of 152.4 m and the one at the right is at a distance of 441.9 m. An automatic gain correction with a 500 ms window has been applied to each trace. A well developed set of reflections is seen at a two way traveltime of 0.550 seconds. The sections are ordered so that the quality of the reflection decreases from left to right.

Figure 3 presents a comparison of the input and output traces for the **DynGrp** data set. Figures 3a and 3b are the input vertical and inline data sets, respectively, while Figures 3c and 3d are the filtered vertical and inline data sets, respectively. The reflection at 0.55 seconds has been enhanced on the vertical components. In addition, much of the reverberation following the direct arrival has been associated with non-linear particle motion and subsequently removed. Some low frequency ground roll is still present in Figure 3c. The inline output, Figure 3d, does not show any good reflections, which it should not for rays nearly vertically incident at the free surface. The low frequency ground roll and the reverberations following the direct P arrival have been reduced, though. Because of the lack of any distinct arrivals on the inline component, we will not present further displays of this component with this data set.

Figure 4 presents the results for the vertical component of the data set **DynNoGrp**. In this case Figure 4a represents the input vertical component data set, Figure 4b represents the polarization filter output, Figure 4c is the polarization filter output with the additional rejection of low frequency P-wave motion, and Figure 4d is the polarization output with the rejection of

the low frequency SV-wave motion. The rejection of low frequency P-wave motion on the vertical component, Figure 3c, is quite effective. The data processing resolves the nature of the reflection at 0.55 seconds very well.

Finally, Figure 5 presents the polarization filtered vertical component traces for each of the above data sets, arranged in order of increasing surface wave signal in the original data set. In addition all low frequency P-wave motion at frequencies less than 35 Hz was attenuated. Figures 5a, 5b, 5c and 5d correspond to the DynGrp, DynNoGrp, VibGrp, and VibNoGrp data sets respectively. In all cases, there is a definite reduction in the ground roll, together with corresponding relative enhancement of the reflections. From this we conclude that the technique works as designed, and that the algorithm does not introduce any spurious arrivals.

Figure 6 presents another *Oklahoma* data set, DYN. These data were collected from a 4 kg dynamite source buried at a depth of 16 m and were recorded at distances between 20 and 1000 meters. Each trace is due to a single geophone, so that the group array is of length 0 m. Figure 6a gives the input vertical component time histories and Figure 6b gives the polarization filter output, with the low frequency P-wave rejected. It is interesting to note that many of the reverberations apparent in the initial record are significantly reduced in amplitude. This would lead to improved results during NMO velocity analysis.

#### Permafrost Field Data

Data sets in the arctic regions are notorious for poor signal to noise, and often are excellent candidates for phase match filters (Barton et al., 1986; McConnell et al., 1986; and Beresford-Smith and Rango, 1988) Our data set, the vertical component traces are shown in Figure 7a, was acquired on land, and is not overwhelmed by the dispersive flexural waves typical of data acquisition on winter ice sheets. The traces range in distance from 1542 m on the left to 100 m on the right. There are some very strong undispersed arrivals with group velocities of 1400 m/s and 300 m/s. The large amplitude of these arrivals is indicated by the apparent muting introduced immediately above them due to the AGC process. These signals are also very narrow band with a center frequency near 15 Hz. The results of processing the vertical component and not rejecting either the low frequency P or SV arrivals is shown in Figure 7b.

Comparing the polarization filter output to the input time history, we note that the direct arrival is eliminated, that the overall record appears simpler due to the elimination of a what may be reverberations. The prominent air wave is not reduced in amplitude, indicating that in this case its particle motion is highly linear.

#### CONCLUSIONS

A polarization filter technique has been presented for use with vertical and inline data traces for the purpose of reducing ground roll. The technique works well when the ground roll components are associated with non-linear particle motion, but does pass linearly polarized components of the ground

roll. This is not unexpected since the ground roll ellipticity can vary significantly from near circular polarization to almost linear polarization as a function of frequency and mode.

The polarization technique also reduced the reverberation following the direct P-wave arrival at large offset, and thus may be useful in enhancing other non-vertically incident arrivals that are important for imaging subsurface structure.

The theory of polarization filtering was developed only sufficiently to accomplish the task of 2-D filtering. Other information, such as the direction of linear particle motion at the surface, a function of the angle of incidence at the free surface, was not used. This other information may be useful for advanced imaging of the vector wavefield, especially in the case of three component data sets, for which it may be possible to focus the data set upon a specific set of offline reflectors.

The improvement in signal to noise ratio is not as profound with the surface sources. On the other hand, in the case of initially good reflection signal to ground roll noise, as is the case for buried dynamite sources, the polarization filter technique yields very good results even with minimal group arrays (Figure 6). Thus the full use of the vectorial nature of ground motion may lead to less intensive data acquisition strategies with no noticeable decrease in processed line quality.

#### ACKNOWLEDGMENTS

This work was supported in part by the U. S. Geological Survey under Grant 14-08-0001-G1391 and by the AFGL under Contract F19628-87-K-0049.

#### REFERENCES

- Barton, C., Beresford-Smith, G., and Rango, R., 1986, Flexural waves on Arctic data: application of new techniques for S/N enhancement: 56th Ann. Internat. Mtg., Soc. Explor. Geophys., Expanded Abstracts, 458-461.
- Beresford-Smith, G., and Rango, R. N., 1988, Dispersive noise removal in t-x: Application to Arctic data: *Geophysics*, 53, 346-358.
- Born., M., and Wolf., E., 1964, *Principles of Optics*, Macmillan, New York.
- Goodman, J. W., 1985, *Statistical Optics*, John Wiley and Sons, New York.
- Harkrider, D. G., 1970, Surface waves in multilayered elastic media. II. Higher mode spectra and spectral ratios from point sources in plane layered earth models, *Bull., Seis. Soc. Am.*, 60, 1937-1988.
- Harvey, D. J., 1981, Seismogram synthesis using normal mode superposition: the locked mode approximation, *Geophys. J. of R. Astr. Soc.*, 66, 37-69.

- Herrmann, R. B., and Russell, D. R., 1990, Ground roll: rejection using adaptive phase matched filters, *Geophysics*, (in press).
- Jurkevics, A., 1988, Polarization analysis of three-component array data, *Bull., Seis. Soc. Am.*, 78, 1725-1743.
- McConnell, J. R., Potts, M. J., Schleicher, K. L., and Wason, C. B., 1986, Dispersive Noise Attenuation: 56th Ann. Internat. Mtg., Soc. Explor. Geophys., Expanded Abstracts, 455-458.
- Mooney, H. M., and Bolt, B. A., 1966, Dispersive characteristics of the first three Rayleigh modes for a single surface layer, *Bull., Seis. Soc. Am.*, 56, 43-67.
- Mott, H., 1986, *Polarization in antennas and radar*, John Wiley and Sons, New York.
- René, R. M., Fitter, J. L., Forsyth, P. M., Kim, K. Y., Murray, D. J., Walters, J. K., and Westerman, J. D., 1986, Multicomponent seismic studies using complex trace analysis: *Geophysics*, 51, 1235-1251.
- Samson, J. C., 1973, Descriptions of the polarization states of vector processes: application to ULF magnetic field, *Geophys. J. of R. Astr. Soc.*, 34, 403-419.
- Samson, J. C., 1977, Matrix and Stokes vector representation of detectors for polarized waveforms: theory, with some application to teleseismic waves, *Geophys. J. of R. Astr. Soc.*, 51, 583-603.
- Samson, J. C., 1983, Pure states, polarized waves, and principal components in the spectra of multiple, geophysical time-series, *Geophys. J. of R. Astr. Soc.*, 72, 647-664.
- Samson, J. C., and Olson, J. V., 1980, Some comments on the description of the polarization states of waves, *Geophys. J. of R. Astr. Soc.*, 61, 115-129.
- Samson, J. C., and Olson, J. V., 1981, Data-adaptive polarization filters for multichannel geophysical data, *Geophysics*, 46, 1423-1431.
- Shieh, C.-F., 1988, *Polarization analysis of complex seismic wave field*, Ph. D. Dissertation, Saint Louis University.
- Vidale, J. H., 1986, Complex polarization analysis of particle motion, *Bull., Seis. Soc. Am.*, 76, 1393-1405.

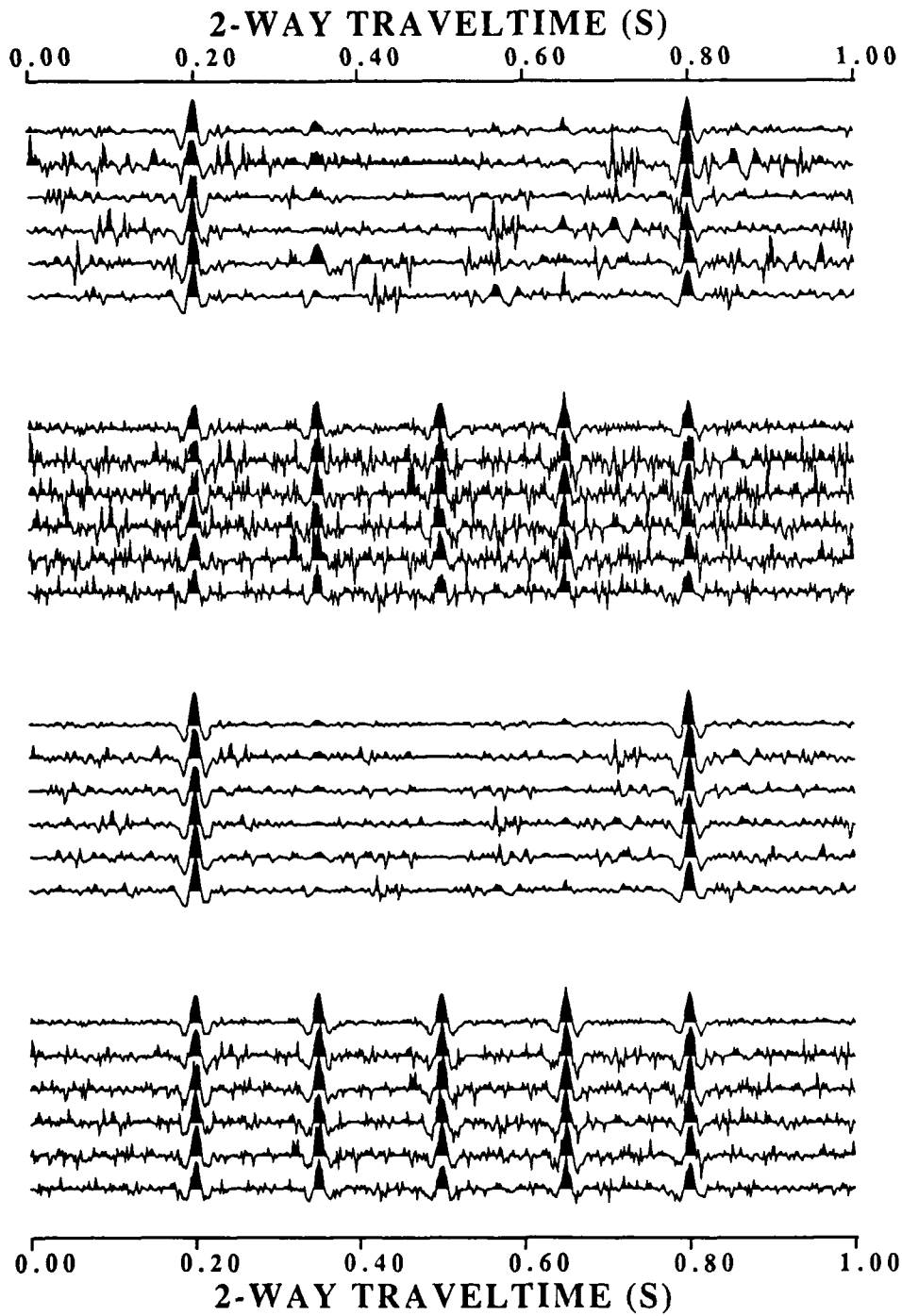


Fig. 1. Comparison of polarization filtering with synthetic data sets. Just the vertical component traces are displayed. In each display, the sixth trace is a stacked sum of the preceding five. a) Input time series with Gaussian noise of amplitude governed by  $A=0.2$ . b) Output of polarization filtering for  $A=0.2$ . c) Input time series with Gaussian noise of amplitude governed by  $A=0.4$ . d) Output of polarization filtering for  $A=0.4$ .

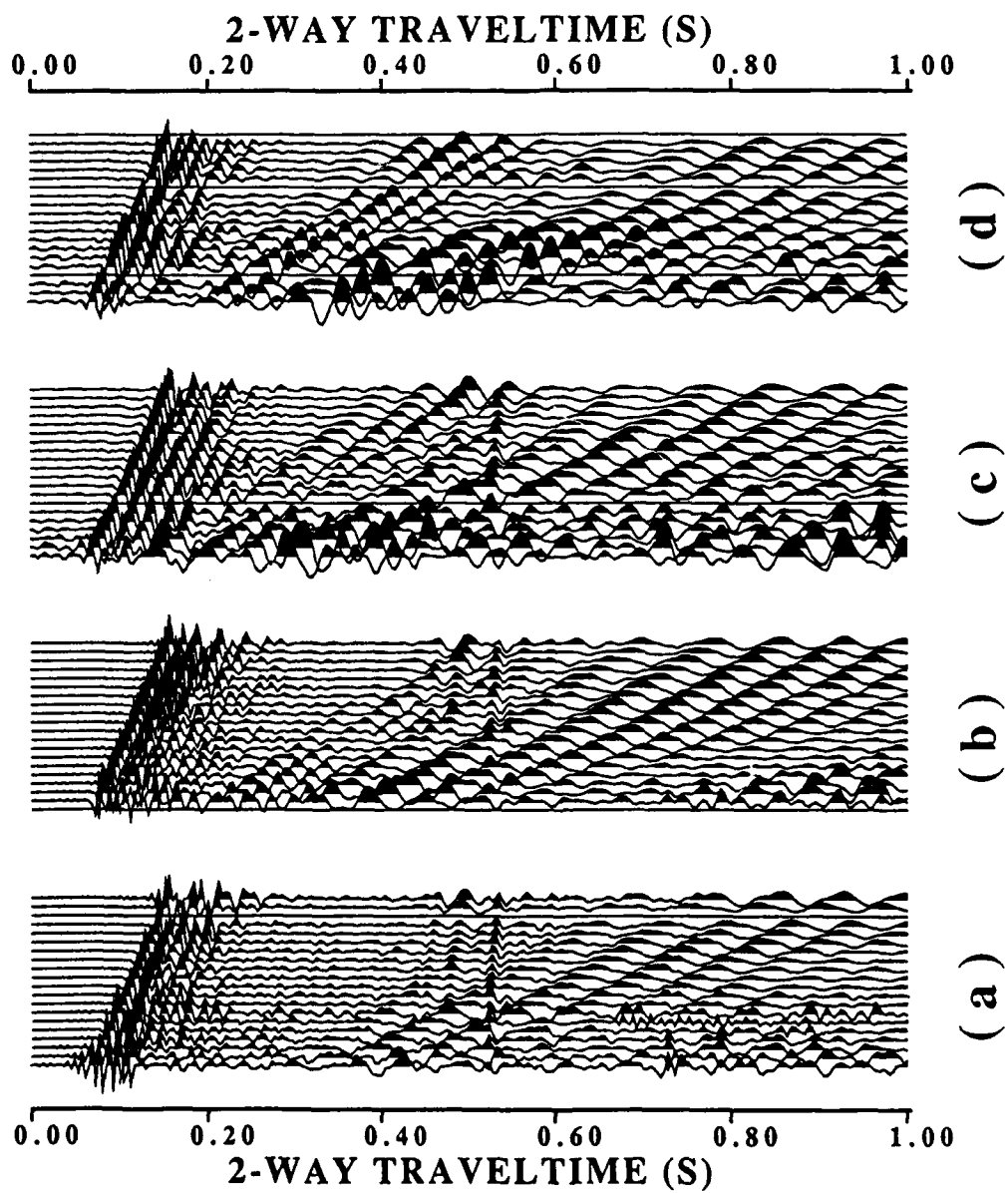


Fig. 2. Input data sets from the Oklahoma test site. a) dynamite source, group array DynGrp; b) dynamite source 1 m group array DynNoGrp; c) vibrator source, group array VibGrp; d) vibrator source, 1 m group array VibNoGrp. All traces are AGC'd with a 500 ms window.

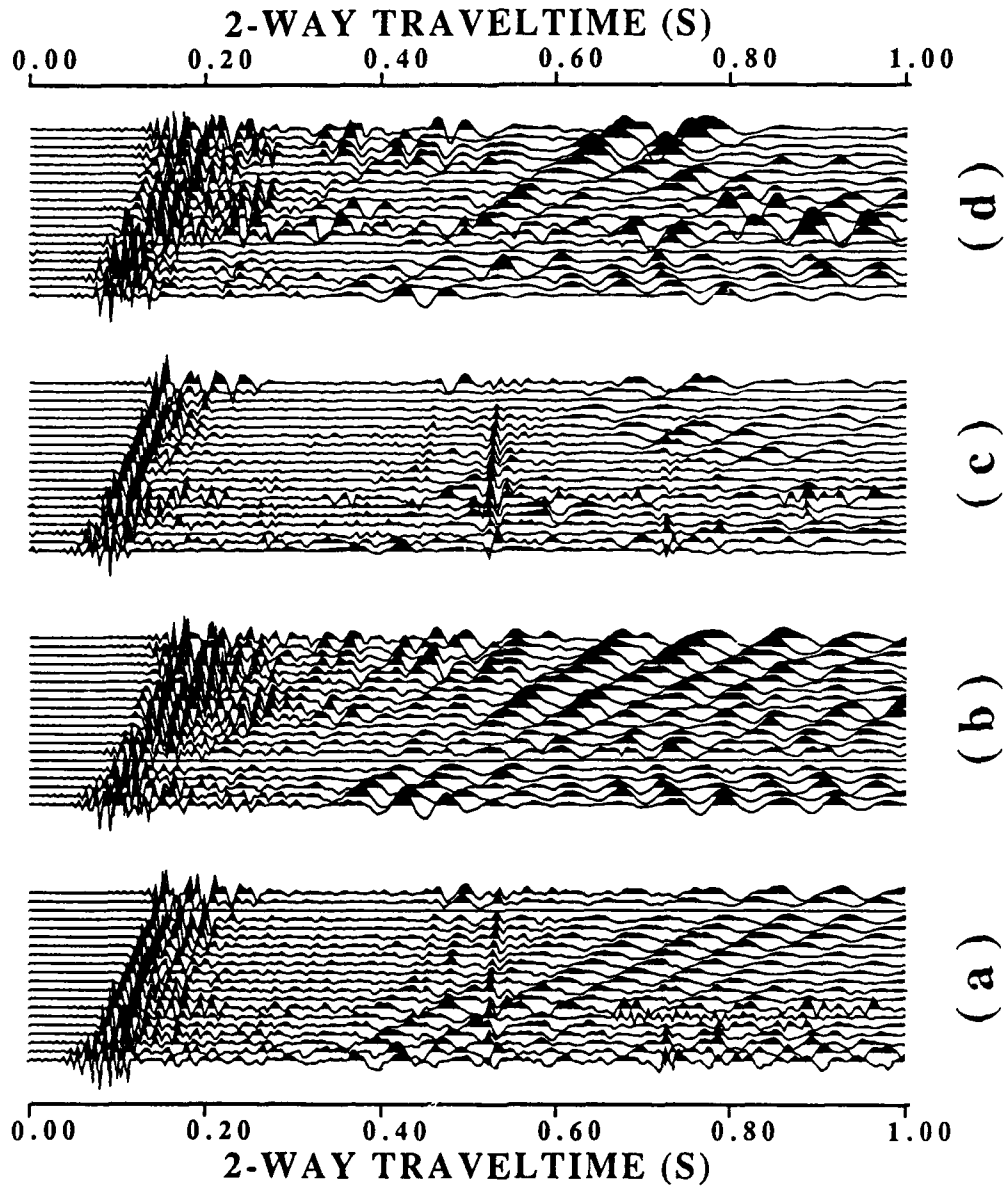


Fig. 3. Polarization processing of the DynGrp data set. All traces in the display have had an AGC applied with a 500 ms window. a) Input vertical component time histories. b) Output vertical component time histories. c) Input inline component time histories. d) Output inline component time histories.

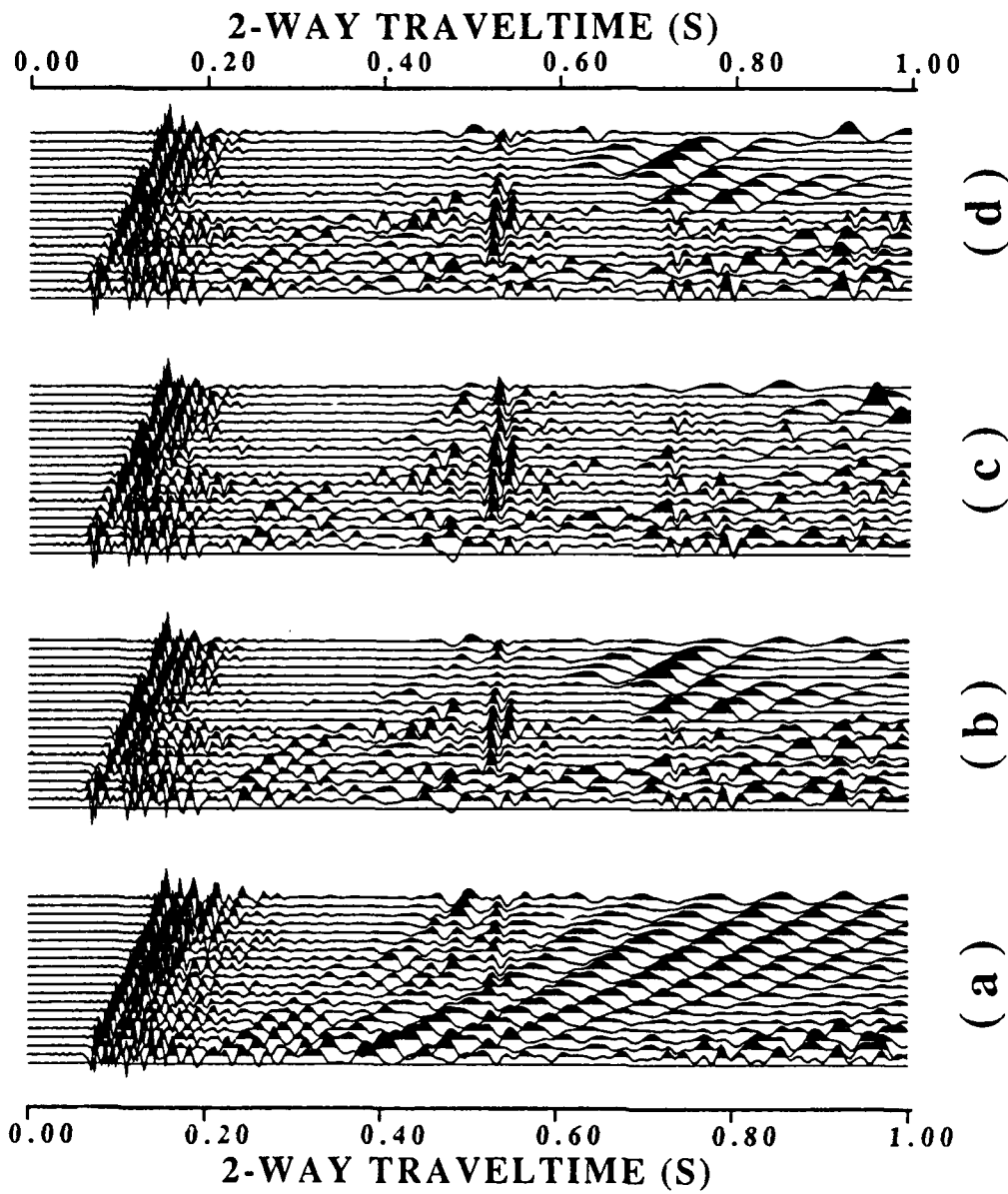


Fig. 4. Polarization processing of the DynNoGrp data set. All traces in the display have had an AGC applied with a 500 ms window. a) Input vertical component time histories. b) Output vertical component time history. c) Output vertical component time history with the constraint the low frequency P-wave motion at frequencies less than 35 Hz is rejected. d) Output vertical component time history with the constraint the low frequency SV-wave motion at frequencies less than 35 Hz is rejected.



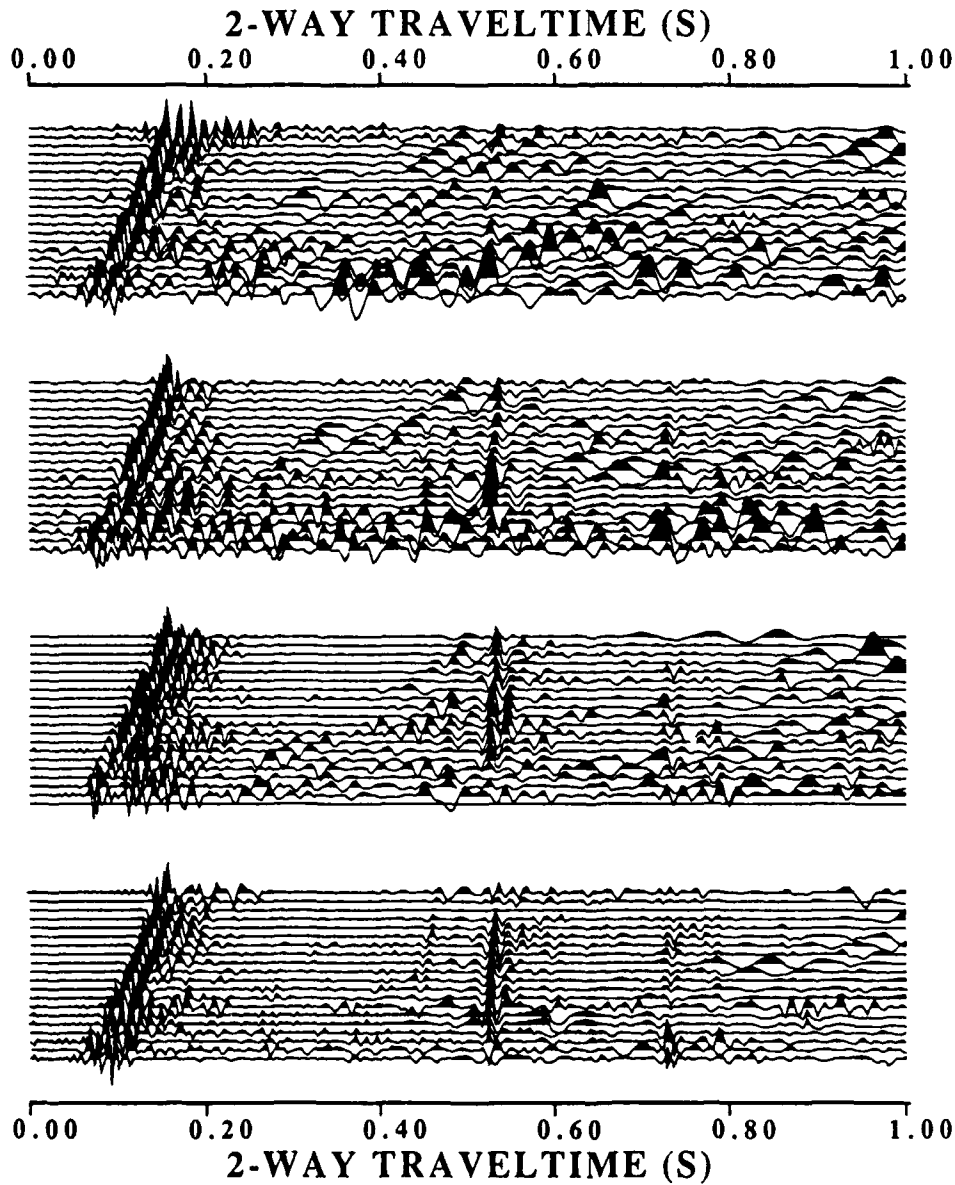


Fig. 5. Polarization processing of all data sets. All traces in the display have had an AGC applied with a 500 ms window. In addition, all have been processed to reject P-wave motion at frequencies less than 35 Hz. a) Output vertical component time history for the DynGrp data set. b) Output vertical component time history for the DynNoGrp data set. c) Output vertical component time history for the VibGrp data set. d) Output vertical component time history for the VibNoGrp data set.

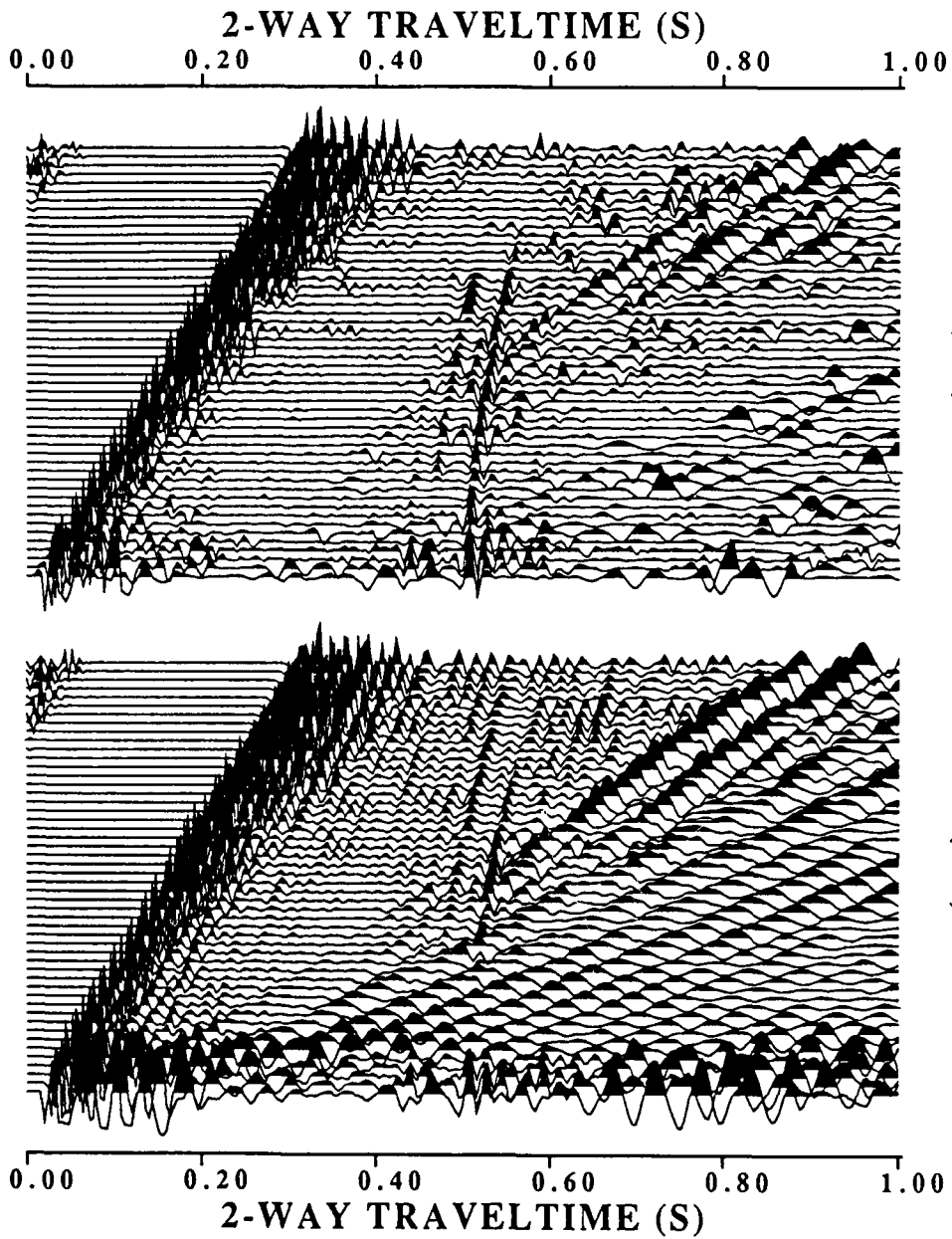
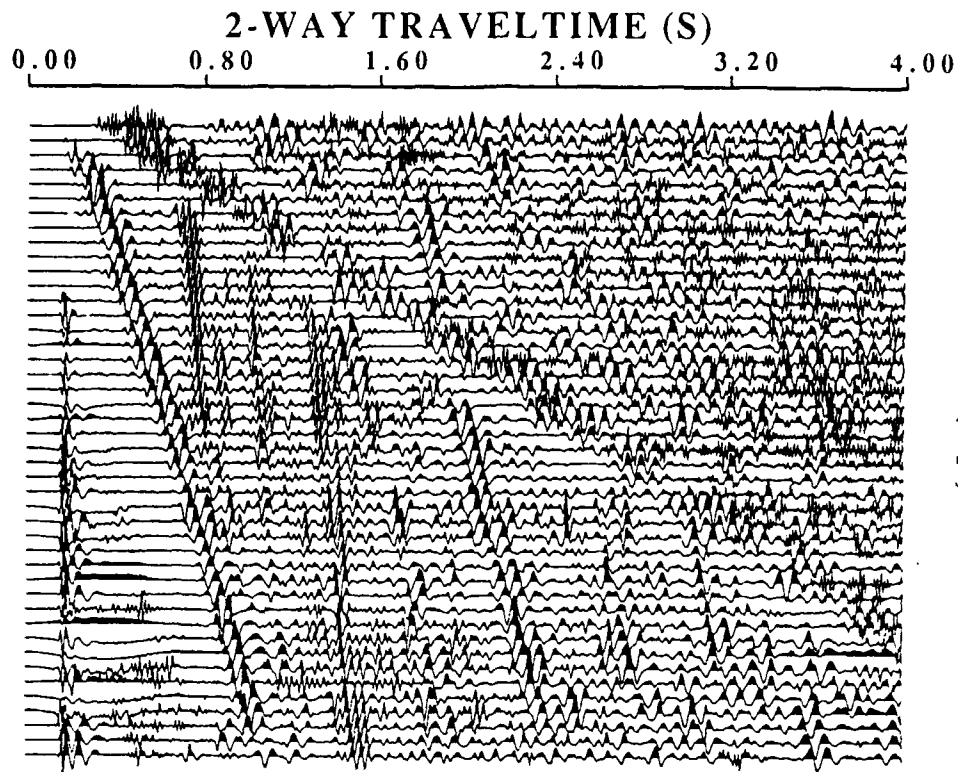
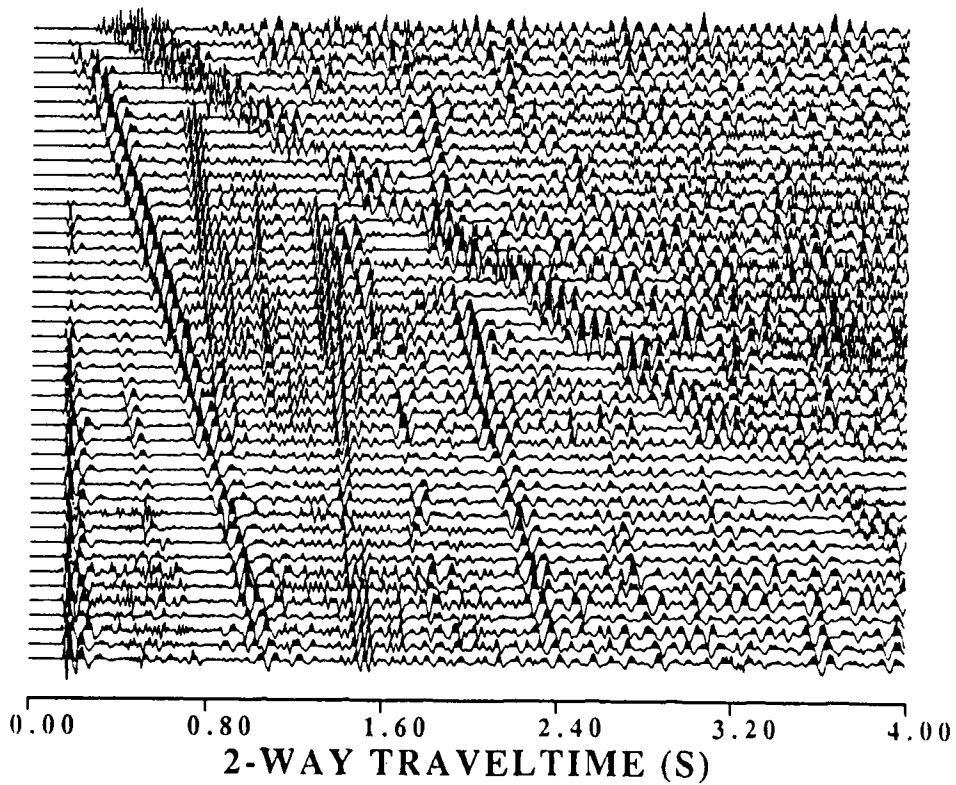


Fig. 6. Polarization processing of the DYN data set. All traces in the display have had an AGC applied with a 500 ms window. In addition, all have been processed to reject P-wave motion at frequencies less than 35 Hz. a) Input vertical component time history. b) Output vertical component time history.



( b )



( a )

Fig. 7. Vertical component time histories for the permafrost data set. All traces in the display have had an AGC applied with a 500 ms window.  
 a) Input time histories. b) Output time histories.

CONTRACTORS (United States)

Prof. Thomas Ahrens  
Seismological Lab, 252-21  
Division of Geological & Planetary Sciences  
California Institute of Technology  
Pasadena, CA 91125

Prof. Charles B. Archambeau  
CIRES  
University of Colorado  
Boulder, CO 80309

Prof. Muawia Barazangi  
Institute for the Study of the Continent  
Cornell University  
Ithaca, NY 14853

Dr. Douglas R. Baumgardt  
ENSCO, Inc  
5400 Port Royal Road  
Springfield, VA 22151-2388

Prof. Jonathan Berger  
IGPP, A-025  
Scripps Institution of Oceanography  
University of California, San Diego  
La Jolla, CA 92093

Dr. Lawrence J. Burdick  
Woodward-Clyde Consultants  
566 El Dorado Street  
Pasadena, CA 91109-3245

Dr. Karl Coyner  
New England Research, Inc.  
76 Olcott Drive  
White River Junction, VT 05001

Prof. Vernon F. Cormier  
Department of Geology & Geophysics  
U-45, Room 207  
The University of Connecticut  
Storrs, CT 06268

Prof. Steven Day  
Department of Geological Sciences  
San Diego State University  
San Diego, CA 92182

Dr. Zoltan A. Der  
ENSCO, Inc.  
5400 Port Royal Road  
Springfield, VA 22151-2388

Prof. John Ferguson  
Center for Lithospheric Studies  
The University of Texas at Dallas  
P.O. Box 830688  
Richardson, TX 75083-0688

Prof. Stanley Flatte  
Applied Sciences Building  
University of California  
Santa Cruz, CA 95064

Dr. Alexander Florence  
SRI International  
333 Ravenswood Avenue  
Menlo Park, CA 94025-3493

Prof. Henry L. Gray  
Vice Provost and Dean  
Department of Statistical Sciences  
Southern Methodist University  
Dallas, TX 75275

Dr. Indra Gupta  
Teledyne Geotech  
314 Montgomery Street  
Alexandria, VA 22314

Prof. David G. Harkrider  
Seismological Laboratory  
Division of Geological & Planetary Sciences  
California Institute of Technology  
Pasadena, CA 91125

Prof. Donald V. Helmberger  
Seismological Laboratory  
Division of Geological & Planetary Sciences  
California Institute of Technology  
Pasadena, CA 91125

Prof. Eugene Herrin  
Institute for the Study of Earth and Man  
Geophysical Laboratory  
Southern Methodist University  
Dallas, TX 75275

Prof. Robert B. Herrmann  
Department of Earth & Atmospheric Sciences  
St. Louis University  
St. Louis, MO 63156

Prof. Bryan Isacks  
Cornell University  
Department of Geological Sciences  
SNEE Hall  
Ithaca, NY 14850

Dr. Rong-Song Jih  
Teledyne Geotech  
314 Montgomery Street  
Alexandria, VA 22314

Prof. Lane R. Johnson  
Seismographic Station  
University of California  
Berkeley, CA 94720

Prof. Alan Kafka  
Department of Geology & Geophysics  
Boston College  
Chestnut Hill, MA 02167

Prof. Fred K. Lamb  
University of Illinois at Urbana-Champaign  
Department of Physics  
1110 West Green Street  
Urbana, IL 61801

Prof. Charles A. Langston  
Geosciences Department  
403 Deike Building  
The Pennsylvania State University  
University Park, PA 16802

Prof. Thorne Lay  
Department of Geological Sciences  
1006 C.C. Little Building  
University of Michigan  
Ann Arbor, MI 48109-1063

Prof. Arthur Lerner-Lam  
Lamont-Doherty Geological Observatory  
of Columbia University  
Palisades, NY 10964

Dr. Christopher Lynnes  
Teledyne Geotech  
314 Montgomery Street  
Alexandria, VA 22314

Prof. Peter Malin  
University of California at Santa Barbara  
Institute for Crustal Studies  
Santa Barbara, CA 93106

Dr. Randolph Martin, III  
New England Research, Inc.  
76 Olcott Drive  
White River Junction, VT 05001

Dr. Gary McCartor  
Mission Research Corporation  
735 State Street  
P.O. Drawer 719  
Santa Barbara, CA 93102 (2 copies)

Prof. Thomas V. McEvilly  
Seismographic Station  
University of California  
Berkeley, CA 94720

Dr. Keith L. McLaughlin  
S-CUBED  
A Division of Maxwell Laboratory  
P.O. Box 1620  
La Jolla, CA 92038-1620

Prof. William Menke  
Lamont-Doherty Geological Observatory  
of Columbia University  
Palisades, NY 10964

Stephen Miller  
SRI International  
333 Ravenswood Avenue  
Box AF 116  
Menlo Park, CA 94025-3493

Prof. Bernard Minster  
IGPP, A-025  
Scripps Institute of Oceanography  
University of California, San Diego  
La Jolla, CA 92093

Prof. Brian J. Mitchell  
Department of Earth & Atmospheric Sciences  
St. Louis University  
St. Louis, MO 63156

Mr. Jack Murphy  
S-CUBED, A Division of Maxwell Laboratory  
11800 Sunrise Valley Drive  
Suite 1212  
Reston, VA 22091 (2 copies)

Dr. Bao Nguyen  
GL/LWH  
Hanscom AFB, MA 01731-5000

Prof. John A. Orcutt  
IGPP, A-025  
Scripps Institute of Oceanography  
University of California, San Diego  
La Jolla, CA 92093

Prof. Keith Priestley  
University of Nevada  
Mackay School of Mines  
Reno, NV 89557

Prof. Paul G. Richards  
Lamont-Doherty Geological Observatory  
of Columbia University  
Palisades, NY 10964

Dr. Wilmer Rivers  
Teledyne Geotech  
314 Montgomery Street  
Alexandria, VA 22314

Dr. Alan S. Ryall, Jr.  
Center for Seismic Studies  
1300 North 17th Street  
Suite 1450  
Arlington, VA 22209-2308

Prof. Charles G. Sammis  
Center for Earth Sciences  
University of Southern California  
University Park  
Los Angeles, CA 90089-0741

Prof. Christopher H. Scholz  
Lamont-Doherty Geological Observatory  
of Columbia University  
Palisades, NY 10964

Prof. David G. Simpson  
Lamont-Doherty Geological Observatory  
of Columbia University  
Palisades, NY 10964

Dr. Jeffrey Stevens  
S-CUBED  
A Division of Maxwell Laboratory  
P.O. Box 1620  
La Jolla, CA 92038-1620

Prof. Brian Stump  
Institute for the Study of Earth & Man  
Geophysical Laboratory  
Southern Methodist University  
Dallas, TX 75275

Prof. Jeremiah Sullivan  
University of Illinois at Urbana-Champaign  
Department of Physics  
1110 West Green Street  
Urbana, IL 61801

Prof. Clifford Thurber  
University of Wisconsin-Madison  
Department of Geology & Geophysics  
1215 West Dayton Street  
Madison, WS 53706

Prof. M. Nafi Toksoz  
Earth Resources Lab  
Massachusetts Institute of Technology  
42 Carleton Street  
Cambridge, MA 02142

Prof. John E. Vidale  
University of California at Santa Cruz  
Seismological Laboratory  
Santa Cruz, CA 95064

Prof. Terry C. Wallace  
Department of Geosciences  
Building #77  
University of Arizona  
Tucson, AZ 85721

Dr. Raymond Willeman  
GL/LWH  
Hanscom AFB, MA 01731-5000

Dr. Lorraine Wolf  
GL/LWH  
Hanscom AFB, MA 01731-5000

Prof. Francis T. Wu  
Department of Geological Sciences  
State University of New York  
at Binghamton  
Vestal, NY 13901

OTHERS (United States)

Dr. Monem Abdel-Gawad  
Rockwell International Science Center  
1049 Camino Dos Rios  
Thousand Oaks, CA 91360

Prof. Keiiti Aki  
Center for Earth Sciences  
University of Southern California  
University Park  
Los Angeles, CA 90089-0741

Prof. Shelton S. Alexander  
Geosciences Department  
403 Deike Building  
The Pennsylvania State University  
University Park, PA 16802

Dr. Kenneth Anderson  
BBNSTC  
Mail Stop 14/1B  
Cambridge, MA 02238

Dr. Ralph Archuleta  
Department of Geological Sciences  
University of California at Santa Barbara  
Santa Barbara, CA 93102

Dr. Thomas C. Bache, Jr.  
Science Applications Int'l Corp.  
10210 Campus Point Drive  
San Diego, CA 92121 (2 copies)

J. Barker  
Department of Geological Sciences  
State University of New York  
at Binghamton  
Vestal, NY 13901

Dr. T.J. Bennett  
S-CUBED  
A Division of Maxwell Laboratory  
11800 Sunrise Valley Drive, Suite 1212  
Reston, VA 22091

Mr. William J. Best  
907 Westwood Drive  
Vienna, VA 22180

Dr. N. Biswas  
Geophysical Institute  
University of Alaska  
Fairbanks, AK 99701

Dr. G.A. Bollinger  
Department of Geological Sciences  
Virginia Polytechnical Institute  
21044 Derring Hall  
Blacksburg, VA 24061

Dr. Stephen Bratt  
Science Applications Int'l Corp.  
10210 Campus Point Drive  
San Diego, CA 92121

Michael Browne  
Teledyne Geotech  
3401 Shiloh Road  
Garland, TX 75041

Mr. Roy Burger  
1221 Serry Road  
Schenectady, NY 12309

Dr. Robert Burrige  
Schlumberger-Doll Research Center  
Old Quarry Road  
Ridgefield, CT 06877

Dr. Jerry Carter  
Rondout Associates  
P.O. Box 224  
Stone Ridge, NY 12484

Dr. W. Winston Chan  
Teledyne Geotech  
314 Montgomery Street  
Alexandria, VA 22314-1581

Dr. Theodore Cherry  
Science Horizons, Inc.  
710 Encinitas Blvd., Suite 200  
Encinitas, CA 92024 (2 copies)

Prof. Jon F. Claerbout  
Department of Geophysics  
Stanford University  
Stanford, CA 94305

Prof. Robert W. Clayton  
Seismological Laboratory  
Division of Geological & Planetary Sciences  
California Institute of Technology  
Pasadena, CA 91125

Prof. F. A. Dahlen  
Geological and Geophysical Sciences  
Princeton University  
Princeton, NJ 08544-0636

Dr. Jeffrey W. Given  
Sierra Geophysics  
11255 Kirkland Way  
Kirkland, WA 98033

Prof. Anton W. Dainty  
Earth Resources Lab  
Massachusetts Institute of Technology  
42 Carleton Street  
Cambridge, MA 02142

Prof. Stephen Grand  
University of Texas at Austin  
Department of Geological Sciences  
Austin, TX 78713-7909

Prof. Adam Dziewonski  
Hoffman Laboratory  
Harvard University  
20 Oxford St  
Cambridge, MA 02138

Prof. Roy Greenfield  
Geosciences Department  
403 Deike Building  
The Pennsylvania State University  
University Park, PA 16802

Prof. John Ebel  
Department of Geology & Geophysics  
Boston College  
Chestnut Hill, MA 02167

Dan N. Hagedorn  
Battelle  
Pacific Northwest Laboratories  
Battelle Boulevard  
Richland, WA 99352

Eric Fielding  
SNEE Hall  
INSTOC  
Cornell University  
Ithaca, NY 14853

Kevin Hutchenson  
Department of Earth Sciences  
St. Louis University  
3507 Laclede  
St. Louis, MO 63103

Prof. Donald Forsyth  
Department of Geological Sciences  
Brown University  
Providence, RI 02912

Prof. Thomas H. Jordan  
Department of Earth, Atmospheric  
and Planetary Sciences  
Massachusetts Institute of Technology  
Cambridge, MA 02139

Prof. Art Frankel  
Mail Stop 922  
Geological Survey  
790 National Center  
Reston, VA 22092

Robert C. Kemerait  
ENSCO, Inc.  
445 Pineda Court  
Melbourne, FL 32940

Dr. Anthony Gangi  
Texas A&M University  
Department of Geophysics  
College Station, TX 77843

William Kikendall  
Teledyne Geotech  
3401 Shiloh Road  
Garland, TX 75041

Dr. Freeman Gilbert  
Inst. of Geophysics & Planetary Physics  
University of California, San Diego  
P.O. Box 109  
La Jolla, CA 92037

Prof. Leon Knopoff  
University of California  
Institute of Geophysics & Planetary Physics  
Los Angeles, CA 90024

Mr. Edward Giller  
Pacific Sierra Research Corp.  
1401 Wilson Boulevard  
Arlington, VA 22209

Prof. L. Timothy Long  
School of Geophysical Sciences  
Georgia Institute of Technology  
Atlanta, GA 30332



Prof. Art McGarr  
Mail Stop 977  
Geological Survey  
345 Middlefield Rd.  
Menlo Park, CA 94025

Dr. George Mellman  
Sierra Geophysics  
11255 Kirkland Way  
Kirkland, WA 98033

Prof. John Nabelek  
College of Oceanography  
Oregon State University  
Corvallis, OR 97331

Prof. Geza Nagy  
University of California, San Diego  
Department of Ames, M.S. B-010  
La Jolla, CA 92093

Prof. Amos Nur  
Department of Geophysics  
Stanford University  
Stanford, CA 94305

Prof. Jack Oliver  
Department of Geology  
Cornell University  
Ithaca, NY 14850

Prof. Robert Phinney  
Geological & Geophysical Sciences  
Princeton University  
Princeton, NJ 08544-0636

Dr. Paul Pomeroy  
Rondout Associates  
P.O. Box 224  
Stone Ridge, NY 12484

Dr. Jay Pulli  
RADIX System, Inc.  
2 Taft Court, Suite 203  
Rockville, MD 20850

Dr. Norton Rimer  
S-CUBED  
A Division of Maxwell Laboratory  
P.O. Box 1620  
La Jolla, CA 92038-1620

Prof. Larry J. Ruff  
Department of Geological Sciences  
1006 C.C. Little Building  
University of Michigan  
Ann Arbor, MI 48109-1063

Dr. Richard Sailor  
TASC Inc.  
55 Walkers Brook Drive  
Reading, MA 01867

Thomas J. Sereno, Jr.  
Science Application Int'l Corp.  
10210 Campus Point Drive  
San Diego, CA 92121

John Sherwin  
Teledyne Geotech  
3401 Shiloh Road  
Garland, TX 75041

Prof. Robert Smith  
Department of Geophysics  
University of Utah  
1400 East 2nd South  
Salt Lake City, UT 84112

Prof. S. W. Smith  
Geophysics Program  
University of Washington  
Seattle, WA 98195

Dr. Stewart Smith  
IRIS Inc.  
1616 North Fort Myer Drive  
Suite 1440  
Arlington, VA 22209

Dr. George Sutton  
Rondout Associates  
P.O. Box 224  
Stone Ridge, NY 12484

Prof. L. Sykes  
Lamont-Doherty Geological Observatory  
of Columbia University  
Palisades, NY 10964

Prof. Pradeep Talwani  
Department of Geological Sciences  
University of South Carolina  
Columbia, SC 29208

Prof. Ta-liang Teng  
Center for Earth Sciences  
University of Southern California  
University Park  
Los Angeles, CA 90089-0741

Dr. R.B. Tittmann  
Rockwell International Science Center  
1049 Camino Dos Rios  
P.O. Box 1085  
Thousand Oaks, CA 91360

Dr. Gregory van der Vink  
IRIS, Inc.  
1616 North Fort Myer Drive  
Suite 1440  
Arlington, VA 22209

William R. Walter  
Seismological Laboratory  
University of Nevada  
Reno, NV 89557

Dr. Gregory Wojcik  
Weidlinger Associates  
4410 El Camino Real  
Suite 110  
Los Altos, CA 94022

Prof. John H. Woodhouse  
Hoffman Laboratory  
Harvard University  
20 Oxford Street  
Cambridge, MA 02138

Dr. Gregory B. Young  
ENSCO, Inc.  
5400 Port Royal Road  
Springfield, VA 22151-2388

GOVERNMENT

Dr. Ralph Alewine III  
DARPA/NMRO  
1400 Wilson Boulevard  
Arlington, VA 01731-5000

Mr. James C. Battis  
GL/LWH  
Hanscom AFB, MA 22209-2308

Dr. Robert Blandford  
DARPA/NMRO  
1400 Wilson Boulevard  
Arlington, VA 87185

Eric Chael  
Division 9241  
Sandia Laboratory  
Albuquerque, NM 01731-5000

Dr. John J. Cipar  
GL/LWH  
Hanscom AFB, MA 01731-5000

Mr. Jeff Duncan  
Office of Congressman Markey  
2133 Rayburn House Bldg.  
Washington, D.C. 20515

Dr. Jack Evernden  
USGS - Earthquake Studies  
345 Middlefield Road  
Menlo Park, CA 94025

Art Frankel  
USGS  
922 National Center  
Reston, VA 22092

Dr. T. Hanks  
USGS  
Nat'l Earthquake Research Center  
345 Middlefield Road  
Menlo Park, CA 94025

Dr. James Hannon  
Lawrence Livermore Nat'l Laboratory  
P.O. Box 808  
Livermore, CA 94550

Paul Johnson  
ESS-4, Mail Stop J979  
Los Alamos National Laboratory  
Los Alamos, NM 87545

Janet Johnston  
GL/LWH  
Hanscom AFB, MA 01731-5000

Dr. Katharine Kadinsky-Cade  
GL/LWH  
Hanscom AFB, MA 01731-5000

Ms. Ann Kerr  
IGPP, A-025  
Scripps Institute of Oceanography  
University of California, San Diego  
La Jolla, CA 92093

Dr. Max Koontz  
US Dept of Energy/DP 5  
Forrestal Building  
1000 Independence Avenue  
Washington, DC 20585

Dr. W.H.K. Lee  
Office of Earthquakes, Volcanoes,  
& Engineering  
345 Middlefield Road  
Menlo Park, CA 94025

Dr. William Leith  
U.S. Geological Survey  
Mail Stop 928  
Reston, VA 22092

Dr. Richard Lewis  
Director, Earthquake Engineering & Geophysics  
U.S. Army Corps of Engineers  
Box 631  
Vicksburg, MS 39180

James F. Lewkowicz  
GL/LWH  
Hanscom AFB, MA 01731-5000

Mr. Alfred Lieberman  
ACDA/VI-OA State Department Bldg  
Room 5726  
320 - 21st Street, NW  
Washington, DC 20451

Stephen Mangino  
GL/LWH  
Hanscom AFB, MA 01731-5000

Dr. Frank F. Pilotte  
HQ AFTAC/TT  
Patrick AFB, FL 32925-6001

Dr. Robert Masse  
Box 25046, Mail Stop 967  
Denver Federal Center  
Denver, CO 80225

Katie Poley  
CIA-OSWR/NED  
Washington, DC 20505

Art McGarr  
U.S. Geological Survey, MS-977  
345 Middlefield Road  
Menlo Park, CA 94025

Mr. Jack Rachlin  
U.S. Geological Survey  
Geology, Rm 3 C136  
Mail Stop 928 National Center  
Reston, VA 22092

Richard Morrow  
ACDA/VI, Room 5741  
320 21st Street N.W  
Washington, DC 20451

Dr. Robert Reinke  
WL/NTEG  
Kirtland AFB, NM 87117-6008

Dr. Keith K. Nakanishi  
Lawrence Livermore National Laboratory  
P.O. Box 808, L-205  
Livermore, CA 94550

Dr. Byron Ristvet  
HQ DNA, Nevada Operations Office  
Attn: NVCG  
P.O. Box 98539  
Las Vegas, NV 89193

Dr. Carl Newton  
Los Alamos National Laboratory  
P.O. Box 1663  
Mail Stop C335, Group ESS-3  
Los Alamos, NM 87545

Dr. George Rothe  
HQ AFTAC/TGR  
Patrick AFB, FL 32925-6001

Dr. Kenneth H. Olsen  
Los Alamos Scientific Laboratory  
P.O. Box 1663  
Mail Stop C335, Group ESS-3  
Los Alamos, NM 87545

Dr. Michael Shore  
Defense Nuclear Agency/SPSS  
6801 Telegraph Road  
Alexandria, VA 22310

Howard J. Patton  
Lawrence Livermore National Laboratory  
P.O. Box 308, L-205  
Livermore, CA 94550

Donald L. Springer  
Lawrence Livermore National Laboratory  
P.O. Box 808, L-205  
Livermore, CA 94550

Mr. Chris Paine  
Office of Senator Kennedy, SR 315

United States Senate  
Washington, DC 20510

Dr. Lawrence Turnbull  
OSWR/NED  
Central Intelligence Agency, Room 5G48  
Washington, DC 20505

Colonel Jerry J. Perrizo  
AFOSR/NP, Building 410  
Bolling AFB  
Washington, DC 20332-6448

Dr. Thomas Weaver  
Los Alamos National Laboratory  
P.O. Box 1663, Mail Stop C335  
Los Alamos, NM 87545

J.J. Zucca  
Lawrence Livermore National Laboratory  
Box 808  
Livermore, CA 94550

Defense Technical Information Center  
Cameron Station  
Alexandria, VA 22314 (5 copies)

GL/SULL  
Research Library  
Hanscom AFB, MA 01731-5000 (2 copies)

Defense Intelligence Agency  
Directorate for Scientific &  
Technical Intelligence  
Washington, DC 20301

Secretary of the Air Force (SAFRD)  
Washington, DC 20330

AFTAC/CA  
(STINFO)  
Patrick AFB, FL 32925-6001

Office of the Secretary Defense  
DDR & E  
Washington, DC 20330

TACTEC  
Battelle Memorial Institute  
505 King Avenue  
Columbus, OH 43201 (Final Report Only)

HQ DNA  
Attn: Technical Library  
Washington, DC 20305

Mr. Charles L. Taylor  
GL/LWH

Hanscom AFB, MA 01731-5000

DARPA/RMO/RETRIEVAL  
1400 Wilson Boulevard  
Arlington, VA 22209

DARPA/RMO/Security Office  
1400 Wilson Boulevard  
Arlington, VA 22209

Geophysics Laboratory  
Attn: XO  
Hanscom AFB, MA 01731-5000

Geophysics Laboratory  
Attn: LW  
Hanscom AFB, MA 01731-5000

DARPA/PM  
1400 Wilson Boulevard  
Arlington, VA 22209

CONTRACTORS (Foreign)

Dr. Ramon Cabre, S.J.  
Observatorio San Calixto  
Casilla 5939  
La Paz, Bolivia

Prof. Hans-Peter Harjes  
Institute for Geophysik  
Ruhr University/Bochum  
P.O. Box 102148  
4630 Bochum 1, FRG

Prof. Eystein Husebye  
NTNF/NORSAR  
P.O. Box 51  
N-2007 Kjeller, NORWAY

Prof. Brian L.N. Kennett  
Research School of Earth Sciences  
Institute of Advanced Studies  
G.P.O. Box 4  
Canberra 2601, AUSTRALIA

Dr. Bernard Massinon  
Societe Radiomana  
27 rue Claude Bernard  
75005 Paris, FRANCE (2 Copies)

Dr. Pierre Mecheler  
Societe Radiomana  
27 rue Claude Bernard  
75005 Paris, FRANCE

Dr. Svein Mykkeltveit  
NTNF/NORSAR  
P.O. Box 51  
N-2007 Kjeller, NORWAY

FOREIGN (Others)

Dr. Peter Basham  
Earth Physics Branch  
Geological Survey of Canada  
1 Observatory Crescent  
Ottawa, Ontario, CANADA K1A 0Y3

Dr. Fekadu Kebede  
Seismological Section  
Box 12019  
S-750 Uppsala, SWEDEN

Dr. Eduard Berg  
Institute of Geophysics  
University of Hawaii  
Honolulu, HI 96822

Dr. Tormod Kvaerna  
NTNF/NORSAR  
P.O. Box 51  
N-2007 Kjeller, NORWAY

Dr. Michel Bouchon  
I.R.I.G.M.-B.P. 68  
38402 St. Martin D'Herès  
Cedex, FRANCE

Dr. Peter Marshal  
Procurement Executive  
Ministry of Defense  
Blacknest, Brimpton  
Reading FG7-4RS, UNITED KINGDOM

Dr. Hilmar Bungum  
NTNF/NORSAR  
P.O. Box 51  
N-2007 Kjeller, NORWAY

Prof. Ari Ben-Menahem  
Department of Applied Mathematics  
Weizman Institute of Science  
Rehovot, ISRAEL 951729

Dr. Michel Campillo  
Observatoire de Grenoble  
I.R.I.G.M.-B.P. 53  
38041 Grenoble, FRANCE

Dr. Robert North  
Geophysics Division  
Geological Survey of Canada  
1 Observatory Crescent  
Ottawa, Ontario, CANADA K1A 0Y3

Dr. Kin Yip Chun  
Geophysics Division  
Physics Department  
University of Toronto  
Ontario, CANADA M5S 1A7

Dr. Frode Ringdal  
NTNF/NORSAR  
P.O. Box 51  
N-2007 Kjeller, NORWAY

Dr. Alan Douglas  
Ministry of Defense  
Blacknest, Brimpton  
Reading RG7-4RS, UNITED KINGDOM

Dr. Jorg Schlittenhardt  
Federal Institute for Geosciences & Nat'l Res.  
Postfach 510153  
D-3000 Hannover 51, FEDERAL REPUBLIC OF  
GERMANY

Dr. Roger Hansen  
NTNF/NORSAR  
P.O. Box 51  
N-2007 Kjeller, NORWAY

Prof. Daniel Walker  
University of Hawaii  
Institute of Geophysics  
Honolulu, HI 96822

Dr. Manfred Henger  
Federal Institute for Geosciences & Nat'l Res.  
Postfach 510153  
D-3000 Hanover 51, FRG

Ms. Eva Johannisson  
Senior Research Officer  
National Defense Research Inst.  
P.O. Box 27322  
S-102 54 Stockholm, SWEDEN